

UNIVERSITY OF BIRMINGHAM

POLYMERIC NANOPARTICLES AS DRUG DELIVERY SYSTEMS FOR BLOOD-BRAIN BARRIER PERMEATION

Eirini Epitropaki

Supervisors: Prof. Rachel K. O'Reilly, Dr. Amanda K. Pearce and Prof. Andrew Dove

A thesis submitted to The University of Birmingham for the degree of

Doctor of Philosophy

DEPARTMENT OF CHEMISTRY

2024

UNIVERSITY OF
BIRMINGHAM

University of Birmingham Research Archive

e-theses repository

This unpublished thesis/dissertation is copyright of the author and/or third parties. The intellectual property rights of the author or third parties in respect of this work are as defined by The Copyright Designs and Patents Act 1988 or as modified by any successor legislation.

Any use made of information contained in this thesis/dissertation must be in accordance with that legislation and must be properly acknowledged. Further distribution or reproduction in any format is prohibited without the permission of the copyright holder.

Table of Contents

List of Figures 4

Acknowledgments 10

Abbreviations 12

Abstract 15

CHAPTER 1-Introduction to polymers and nanoparticles for Blood Brain Barrier permeation 15

1.1 Diseases and Treatments across the blood and brain barrier 16

1.2 Permeation through the Blood and Brain Barrier (BBB) 19

1.3 Ring Opening Polymerization 23

1.4 Reversible addition-fragmentation chain transfer 25

1.5 Packing parameter 27

1.6 Different techniques of self-assembly 29

1.7 Crystallization Driven Self Assembly 33

1.8 Polymerisation Induced Self Assembly 35

1.9 Cytotoxicity Studies 36

1.10 Protein corona 38

1.11 *In vitro* BBB 40

1.12 References 42

CHAPTER 2- Exploring self-assembled polymeric systems depending on dynamic and kinetic equilibrium 51

2.1 Introduction 52

2.1.1 Diblock copolymers for drug delivery 52

2.1.2 Packing parameter 53

2.1.3 Self-assembly techniques and parameters 53

2.1.4 Fluorescent nanoparticles 55

2.1.5 Protein corona formation 56

2.2 Results & Discussion 58

2.2.1 Synthesis of Poly(lactide) 58

2.2.2 Synthesis of positively charged diblock copolymer PDMAEMA-b-PLLA 62

2.2.3 Self-assembly of block copolymers with positive charge 69

2.2.4 Self-assembly in biological media of positively charge NPs 75

2.2.5 Self-assembly of block copolymers with neutral charged 88

2.2.6 Self-assembly of block copolymers with negative charged 96

2.3 Conclusions 98

2.4 Materials & Methods 99

Materials 99

Methods 101

2.5 References 132

CHAPTER 3-Crystallization Driven Self-assembly of Diblock Copolymers 131
3.1 Introduction 142

3.1.2 Multilayer crystals 147

3.1.3 Edge and screw dislocations 148

3.2 Results and Discussion 150

3.2.1 Positively charged microstructures. 150

3.2.1.1 Positively charged diamond shaped nanoparticles 151

3.2.1.2 Optimisation of size of positively charged microstructures 155

3.2.1.3 Protein Corona effect 158

3.2.1.4 Morphological variations of positively charged nanoparticles. 167

3.2.2. Neutrally charged microstructures 170

3.2.2.1 PDMA microstructures through CDSA 171

3.2.2.2 PTEGA microstructures through CDSA 173

3.2.3 Negatively charged microstructures 177

3.2.3.1 Negatively charged cylinders 177

3.2.3.2 Protein corona effect of negatively charged cylinders 178

3.3 Conclusions 180

3.4 Experimental 182

Materials 182

Methods 186

3.5 References 196

Chapter 4-Polymerisation induced self-assembly nanoparticles for blood and brain barrier permeation 204
4.1 Introduction 207

4.1.1 Polymerization induced self-assembly (PISA) 207

4.1.2 PISA assembly, and morphological kinetics 208

4.1.3 Polymeric nanoparticles for BBB permeation 209

4.1.4 Biological evaluation of BBB and assessment of permeation 210

4.2 Results and Discussion 212

4.2.1 Synthesis and characterization of PISA nanoparticles 212
4.2.2. Fluorescent tagging of PISA nanoparticles 220
4.2.3 Protein tagging of PISA nanoparticles 224
4.2.4 Quantification of internalized nanoparticles 229
4.2.5 Permeability evaluation of an *in vitro* BBB 233
4.2.6 Transferrin receptor efficiency for nanoparticles permeation 244
4.3 Conclusions 245
4.4 Experimental 247
Materials 247
Methods 250
4.5 References 256

CHAPTER 5- Conclusions and future work 263
5.1 Overview 266
5.2 Conclusions 266
5.2.1 Diblock copolymers & protein corona limitations 266
5.2.2 CDSA microstructures & protein corona limitations 267
5.2.3 PISA NPs and BBB permeation 268
5.3 Future work 269

List of Figures

Figure 1.1 Various methodologies for drug delivery across the BBB. Passive diffusion utilised of small molecules and lipophilic drugs(left), Invasive methods interrupting the BBB like ultrasound or osmotic (central), non-invasive like nanoparticles (right). Adapted from Mishra *et al.*[7] 18
Figure 1.2 A) Composition of BBB, B) Disruption of BBB due to a pathological disease [23] (recreated with permission) 20
Figure 1.3 Ring-opening polymerisation of L-lactide using a thiourea/(-)-sparteine 24
Figure 1.4 Proposed mechanism of ROP with DBU organic catalyst for PLLA synthesis[41] 24
Figure 1.5 Mechanism of RAFT polymerization 26
Figure 1.6 Various structures arise according to the packing parameter (red hydrophobic block with l_c representing the length and v the volume, a_0 is defined as the optimal area of the hydrophilic interface. Reproduced with permission from ref [49] 28
Figure 2.1. ^{1}H NMR spectrum ($CDCl_3$, 300 MHz) of poly (L-lactide)$_{37}$ 60

Figure 2.2. Representation of molecular weight distribution from THF SEC of poly(L-lactide)$_{37}$ (λ = 309 nm). 60
Figure 2.3. Maldi-TOF mass spectroscopy of poly(L-lactide)$_{37}$ in dithranol matrix with THF as solvent 62
Figure 2.4. ^{1}H NMR spectrum ($CDCl_3$, 300 MHz) of poly(L-lactide)$_{37}$ -b-poly(N,N-dimethylaminoethyl methacrylate)$_{225}$ diblock copolymers. 64
Figure 2.5. Representation of Molecular weight distribution from THF GPC of poly(L-lactide)$_{37}$-b-poly(N,N-dimethylaminoethyl methacrylate)$_{225}$ diblock copolymers (λ = 309 nm). 64
Figure 2.6. ^{1}H NMR spectrum ($CDCl_3$, 300 MHz) of fluorescent Macro CTA 66
Figure 2.7. Representation of Molecular weight distribution from Chloroform GPC of fluorescent Macro CTA Poly(L-lactide)$_{36}$ (λ=309 nm) 66
Figure 2.8 MALDI-TOF analysis of fluorescent Macro CTA Poly(L-lactide)$_{36}$ 67
Figure 2.9. ^{1}H NMR spectrum ($CDCl_3$, 300 MHz) of fluorescent PLLA$_{36}$-b-PDMAEMA$_{204}$ 68
Figure 2.10. Representation of Molecular weight distribution from chloroform SEC of poly(L-lactide)$_{36}$-b-poly(N,N-dimethylaminoethyl methacrylate)$_{204}$ diblock copolymers. (λ=309 nm) 69
Figure 2.11 DLS data of self-assembly of P2 in DMF with flash nanoprecipitation, freeze drying, slow addition. (errors bar represent standard deviation) 70
Figure 2.12 DLS data of P3 FNP(left), after freeze dry (right) 71
Figure 2.13. TEM DATA of P3 after FNP (sample of 20),scale bar 500 nm (left), scale bar 1000 nm (right) 72
Figure 2.14 DLS and AFM data of a,c) P2 and b,d) P1 after FNP (errors represent standard deviation) 72
Figure 2.15 Microfluidics of P3 and P4 and filtration effect (1st population in black and 2nd population in red) 74
Figure 2.16.DLS results of (A) P2 (B) P1 spheres in different temperatures of 25℃, 36.5℃, 36.5℃ for 24hrs and 36.5℃ for 24hrs with BSA 4mg/ mL. 75
Figure 2.17. A) D_h sizes of PDMAEMA$_{200}$-b-PDLLA$_{30}$ with ACM probe in various biological media B) DLS measurements of PDMAEMA$_{200}$-b-PDLLA$_{30}$ with ACM probe self-assembled in BSA 4 mg/mL 77
Figure 2.18. AFM images of 1 mg/mL (left) and 0.25 mg/mL (right) of the water self-assembled diblock PDMAEMA$_{200}$-b-PDLLA$_{30}$ 78
Figure 2.19. Protein corona formation of PDMAEMA$_{200}$-b-PDLLA$_{30}$ particles at 2 μm (left) and at 1 μm (right). 78
Figure 2.20. DLS graphs of A) Self-assembled P4 with FNP in Acetone B) Protein corona addition to P4 NPs. 81
Figure 2.21. Self-assembly of spherical particles and afterwards addition of BSA-Cy5 DIALYZED ACM probe channel (up left), Cy5 channel(up right), both channels (down) 82
Figure 2.22. A)DLS measurements of PDMAEMA$_{200}$-b-PDLLA$_{30}$ self-assembled with 4 mg/mL BSA-Cy5, B) Dialysed sampled with the excess of BSA-Cy5 removed 84
Figure 2.23. Self-assembly of spherical particles with 4mg/mL addition of BSA-Cy5 overlap of channels (green+red). 84
Figure 2.24. Self-assembly of spherical particles with 4mg/mL addition of BSA-Cy5 after DIALYSIS. ACM probe channel (up left), Cy5 channel (up right), no channel (down left), and both channels (down right) area 3 85
Figure 2.25. ITC experiment of BSA protein attaching to PDMAEMA$_{204}$-b-PLLA$_{30}$ nanoparticles 86

Figure 2.26. Comparison of different nanoparticle size prepared by flash nanoprecipitation of neutrally charged polymers (error bars represent standard deviation of 3 consecutive runs of 100 measurements) 89
Figure 2.27. Comparison of different self-assembly methods with PNIPAM diblock copolymers, a) $PNIPAM_{136}$-$PLLA_{40}$ self-assembly, b) $PNIPAM_{110}$-$PLLA_{30}$ self-assembly with FNP (black), microfluidics reactor (red), slow addition (blue) (errors bar represent standard deviation)..... 91
Figure 2.28 DLS measurements of $PDMA_{87}$-b-$PLLA_{30}$, $PTEGA_{63}$-b-$PLLA_{36}$ (non fl) & $PTEGA_{82}$-b-$PLLA_{45}$ (fl) at 25°C, 36.5°C and with BSA at 36.5°C 92
Figure 2.2.29. Zebrafish studies of acute toxicity of $PDMA_{88}$-b-$PLLA_{30}$..... 94
Figure 2.2.30. Chronic toxicity in zebrafish of $PDMA_{88}$-b-$PLLA_{30}$ nanoparticles 95
Figure 2.31. AFM image of PAA_{486}-b-$PLLA_{30}$ 98
Figure 2.4.1. Synthesis of 2-cyano-5-hydroxypentan-2-yl ethyl carbonotrithioate (CEP) RAFT-agent initiator..... 101
Figure 2.4.2. ^{1}H NMR (300MHz, $CDCl_3$) 2-cyano-5-hydroxypentan-2-yl ethyl carbonotrithioate (CEP) RAFT-agent initiator 103
Figure 2.4.3. ^{13}C NMR of 2-cyano-5-hydroxypentan-2-yl ethyl carbonotrithioate (CEP) RAFT-agent initiator..... 104
Figure 2.4.4. Synthesis of 2-cyano-5-(3,4-dichloro-2,5-dioxo-2,5-dihydro-1H-pyrrol-1-yl)pentan-2-yl ethyl carbonotrithioate..... 105
Figure 2.4.5. Synthesis of fluorescent CTA..... 106
Figure 2.4.6. ^{1}H NMR (300MHz, $CDCl_3$) spectrum of 2-cyano-5-(3,4-dichloro-2,5-dioxo-2,5-dihydro-1H-pyrrol-1-yl)pentan-2-yl ethyl carbonotrithioate..... 107
Figure 2.4.7. ^{13}C NMR spectrum of 2-cyano-5-(3,4-dichloro-2,5-dioxo-2,5-dihydro-1H-pyrrol-1-yl)pentan-2-yl ethyl carbonotrithioate 108
Figure 2.4.8. ^{1}H NMR (300MHz, $CDCl_3$) spectrum of 5-(3-chloro-4-((2-hydroxyethyl)amino)-2,5-dioxo-2,5-dihydro-1H-pyrrol-1-yl)-2-cyanopentan-2-yl ethyl carbonotrithioate (fluorescent CTA)..... 109
Figure 2.4.9. ^{13}C (DOWN) spectrum of 5-(3-chloro-4-((2-hydroxyethyl)amino)-2,5-dioxo-2,5-dihydro-1H-pyrrol-1-yl)-2-cyanopentan-2-yl ethyl carbonotrithioate (fluorescent CTA)..... 110
Figure 2.4.10.Scheme of ROP of DL-Lactide and ^{1}H NMR (300MHz, $CDCl_3$) and $CHCl_3$ GPC characterization 111
Figure 2.4.11. Synthesis of diblock $PDMAEMA_{200}$-b-$PDLLA_{30}$ with fluorescent probe 113
Figure 2.4.12. 1^{H} NMR spectrum of $PDMAEMA_{200}$-b-PD,LLA_{30} with fluorescent probe..... 113
Figure 4.13. Representation of Molecular weight distribution from chloroform GPC (λ=309 nm) of $PDMAEMA_{200}$-b-$PDLLA_{30}$..... 114
Figure 4.14. Synthesis of diblock $PDMAEMA_{199}$-b-$PDLLA_{36}$ 114
Figure 4.15. ^{1}H NMR (300MHz, $CDCl_3$) of diblock $PDMAEMA_{199}$-b-PD,LLA_{36}..... 115
Figure 4.16. Representation of Molecular weight distribution from chloroform GPC (λ=309 nm) of $PDMAEMA_{199}$-b-$PDLLA_{36}$..... 116
Figure 4.17 Synthesis of diblock $PTEGA_{28}$-b-PD,LLA_{30} 116
Figure 4.18. ^{1}H NMR (300MHz, $CDCl_3$) of diblock $PTEGA_{28}$-b-PD,LLA_{30} with fluorescent probe..... 117
Figure 4.19. Representation of Molecular weight distribution from chloroform GPC (λ=309 nm) of $PTEGA_{28}$-b-PD,LLA_{30} with fluorescent probe..... 118
Figure 4.20. Synthesis of $PTEGA_{65}$ -b-P D,LLA_{36}..... 118
Figure 4.21. ^{1}H NMR (300MHz, $CDCl_3$) of diblock $PTEGA_{65}$-b-PD,LLA_{36} 119
Figure 4.22. Representation of Molecular weight distribution from chloroform GPC (λ=309 nm) of $PTEGA_{65}$-b-PD,LLA_{36} 120

Figure 4.23 ^{1}H NMR (300MHz, $CDCl_3$) of clean. poly(D, L-lactide)27-b-poly(N,N-dimethylacrylamide)57 diblock copolymers 125
Figure 4.24.Representation of Molecular weight distribution from chloroform GPC (λ=309 nm) of poly(D, L-lactide)$_{27}$-b-poly(N,N-dimethylacrylamide)$_{57}$ diblock copolymers..... 126
Figure 4.25. ^{1}H NMR (300MHz, $CDCl_3$) of clean. poly(D, L-lactide)$_{27}$-b-poly(TEGA) diblock copolymer. 127
Figure 4.26. Representation of Molecular weight distribution from chloroform GPC (λ=309 nm) of poly(D, L-lactide)$_{27}$-b-poly(TEGA)$_{47}$ diblock copolymers 128
Figure 4.27.RAFT polymerization 130
Figure 4.28. ^{1}H NMR spectra (300MHz) of clean $PLLA_{30}$-b-$PDMA_{87}$ 130
Figure 4.29. Representation of Molecular weight distribution from chloroform GPC (λ=309 nm) of poly(L-lactide)$_{30}$-b-poly(N,N-dimethylacrylamide)$_{87}$ diblock copolymers 131
Figure 3.1.1. Crystallization Driven Self-Assembly (CDSA) morphologies and applications[167] (figure adapted with permission from C. Zhu *et al*)..... 143
Figure 3.1.2 Schematic representation molecular ties forming a multilayer lamella and TEM data of PLLA crystal demonstrating the phenomenon[187, 188] adapted from Chen *et al* [187]..... 147
Figure 3.1.3. Schematic representation of screw dislocation[188, 191] and TEM micrograph depicting the screw dislocation of PLLA crystal presented by Chen and coworkers[187] 148
Figure 3.2.1. DLS graph of (a) non-fluorescent $PLLA_{37}$-b-$PDMAEMA_{225}$ in diamond morphology in water with pH 6.5 and (b) of fluorescent $PLLA_{36}$-b- $PDMAEMA_{204}$ with ACM probe in diamond morphology and redispersed in water with pH 6.5 152
Figure 3.2.2 AFM images of non-fluorescent $PLLA_{37}$-b-$PDMAEMA_{225}$ (left) and of fluorescent $PLLA_{36}$-b-$PDMAEMA_{204}$ with ACM probe (right) with dispersed media water pH 6.5 with concentration 0.25 mg/mL, scale bar 1µm (up) and 2 µm (down)..... 154
Figure 3.2.3. TEM results of optimisation of non-fluorescent $PLLA_{37}$-b-$PDMAEMA_{225}$ (a,c) and of fluorescent $PLLA_{36}$-b- $PDMAEMA_{204}$ with ACM probe (b,d) diamond shaped nanoparticles with scale bar 5 µm (up) and scale bar 2 µm (down)..... 156
Figure 3.2.4 Statistical analysis from TEM images on the optimisation of non-fluorescent $PLLA_{37}$-b-$PDMAEMA_{225}$ (left) and of fluorescent $PLLA_{36}$-b- $PDMAEMA_{204}$ with ACM probe (right) diamond-shaped structures (sample of 100)..... 157
Figure 3.2.5. Screw dislocation of fluorescent $PLLA_{36}$-b- $PDMAEMA_{204}$ with ACM probe dispersed in water with pH 6.5, scale bar 2000 nm. 158
Figure 3.2.6. Protein corona effect with molar ratio 1:1 (a, c) Fluorescent $PLLA_{36}$-b- $PDMAEMA_{204}$ diamond-shaped microstructures in water pH 6.5 , (b, d)BSA, scale bar 1000 nm. 159
Figure 3.2.7. Protein corona effect with molar ratio 1:0.25 (a, c) Fluorescent $PLLA_{36}$-b- $PDMAEMA_{204}$ diamond-shaped microstructures in water pH 6.5 , (b, d)BSA, scale bar 2000 nm 161
Figure 3.2.8. Confocal image of fluorescent $PDMAEMA_{204}$-b-$PLLA_{36}$ with ACM probe and BSA-Cy5 1:1 molar ratio prior to dialysis 0.05 mg/mL concentration a) composite of green and red channel, b)green channel ACM probe fluorophore emission(533nm), c) red channel Cy5 fluorophore emission (644nm), d) microscope image, scale bar 4µm 162
Figure 3.2.9. Confocal image of fluorescent $PDMAEMA_{204}$-b-$PLLA_{36}$ with ACM probe and BSA-Cy5 1:1 molar ratio 0.05 mg/mL concentration a)red channel Cy5 fluorophore emission (644nm), b)green channel ACM probe fluorophore emission(533nm), c)composite of green and red channel, d) microscope image, scale bar 2µm..... 163
Figure 3.2.10. Confocal image of fluorescent $PDMAEMA_{204}$-b-$PLLA_{36}$ with ACM probe and BSA-Cy5 1:0.25 molar ratio 0.05 mg/mL concentration a)red channel Cy5 fluorophore emission, b)green

channel ACM probe fluorophore emission, c)composite of green and red channel, d) microscope image, scale bare 3µm 164
Figure 3.2.11. ITC experiment of $PLLA_{36}$-b- $PDMAEMA_{204}$ diamond shaped nanoparticles with BSA as ligand in water pH 6.5. A) Heat rate of the titration. B) Normalized heats from each titration step corrected by the heats of dilution (filled spheres) together with a fit corresponding to an independent binding model (straight line). Visual representation of the parameters obtained by ITC experiments within the adsorption isotherm. KD is derived from the curve's slope in its inflection point, ΔH is represented by the difference between the curve's upper and lower plateaus (blue line) and N is the binding sites at the curve's inflection point (orange line). 165
Figure 3.2.12. AFM image of non-fluorescent $PLLA_{37}$-b-$PDMAEMA_{225}$ (right) and of fluorescent $PLLA_{36}$-b- $PDMAEMA_{204}$ with ACM probe (left) at 60^{o}C for 2.5 hours in ethanol.(concentration 0.2 mg/mL in water) 168
Figure 3.2.13. AFM image of non-fluorescent $PLLA_{37}$-b-$PDMAEMA_{225}$ (right) and of fluorescent $PLLA_{36}$-b- $PDMAEMA_{204}$ with ACM probe (left) at 60 ^{o}C for 36 hours in ethanol.(concentration 0.2 mg/mL in water) ,scale bar 1um (up), 500nm (down) 169
Figure 3.2.14 CDSA microstructures of PDMA-b-PLLA a) $PDMA_{69}$-b-$PLLA_{40}$ 1:2 core : corona ratio, b) $PDMA_{88}$-b-$PLLA_{30}$ 1:3 core : corona ratio, c) $PDMA_{527}$-b-$PLLA_{40}$ 1:13 core : corona ratio..... 172
Figure 3.2.15 CDSA microstructure of PTEGA-b-PLLA a) 5µm scale bar b) 1µm scale bar..... 176
Figure 3.2.16 TEM data of PAA_{63}-b-$PLLA_{32}$-b-PAA_{63} a) 0.2 mg/mL concentration, scale bar 1000nm ,b) 0.05 mg/mL concentration, scale bar 1000nm 178
Figure 3.2.17. TEM data of protein corona effect of lysozyme with PAA_{63}-b-$PLLA_{32}$-b-PAA_{63} cylinders 1:1 molar ratio. a,b) scale bar 500 nm, c,d,e) scale bar 200 nm. 179
Figure 4.1.1 . Photo and Thermo initiated PISA structures and packing parameter. [217] (Adapted with permission)..... 208
Figure 4. 2.1. PISA NPs DLS size measurements in nm (based on intensity data) at RT in water pH = 7 216
Figure 4.2.2. Zeta Potential measurements of PISA NPs at RT in water pH = 7..... 217
Figure 4.2.3. TEM measurements of PISA NPs in water pH = 7(scale bar 500nm) (D-diameter, size measurements from sample of 100)..... 218
Figure 4.2.4. 3T3 NIH cell viability studies of PISA NPs 48hours concentrations 1-0.01 mg/mL. (Control is define as the untreated cell lines) 219
Figure 4.2.5. TEM data of fluorescent NPs a)PDMA b)PAA and c)PQDMAE..... 222
Figure 4.2.6. Endothelial cell line cytotoxicity $CD34^{+}$ of PISA nanoparticles with BODIPY fluorophore. (Control is define as the untreated cell lines) 223
Figure 4.2.7 Maldi-Tof spectra of PISA NPs attached with Transferrin. Matrix used Sinapinic acid 1:1 225
Figure 4.2.8. TEM of PISA NPs a,b,c) PDMA Tf, PQDMAE Tf, PAA Tf scale bar 1000nm, d,e,f) PDMA Tf, PQDMAE Tf, PAA Tf scale bar 500nm..... 228
Figure 4.2.9. Endothelial cell line cytotoxicity $CD34^{+}$ of PISA nanoparticles with BODIPY fluorophore and Transferrin coating A) 1mg/mL concentration B) PQDMAE Tf 0.01 mg/mL concentration. Blank is defined as untreated $CD34^{+}$ cells. 229
Figure 4.2.10. Live imaging fluorescence data from incell of seeded NPs for 24 hours in CD34+ cell line a)control (no nps) b) PDMA 1mg/mL c) PDMA Tf 1mg/mL d) PAA 1mg/mL e)PAA Tf 1mg/mL f)PQDMAE 0.01 mg/mL g)62 1mgm/mL h)62 Tf 1mg/mL i)75 1mg/mL j) 75 Tf 1mg/mL k)PQDMAE Tf 0.01 mg/mL (green) BODIPY™ FL hydrazide, Nucleus (blue) Hoechst blue, Lysozyme tracker (red) lysosomes..... 230

Figure 4.2.11. Colocalization fluorescence of lysotracker with BODIPY analysis of PISA NPs 232
Figure 4.2.12 Integrity of *in vitro* BBB validation via TEER , LY and Presto blue 236
Figure 2.13 Confocal image of ECs of 0.4µm *in vitro* BBB internalisation evaluation..... 238
Figure 4.2.14 BBB integrity investigation via TEER, LT and Presto blue PISA NPs 1 mg/mL 241
Figure 4.2.15. Confocal microscopy data of 24hours seeded BBB model ($CD34^+$monolayer with tight junctions developed) a)PDMA 1 mg/mL b) PAA 1mg/mL, c) PAA Tf 1 mg/mL, d) 62 1mg/mL and e) 75 1mg/mL, f) 75 Tf 1mg/mL NPs (green) BODIPY™ FL EDA, Nucleus (blue) DAPI , Membrane (red) Anti-Rabbit antibody Alexa 555 243
Figure 4.2.16. Transferrin receptor in CD34+, in CD34+ in conditioned pericyte media and in an *in vitro* BBB environment. Data analysed with flow cytometry, incell and confocal..... 244
Figure 4.4.1. Emission- excitation graphs after addition of BODIPY in PISA NPs..... 252

List of Schemes

Scheme 1. Self-assembly methods a) flash nanoprecipitation, b) slow addition with syringe pump .. 29
Scheme 2. Microfluidics device to self-assemble nanoparticles. Polymer must be completely dissolved in a good solvent. The device consists of a syringe pump that can determine the mixing ratio and PTFE tubing, and tubing connector that constitutes as the micromixer. 32
Scheme 3.Variables affecting nanoparticles-biomolecules interactions[89] (recreated with permission) 38
Scheme 4. Protein corona formation due to interactions. 39
Scheme 5. *In vitro* BBB biculture in a transwell filter of endothelial cells in the Upper layer and pericytes in the basolateral layer. 41
Scheme 6. Representation of ROP of L-lactide 59
Scheme 7. Reaction scheme of poly(L-lactide)$_{37}$ -b-poly(N,N-dimethylaminoethyl methacrylate)$_{225}$ diblock copolymers. 62
Scheme 8. ROP of L-Lactide with fluorescent initiator 65
Scheme 9. Reaction scheme of poly (L-lactide)-b-poly (N,N-dimethylaminoethyl methacrylate) fluorescent diblock copolymers. 68
Scheme 10. Attachment of Cy5 ester dye to BSA. 79
Scheme 11. Self-assembly of spherical particles and afterwards addition of BSA-Cy5. 80
Scheme 12. Direct Self-assembly of spherical particles with addition of 4mg/mL BSA-Cy5 83
Scheme 3.1.13. Hierarchical self-assembly and Crystallization Driven Self-assembly (CDSA)..... 145
Scheme 14 CDSA of TEGA-b-PLLA 175
Scheme 15. A) Representation of *in vitro* BBB with CD34+ brain like endothelial cells (human derived) seeded on matrix gel in the Upper compartment and pericytes in the lower one. B) Visualization of transport efficiency experiment, measuring media every 2 & 24 hours 211
Scheme 16. Reaction scheme of EDC coupling of BODIPY™ FL hydrazide reacting with the carbonyl group of PDMA NPs..... 220

Scheme 17. EDC coupling of Holo Transferrin on PISA NPs (PDMA model) 224
Scheme 18. Internalization experiment of PISA NPs in CD34+ 229
Scheme 19. In vitro BBB permeability and viability control and experimentation explanation..... 233
Scheme 20. In vitro BBB creation 3 µm filters and evaluation of PISA NPs 1 mg/mL concentration and experimentation explanation..... 239
Scheme 21. Schematic representation of TEER 255

Acknowledgments

To begin with I am thankful to Professor Rachel O'Reilly for the opportunity to work in her group and in the NANOSTEM program in such an amazing multidisciplinary field. I am grateful for the encouragement, advice and guidance that you have offered me all those years and for the support during the hard times in my PhD studies. I would also like to offer my thanks to Dr. Amanda Pearce for giving me a focus and essentially teaching me how to progress my science and sharing with me a common passion about biological expertise.

Next, I would like to give my whole-hearted thanks to the whole Marie Curie ITN NANOSTEM group. Thanks for the support, the laughs, the great times, the interesting conversations and for the exchange of knowledge, culture and for friendships that will last a lifetime. Honestly the fact that I didn't quit in the middle of my PhD I owe it to you guys. Special thanks to Professor Marina Resmini, who taught me invaluable lessons inside and outside of the lab, and for her support to acquire as much expertise in multiple labs as possible. I would also like to thank my best friend that I met through the program Dr. Alena Vdovchenko, for all the adventures that we had together and for many more to come. For the exceptional secondment in the University of Coimbra I would like to thank Professor Lino Ferreira and Dr. Susana Carvalho Rosa, who shared with me their experience in the more advanced biological work and for helping me with the *in vitro* BBB studies. For their hospitality,

company and help in Portugal I would like to thank Ms Ines Albino, Ms Sara Bernando Castro, Ms Francesca Tomatis, Ms Angela Barrera and all the UC-Biotech team, you guys made me feel more at home than I ever was in the UK.

Special thanks to the entire O'Reilly and Dove group members for helping me countless times and for being my personal google for scientific questions and not only. My genuine thanks have to go to Dr. Amrita Sikder for being the most awesome labmate a person can ask, and of course, for countless proofreading and help. Also I would like to thank her for the great musical breaks and dancing in the lab that made my PhD experience unforgettable. I would like to thank also my anime friends Dr. Sam Parkinson and Dr. Natalia Reis for engaging conversations in and out of the lab. Especially Dr. Sam Parkinson I have to thank for making the permeation through the blood and brain barrier a success with his incredible PISA and microfluidics skills, I couldn't have done it without you. Here I would like to take the opportunity to thank also Dr Wei Yu for helping me with the CDSA worms and Dr. Yujie Xie for helping me master the confocal microscopy technique and for helping me with the fluorophore synthesis.

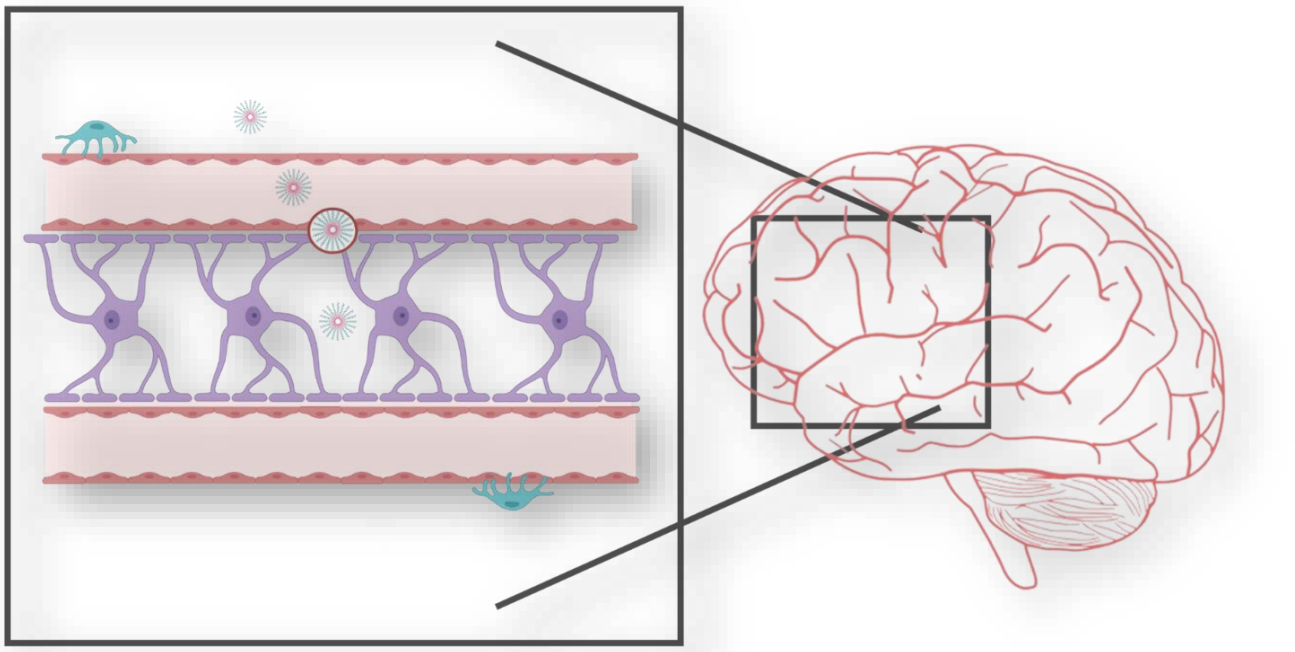
I would also like to acknowledge NANOSTEM, a Marie Skłodowska-Curie Innovative Training Network (ITN) funded by the European Commission through the Horizon 2020 , for the funding and training all those years. I am also very grateful to all technical stuff in the department of chemistry for teaching and helping me with ITC, MALDI and HPLC.

Finally I would like to thank my family for their love and understanding, and for always being there for me. Thank you for supporting me to go after science, and for caring always after my health and spoil me every time I come back home. I am so glad dad survived to see me finish this. Dad taught me persistence, mom taught me resilience and my sister taught me strength, so I can survive my PhD so this belongs to you as much as me.

Abbreviations

BBB: Blood and brain barrier
NSCs: Neural stem cells
CNS: Central nervous system
CAC : Critical aggregation concentration
PLLA: Poly L-lactic acid
PDLLA: Poly DL-lactic acid
PCL: Poly caprolactone
PDMAEMA: Poly(2- dimethylaminoethyl methacrylate)
PQDMAEMA: quaternized Poly(2-(dimethylamino)ethyl methacrylate)
PDMA: Poly (N,N-dimethylacrylamide)
PTEGA: Poly triethylenoglycolacrylate
PNIPAM: Poly isopropylacrylamide
PtBA: Poly tert Butyl Acrylate
PAA: Poly(Acrylic Acid)
PBCA :Poly(butylcyanoacrylate)
PLGA: Poly(lactic-co-glycolic acid
PHEA: Poly(2-hydroxyethyl acrylate)
DAA: Diacetone acrylamide
PBS: Phosphate buffer saline
BSA: Bovine serum albumin
NPs: Nanoparticles
FNP: Flash nanoprecipitation
CDSA: Crystallization driven self assembly
PISA: Polymer induced self assembly
ROP: Ring opening polymerization
RAFT: Reversible addition-fragmentation chain transfer
MMP: Matrix metalloproteinase
ROS: Reactive oxygen
eNOS: Endothelial nitric acid oxidation synthase
CDSA: Crystallization driven self-assembly
CTA: Chain transfer agent

ACM: Aminochloromaleimides
DTM : Dithiolmaleimides
SEC: Second elution chromatography
RI: Refrective index
TLC: Thin layer chromatography
UV-vis: Ultraviolet-visible
DLS: Dynamic light scattering
SLS: Static light scattering
AFM: Atomic force microscopy
NTA: Nanoparticle Tracker Analysis
MALDI: Matrix-assisted laser desorption/ionization
TEM: Transmission electron microscopy
ITC: Isothermal Titration Calorimetry
LCST: Lower critical solution temperature
PD : Polydispersity
M_w: weight average molecular weight
M_n: number average molecular weight
*Đ*M: Polydispersity
D_h: Hydrodynamic radius
DP: Degree of polymerization
THF: Tetrahydrofuran
ECs: Endothelial cells



CHAPTER 1-Introduction to polymers and nanoparticles for Blood Brain Barrier permeation

Abstract

Neurodegenerative diseases pose a significant and escalating threat, characterized by the progressive degeneration of neurons and cognitive decline. Addressing this challenge requires the development of innovative therapeutic modalities aimed at neural regeneration, contingent upon overcoming the formidable obstacle presented by the blood-brain barrier (BBB). This research explores the utilization of polymeric nanoparticles as tailored drug delivery systems, specifically designed for non-invasive permeation of the BBB.

Methodologically, diblock copolymers serve as foundational components for the self-assembly of polymeric nanoparticles, utilizing a variety of techniques including flash nanoprecipitation, slow addition, dialysis, and microfluidic systems. However, it was observed that the nanoparticles exhibit increased size and high polydispersity, attributed to kinetic entrapment, and the protein corona phenomenon indicating significant NP-protein interactions. Furthermore, *in vivo* zebrafish studies revealed acceptable viability and size for $PDMA_{87}$-b-$PLLA_{30}$ nanoparticles, though further investigation is warranted.

Crystallization-driven self-assembly (CDSA) was employed to generate diverse morphologies from the aforementioned diblock copolymers, aiming to enhance retention time. Despite the successful acquisition of diamond-shaped and cylindrical microstructures, the restrictive size and challenges associated with the protein corona phenomenon underscore the need for extensive optimization to facilitate BBB permeation.

Additionally, polymerization-induced self-assembly (PISA) nanoparticles underwent comprehensive evaluation, including cytotoxicity, internalization, and permeability studies using an *in vitro* BBB model. Notably, PISA NP 62 Tf exhibited high levels of endocytosis in the $CD34^+$ cell line, while PISA NP PDMA demonstrated the highest permeability percentage without compromising the integrity of the *in vitro* BBB model.

Overall, the results demonstrate the versatility of polymeric nanoparticles in enabling BBB penetration, offering promising avenues for targeted drug delivery to the central nervous system (CNS). Through meticulous optimization of nanoparticle design and fabrication

methods, this research contributes to the advancement of nanomedicine, with implications for the development of effective therapies for neurodegenerative diseases and beyond.

1.1 Diseases and Treatments across the blood and brain barrier

The treatment of neurodegenerative diseases such as Alzheimer's, Parkinson's, Huntington's, and ischemic stroke remains a significant challenge due to the limited permeability of the blood-brain barrier (BBB).[1] Overcoming the BBB is crucial for developing more effective treatments that can directly target the underlying pathologies of neurodegenerative diseases.

Patients with neurodegenerative diseases often exhibit BBB dysfunction, characterized by increased permeability and alterations in transporter expression.[2] The compromised BBB integrity in neurodegenerative diseases may facilitate the entry of therapeutic agents, but also toxins into the CNS. Providing easier permeation to the BBB in diseased states can be an opportunity to exploit disease-associated alterations for enhanced drug delivery to the CNS.[2] For instance, Alzheimer's disease compromises the integrity of the tight junctions between the endothelial cells of the BBB, increasing permeability.[3] This breakdown of the BBB allows for the entry of amyloid-beta peptides and neurotoxic proteins, exacerbating neuronal damage and cognitive decline.[4] Similarly, in Parkinson's disease, alterations in transporter expression at the BBB can disrupt the homeostasis of neurotransmitters such as dopamine, leading to dopaminergic neuron degeneration.[5]

Furthermore, the deterioration of the BBB may vary among different neurodegenerative diseases, reflecting the distinct pathological mechanisms underlying each condition. For example, in Huntington's disease, disruptions in mitochondrial function and energy metabolism can impair the function of endothelial cells comprising the BBB, leading to increased permeability and neuronal dysfunction.[2] Understanding the specific alterations occurring at the BBB in different neurodegenerative diseases is crucial for developing

targeted therapeutic strategies aimed at preserving BBB integrity and mitigating disease progression.

Several hydrophobic drugs have received FDA approval for crossing the BBB and treating CNS disorders. Notable examples include l-DOPA for Parkinson's disease and memantine for Alzheimer's disease.[6] These drugs leverage passive diffusion mechanisms to penetrate the BBB and exert their therapeutic effects in the CNS.[6] However, their efficacy may be limited by poor brain penetration and off-target effects, underscoring the need for innovative drug delivery strategies to enhance BBB permeability and improve therapeutic outcomes.[7]

Addressing the formidable challenge posed by neurodegenerative diseases entails innovative strategies, including the targeted manipulation of neural stem cells and astrocytes within critical brain regions such as the choroid plexus and hippocampus.[8] These regions harbour reservoirs of neural precursor cells that, when stimulated, can proliferate and differentiate into functional neurons, potentially replenishing the neural loss characteristic of such diseases.[8] Leveraging this regenerative potential necessitates the delivery of specific therapeutic agents capable of modulating cellular processes involved in neurogenesis and neural repair.

Many drugs and factors can be utilised to promote neurogenesis. Apart from retinoic acid, which has shown promise in promoting neural proliferation,[9] growth factors such as brain-derived neurotrophic factor (BDNF) and nerve growth factor (NGF) have demonstrated neuroprotective effects and the ability to stimulate neurogenesis.[10] Furthermore, small molecules targeting disease-specific pathways and nucleic acid-based therapeutics have been investigated for their potential in nanoparticle-based drug delivery.[11]

However, the delivery of the above therapeutic agents in specific regions of the CNS, can be challenging. In order to permeate through the BBB different a variety of passive, invasive and non-invasive strategies have been studied.[12] Figure 1.1 demonstrates these three categories and outlines the various modes of drug delivery across the BBB. The passive diffusion allows permeation of the BBB, by small molecules with high lipophilicity, low molecular weight below 450 Da like nicotine, morphine etc.[7] Usually, these drug molecules are utilising an already disrupted BBB and accumulating in the desired brain regions, which is

not sustainable.[13] The invasive strategies implementing a chemical, mechanical or osmotic methods in order to disrupt the BBB and create bigger pore size.[7] These techniques are not patient-friendly, despite the fact that they have been successful in a number of in vitro models.[14] Prolonged use of these techniques may result in unfavourable side effects, namely the buildup of toxins and blood components.[14]

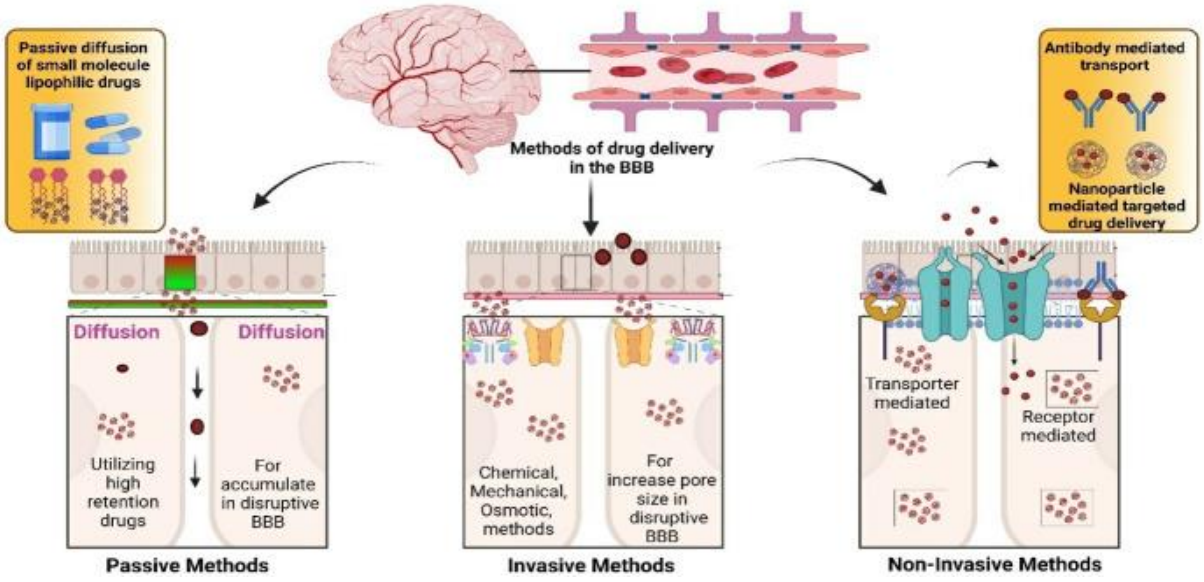


Figure 1.1 Various methodologies for drug delivery across the BBB. Passive diffusion utilised of small molecules and lipophilic drugs(left), Invasive methods interrupting the BBB like ultrasound or osmotic (central), non-invasive like nanoparticles (right). Adapted from Mishra *et al.*[7]

Non-invasive methods include the modern nanomedicine solutions,[7] that will be implemented in this thesis in order to achieve BBB permeation with nanoparticles as drug delivery systems. This potent system can be functionalised and can be tailored to specific transporters or receptors in order to permeate the BBB.[7]

Polymeric nanoparticles have gained attention as promising carriers for drug delivery across the blood-brain barrier (BBB). According to Saraiva *et al.*, the design of nanoparticles with suitable physicochemical properties is crucial for enhancing BBB permeability and facilitating drug transport into the CNS.[15] Surface modification of nanoparticles with ligands targeting specific receptors expressed on BBB endothelial cells, can improve their uptake and transport across the barrier.[16] These strategies offer hope for overcoming the challenges

associated with delivering therapeutic agents to the CNS for the treatment of neurodegenerative diseases.

Studies by Saraiva *et al.* and Wu *et al.* emphasize the importance of targeted drug delivery to specific brain regions affected by neurodegenerative diseases.[15, 17] Nanoparticle-mediated delivery of therapeutic agents enables precise targeting, minimizing off-target effects and enhancing therapeutic efficacy.[16] This approach holds promise for diseases such as Alzheimer's, Parkinson's, Huntington's, and ischemic stroke,[18] where precise delivery of drugs to affected brain regions is essential for optimal therapeutic outcomes.

1.2 Permeation through the Blood and Brain Barrier (BBB)

Over the years, numerous attempts have been undertaken to break through the blood-brain barrier (BBB).[19] The BBB, a partially permeable membrane barrier that separates blood from the brain's extracellular fluid in the central nervous system (CNS), controls blood flow, supplies nutrients to neurons, and guards against oxidative stress and metal toxicity.[2] It also limits the entry of foreign substances.[20] Pericytes, astrocytes, neurons, basement membrane, and junctional complexes make up its structure. The pericytes are linked to the top layer of endothelial cells, as shown in Figure 1.2A. Through contraction and relaxation, pericytes are in charge of controlling blood flow in brain capillaries.[21, 22] Additionally found on the outer layer are astrocytes, which connect the brain capillaries and neurons. [23] Only small molecules can get through the BBB's high trans endothelial barrier, which is created by the tight connections between the brain's endothelial cells and the basement membrane, which surrounds the discontinuous layer of pericytes and endothelial cells.[24] Pathological diseases like ischemic stroke or Alzheimer's elicit an inflammatory response that changes the BBB in numerous ways. Increased matrix metalloproteinase (MMP) activity, the generation of reactive oxygen species (ROS), activated endothelial nitric acid oxidation synthase (eNOS), and the release of cytokines and chemokines by macrophages are all factors in basement membrane breakdown.[23] As seen in Figure 1.2B, this results in tight junction rupture, which makes the system more permeable.[23]

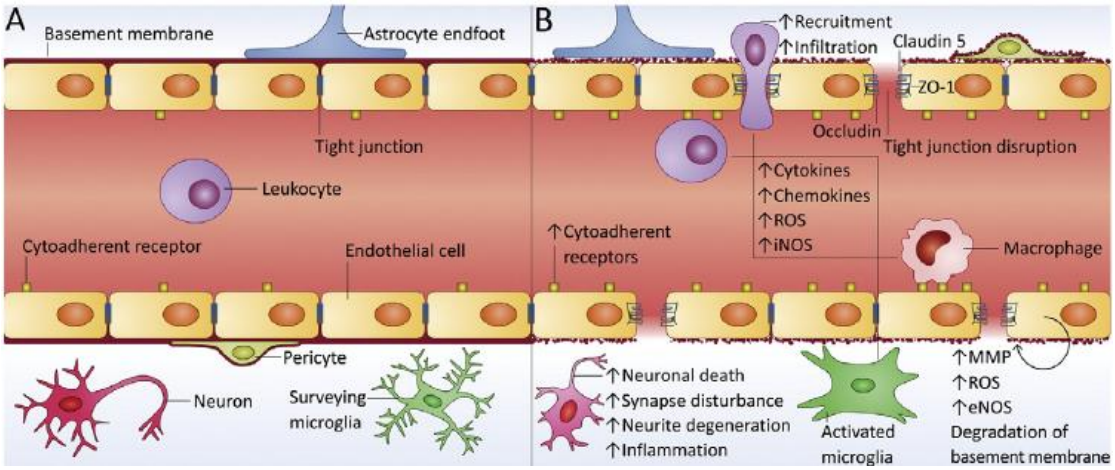


Figure 1.2 A) Composition of BBB, B) Disruption of BBB due to a pathological disease [23] (recreated with permission)

From the above it is clearly visible that BBB is critical for protecting the CNS as a crucial physiological barrier that shields the CNS from toxins and infections while permitting the selective flow of nutrients and signalling molecules.[25] The transport of therapeutic agents to the CNS, however, is severely hampered by this barrier. Large and hydrophilic molecules are unable to permeate the BBB due to tight junctions between endothelial cells that line the CNS capillaries and blood arteries. Efflux transporters additionally impose further restrictions on the transportation of drugs and other therapeutic substances.[26, 27]

Both invasive and non-invasive techniques are being investigated as CNS delivery channels.[28] Nanotechnology could be used to create non-invasive drug delivery methods that would improve the transport of therapeutic substances across the blood-brain barrier. As a result of many intrinsic benefits, nanoparticle-based therapies are of great interest as drug delivery and diagnostic instruments. Non-invasiveness, the capacity for biodegradability and biocompatibility, regulated drug loading and release, and possibly high targeting efficiencies are just a few of these .[26, 27]

According to the literature, effective delivery to the CNS depends on the size, shape, and surface charge of the nanoparticles. Larger particles cannot move via the extracellular space in the brain, according to numerous studies, most notably Saraiva et al. [23], who found that only nanoparticles with diameters less than 100 nm can permeate the BBB. However, Cena et al. demonstrated that nanoparticles with a diameter of up to 200 nm are capable of being

taken up via endocytosis[29] and of penetrating due to the improved permeability and retention effect.[30]

The process of cellular uptake known as endocytosis involves engulfing macromolecules from the outer cell membrane and introducing them into the cytoplasm. The mechanism of transcytosis is the same as that of endocytosis, except the produced vesicles are conveyed into a cell's interior before ejecting through the opposite side of the membrane [29]. The brain can be accessed by nanoparticles utilising this mechanism as a transport pathway. Receptor-mediated transcytosis, which permits functionalized nanoparticles with various types of ligands (such as insulin, transferrin, brain neural growth factor, lactoferrin, or antibodies against some endothelial receptors) to enter the brain, [23] constitutes one of the most popular trafficking pathways that enables permeation of the BBB.[5] Adsorptive transcytosis using nanoparticles coated with albumin or chitosan is another common method of penetrating the BBB.[23] For this project, the choice of coating material to be investigated is transferrin a, which have exhibited great cellular uptake.[31, 32] For this method to succeed, negatively charged proteins must interact with cationic nanoparticles. Another approach could be functional nanoparticles with molecular handles that are allowing functionalization with the transferrin protein.

Another factor that needs to be taken into consideration for nanoparticles to effectively permeate the BBB is the surface charge. For instance, it has been demonstrated that nanoparticles need to have a negative zeta potential of 5–15 mV in order to successfully travel over the BBB since nanoparticles with large positive charges cause toxicity to the BBB.[23] Due to a higher rate of cellular absorption, Rivera et al. observed that small, positively charged nanoparticles are more hazardous than large, negatively charged particles.[33] Since the exterior membrane of the endothelial cell is negatively charged, positively charged nanoparticles can utilise the adsorptive transcytosis pathway more successfully than other polarities.[34] On the contrary, neutral or negatively charged nanoparticles exhibit less protein adsorption in the blood, resulting in slower circulation times. Longer circulation periods can also be attained by coating the nanoparticles with stealth substances like PEG and causing sterical interactions. PEGylation can prevent the mononuclear phagocyte system from causing opsonization to the particles and thus eliminating them. Zwitterionic

nanoparticles can also produce the desired outcome, perhaps overcoming the low cellular uptake efficiency reported for PEG-coated nanoparticles.[34]

Saraiva *et al.* also, demonstrated that rod-like nanoparticles have improved cellular uptake efficiency compared to other nanoparticle morphologies[23]. In contrast to this, Rivera *et al.* reported a comparison between spherical and rod-like nanoparticles of a similar size, where the nanospheres had the best cellular uptake.[33] Overall, creation of nanospheres requires a simpler synthetic route and allows more control over final size, but results in shorter blood circulation times.[35] Only a small number of studies have been conducted, investigating the effect of multiple structures according to their permeation ability of the BBB.

The potential to permeate the BBB via numerous nanoparticle systems with various physicochemical characteristics has been explored. Researchers have examined and successfully proven the distribution of various types of nanoparticles to the CNS, including carbon dots, carbon nanotubes, inorganic nanoparticles, micelles, nanogels, nanoemulsions, dendrimers, exosomes, polymersomes, liposomes, and polymeric nanoparticles, but only a handful of them has made it into clinical studies.[36] To create a biodegradable drug delivery system in the current work, we have selected amphiphilic polymeric nanoparticles as the platform technology.

A potential approach for permeating the BBB and delivering medications and other therapeutic substances to the CNS utilises nanoparticles. Due to their biocompatibility, biodegradability, and diversity in terms of size, shape, and surface features, polymeric nanoparticles, in particular, have garnered a lot of attention. Producing and optimising polymeric nanoparticles for BBB penetration is still a challenging issue.

Based on this, the current work aimed to produce amphiphilic nanoparticles with various morphologies, different sizes and a biodegradable nature. Furthermore, the pH responsive properties and the positive charge can be used to manipulate drug release and create electrostatic interactions with protein ligands. Finally, the core crystallinity can adjust and prolong the degradation time for efficient delivery, and therefore this system shows great promise for drug delivery and pharmaceutical applications to the brain.

1.3 Ring Opening Polymerization

The form of chain-growth polymerization known as ring-opening polymerization (ROP) occurs when the active chain end reacts with a cyclic monomer by breaking open its ring system, reforming the active chain end at the terminal end of the opened monomer. ROP is regarded as one of the most versatile techniques to synthesise biopolymers and has a significant impact on the large-scale industrial production of polymers.[37]

ROP can be used to create Poly(lactide) (PLA), an aliphatic polyester made from renewable materials such corn starch, cassava roots, and sugarcane.[38] It has become one of the most commonly used bioplastics in the world because of its exceptional biodegradability, biocompatibility, and low toxicity.[38] As a result, PLA has garnered a lot of attention from researchers in the fields of biomedicine and pharmaceuticals as a viable contender for tissue engineering and drug delivery therapies.

Depending on the tacticity of the cyclic monomer utilised, PLA's composition can take on a variety of forms. Enantiopure L-lactide has two S-stereocenters, enantiopure D-lactide has two R-stereocenters, racemic D,L-lactide and meso-lactide has one S-stereocenter and one R-stereocenter, respectively.[39] The two enantiopure isomers can combine to create semi-crystalline polymers, making them suitable for use in assembly procedures that rely on crystallisation. The stereoisomers of polylactide are PLLA and PDLA. Poly(L-lactide), often known as PLLA, is made up of lactic acid monomers having the L-configuration. Contrarily, PDLA stands for poly(D-lactide), which is made up of monomers having the D-configuration.[40] The lactide monomers' chirality is represented by the L and D configurations.

The L and D crystallinity symbols in polylactide denote the presence of crystalline areas with various stereoisomeric compositions. The terms L crystallinity and D crystallinity refer to crystalline regions that are primarily made up of PLLA chains (L-configuration) and PDLA chains (D-configuration), respectively.[40] Due to the different stereochemistry of the monomers, these areas have unique packing patterns and crystalline structures.

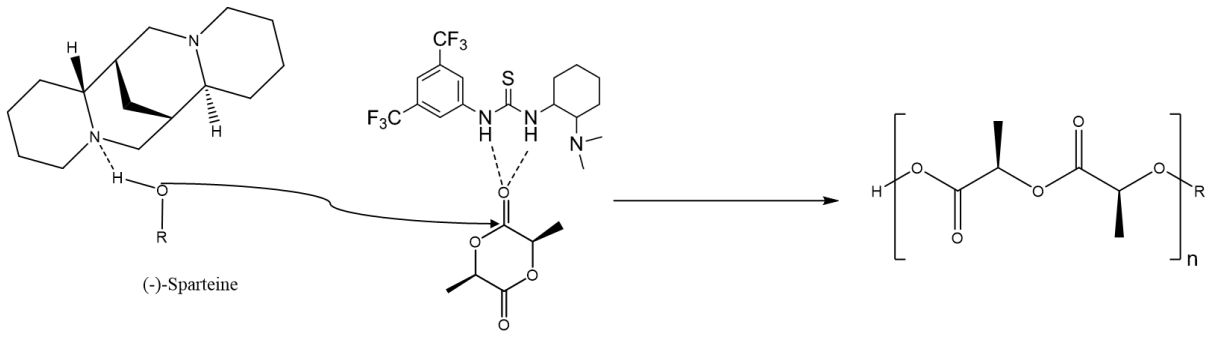


Figure 1.3 Ring-opening polymerisation of L-lactide using a thiourea/(-)-sparteine

In 2005, Dove and colleagues reported the ROP of L-lactide utilising an organocatalytic system based on thiourea and (-)-sparteine that was metal-free and produced very low dispersity and negligible transesterification of the polymer backbone.[49, 50] In this procedure, hydrogen bonding interactions between the cyclic ester monomer and alcohol initiator boost the lactide carbonyl's electrophilicity and the alcohol initiator's nucleophilicity (Figure 1.3) . The ester of the linear polymer was shown to be less recognised by the thiourea molecule than the ester of the cyclic lactide monomer, lessening the likelihood that the propagating alcohol would attack the already created PLA chain and resulting in a lower dispersity .

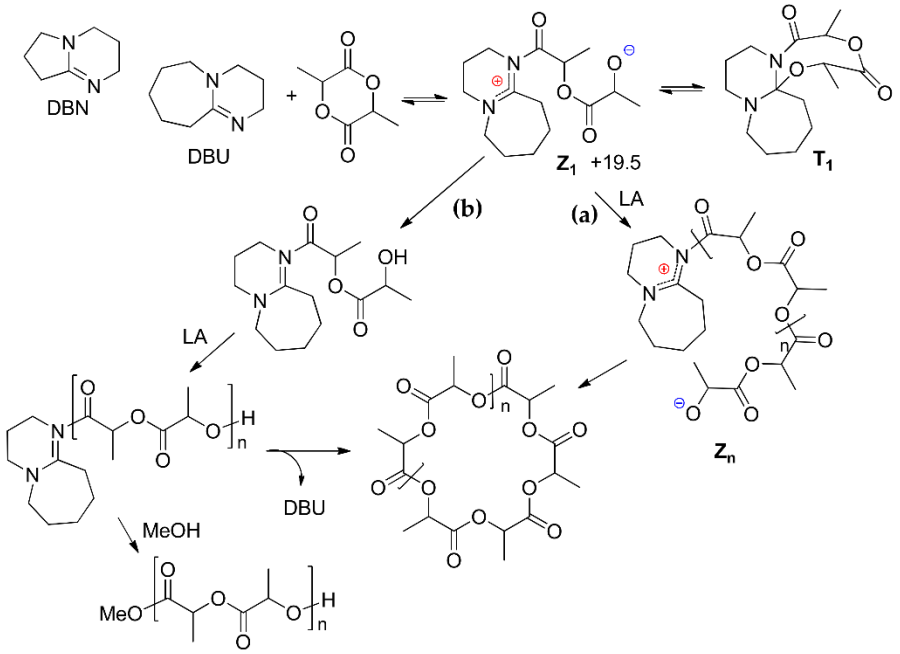


Figure 1.4 Proposed mechanism of ROP with DBU organic catalyst for PLLA synthesis[41]

Dove *et al* proposed a different mechanism with another organic catalyst for faster and more efficient results in the ROP synthesis of PLLA.[42] More powerful basic amines than (-)-sparteine could be used to produce ROP of lactide without the extra H-bond donor cocatalyst. [40] Numerous researchers have used the widely available base 1,8-diazabicyclo[5.4.0]undec-7-ene (DBU), which has demonstrated to be an effective ROP catalyst (Figure 1.4). While transesterification side reactions can occur with this catalyst at greatly prolonged reaction times, quenching the reaction by addition of a (solid-supported) acid results in its deactivation. DBU exhibits high catalytic activity with >98% monomer conversion being observed within 2 h for 500 eq. L-lactide (to initiator) with 1 mol% catalyst and [LA] = 0.7 M at ambient temperature.[42] The aforementioned mechanisms will be utilized in this work to perform ROP for PLLA.

1.4 Reversible addition-fragmentation chain transfer

In order to minimise radical-radical termination events happening in radical polymerizations, controlled radical polymerization can be accomplished using a degenerative transfer mechanism, which differs from the persistent radical effect in that the active polymer radical is in equilibrium with a second dormant polymer chain.[43] Particularly, this mechanism is utilised by the most recent radical methodology, the reversible addition-fragmentation chain transfer (RAFT) polymerisation process (Figure 1.5). A thiocarbonyl chain transfer agent (CTA) with an effectively selected R group and Z group is employed in this technique to advance the mechanism.[43]

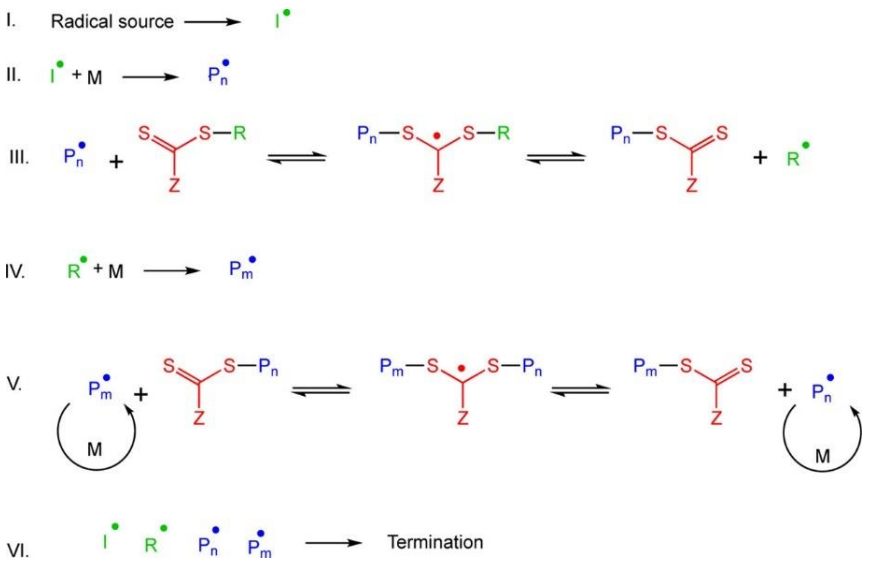


Figure 1.5 Mechanism of RAFT polymerization

The thiocarbonyl is employed to create a radical intermediate that can later disintegrate to create a polymeric thiocarbonyl molecule and a reinitiating group.[44] When all of the CTA has reacted, reinitiating groups can react with a different monomer to create a new polymer chain, which can then go through the same process and eventually reach chain equilibrium. With few actively growing polymer chains remaining as a result of this equilibrium process, the number of termination occurrences is minimised. The mediating group, in this case the chain transfer agent, is kept at the end of the polymer chain similarly to ATRP and NMP. Block copolymers can therefore be created by RAFT polymerization.[45]

Possibly one of the most adaptable and reliable polymerization techniques is RAFT polymerization. RAFT polymerization has been used successfully with a variety of functional monomers while retaining good control because of its great tolerance of functional groups.[45, 46]

Methyl methacrylate (MMA), styrene (St), methyl acrylate (MA), acrylamide (AM), and acrylonitrile (AN) are examples of more activated monomers that call for a more active CTA with an electron withdrawing or weakly electron donating Z group. The resulting stable thiocarbonyl intermediate radical ensures that this kind of monomer propagates sufficiently. The R group must similarly function as an efficient homolytic leaving group from the

intermediate radical while simultaneously continuing to function as an efficient initiating species for the monomer.

However, employing functional CTAs in RAFT, ATRP, and NMP techniques as well as other methods, it is simple to produce end-functionalized polymers. Notably, RAFT may be used to construct a variety of topologies including linear block copolymers,[46] star-shaped polymers,[47] hyperbranched polymers, and different higher order supramolecular structures. It can also be carried out in a variety of environments, including aquatic media.[48]

1.5 Packing parameter

Amphiphilic block copolymers, composed of hydrophilic and hydrophobic regions, can spontaneously self-assemble when above a critical aggregation concentration (CAC) and in selective solvents [49]. The solvent in use is thermodynamically selective for one of the blocks in the copolymer, in order to minimise energetically unfavourable interactions and generate a vast array of microstructures[50, 51]. For this project, the hydrophobic core of the particles will be the commonly used polyester poly(L-lactide) (PLLA), which is widely used in pharmaceutical applications and in self-assemblies and shown to be biocompatible [52]. PLLA has the ability to degrade naturally and controllably into lactic acid, which can be absorbed by the organism without cytotoxic effects [53]. Different hydrophilic corona chemistries will be studied, however initially the work will focus on the use of poly[2-(dimethylamino)ethyl methacrylate] (PDMAEMA). PDMAEMA is a biocompatible, water-soluble cationic synthetic polymer with pH responsive abilities, which are ideal properties for bioapplications.[54] Manipulating the ratio of these blocks has led to the formation of a range of structures including spherical,[55] vesicular,[56] and cylindrical [57] morphologies. A packing parameter, p, can be used to predict the most likely morphology of block copolymers using the influence of molecular curvature, as shown in Figure 1.6.

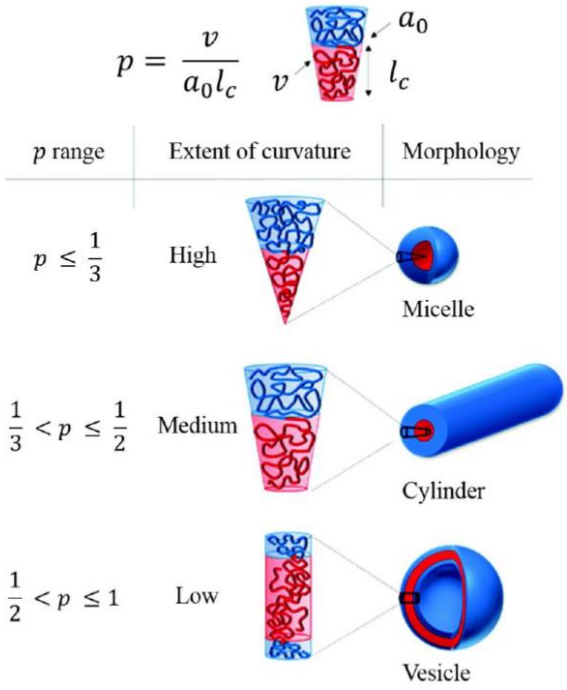


Figure 1.6 Various structures arise according to the packing parameter (red hydrophobic block with l_c representing the length and v the volume, a_0 is defined as the optimal area of the hydrophilic interface. Reproduced with permission from ref [49]

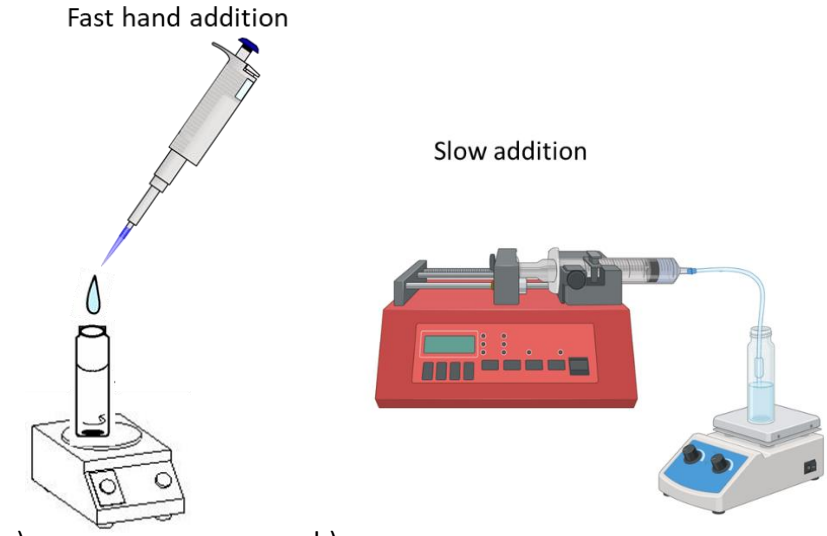
Amphiphilic block copolymers, that are formed of solvophilic and solvophobic blocks, can spontaneously self-assemble in solvents that are selective for one of the copolymer's blocks.[58] Block copolymer chains, for instance, can automatically self-assemble in a hydrophilic solvent to produce a core-corona micellar structure, where the core is made up of the hydrophobic block and the corona is made up of the hydrophilic block.[58] In order to limit energetically unfavourable interactions between the solvophobic core-forming block and the solvophilic solvent as well as entropically unfavourable ordering of the solvent, such an assembly is driven by the solvophobic effect.[59] The core-forming block's stretching, the repulsive interactions of the corona-forming block, and the interfacial tension between it and the solvent all influence the micellar structure's shape. The morphology of the self-assembled structure can be impacted by changes to the polymer composition and the self-assembly parameters, such as temperature, solvent, and salt concentration.[60]

One of the strategies for improving nanoparticle permeation across the BBB is to use diblock copolymers with optimal packing parameters. The packing parameters of diblock

copolymers, such as the Flory-Huggins parameter and the degree of polymerization, can influence the self-assembly of the copolymers into nanoparticles and their properties, such as size, shape, and surface chemistry.[61]

1.6 Different techniques of self-assembly

Direct dissolution or solvent-switch techniques are frequently employed to produce polymer assemblies that adhere to packing parameter criteria. Adding a corona block-specific selective solvent directly to the polymer results in the assembly of a micellar structure, which is known as direct dissolution. In contrast, a solvent-switch procedure gradually incorporates the selective solvent into a solution of the polymer dissolved in a suitable solvent for both blocks. After the effective solvent is eliminated, the resulting micelle assembly is then kept. These techniques have been used to assemble cylindrical particles, however they can frequently lead to the creation of other morphologies.



Scheme 1. Self-assembly methods a) flash nanoprecipitation, b) slow addition with syringe pump

A continuous flow procedure called flash nanoprecipitation (FNP) is used to self-assemble nanoparticles.[62] In order to create nanoparticles, it entails quickly mixing two immiscible fluids that contain the desired ingredients. With benefits including simplicity, scalability, and adaptability, FNP is a well-liked technique for creating different nanoparticle systems.[62] In scheme 1 a) is referred to as fast hand addition, which describes the process of the fast

addition of hydrophobic components soluble in an organic phase in a hydrophilic media. The self-assembly of nanoparticles is induced by FNP using the idea of fast mixing that is utilising a solvent/antisolvent system frequently. The hydrophobic component of these two phases supersaturates and leads to nucleation as a result of the quick mixing, creating nanoparticles. The size, shape, and homogeneity of the produced nanoparticles are strongly influenced by the mixing speed, flow rates, and geometry of the mixing chamber. The hydrophobic component's solubility and precipitation kinetics are impacted by the solvent and antisolvent choices, which also affect particle size and morphology. The self-assembly process in flash nanoprecipitation (FNP) can be influenced by both thermodynamic equilibrium and kinetic entrapment effects. The size, shape, and stability of the final nanoparticles are greatly influenced by these variables.[63] In FNP, the quick mixing and precipitation can lead to kinetic entrapment, in which the newly produced nanoparticles are prevented from rearranging into their most thermodynamically stable configuration.[64] This can result in the development of out-of-equilibrium structures or surface characteristics, which could impair the stability and functionality of the nanoparticles. As an alternative to FNP, the slow addition approach entails the slow addition of the hydrophobic phase into the aqueous phase over time. As a result, the system has extra time throughout the self-assembly process to establish thermodynamic equilibrium. As depicted in scheme 1 b) slow addition is performed through a syringe pump and that can offer control over the flow rate and more controlled and gradual addition. In comparison to FNP, the gradual addition approach may provide better control over particle size, morphology, and stability since it gives the system more time to stabilise and lowers the risk of kinetic entrapment. It's crucial to remember that each approach—FNP and gradual addition—has benefits and drawbacks. The slow addition approach has the potential for more stable nanoparticles and allows for better control over the thermodynamic equilibrium, whereas FNP enables rapid and continuous synthesis with potential scalability.[65] The decision between the two approaches is influenced by the particular specifications of the nanoparticle system, desired attributes, and the equilibrium between speed and control in the production process. The immediate and continuous production of FNP, adjustable particle size and composition, high drug loading capacity, and possible scalability are only a few benefits. The control of particle size

distribution, repeatability, and potential problems with particle stability and aggregation are among the difficulties it poses.

Overall, flash nanoprecipitation is a flexible method for the self-assembly of nanoparticles. It offers a reliable and scalable way to synthesise different nanoparticle systems, which may find use in nanomedicine and other fields.[66]

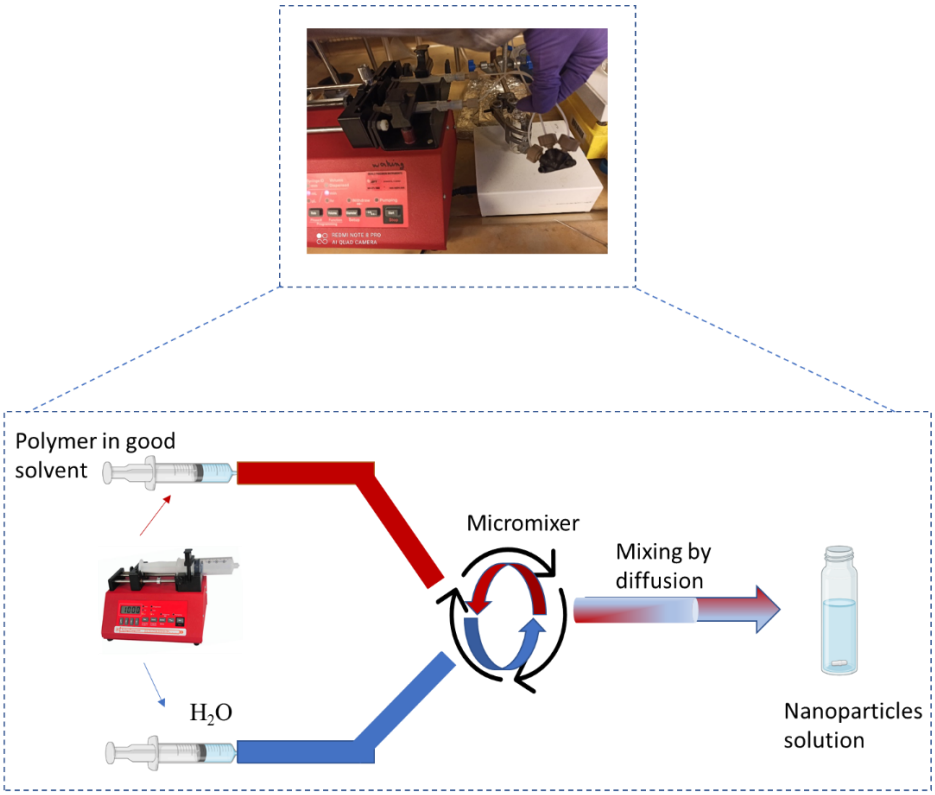
In order to accurately regulate the flow, mixing, and manipulation of nanoparticles and other components to induce self-assembly processes, microfluidic systems for nanoparticle self-assembly utilise microscale channels or chambers.[67] The precise control of fluid flow and diffusion is made possible by microfluidic systems, allowing for the controlled mixing of nanoparticle suspensions with reagents or solvents to initiate self-assembly.

Some of the advantage of a microfluidic system can be:[67]

- Precise control: High control over fluid flow rates, mixing ratios, and reaction times provided by microfluidic systems enable exact control of the self-assembly process.
- Scalability: To create nanoparticles with the necessary sizes and qualities, microfluidic procedures may be simply scaled up or down.
- High-throughput capabilities: Microfluidic devices' multiple parallel channels or integrated designs make it possible to quickly produce vast numbers of self-assembled nanoparticles.

Several microfluidic methods, such as droplet-based microfluidics, flow focusing, co-flow, and segmented flow, can be used to assemble nanoparticles. Herein, in this system control parameters include the Flow rates, mixing ratios and reaction conditions. Flow rates is the mixing dynamics and assembly kinetics are controlled by varying the flow rates of the nanoparticle suspension and other reagents.[68] Mixing ratios can be utilised for specific architectures or compositions that can be formed by carefully controlling the ratio of a nanoparticle suspension to other ingredients. Within the microfluidic system, temperature, pH, solvent composition, and other parameters can be precisely adjusted to effect self-assembly.[68, 69]

Microfluidic systems have difficulties with device construction, channel clogging, repeatability, and scaling up for industrial manufacturing.



Scheme 2. Microfluidics device to self-assemble nanoparticles. Polymer must be completely dissolved in a good solvent. The device consists of a syringe pump that can determine the mixing ratio and PTFE tubing, and tubing connector that constitutes as the micromixer.

Application areas for microfluidic devices for nanoparticle self-assembly include drug delivery, nanomedicine, catalysis, and materials science.[67]

In conclusion, microfluidic systems offer a framework for refined control of fluid flow, mixing, and diffusion, enabling the manipulation of thermodynamic conditions. With its quick mixing, flash nanoprecipitation induces a non-equilibrium condition that may result in kinetic entrapment. The system can achieve thermodynamic equilibrium via the gradual addition strategy, which gives the system superior control over the nucleation and growth processes.[70] The decision between these approaches is made based on the application-specific nanoparticle properties, process requirements, and desired results.

1.7 Crystallization Driven Self Assembly

A potent technology called crystallization-driven self-assembly (CDSA) combines the crystallisation and self-assembly processes to create precise and useful microstructures from polymer building blocks. In CDSA, a polymer segment or block crystallises to act as the catalyst for the hierarchical assembly of the polymer chains into the desired microstructures, such as nanoparticles, vesicles, fibres, or other complex morphologies.[71]

Usually, the procedure entails creating block copolymers, which are made up of at least one crystallizable block and one amorphous or non-crystallizable block. The creation of ordered domains or areas inside the polymer matrix results from the controlled crystallisation of the crystallizable block under the right circumstances.[72] The polymer chains subsequently arrange themselves into precise microstructures with well-defined forms and sizes as a result of the self-assembly process, which is then initiated by the expanding crystalline domains.

In CDSA, the interaction between the crystallisation and self-assembly processes is essential. The self-assembled structures offer a constrained setting for crystallisation, affecting the crystalline domains' nucleation and development.[73] The growing crystals can be oriented and arranged according to the self-assembly template, producing well-ordered microstructures.

Depending on the particular block copolymer system and the conditions used, CDSA's precise mechanism may change.[74] The final microstructure is greatly influenced by variables like polymer composition, molecular weight, solvent interactions, and processing parameters.

The size, shape, and organisation of the resulting microstructures can be fine-tuned by carefully regulating the variables that influence the self-assembly and crystallisation processes. With the use of this control, a variety of morphologies, including spheres,

cylinders, lamellae, and more intricate structures like diamond-shaped crystals, can be created.

One of the most interesting shapes are those of the diamonds . O'Reilly group has expertise in facilitating this assembly.[75] Diamond-shaped crystals in PDMAEMA-PLLA systems are thought to arise as a result of the interaction between self-assembly and crystallisation processes. The hydrophobic PLLA blocks initially drive the block copolymers' self-assembly. As a result, spherical aggregates or micelles with PDMAEMA blocks on the surface and crystalline PLLA cores are formed. Then, under the right circumstances, the PLLA blocks crystallise, changing the spherical aggregates into diamond-shaped crystals.

The block copolymers' inherent qualities and the self-assembly process combine to produce the distinctive diamond shape. As the PLLA blocks begin to crystallise inside the spherical aggregates, an anisotropic growth front forms, which causes the aggregates to lengthen and facet into diamond-like formations. effect of T.[76]

Contrary to conventional self-assembly techniques, CDSA offers several benefits. First, by varying the polymer composition, molecular weight, and processing conditions, it makes it possible to have exact control over the morphology and structure of the emerging microstructures. Complex architectures with specialised features and functionalities can be created thanks to this control. Second, a variety of polymer systems, including block copolymers, random copolymers, and homopolymers, can be subjected to CDSA, allowing for a greater choice of material.[77] Finally, CDSA is a promising candidate for applications in nanotechnology, materials science, and healthcare due to its simplicity in scaling up for industrial production.

However, CDSA also has several drawbacks and restrictions. Block copolymers with clearly defined structures and suitable crystallisation behaviour can be difficult to design and make, necessitating knowledge of polymer chemistry. It can be challenging to manipulate the kinetics and thermodynamics of crystallisation in order to produce the appropriate microstructures, hence processing parameter optimisation is frequently required. Furthermore, it is important to carefully analyse how external variables like temperature, solvent, and confinement may affect the CDSA process.

One of the most interesting shapes are those of the diamonds . O'Reilly group has expertise in facilitating CDSA.[75] Diamond-shaped crystals in PDMAEMA-PLLA systems are thought to arise as a result of the interaction between self-assembly and crystallisation processes. The hydrophobic PLLA blocks initially drive the block copolymers' self-assembly.[78] As a result, spherical aggregates or micelles with PDMAEMA blocks on the surface and crystalline PLLA cores are formed. Then, under the right circumstances, the PLLA blocks crystallise, changing the spherical aggregates into diamond-shaped crystals.

Overall, CDSA is a promising method for producing precisely tailored polymer microstructures with predetermined features and functions.[79] Its distinct mix of self-assembly and crystallisation processes opens up new doors for the creation of innovative materials and applications in a variety of industries.[77]

1.8 Polymerisation Induced Self Assembly

A powerful process known as polymerization-induced self-assembly (PISA) may create diblock copolymer nanoparticles with precise control over their size, shape, and surface characteristics.[80] Due to their small size and surface changes, PISA-formed nanoparticles may have an advantage when attempting to penetrate the BBB.[16]

PISA, or polymerization-induced self-assembly, has become an effective method for creating precise microstructures in solution. With careful control over their size, shape, and characteristics, a variety of microstructures, including micelles, vesicles, and nanoparticles, can be produced using this ground-breaking method, which combines polymerization and self-assembly processes.[81]

PISA makes use of hydrophilic and hydrophobic segmented macromonomers or amphiphilic block copolymers. These polymers are created using a controlled radical polymerization method, such as atom transfer radical polymerization (ATRP) or reversible addition-fragmentation chain transfer (RAFT). The hydrophilic segments create a corona around the hydrophobic core as the polymerization process continues, whereas the hydrophobic segments tend to congregate and form a hydrophobic core.[82]

1.9 Cytotoxicity Studies

Studies on the toxicity of drugs or materials on living cells are known as cytotoxicity studies. These investigations are crucial for comprehending the potentially hazardous impacts of different substances and assessing the safety of those substances in biomedical, pharmacological, and environmental applications.

Nanoparticles can exhibit particular toxicity mechanisms, such as metal ion release, reactive surface groups, or reactive oxygen species (ROS).[83] Traditional cytotoxicity assays might not be able to capture these pathways, necessitating the use of additional supplementary techniques for a thorough analysis.

Nanoparticles cytotoxicity can be measured by multiple viability assays. In this thesis, presto blue and Glomax was used to measure metabolic activity and viability of various cell lines treated with nanoparticles.

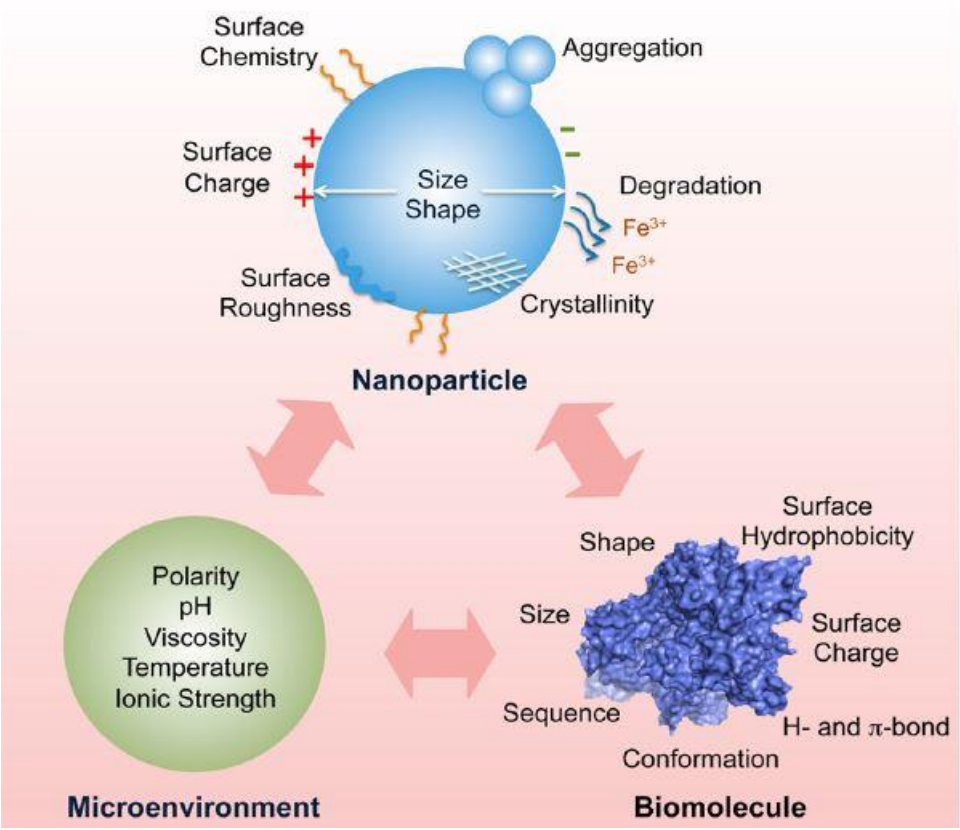
Each nanoparticle has distinct physicochemical characteristics that can affect how cytotoxic it is. The effects of nanoparticle size, shape, surface charge, surface coatings, and other nanoparticle-specific characteristics on biological responses can be assessed by studying nanoparticle systems. The ability to identify nanoparticle-specific effects, comprehend nanoparticle-cell interactions, and gauge the safety of nanoparticle formulations for targeted distribution are benefits of cytotoxicity studies for nanoparticles.[84] The requirement for standardised techniques to ensure consistency and potential nanoparticle interference with assay readouts can constitute obstacles and lead to inaccuracies.

To assess the results across multiple cell types, cytotoxicity experiments are often carried out using a variety of cell lines. Different cell lines may display variable sensitivities or responses to chemicals as they represent various tissues or organs.[85] Utilising several cell lines enables comparisons across different cell types and offers a deeper understanding of the potential cytotoxic effects.[85] Additionally, certain cell lines could be chosen in accordance with how well they apply to the targeted exposure route or the goal application. For instance, cell lines that represent the target organ or the site of the disease are

frequently used while researching therapeutic prospects.[86] Researchers can learn more about the general harmful effects of drugs, identify potential differences in sensitivity, and determine the precise cellular mechanisms behind the observed responses by conducting cytotoxicity studies in various cell lines.[86]

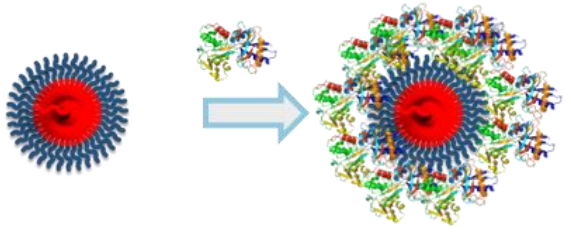
It is considered critical to assess the biodegradable nature of nanoparticles in order to predict its eventual fate and any potential accumulation in cells or tissues. This can also provide information about the nanoparticles retention time in a biological solution. Analysing how nanoparticles interact with biological systems, including potential inflammatory and immunotoxicity reactions, is necessary to determine how biocompatible they are.[87] Due to stress reactions brought on by nanoparticle treatment, cells can demonstrate viability levels above 100% (with 100% being the untreated cell with just medium). Multiple cytotoxicity assays (like MTT or MTS) rely on a mitochondrial reductase to convert the tetrazole to formazan. But there is always the possibility that treatment of the cells may result with increased enzymatic activity without actually having an effect on cell number or cell viability. This might involve cellular repair procedures, compensating reactions, or adaptive mechanisms.[87] In this case various cell lines were examined with presto blue viability assay as aforementioned. Presto blue reagent is resazurin based, membrane permeable solutions that upon reduction form resorufin, a red fluorescent compound which can be quantitatively measured to determine viability either visually, using absorbance or utilising the fluorescent outputs.[88] The data can be sensitive to prolong exposure to light and bacterial contaminations, so the solution was always covered and a mycoplasma testing was executed to determine the non-contamination of the cell lines. Thus, the higher viability ratio could be attributed to seeding error or increased enzymatic activity that leaded to faster cellular proliferation due to stressful conditions.

1.10 Protein corona



Scheme 3.Variables affecting nanoparticles-biomolecules interactions[89] (recreated with permission)

Nanoparticles are encircled by an excessive number of biomolecules (such as proteins, enzymes, macrophages etc.) when entering a biological environment, which may lead the nanoparticle surface to become saturated. Regardless of whether the nanoparticles are within the human organism or in a cellular setting, this occurrence takes place. These biologically modified nanoparticles are primarily involved in the nano-bio interactions (Scheme 3). Some of these interactions can be attributed to surface charge, surface chemistry or roughness, crystallinity, size and shape of the nanoparticles as aforementioned in section 1.2. Additionally, these alterations have an impact on nanoparticle internalisation and cell binding activities.



Scheme 4. Protein corona formation due to interactions.

In biological media like blood, NPs engage in extremely intricate interactions with the various biomolecules present in their surroundings, resulting in the creation of a biomolecule corona. On the characteristics and behaviour of NPs in biological media, interactions with proteins in particular have a dramatic effect.[90] As a result, the term "protein corona," which refers to the coating of proteins that have been adsorbed surrounding NPs, is widely used in nanomedicine research (Scheme 4).[90] Gaining control of NP-protein interactions (and consequently, the protein corona) is necessary in order to obtain a controlled behaviour of NPs in medicine. As a result, current research focuses on the physical mechanism of interactions at the nano-bio interface.

"Hard corona" and "soft corona" are two categories for protein corona.[91] Higher affinity proteins found in hard corona on the surface of NPs have the potential to bind to them permanently. In contrast, lesser affinity proteins that form soft corona are reversibly linked to NPs and allow for easy detachment during experimentation or additional exchange over time. Depending on the circumstances of physicochemical and biological interaction, the organisation and quantity of proteins can alter in the protein corona, a dynamic layer.[91]

Understanding NP-protein interactions is a difficult endeavour to tackle because most analytical methods only reveal the final protein corona composition (or rather, portions of it) and do not explain the mechanism underlying corona creation.[92] Future development of nanomedicines will mostly rely on assumptions if the numerous uncertainties regarding the specifics at the nano-bio interface are not addressed. Isothermal titration calorimetry (ITC) is one of the methods that can be utilised in order to provide a better understanding of the interactions that could be taking place between NPs and proteins. When heat is absorbed or released as a result of intermolecular interactions, ITC generates quantifiable adsorption

parameters.[93] In-depth understanding of the mechanism governing NP-protein interactions and the destiny of nanoparticles covered in proteins can be obtained by fusing the thermodynamic data from ITC experiments with data from other techniques (like DLS, confocal microscopy, cryoTEM etc.).[5]

The charge of the NPs will interact with the proteins based on electrostatic interactions. In comparison to their negatively charged NPs counterparts, the positively charged NPs demonstrated significantly greater cell attachment and a faster rate of cellular uptake. These findings revealed that the NP charge may have modified the internal structure of BSA.[94] In reality, BSA adsorbed onto negatively charged polystyrene NPs maintains its original structure as opposed to BSA's conformational change when combined with positively charged NPs, which causes the protein-NP complex to be directed towards scavenger receptors.[95]

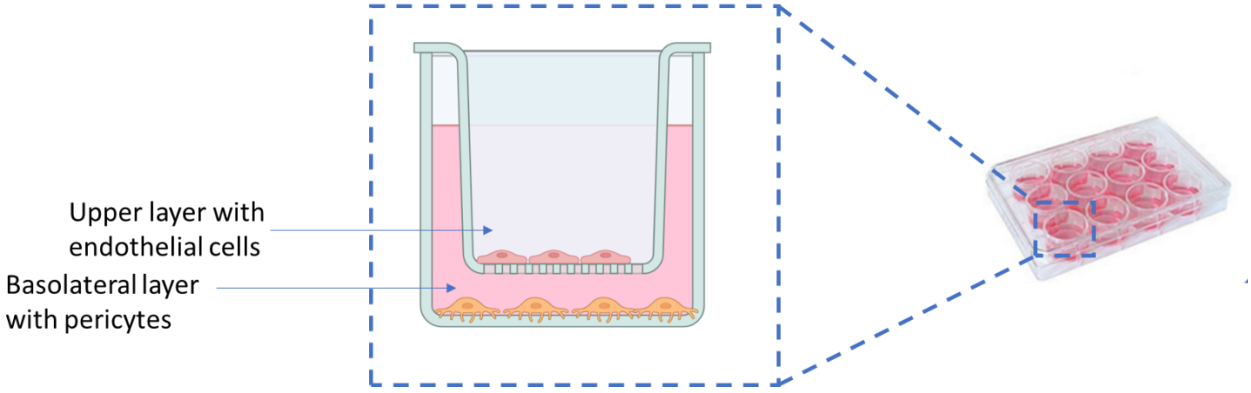
1.11 *In vitro* BBB

The blood-brain barrier (BBB) is important physiological barrier that protect the central nervous system (CNS) from toxins and pathogens while allowing for the selective transport of nutrients and signalling molecules.[96] However, this barrier also presents a significant challenge for the delivery of therapeutic agents to the CNS. The BBB is composed of tight junctions between endothelial cells that line the capillaries and blood vessels in the CNS, which restrict the passage of large and hydrophilic molecules.[97] In addition, efflux transporters further limit the transport of drugs and other therapeutic agents.[97]

Nanoparticles have emerged as a promising strategy to overcome the BBB and deliver drugs and other therapeutic agents to the CNS. Polymeric nanoparticles, in particular, have attracted significant interest due to their biocompatibility, biodegradability, and versatility in terms of size, shape, and surface properties.[16] However, the design and optimization of polymeric nanoparticles for BBB permeation remains a complex and challenging task.[98]

The biological evaluation and assessment can be examined in an *in vitro* or *in vivo* BBB model, where a drug delivery system can be evaluated. In *in vitro* co-culture static models,

astrocytes (or pericytes) are often seeded on the basolateral (abluminal) side of the membrane, whereas an endothelial cell monolayer is usually seeded on the upper (luminal) side of the membrane. Endothelial cells can co-culture with astrocytes or pericytes (biculture) either in non-contact or in contact. When endothelial cells and pericytes are co-cultured, the upregulation of the efflux pump protein is increased.[99]



Scheme 5. *In vitro* BBB biculture in a transwell filter of endothelial cells in the Upper layer and pericytes in the basolateral layer.

The *in situ* brain perfusion approach, which can provide an even more precise prediction of human permeability if humanised transporter-expressing transgenic mice are utilised, is one of the most accurate methods to test a drug's *in vivo* permeability. But *in vivo* testing is getting more and more costly, and is difficult and costly to be utilized for large scale screening, so an alternative is frequently employed in the early stages of drug development. *In vitro* models have the potential to be effective methods that meet the key requirements set forth by the pharmaceutical industry.

There is a variety of BBB models trying to optimize the current systems and each one has advantages and disadvantages.[100] An ideal BBB model, would carry all the characteristics of an *in vivo* model, but a useful BBB model would just needed to indicate reproducibility of permeability, development of tight junctions, easy cell culture, realistic physiology and functional expression of transporters.[101] Some of the current BBB models are monoculture with endothelial cells,[102] cocultures in transwell filters with astrocytes or pericytes (Scheme 5),[103] triple cell coculture with endothelial in the upper layer, pericytes in the other side of the membrane and glia cells in the basolateral,[104] and even microfluidics models. [105]

The BBB model selected for this screening, was the coculture of endothelial cells with pericytes as presented on scheme 5. The reason for this selection was that the cells synergistically take into account the influence of other elements and can represent a better physiology and tight junctions. The disadvantage of this technique is that it can be time consuming. More information about the technique and the results can be found in ***Chapter 4***.

1.12 References

1. N. Poovaiah, Z. Davoudi, H. Peng, B. Schlichtmann, S. Mallapragada, B. Narasimhan and Q. Wang, *Nanoscale*, 2018, **10**, 16962-16983.
2. M. D. Sweeney, Z. Zhao, A. Montagne, A. R. Nelson and B. V. Zlokovic, *Physiol Rev*, 2019, **99**, 21-78.
3. E. Zenaro, G. Piacentino and G. Constantin, *Neurobiol Dis*, 2017, **107**, 41-56.
4. M. D. Sweeney, A. P. Sagare and B. V. Zlokovic, *Nat Rev Neurol*, 2018, **14**, 133-150.
5. J. Baskin, J. E. Jeon and S. J. G. Lewis, *Journal of Neurology*, 2021, **268**, 1981-1994.
6. W. M. Pardridge, *Expert Opinion on Drug Delivery*, 2016, **13**, 963-975.
7. A. Mishra, R. Kumar, J. Mishra, K. Dutta, P. Ahlawat, A. Kumar, S. Dhanasekaran, A. K. Gupta, S. Sinha, D. K. Bishi, P. K. Gupta and S. Nayak, *Journal of Drug Delivery Science and Technology*, 2023, **86**, 104694.
8. D. E. Nayab, F. U. Din, H. Ali, W. A. Kausar, S. Urooj, M. Zafar, I. Khan, K. Shabbir and G. M. Khan, *J Nanobiotechnology*, 2023, **21**, 477-493.
9. A. Janesick, S. C. Wu and B. Blumberg, *Cellular and Molecular Life Sciences*, 2015, **72**, 1559-1576.
10. S. L. B. Oliveira, M. M. Pillat, A. Cheffer, C. Lameu, T. T. Schwindt and H. Ulrich, *Cytometry Part A*, 2013, **83A**, 76-89.
11. B. Srinageshwar, M. Florendo, B. Clark, K. Johnson, N. Munro, S. Peruzzaro, A. Antcliff, M. Andrews, A. Figacz, D. Swanson, G. L. Dunbar, A. Sharma and J. Rossignol, *Pharmaceutics*, 2020, **12**, 619-631.
12. Y. Zhou, Z. Peng, E. S. Seven and R. M. Leblanc, *Journal of Controlled Release*, 2018, **270**, 290-303.
13. H. Luo and E. V. Shusta, *Pharmaceutics*, 2020, **12**, 1085.
14. C. W. Fong, *The Journal of Membrane Biology*, 2015, **248**, 651-669.
15. C. Saraiva, C. Praça, R. Ferreira, T. Santos, L. Ferreira and L. Bernardino, *Journal of Controlled Release*, 2016, **235**, 34-47.
16. R. G. R. Pinheiro, A. J. Coutinho, M. Pinheiro and A. R. Neves, *Int J Mol Sci*, 2021, **22**, 11654-11666.
17. D. Wu, Q. Chen, X. Chen, F. Han, Z. Chen and Y. Wang, *Signal Transduction and Targeted Therapy*, 2023, **8**, 217-230.
18. C. Jiang, Y. Zhou, R. Chen, M. Yang, H. Zhou, Z. Tang, H. Shi and D. Qin, *Pharmaceutics*, 2023, **15**, 2669-2678.
19. P. K. Pandey, A. K. Sharma and U. Gupta, *Tissue Barriers*, 2016, **4**, e1129476.
20. Y. Zhou, Z. Peng, E. S. Seven and R. M. Leblanc, *J Control Release*, 2018, **270**, 290-303.

21. A.-C. Lussint, *Fluids and Barriers of the CNS*, 2012, **23**, 21-32.
22. D. J. Begley, *Pharmacology & Therapeutics*, 2004, **104**, 29-45.
23. C. Saraiva, *Journal of Controlled Release*, 2016, **235**, 34-47.
24. T. Patel, *Adv Drug Deliv Rev*, 2012 May 15, **64**, 701-705.
25. D. M. Teleanu, C. Chircov, A. M. Grumezescu, A. Volceanov and R. I. Teleanu, *Pharmaceutics*, 2018, **10,** 269-285.
26. T. T. Zhang, *Biomaterial Science*, 2016, **4**, 119-129.
27. E. Nance, *J Control Release*, 2014, **189**, 123-132.
28. D. M. Teleanu, C. Chircov, A. M. Grumezescu, A. Volceanov and R. I. Teleanu, 2018, **10**, 269-285.
29. V. Cena, *Nanomedicine*, 2018, **13**, 1513-1516.
30. X. Dong, *Theranostics*, 2018, **8**, 1481-1493.
31. R. L. Roberts, R. E. Fine and A. Sandra, 1993, **104**, 521-532.
32. L. Aloe, P. Bianchi, A. De Bellis, M. Soligo and M. L. Rocco, *Neural Regen Res*, 2014, **9**, 1025-1030.
33. P. Rivera-Gil, *Accounts of chemical research*, 2013, **46**, 743–749.
34. T. C. H Ou , Y. Zhang *Acta Biomater*, 2018, **65**, 339–348
35. Y. W. Yating Zhao, Fu Ran, Yu Cui, Chang Liu, Qinfu Zhao, Yikun Gao, Da Wang & Siling Wang, *Scientific Reports*, 2017, **7**.
36. X. Li, *Journal of Drug Targeting*, 2016, **25**, 17–28.
37. C. M. Plummer, L. Li and Y. Chen, *Macromolecules*, 2023, **56**, 731-750.
38. E. Balla, V. Daniilidis, G. Karlioti, T. Kalamas, M. Stefanidou, N. D. Bikiaris, A. Vlachopoulos, I. Koumentakou and D. N. Bikiaris, *Polymers (Basel)*, 2021, **13**, 1822-1835.
39. A. Peterson, R. Hador, M. Pink, Y. Popowski, M. Kol and W. B. Tolman, *Journal of the American Chemical Society*, 2022, **144**, 20047-20055.
40. J. O. C. de França, D. da Silva Valadares, M. F. Paiva, S. C. L. Dias and J. A. Dias, *Polymers (Basel)*, 2022, **14,** 2317-2329.
41. I. Nifant'ev and P. Ivchenko, *Polymers (Basel)*, 2019, **11**, 2078.
42. A. P. Dove, *ACS Macro Letters*, 2012, **1**, 1409-1412.
43. S. Perrier, *Macromolecules*, 2017, **50**, 7433-7447.
44. A. Postma, T. P. Davis, G. Moad and M. S. O'Shea, *Macromolecules*, 2005, **38**, 5371-5374.
45. N. P. Truong, G. R. Jones, K. G. E. Bradford, D. Konkolewicz and A. Anastasaki, *Nature Reviews Chemistry*, 2021, **5**, 859-869.
46. F. M. Winnik, A. R. Davidson, G. K. Hamer and H. Kitano, *Macromolecules*, 1992, **25**, 1876-1880.
47. E. M. Todd and S. C. Zimmerman, *Journal of the American Chemical Society*, 2007, **129**, 14534-14535.
48. M. H. Stenzel, *Chemical Communications*, 2008, DOI: 10.1039/B805464A, 3486-3503.
49. K. E. B. Doncom, L. D. Blackman, D. B. Wright, M. I. Gibson and R. K. O'Reilly, *Chemical Society Reviews*, 2017, **46**, 4119-4134.
50. Y. Mai and A. Eisenberg, *Chemical Society Reviews*, 2012, **41**, 5969-5985.
51. A. Blanazs, S. P. Armes and A. J. Ryan, 2009, **30**, 267-277.
52. J. K. Oh, *Polylactide (PLA)-based amphiphilic block copolymers: Synthesis, self-assembly, and biomedical applications*, 2011, **7**, 5096-5119.
53. N. Kamaly, B. Yameen, J. Wu and O. C. Farokhzad, *Chem Rev*, 2016, **116**, 2602-2663.
54. Y. Li and D. Ju, in *Neurotoxicity of Nanomaterials and Nanomedicine*, eds. X. Jiang and H. Gao, Academic Press, 2017, **12,** pp. 285-329.
55. P. Bhargava, J. X. Zheng, P. Li, R. P. Quirk, F. W. Harris and S. Z. D. Cheng, *Macromolecules*, 2006, **39**, 4880-4888.
56. L. Zhang and A. Eisenberg, 1995, **268**, 1728-1731.

57. J. X. Zheng, H. Xiong, W. Y. Chen, K. Lee, R. M. Van Horn, R. P. Quirk, B. Lotz, E. L. Thomas, A.-C. Shi and S. Z. D. Cheng, *Macromolecules*, 2006, **39**, 641-650.
58. K. Kuperkar, D. Patel, L. I. Atanase and P. Bahadur, *Polymers (Basel)*, 2022, **14**.
59. Q. Tian, C. Fei, H. Yin and Y. Feng, *Progress in Polymer Science*, 2019, **89**, 108-132.
60. Y. H. A. Hussein and M. Youssry, *Materials (Basel)*, 2018, **11**.
61. A. Vardaxi, M. Kafetzi and S. Pispas, *Polymers (Basel)*, 2022, **14**.
62. N. J. Caggiano, S. K. Nayagam, L. Z. Wang, B. K. Wilson, P. Lewis, S. Jahangir, R. D. Priestley, R. K. Prud'homme and K. D. Ristroph, *Int J Pharm*, 2023, **640**, 122985.
63. X. Yan, J. Bernard and F. Ganachaud, *Advances in Colloid and Interface Science*, 2021, **294**, 102474.
64. J. Tao, S. F. Chow and Y. Zheng, *Acta Pharm Sin B*, 2019, **9**, 4-18.
65. J. He, X. Huang, Y.-C. Li, Y. Liu, T. Babu, M. A. Aronova, S. Wang, Z. Lu, X. Chen and Z. Nie, *Journal of the American Chemical Society*, 2013, **135**, 7974-7984.
66. W. S. Saad and R. K. Prud'homme, *Nano Today*, 2016, **11**, 212-227.
67. S. Damiati, U. B. Kompella, S. A. Damiati and R. Kodzius, *Genes (Basel)*, 2018, **9**,103-113.
68. B. G. Carvalho, B. T. Ceccato, M. Michelon, S. W. Han and L. G. de la Torre, *Pharmaceutics*, 2022, **14**,141-154.
69. B. Küçüktürkmen, W. Inam, F. Howaili, M. Gouda, N. Prabhakar, H. Zhang and J. M. Rosenholm, *Biosensors (Basel)*, 2022, **12,**181-190.
70. V. Uskoković, *Rev J Chem*, 2013, **3**, 271-303.
71. W. Xu, Y. Zheng and P. Pan, *Journal of Polymer Science*, 2022, **60**, 2136-2152.
72. R. M. Michell and A. J. Müller, *Progress in Polymer Science*, 2016, **54-55**, 183-213.
73. J. F. Kang, J. Zaccaro, A. Ulman and A. Myerson, *Langmuir*, 2000, **16**, 3791-3796.
74. P. J. Hurst, A. M. Rakowski and J. P. Patterson, *Nat Commun*, 2020, **11**, 4690.
75. M. Inam, J. C. Foster, J. Gao, Y. Hong, J. Du, A. P. Dove and R. K. O'Reilly, *Journal of Polymer Science Part A: Polymer Chemistry*, 2019, **57**, 255-259.
76. J. C. Foster, S. Varlas, B. Couturaud, Z. Coe and R. K. O'Reilly, *Journal of the American Chemical Society*, 2019, **141**, 2742-2753.
77. S. Ganda and M. H. Stenzel, *Progress in Polymer Science*, 2020, **101**, 101195.
78. W. Yu, M. Inam, J. R. Jones, A. P. Dove and R. K. O'Reilly, *Polymer Chemistry*, 2017, **8**, 5504-5512.
79. L. MacFarlane, C. Zhao, J. Cai, H. Qiu and I. Manners, *Chem Sci*, 2021, **12**, 4661-4682.
80. H. Phan, M. Cossutta, C. Houppe, C. Le Cœur, S. Prevost, I. Cascone, J. Courty, J. Penelle and B. Couturaud, *Journal of Colloid and Interface Science*, 2022, **618**, 173-184.
81. N. J. Warren and S. P. Armes, *Journal of the American Chemical Society*, 2014, **136**, 10174-10185.
82. M. S. Haider, M. M. Lübtow, S. Endres, S. Forster, V. J. Flegler, B. Böttcher, V. Aseyev, A. C. Pöppler and R. Luxenhofer, *ACS Appl Mater Interfaces*, 2020, **12**, 24531-24543.
83. P. P. Fu, Q. Xia, H. M. Hwang, P. C. Ray and H. Yu, *J Food Drug Anal*, 2014, **22**, 64-75.
84. A. Sharma, S. V. Madhunapantula and G. P. Robertson, *Expert Opin Drug Metab Toxicol*, 2012, **8**, 47-69.
85. J. M. Hillegass, A. Shukla, S. A. Lathrop, M. B. MacPherson, N. K. Fukagawa and B. T. Mossman, *Wiley Interdiscip Rev Nanomed Nanobiotechnol*, 2010, **2**, 219-231.
86. M. Niepel, M. Hafner, M. Chung and P. K. Sorger, *Curr Protoc Chem Biol*, 2017, **9**, 55-74.
87. S. J. Cameron, J. Sheng, F. Hosseinian and W. G. Willmore, *Int J Mol Sci*, 2022, **23**.
88. N. Lall, C. J. Henley-Smith, M. N. De Canha, C. B. Oosthuizen and D. Berrington, *Int J Microbiol*, 2013, **2013**, 420601.
89. Q. Mu, G. Jiang, L. Chen, H. Zhou, D. Fourches, A. Tropsha and B. Yan, *Chem Rev*, 2014, **114**, 7740-7781.

90. D. Docter, S. Strieth, D. Westmeier, O. Hayden, M. Gao, S. K. Knauer and R. H. Stauber, *Nanomedicine (Lond)*, 2015, **10**, 503-519.
91. V. H. Nguyen and B. J. Lee, *Int J Nanomedicine*, 2017, **12**, 3137-3151.
92. C. Weber, J. Simon, V. Mailänder, S. Morsbach and K. Landfester, *Acta Biomater*, 2018, **76**, 217-224.
93. W. Ma, L. Yang and L. He, *J Pharm Anal*, 2018, **8**, 147-152.
94. D. Hühn, K. Kantner, C. Geidel, S. Brandholt, I. De Cock, S. J. H. Soenen, P. Rivera_Gil, J.-M. Montenegro, K. Braeckmans, K. Müllen, G. U. Nienhaus, M. Klapper and W. J. Parak, *ACS Nano*, 2013, **7**, 3253-3263.
95. W. Huang, G. Xiao, Y. Zhang and W. Min, *Biomedicine & Pharmacotherapy*, 2021, **139**, 111541.
96. A. I. Khan, Q. Lu, D. Du, Y. Lin and P. Dutta, *Biochim Biophys Acta Gen Subj*, 2018, **1862**, 2779-2787.
97. J. Sargento-Freitas, S. Aday, C. Nunes, M. Cordeiro, A. Gouveia, F. Silva, C. Machado, B. Rodrigues, G. C. Santo, C. Ferreira, A. Amorim, S. Sousa, A. C. Gomes, M. Castelo-Branco, L. Ferreira and L. Cunha, *Neurology*, 2018, **90**, e127-e134.
98. J. Ahlawat, G. Guillama Barroso, S. Masoudi Asil, M. Alvarado, I. Armendariz, J. Bernal, X. Carabaza, S. Chavez, P. Cruz, V. Escalante, S. Estorga, D. Fernandez, C. Lozano, M. Marrufo, N. Ahmad, S. Negrete, K. Olvera, X. Parada, B. Portillo, A. Ramirez, R. Ramos, V. Rodriguez, P. Rojas, J. Romero, D. Suarez, G. Urueta, S. Viel and M. Narayan, *ACS Omega*, 2020, **5**, 12583-12595.
99. M. Heymans, R. Figueiredo, L. Dehouck, D. Francisco, Y. Sano, F. Shimizu, T. Kanda, R. Bruggmann, B. Engelhardt, P. Winter, F. Gosselet and M. Culot, *Fluids Barriers CNS*, 2020, **17**, 48-72.
100. I. Wilhelm and I. A. Krizbai, *Molecular Pharmaceutics*, 2014, **11**, 1949-1963.
101. A. Reichel, *Curr Drug Metab*, 2006, **7**, 183-203.
102. V. Berezowski, C. Landry, S. Lundquist, L. Dehouck, R. Cecchelli, M. P. Dehouck and L. Fenart, *Pharmaceutical Research*, 2004, **21**, 756-760.
103. R. Cecchelli, S. Aday, E. Sevin, C. Almeida, M. Culot, L. Dehouck, C. Coisne, B. Engelhardt, M. P. Dehouck and L. Ferreira, *PLoS One*, 2014, **9**, e99733.
104. S. Nakagawa, M. A. Deli, H. Kawaguchi, T. Shimizudani, T. Shimono, A. Kittel, K. Tanaka and M. Niwa, *Neurochem Int*, 2009, **54**, 253-263.
105. R. Booth and H. Kim, *Lab Chip*, 2012, **12**, 1784-1792.
106. M. Clemens-Hemmelmann, C. Kuffner, V. Metz, L. Kircher, U. Schmitt, C. Hiemke, R. Postina and R. Zentel, *Amphiphilic Copolymers Shuttle Drugs Across the Blood–Brain Barrier* Macromolecular bioscience, 2016.
107. C. Celia, D. Cosco, D. Paolino and M. Fresta, *Med Res Rev*, 2011, **31**, 716-756.
108. W. Zhang, A. Mehta, Z. Tong, L. Esser and N. H. Voelcker, *Adv Sci (Weinh)*, 2021, **8**, 2003937.
109. K. A. Woodrow, Y. Cu, C. J. Booth, J. K. Saucier-Sawyer, M. J. Wood and W. Mark Saltzman, *Nature Materials*, 2009, **8**, 526-533.
110. S. L. Demento, S. C. Eisenbarth, H. G. Foellmer, C. Platt, M. J. Caplan, W. Mark Saltzman, I. Mellman, M. Ledizet, E. Fikrig, R. A. Flavell and T. M. Fahmy, *Vaccine*, 2009, **27**, 3013-3021.
111. T. Patel, J. Zhou, J. M. Piepmeier and W. M. Saltzman, *Advanced Drug Delivery Reviews*, 2012, **64**, 701-705.
112. Y. Bai, F.-Y. Xie and W. Tian, *Chinese Journal of Polymer Science*, 2018, **36**, 406-416.
113. H. Liu, H. Chen, F. Cao, D. Peng, W. Chen and C. Zhang, *Polymers (Basel)*, 2019, **11**, 820.
114. A. Car, P. Baumann, J. T. Duskey, M. Chami, N. Bruns and W. Meier, *Biomacromolecules*, 2014, **15**, 3235-3245.
115. C. A. Figg, R. N. Carmean, K. C. Bentz, S. Mukherjee, D. A. Savin and B. S. Sumerlin, *Macromolecules*, 2017, **50**, 935-943.

116. N. Raval, D. Kalyane, R. Maheshwari and R. K. Tekade, in *Basic Fundamentals of Drug Delivery*, ed. R. K. Tekade, Academic Press, 2019, **5**, pp. 173-201.
117. J. C. Olivier, L. Fenart, R. Chauvet, C. Pariat, R. Cecchelli and W. Couet, *Pharm Res*, 1999, **16**, 1836-1842.
118. L. E. Freed, G. Vunjak-Novakovic, R. J. Biron, D. B. Eagles, D. C. Lesnoy, S. K. Barlow and R. Langer, *Bio/Technology*, 1994, **12**, 689-693.
119. Y. S. Yim, J.-s. Choi, G. T. Kim, C. H. Kim, T.-H. Shin, D. G. Kim and J. Cheon, *Chemical Communications*, 2012, **48**, 61-63.
120. Y. Zhu, C. Liu and Z. Pang, *Biomolecules*, 2019, **9**.
121. D. B. Vieira and L. F. Gamarra, *Int J Nanomedicine*, 2016, **11**, 5381-5414.
122. S. Whitelam and R. L. Jack, *Annu Rev Phys Chem*, 2015, **66**, 143-163.
123. P. J. Lu, E. Zaccarelli, F. Ciulla, A. B. Schofield, F. Sciortino and D. A. Weitz, *Nature*, 2008, **453**, 499-503.
124. R. Gutzler, L. Cardenas and F. Rosei, *Chemical Science*, 2011, **2**, 2290-2300.
125. C.-A. Palma, M. Bonini, T. Breiner and P. Samorì, *Advanced materials* 2009, **21**, 1383-1386.
126. W. Lu, in *Encyclopedia of Nanotechnology*, ed. B. Bhushan, Springer Netherlands, Dordrecht, 2012, DOI: 10.1007/978-90-481-9751-4_274, pp. 2371-2382.
127. M. C. Branco and J. P. Schneider, *Acta Biomater*, 2009, **5**, 817-831.
128. V. P. Torchilin, *Pharm Res*, 2007, **24**, 1-16.
129. D. Bennet and S. Kim, 2014, **8,**pp. 257-310.
130. D. J. Overstreet, H. A. Von Recum and B. L. Vernon, in *Injectable Biomaterials*, ed. B. Vernon, *Woodhead Publishing,* 2011, **6**, pp. 95-141.
131. K. M. Pustulka, A. R. Wohl, H. S. Lee, A. R. Michel, J. Han, T. R. Hoye, A. V. McCormick, J. Panyam and C. W. Macosko, *Molecular pharmaceutics*, 2013, **10**, 4367-4377.
132. X. Wang, P. Gao, Y. Yang, H. Guo and D. Wu, *Nature Communications*, 2018, **9**, 2772.
133. M. C. García, C. Aloisio, R. Onnainty and G. Ullio-Gamboa, in *Nanobiomaterials*, ed. R. Narayan, *Woodhead Publishing*, 2018, **9**, pp. 41-94.
134. Y. Xie, J. T. Husband, M. Torrent-Sucarrat, H. Yang, W. Liu and R. K. O'Reilly, *Chemical Communications*, 2018, **54**, 3339-3342.
135. A. B. Mabire, M. P. Robin, H. Willcock, A. Pitto-Barry, N. Kirby and R. K. O'Reilly, *Chemical Communications*, 2014, **50**, 11492-11495.
136. A. B. Mabire, M. P. Robin, W. D. Quan, H. Willcock, V. G. Stavros and R. K. O'Reilly, *Chem Commun (Camb)*, 2015, **51**, 9733-9736.
137. A. B. Mabire, M. P. Robin, W.-D. Quan, H. Willcock, V. G. Stavros and R. K. O'Reilly, *Chemical Communications*, 2015, **51**, 9733-9736.
138. R. Nicoară, M. Ilieș, A. Uifălean, C. A. Iuga and F. Loghin, *Applied Sciences*, 2019, **9**, 4789.
139. J. Wolfram, Y. Yang, J. Shen, A. Moten, C. Chen, H. Shen, M. Ferrari and Y. Zhao, *Colloids and Surfaces B: Biointerfaces*, 2014, **124**, 17-24.
140. M. P. Monopoli, C. Åberg, A. Salvati and K. A. Dawson, *Nature Nanotechnology*, 2012, **7**, 779-786.
141. S. Milani, F. Baldelli Bombelli, A. S. Pitek, K. A. Dawson and J. Rädler, *ACS Nano*, 2012, **6**, 2532-2541.
142. L. B. Nguyen VH, *Int J Nanomedicine*, 2017, **12**, 3137-3151.
143. T. Cedervall, I. Lynch, S. Lindman, T. Berggård, E. Thulin, H. Nilsson, K. A. Dawson and S. Linse, *Proceedings of the National Academy of Sciences*, 2007, **104**, 2050-2055.
144. F. Alexis, E. Pridgen, L. K. Molnar and O. C. Farokhzad, *Molecular Pharmaceutics*, 2008, **5**, 505-515.
145. Z. J. Deng, M. Liang, I. Toth, M. J. Monteiro and R. F. Minchin, *ACS Nano*, 2012, **6**, 8962-8969.
146. V. Mirshafiee, M. Mahmoudi, K. Lou, J. Cheng and M. L. Kraft, *Chemical Communications*, 2013, **49**, 2557-2559.

147. A. Kurtz-Chalot, C. Villiers, J. Pourchez, D. Boudard, M. Martini, P. N. Marche, M. Cottier and V. Forest, *Materials Science and Engineering: C*, 2017, **75**, 16-24.
148. A. Salvati, A. S. Pitek, M. P. Monopoli, K. Prapainop, F. B. Bombelli, D. R. Hristov, P. M. Kelly, C. Åberg, E. Mahon and K. A. Dawson, *Nature Nanotechnology*, 2013, **8**, 137-143.
149. Q. Dai, C. Walkey and W. C. Chan, *Angew Chem Int Ed Engl*, 2014, **53**, 5093-5096.
150. C.-Y. Sun, S. Shen, C.-F. Xu, H.-J. Li, Y. Liu, Z.-T. Cao, X.-Z. Yang, J.-X. Xia and J. Wang, *Journal of the American Chemical Society*, 2015, **137**, 15217-15224.
151. I. García, A. Sánchez-Iglesias, M. Henriksen-Lacey, M. Grzelczak, S. Penadés and L. M. Liz-Marzán, *Journal of the American Chemical Society*, 2015, **137**, 3686-3692.
152. F. Xu, M. Reiser, X. Yu, S. Gummuluru, L. Wetzler and B. M. Reinhard, *ACS Nano*, 2016, **10**, 1189-1200.
153. M. Inam, G. Cambridge, A. Pitto-Barry, Z. P. L. Laker, N. R. Wilson, R. T. Mathers, A. P. Dove and R. K. O'Reilly, *Chemical Science*, 2017, **8**, 4223-4230.
154. M. Inam, J. R. Jones, M. M. Pérez-Madrigal, M. C. Arno, A. P. Dove and R. K. O'Reilly, *ACS Central Science*, 2018, **4**, 63-70.
155. N. Petzetakis, A. P. Dove and R. K. O'Reilly, *Chemical Science*, 2011, **2**, 955-960.
156. N. Petzetakis, D. Walker, A. P. Dove and R. K. O'Reilly, *Soft Matter*, 2012, **8**, 7408-7414.
157. A. Pitto-Barry, N. Kirby, A. P. Dove and R. K. O'Reilly, *Polymer Chemistry*, 2014, **5**, 1427-1436.
158. L. Sun, A. Pitto-Barry, N. Kirby, T. L. Schiller, A. M. Sanchez, M. A. Dyson, J. Sloan, N. R. Wilson, R. K. O'Reilly and A. P. Dove, *Nature Communications*, 2014, **5**, 5746.
159. L. Sun, N. Petzetakis, A. Pitto-Barry, T. L. Schiller, N. Kirby, D. J. Keddie, B. J. Boyd, R. K. O'Reilly and A. P. Dove, *Macromolecules*, 2013, **46**, 9074-9082.
160. I. Andreana, V. Bincoletto, M. Manzoli, F. Rodà, V. Giarraputo, P. Milla, S. Arpicco and B. Stella, *Materials (Basel)*, 2023, **16,** 1212-1226.
161. E. Trenkenschuh and W. Friess, *European Journal of Pharmaceutics and Biopharmaceutics*, 2021, **165**, 345-360.
162. T. Chen, X. Zhao and Y. Weng, *Front Chem*, 2022, **10**, 1107620.
163. N. Petzetakis, M. P. Robin, J. P. Patterson, E. G. Kelley, P. Cotanda, P. H. Bomans, N. A. Sommerdijk, A. P. Dove, T. H. Epps, 3rd and R. K. O'Reilly, *ACS Nano*, 2013, **7**, 1120-1128.
164. M. Oyo and Y. Masaaki, 1967, **40**, 2380-2382.
165. R. Augustine, A. Hasan, R. Primavera, R. J. Wilson, A. S. Thakor and B. D. Kevadiya, *Materials Today Communications*, 2020, **25**, 101692.
166. L. Johnson, D. M. Gray, E. Niezabitowska and T. O. McDonald, *Nanoscale*, 2021, **13**, 7879-7896.
167. C. Zhu and J. Nicolas, *Biomacromolecules*, 2022, **23**, 3043-3080.
168. L. MacFarlane, C. Zhao, J. Cai, H. Qiu and I. Manners, *Chemical Science*, 2021, **12**, 4661-4682.
169. M. C. Arno, M. Inam, Z. Coe, G. Cambridge, L. J. Macdougall, R. Keogh, A. P. Dove and R. K. O'Reilly, *Journal of the American Chemical Society*, 2017, **139**, 16980-16985.
170. X. He, Y. He, M.-S. Hsiao, R. L. Harniman, S. Pearce, M. A. Winnik and I. Manners, *Journal of the American Chemical Society*, 2017, **139**, 9221-9228.
171. M. Brzeziński and T. Biela, *Polymer International*, 2015, **64**, 1667-1675.
172. G. C. Sosso, J. Chen, S. J. Cox, M. Fitzner, P. Pedevilla, A. Zen and A. Michaelides, *Chem Rev*, 2016, **116**, 7078-7116.
173. U. Tritschler, S. Pearce, J. Gwyther, G. R. Whittell and I. Manners, *Macromolecules*, 2017, **50**, 3439-3463.
174. E. Capuana, F. Lopresti, M. Ceraulo and V. La Carrubba, *Polymers (Basel)*, 2022, **14**, 1153
175. J. R. Finnegan, X. He, S. T. G. Street, J. D. Garcia-Hernandez, D. W. Hayward, R. L. Harniman, R. M. Richardson, G. R. Whittell and I. Manners, *Journal of the American Chemical Society*, 2018, **140**, 17127-17140.

176. H.-x. Lin, Z.-c. Lei, Z.-y. Jiang, C.-p. Hou, D.-y. Liu, M.-m. Xu, Z.-q. Tian and Z.-x. Xie, *Journal of the American Chemical Society*, 2013, **135**, 9311-9314.
177. N. Baig, I. Kammakakam and W. Falath, *Materials Advances*, 2021, **2**, 1821-1871.
178. A. Mattei, R. S. Hong, H. Dietrich, D. Firaha, J. Helfferich, Y. M. Liu, K. Sasikumar, N. S. Abraham, R. Miglani Bhardwaj, M. A. Neumann and A. Y. Sheikh, *Journal of Chemical Theory and Computation*, 2022, **18**, 5725-5738.
179. M. Karimi, P. S. Zangabad, F. Mehdizadeh, H. Malekzad, A. Ghasemi, S. Bahrami, H. Zare, M. Moghoofei, A. Hekmatmanesh and M. R. Hamblin, *Nanoscale*, 2017, **9**, 1356-1392.
180. S. Yadav, A. K. Sharma and P. Kumar, *Front Bioeng Biotechnol*, 2020, **8**, 127.
181. F. C. Meldrum and C. O'Shaughnessy, *Advanced Materials*, 2020, **32**, 2001068.
182. C. E. Ellis, J. D. Garcia-Hernandez and I. Manners, *Journal of the American Chemical Society*, 2022, **144**, 20525-20538.
183. Y. Fu and W. J. Kao, *Expert Opin Drug Deliv*, 2010, **7**, 429-444.
184. Y. Qiao and Y. Men, *Macromolecules*, 2017, **50**, 5490-5497.
185. W. Zhou, S. Z. D. Cheng, S. Putthanarat, R. K. Eby, D. H. Reneker, B. Lotz, S. Magonov, E. T. Hsieh, R. G. Geerts, S. J. Palackal, G. R. Hawley and M. B. Welch, *Macromolecules*, 2000, **33**, 6861-6868.
186. a. B. L. Stephen Z. D. Cheng, *Philosophical Transactions: Mathematical, Physical and Engineering Sciences*, 2003,**156**, 517–537.
187. J. Yang, T. Zhao, Y. Zhou, L. Liu, G. Li, E. Zhou and X. Chen, *Macromolecules*, 2007, **40**, 2791-2797.
188. C. Yang, Z.-X. Li and J.-T. Xu, *Journal of Polymer Science*, 2022, **60**, 2153-2174.
189. C. Park, C. De Rosa, L. J. Fetters and E. L. Thomas, *Macromolecules*, 2000, **33**, 7931-7938.
190. Y. Gong, W. Song, Y. Wu, D. Zhang, Y. Liu, Q. Zhao, M. He and X. Chen, *Polymers and Polymer Composites*, 2019, **28**, 77-88.
191. Y. Zhu, L. Han, H. Fan, M. Wang, R. Qi, Y. Zhao and F. He, *Macromolecules*, 2020, **53**, 3217-3223.
192. M. Awashra and P. Młynarz, *Nanoscale Advances*, 2023, **5**, 2674-2723.
193. M. Inam, J. R. Jones, M. M. Pérez-Madrigal, M. C. Arno, A. P. Dove and R. K. O'Reilly, *ACS Cent Sci*, 2018, **4**, 63-70.
194. E. G. Knox, M. R. Aburto, G. Clarke, J. F. Cryan and C. M. O'Driscoll, *Mol Psychiatry*, 2022, **27**, 2659-2673.
195. M. Brust, O. Aouane, M. Thiébaud, D. Flormann, C. Verdier, L. Kaestner, M. W. Laschke, H. Selmi, A. Benyoussef, T. Podgorski, G. Coupier, C. Misbah and C. Wagner, *Scientific Reports*, 2014, **4**, 4348-4369.
196. A. E. Nel, L. Mädler, D. Velegol, T. Xia, E. M. Hoek, P. Somasundaran, F. Klaessig, V. Castranova and M. Thompson, *Nat Mater*, 2009, **8**, 543-557.
197. M. Jiang, J. D. Olarte-Plata and F. Bresme, *The Journal of Chemical Physics*, 2022, **4,** 044701.
198. Q. Wei, T. Becherer, S. Angioletti-Uberti, J. Dzubiella, C. Wischke, A. T. Neffe, A. Lendlein, M. Ballauff and R. Haag, *Angewandte Chemie International Edition*, 2014, **53**, 8004-8031.
199. J. W. Chang, A. Armaou and R. M. Rioux, *The Journal of Physical Chemistry B*, 2021, **125**, 8075-8087.
200. M. Winiewska, E. Bugajska and J. Poznański, *PLoS One*, 2017, **12**, e0173260.
201. V. K. Srivastava and R. Yadav, in *Data Processing Handbook for Complex Biological Data Sources*, ed. G. Misra, Academic Press, 2019, **4**, pp. 125-137.
202. F. Villanueva-Flores, A. Castro-Lugo, O. T. Ramírez and L. A. Palomares, *Nanotechnology*, 2020, **31**, 132002.
203. M. Inam, G. Cambridge, A. Pitto-Barry, Z. P. L. Laker, N. R. Wilson, R. T. Mathers, A. P. Dove and R. K. O'Reilly, *Chem Sci*, 2017, **8**, 4223-4230.

204. C. Sinturel, M. Vayer, R. Erre and H. Amenitsch, *European Polymer Journal*, 2009, **45**, 2505-2512.
205. T. Vilgis and A. Halperin, *Macromolecules*, 1991, **24**, 2090-2095.
206. L. R. MacFarlane, X. Li, C. F. J. Faul and I. Manners, *Macromolecules*, 2021, **54**, 11269-11280.
207. Y. He, J.-C. Eloi, R. L. Harniman, R. M. Richardson, G. R. Whittell, R. T. Mathers, A. P. Dove, R. K. O'Reilly and I. Manners, *Journal of the American Chemical Society*, 2019, **141**, 19088-19098.
208. Z. Liu, H. Fan, W. Li, G. Bai, X. Li, N. Zhao, J. Xu, F. Zhou, X. Guo, B. Dai, E. Benassi and X. Jia, *Nanoscale*, 2019, **11**, 4751-4758.
209. Y. Chen, L. Wang, W. Chen, C. Zhong, S. Li, J. Shao, G. Li and H. Hou, *CrystEngComm*, 2022, **24**, 3903-3912.
210. J. Sun, Z. Hong, L. Yang, Z. Tang, X. Chen and X. Jing, *Polymer*, 2004, **45**, 5969-5977.
211. R. V. Castillo and A. J. Müller, *Progress in Polymer Science*, 2009, **34**, 516-560.
212. N. Petzetakis, M. P. Robin, J. P. Patterson, E. G. Kelley, P. Cotanda, P. H. H. Bomans, N. A. J. M. Sommerdijk, A. P. Dove, T. H. Epps, III and R. K. O'Reilly, *ACS Nano*, 2013, **7**, 1120-1128.
213. M. Jafari and F. Mehrnejad, *PLoS One*, 2016, **11**, e0165213.
214. P. Ferraboschi, S. Ciceri and P. Grisenti, *Antibiotics (Basel)*, 2021, **10**, 1534-1550
215. G. Bashiri, M. S. Padilla, K. L. Swingle, S. J. Shepherd, M. J. Mitchell and K. Wang, *Lab Chip*, 2023, **23**, 1432-1466.
216. N. J. Warren, O. O. Mykhaylyk, D. Mahmood, A. J. Ryan and S. P. Armes, *Journal of the American Chemical Society*, 2014, **136**, 1023-1033.
217. B. Charleux, G. Delaittre, J. Rieger and F. D'Agosto, *Macromolecules*, 2012, **45**, 6753-6765.
218. H. Phan, V. Taresco, J. Penelle and B. Couturaud, *Biomaterials Science*, 2021, **9**, 38-50.
219. N. J. W. Penfold, J. Yeow, C. Boyer and S. P. Armes, *ACS Macro Letters*, 2019, **8**, 1029-1054.
220. M. J. Derry, L. A. Fielding and S. P. Armes, *Progress in Polymer Science*, 2016, **52**, 1-18.
221. J. Wan, B. Fan and S. H. Thang, *Chem Sci*, 2022, **13**, 4192-4224.
222. P.-E. Millard, L. Barner, M. H. Stenzel, T. P. Davis, C. Barner-Kowollik and A. H. E. Müller, *Macromolecular Rapid Communications*, 2006, **27**, 821-828.
223. M. Y. Khan, M.-S. Cho and Y.-J. Kwark, *Macromolecules*, 2014, **47**, 1929-1934.
224. Y. Ma, P. Gao, Y. Ding, L. Huang, L. Wang, X. Lu and Y. Cai, *Macromolecules*, 2019, **52**, 1033-1041.
225. S. L. Brown, C. M. Rayner, S. Graham, A. Cooper, S. Rannard and S. Perrier, *Chem Commun (Camb)*, 2007, **21**, 2145-2147.
226. J. Yeow and C. Boyer, *Adv Sci (Weinh)*, 2017, **4**, 1700137.
227. L. D. Blackman, K. E. B. Doncom, M. I. Gibson and R. K. O'Reilly, *Polymer Chemistry*, 2017, **8**, 2860-2871.
228. W. M. Pardridge, *J Drug Target*, 2010, **18**, 157-167.
229. J. Kreuter, *J Microencapsul*, 2013, **30**, 49-54.
230. J. Samal, A. L. Rebelo and A. Pandit, *Adv Drug Deliv Rev*, 2019, **148**, 68-145.
231. T. Patel, J. Zhou, J. M. Piepmeier and W. M. Saltzman, *Adv Drug Deliv Rev*, 2012, **64**, 701-705.
232. M. Vert, Y. Doi, K.-H. Hellwich, M. Hess, P. Hodge, P. Kubisa, M. Rinaudo and F. Schué, *Pure and Applied Chemistry*, 2012, **84**, 377-410.
233. T. T. Zhang, W. Li, G. Meng, P. Wang and W. Liao, *Biomater Sci*, 2016, **4**, 219-229.
234. S. Aday, R. Cecchelli, D. Hallier-Vanuxeem, M. P. Dehouck and L. Ferreira, *Trends in Biotechnology*, 2016, **34**, 382-393.
235. C. D. Kuhnline Sloan, P. Nandi, T. H. Linz, J. V. Aldrich, K. L. Audus and S. M. Lunte, *Annu Rev Anal Chem (Palo Alto Calif)*, 2012, **5**, 505-531.
236. S. J. Parkinson, S. Tungsirisurp, C. Joshi, B. L. Richmond, M. L. Gifford, A. Sikder, I. Lynch, R. K. O'Reilly and R. M. Napier, *Nature Communications*, 2022, **13**, 7385-7399.

237. S. Varlas, R. Keogh, Y. Xie, S. L. Horswell, J. C. Foster and R. K. O'Reilly, *Journal of the American Chemical Society*, 2019, **141**, 20234-20248.
238. M. Weiss, J. Fan, M. Claudel, T. Sonntag, P. Didier, C. Ronzani, L. Lebeau and F. Pons, *Journal of Nanobiotechnology*, 2021, **19**, 5.
239. J. K. Patra, G. Das, L. F. Fraceto, E. V. R. Campos, M. d. P. Rodriguez-Torres, L. S. Acosta-Torres, L. A. Diaz-Torres, R. Grillo, M. K. Swamy, S. Sharma, S. Habtemariam and H.-S. Shin, *Journal of Nanobiotechnology*, 2018, **16**, 71.
240. H. Xu, S. Li and Y.-S. Liu, *Signal Transduction and Targeted Therapy*, 2022, **7**, 231.
241. S. Saha, N. Sachivkina, A. Karamyan, E. Novikova and T. Chubenko, *Biomedicines*, 2024, **12**.
242. H. Sun, C. Jiang, L. Wu, X. Bai and S. Zhai, *Front Bioeng Biotechnol*, 2019, **7**, 414.
243. P. Khanna, C. Ong, B. H. Bay and G. H. Baeg, *Nanomaterials (Basel)*, 2015, **5**, 1163-1180.
244. T. Kowada, H. Maeda and K. Kikuchi, *Chemical Society Reviews*, 2015, **44**, 4953-4972.
245. S. J. Byard, M. Williams, B. E. McKenzie, A. Blanazs and S. P. Armes, *Macromolecules*, 2017, **50**, 1482-1493.
246. D. Bartczak and A. G. Kanaras, *Langmuir*, 2011, **27**, 10119-10123.
247. L. D. Field, S. A. Walper, K. Susumu, E. Oh, I. L. Medintz and J. B. Delehanty, *Sensors*, 2015, **15**, 30457-30468.
248. A. S. Pitek, D. O'Connell, E. Mahon, M. P. Monopoli, F. B. Bombelli and K. A. Dawson, *PLOS ONE*, 2012, **7**, e40685.
249. K. Amornwachirabodee, S. Khramchantuk, P. Pienpinijtham, N. Israsena, T. Palaga and S. Wanichwecharungruang, *ACS Omega*, 2018, **3**, 6833-6840.
250. G. D. Byrne, D. Vllasaliu, F. H. Falcone, M. G. Somekh and S. Stolnik, *Molecular Pharmaceutics*, 2015, **12**, 3862-3870.
251. V. Capella, R. E. Rivero, A. C. Liaudat, L. E. Ibarra, D. A. Roma, F. Alustiza, F. Mañas, C. A. Barbero, P. Bosch, C. R. Rivarola and N. Rodriguez, *Heliyon*, 2019, **5**, e01474.
252. H. Yu, Y. Zou, Y. Wang, X. Huang, G. Huang, B. D. Sumer, D. A. Boothman and J. Gao, *ACS Nano*, 2011, **5**, 9246-9255.
253. S. Mazumdar, D. Chitkara and A. Mittal, *Acta Pharmaceutica Sinica B*, 2021, **11**, 903-924.
254. M. S. Khan, N. S. Dosoky and J. D. Williams, *Int J Mol Sci*, 2013, **14**, 21561-21597.
255. W. Au - Zhao, L. Au - Han, Y. Au - Bae and D. S. Au - Manickam, *JoVE*, 2019, DOI: doi:10.3791/58900, e58900.
256. X. Wang, J. Iqbal, D. Rahmat and A. Bernkop-Schnürch, *Int J Pharm*, 2012, **438**, 217-224.
257. F. Leve, D. P. Bonfim, G. Fontes and J. A. Morgado-Díaz, *Nanomedicine*, 2019, **14**, 1565-1578.
258. J. Gavard, *Cell Adh Migr*, 2014, **8**, 158-164.
259. A. Prlj, L. Vannay and C. Corminboeuf, *Helvetica Chimica Acta*, 2017, **100**, e1700093.
260. M. G. Paez-Segala, M. G. Sun, G. Shtengel, S. Viswanathan, M. A. Baird, J. J. Macklin, R. Patel, J. R. Allen, E. S. Howe, G. Piszczek, H. F. Hess, M. W. Davidson, Y. Wang and L. L. Looger, *Nature Methods*, 2015, **12**, 215-218.
261. S. B. Keel, R. Doty, L. Liu, E. Nemeth, S. Cherian, T. Ganz and J. L. Abkowitz, *Exp Hematol*, 2015, **43**, 469-478.e466.
262. B. Srinivasan, A. R. Kolli, M. B. Esch, H. E. Abaci, M. L. Shuler and J. J. Hickman, *J Lab Autom*, 2015, **20**, 107-126.
263. A. M. Butt, H. C. Jones and N. J. Abbott, *J Physiol*, 1990, **429**, 47-62.

CHAPTER 2- Exploring self-assembled polymeric systems depending on dynamic and kinetic equilibrium

2.1 Introduction

2.1.1 Diblock copolymers for drug delivery

Neurodegenerative diseases affect a large percent of the population and the need for effective treatments increases daily. Nanomedicine can be used as a non-invasive technique as medical treatment of diseases of the central nervous system (CNS) that require transport of drugs across the blood–brain barrier (BBB).[106] Polymeric drug delivery vehicles are proven be promising systems to transfer drugs through the BBB.[107] Polymeric nanoparticles (NPs) have been widely synthesised and used in clinical practise for decades because of their biocompatibility, high stability, simple preparation method, and easy conjugation techniques with other small molecules such as drug, fluorophore, targeting ligand etc. [108] In addition with conventional drug delivery, polymeric NPs also have been utilised as a cargo for nucleic acids,[109] proteins,[110] and diagnostic agents delivery. Poly(butylcyanoacrylate) (PBCA) and poly(lactic-co-glycolic acid) (PLGA) NPs have been already approved by the USA Food and drug administration as materials for pharmaceutical applications to humans due to their biodegradable and biocompatible nature.[111] Studies with different amphiphilic diblock copolymers reveal that these nanoparticles not only can offer desired slow-release kinetics of encapsulation drug, but also can be used for on demand drug release by utilising responsive polymers as one of the blocks. For example, poly(N-isopropylacrylamide (PNIPAM)[112] polymers have been widely used due to their thermoresponsive nature, whereas poly(acrylic acid) (PAA)[113] and poly(2-dimethylaminoethyl methacrylate) (PDMAEMA)[114] polymers have been utilised to prepare pH responsive NPs. Other monomers have been also used to prepare responsive NPs. A series of thermo-responsive block co-polymers [N,N-dimethylacrylamide (DMA) -b- diacetone acrylamide (DAA)] with tunable LCST properties have been made by varying the ratio of hydrophilic-hydrophobic block length.[115] Despite the substantial research conducted on the aforementioned polymers, biodegradable polymers are attracting focus due to their application in the field of biomedical or drug delivery owing to their ability to be easily metabolised and excreted from the body.[116] However, the pharmaceutical advances are still limited by their unknown possible toxicity, which includes both chemical toxicity, which is determined by the purity and concentration of NPs, and biological toxicity, which is determined by the size, shape and

surface charge of the NPs.[117] In this regard, the polyester poly(lactic acid) (PLA) and its copolymers have been used in biomedical applications for more than 20 years and are preferred because of their biocompatibility, biodegradability and nontoxic nature.[118] From this forgoing discussion, it can be concluded that future development of new block copolymers will undoubtedly offer novel drug delivery systems. Block copolymers are a viable and appealing alternative to more traditional formulation methods, like inorganic NPs[119], dendrimers[120], liposomes[121] etc.

2.1.2 Packing parameter

Amphiphilic block copolymers, composed of hydrophilic and hydrophobic blocks, which can spontaneously self-assemble above a critical aggregation concentration (CAC) in aqueous medium.[49] In order to generate a vast array of self-assembled microstructures the solvent should be thermodynamically selective for one of the blocks (hydrophilic block) in the copolymer, to minimise energetically unfavourable interactions with the hydrophobic block.[50, 51] Manipulating the ratio of these blocks has led to the formation of a range of morphologies including micelles,[55] vesicles,[56] and cylinders.[57] A packing parameter, denoted by 'p', can be used to predict the most likely morphology of block copolymers using the influence of molecular curvature, as previously shown in Figure 1.4 in **Chapter 1**. For this project, the hydrophobic core of the particles will be the commonly used polyester poly(L-lactide) (PLLA) and poly(DL-lactide) (PDLLA), which is widely used in pharmaceutical applications and in self-assemblies and shown to be biocompatible.[52] PLLA has the ability to degrade naturally and controllably into lactic acid, which can be absorbed by the organism without cytotoxic effects.[53] Different hydrophilic corona chemistries have been explored, in order to achieve polymers NPs of different shapes and functionalities.

2.1.3 Self-assembly techniques and parameters

Self-assembly is a dynamic process where a disordered system undergoes reorganisations to an ordered structure. In the process of reorganization, some components self-assemble first as a thermodynamically metastable structure to generate a 'local minimum' of free energy, but that is not always the case. Even if the structure formed first appears to be ordered, it

may not conform to a local minimum of free energy. To describe these phenomena, two terms have been introduced: near-equilibrium assembly, in which thermodynamic forces are dominant, and far-from-equilibrium assembly, in which dynamic effects are critical to the outcome, resulting in kinetically-trapped metastable structures.[122, 123] Depending on the circumstances, a typical self-assembly may exhibit both types of behaviour. Interactions between molecular building blocks, solvent molecules and the surface are crucial in defining the morphologies of a self-assembled state.[124] Apart from these interactions, which constitute a variation of the more complex thermodynamic explanation of the self-assembly mechanism, other important parameters are temperature, entropy, or chemical potentials.[125] In a more practical matter if all the external parameters are maintained, some variables like the type of solvent, concentration of the molecular building block, intermolecular interactions, size and structure of the adsorbing molecules, and type of surface must be taken into account that can affect the system.[124] The interactions between the building blocks can be affected by forces of various physical origins. Forces including ionic, covalent, or metallic bonding, hydrogen bonding, and Van der Waals interaction govern the short-range interaction. Whereas, long-range interactions have an effective range that is much longer than the atomic wavelength, and can be originated from elasticity, electrostatic or magnetic field, colloidal, capillary forces hydrodynamic interaction etc.[126] Different amphiphilic molecules can self-assemble in ordered structure by utilizing different noncovalent forces depending on their chemical groups and the ratio of their hydrophobic/hydrophilic components.[127] As previously described, micellar structures tend to form spontaneously from polymers with low hydrophobic content above a critical micelle concentration (CMC) and temperature (CMT).[128]

Different self-assembly methods have been developed over the years to achieve polymeric nanoparticles. The most popular methods are direct dissolution, flash nanoprecipitation, dialysis and emulsification-solvent evaporation.[129] Direct dissolution is solvating of an amphiphilic block copolymer in an aqueous solution.[130] FNP (flash nanoprecipitation) is a procedure that stabilises an insoluble low molecular weight compound in a nano-sized, polymer-stabilized delivery vehicle by rapid mixing.[131] The polymer is dissolved in a good solvent (promoting good solvability parameter between the polymer and molecules of the

solvent that constitute the polymer dispersed) and rapidly introduced in the aquatic solution while stirring. This method takes advantage of the kinetic entrapment dynamics to create a self-assembled system with high encapsulation rate of drug uploading.[131] Another technique used is the slow addition of organic solution to the water solution in order to have a more thermodynamically stable solution.[132] All techniques have advantages and disadvantages, and a variety of factors influence the method of preparation, including the form of polymeric system, the application region, and the size requirement,[133] so they are to be used and explored upon to one's discretion.

2.1.4 Fluorescent nanoparticles

Fluorophores play an important role as probes in biological systems, for imaging, and for the study of dynamic processes. These applications result from the high sensitivity and ease of measurement for fluorescence emission, and the responsivity of dyes to the physical nature of their environment – for example solvatochromism.[134] Response of fluorophores to chemical stimuli is also highly desirable, and is frequently utilised in the study of conjugation to biological macromolecules. One mechanism for response is the conversion of a latent quenched fluorophore to an emissive fluorophore upon the desired chemical stimulus.[135] Aminomaleimides are easily functionalised, providing a versatile fluorescent probe. Herein the innovative aminomaleimide will be incorporated in the diblock copolymer system in the intermediate position (between hydrophobic and hydrophilic). The fluorescence emission of aminomaleimide highly depends on surrounding microenvironment.[136] It is very emissive when it is in a hydrophobic core and quenched in presence of protic solvent such as water. The fluorescent molecule can not only track/confirm the position of the nanoparticles to verify their permeation of the BBB, but it can also provide evidences on the drug release potential studies since the fluorophore can be quenched as mentioned earlier.

Conversely, one advantage of aminochloromaleimide is that they do not undergo further substitution with the addition of excess amine or thiol. ACMs do not require di-substitution to generate intense emission overtime, which provide stability.[137] Considering this, further

investigation into the self-assembly behaviour of diblock copolymers with different coronas will be examined through fluorescence analysis will be explored using an ACM fluorophore.

2.1.5 Protein corona formation

As discussed in ***Chapter 1***, the nanoparticles that are designed for biomedical applications such as drug delivery must be evaluated during their encounter with biological fluids. These fluids usually contain large amounts of proteins that are necessary for the organism regulation, thus the interaction between these proteins and the nanoparticles is important to be studied. Protein corona is defined as the coating formation and deposition of biomolecules on the surface of the nanoparticles.[138] This absorption of proteins creating this proteomic interface is a result of binding forces such as Van der Waals interactions, hydrogen bonding, hydrophobic interactions, electrostatic interactions, and π– π interactions.[139] The distribution of the biomolecules on NPs surface and how embedded they are varies depending on the nature of nanoparticle surface. According to the current theory, the corona formation can be divided into two layers: hard and soft (Fig 2.1.1).[140] The degree to which the biomolecules are bound to the nanoparticles distinguishes these components. The soft layer is often thought to be more dynamic, since it is made up of rapidly exchanging biomolecules making them easier to interact with the solution and forming weaker bonds with the particles. Hard corona proteins have higher binding affinity, than soft corona proteins because they present more tightly bonds with the particle surface.[141] Thus, the strongly absorbed proteins of the hard corona are more difficult to displace and more firmLy attached under physiological conditions (changes in conditions such as pH, temperature, or the presence of other biomolecules can potentially alter the composition of the protein corona over time) unlike the soft corona proteins, which will allow reconfigurations in the corona of the particle over time, due to their mobility creating a more dynamic system.

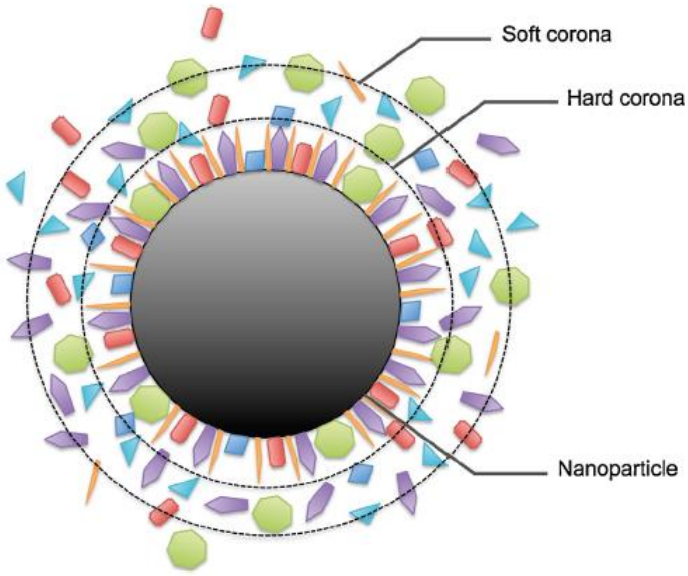


Figure 2.1.1. Schematic representation of the current protein corona hypothesis.

Such interaction of proteins with nanoparticle surface can modify the physicochemical properties of nanoparticles such as size, surface charge, shape, surface composition, and functionality, hence giving to the system a new biological identity.[142] Multiple studies have demonstrated that protein absorption can lead to bigger particles, which offer a higher surface area.[143] Positively charge particles are creating electrostatic interactions more effectively, since the majority of the protein are negatively charged.[144] The shape of the nanoparticles have also been indicated to effect the type of the corona that will form.[145]

The corona's screening of the nanoparticle surface has proven useful in successful targeting with particular ligands. However, it has been demonstrated that when these functionalized particles are put in a biological environment, their binding potential is lost.[146, 147] The interaction of the special functionalized bioligands with other medium proteins, as well as the formation of the protein corona, appears to be the cause of their lack of targeting specificity. As a consequence, in a biological medium, the nanoparticles struggle to recognize specific target in biological milieu. For example, Salvati *et al*. (2013) found that the protein corona could shield the basic binding between transferrin on nanoparticles and free transferrin receptors or cellular transferrin receptors, resulting in reduced cellular uptake by target cells and losing its targeting specificity.[148] Several methods have been devised to overcome the protein corona effect, like PEG coating,[149] de-shielding ligands[150, 151] and lipid

coverings[152] but none of them can eradicate the influence of the protein corona completely. As a result, it is critical to assess protein corona formation and its impact on drug delivery systems for brain targeting capability, as well as optimize nanoparticles composition to reduce the impact of protein corona.

2.2 Results & Discussion

A series of diblock copolymers have been synthesized to prepare nanoparticles with different core/corona for the purpose of permeating the blood and brain barrier. Diblock copolymers have been proven to be very efficient drug delivery systems. Polylactide has been used as one of the blocks as the lactide core imparts biodegradability in the system which is highly desired for practical applicability. Different hydrophilic blocks have been used to prepare nanoparticles with different corona and surface functionality.

2.2.1 Synthesis of Poly(lactide)

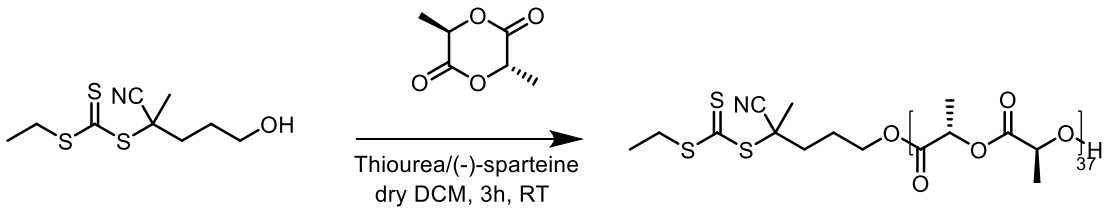
The overall goal of this project is synthesis and characterization of a library of amphiphilic diblock copolymers and to study their self-assembly properties in aqueous medium PLLA was selected as the hydrophobic core material due to its biodegradable and biocompatible nature, as well as its crystallinity, which not only can provide different structures with CDSA, but can offer prolonged circulation times according to the percentage of crystallinity. PDLLA was also explored as a core in order to verify if the crystallinity of the core obstructs the particles of forming smaller particles. PDMAEMA has been selected as the corona-forming block, as it is biocompatible and water-soluble cationic polymer capable of forming compact complexes by electrostatic interactions with negatively charged proteins such as transferrin. Previous work in the group has validated the formation of different structures using PDMAEMA-*b*-P*L*LA diblock copolymers,[153-159] and therefore the similar synthetic strategy has been employed in this work. Here an aminochloromalemide fluorescent probe was incorporated in the diblock copolymer system.

The PDMAEMA-*b*-PLLA diblock was synthesized using a combination of ring opening polymerization (ROP) of L-lactide and reversible addition-fragmentation chain transfer (RAFT) polymerization of the pro-cationic monomer. The polymerizations were done using a

bifunctional initiator, which could be used for ROP due to the active hydroxyl group and for subsequent RAFT polymerization due to the thiocarbonyl group. The overall approach was to first synthesize a macroinitiator through ROP of L-lactide with the dual chain transfer agent (CTA) initiator, followed by the RAFT polymerization of DMAEMA with this macroinitiator to form the diblock copolymer.

Synthesis of Macro-CTA PLLA (ROP of L-lactide)

The ROP of L-lactide was carried out in a nitrogen-filled glove box to avoid any unwanted initiation from water in the atmosphere (Scheme 6). The reaction was conducted using reported procedure as done by our group.[156] 1-[3,5-bis(trifluoromethyl)phenyl]-3-cyclohexylthiourea and (-)-sparteine have been used as organocatalytic system, and a RAFT CTA as initiator as previously produced (see experimental). The reaction reached almost full conversion after 3 hours, and it was quenched by direct precipitation into cold hexane. The PLLA generated with a DP of 37 and a *M*n of 5.6 kDa, as calculated by ^{1}H NMR end-group analysis (Fig. 2.1).



Scheme 6. Representation of ROP of L-lactide

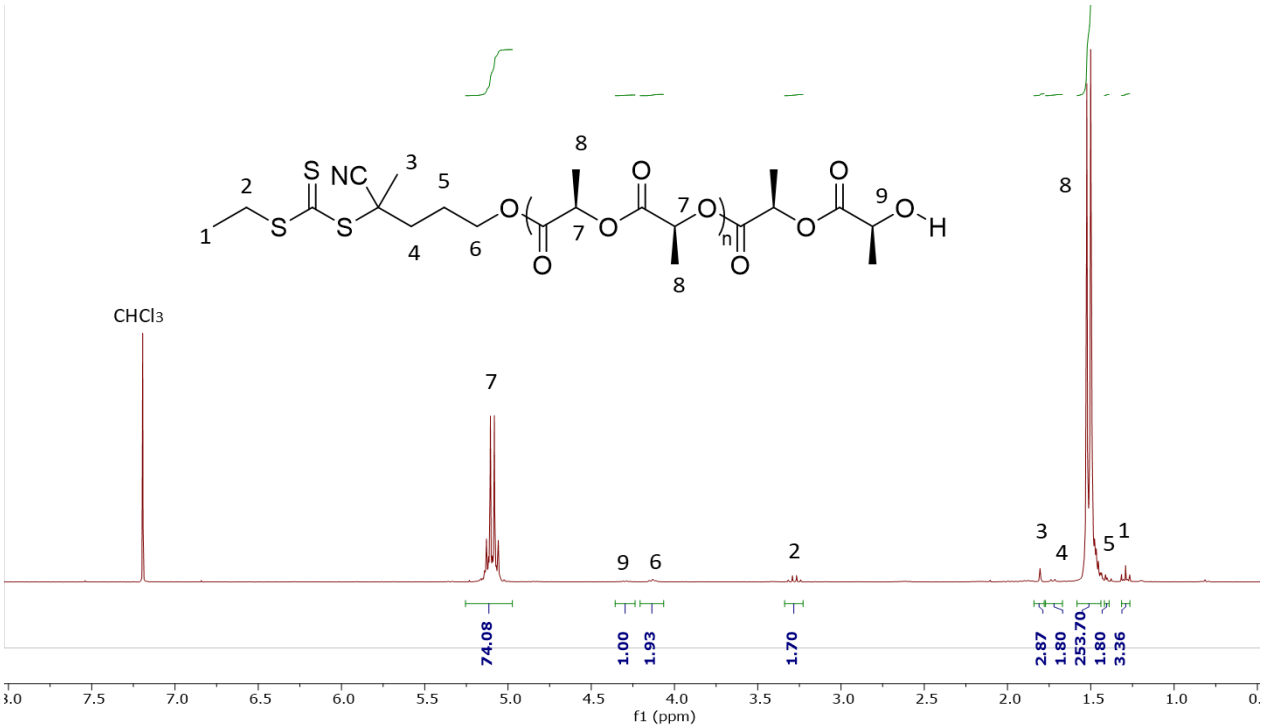


Figure 2.1. ^{1}H NMR spectrum ($CDCl_3$, 300 MHz) of poly (L-lactide)$_{37}$

The reaction reached full conversion after 3 hours, generating a degree of polymerisation (DP) of 37 as calculated by end–group analysis. The polymerization was verified by methine resonance of the repeat units was observed at δ = 5.16 ppm.

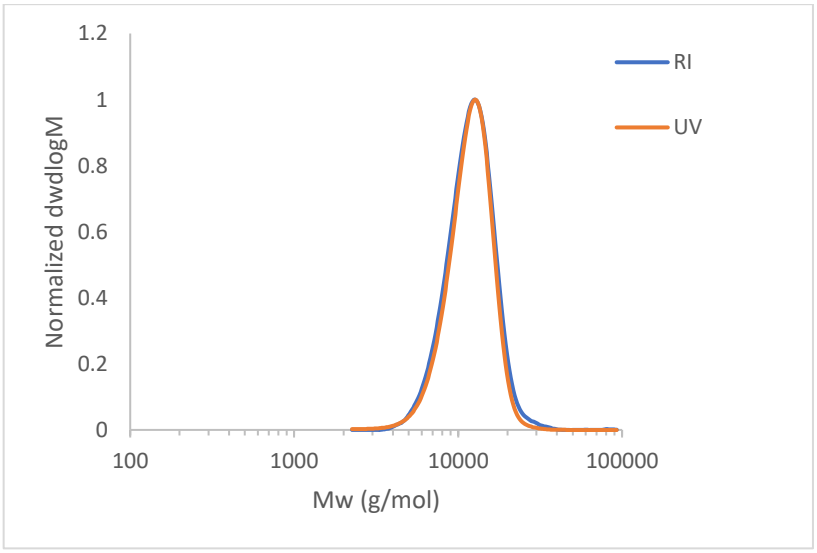


Figure 2.2. Representation of molecular weight distribution from THF SEC of poly(L-lactide)$_{37}$ (λ = 309 nm).

After conducting size exclusion chromatography (SEC) analysis, we obtained a number-average molecular weight (Mn) of 11 kDa. This measurement indicates the average molecular weight of the polymer chains in our sample. However, here it is important to note that there appears to be a discrepancy between the molecular weight determined by SEC and that obtained from nuclear magnetic resonance (NMR) analysis.

This disparity could potentially be attributed to the calibration standards utilized in SEC analysis. In SEC, polymer samples are compared to a set of standards with known molecular weights to estimate their own molecular weights. However, the accuracy of this estimation heavily relies on the similarity between the polymer being analysed and the standards used for calibration.

In our case, the standards employed for SEC calibration were poly(methyl methacrylate) (PMMA) standards. While PMMA is commonly used as a reference material in SEC due to its well-defined molecular weight distribution, its structure and behaviour are not aligning with polymer PLLA sample. As a result, this discrepancy between the SEC and NMR results suggests the need for further investigation into the calibration methods and potentially the development or selection of more appropriate standards that better represent the characteristics of this polymer. A low polydispersity of $Đ$M = 1.12 was observed with good overlap of the RI and UV traces (λ = 309 nm), confirming retention of the RAFT end group (Fig. 2.2).

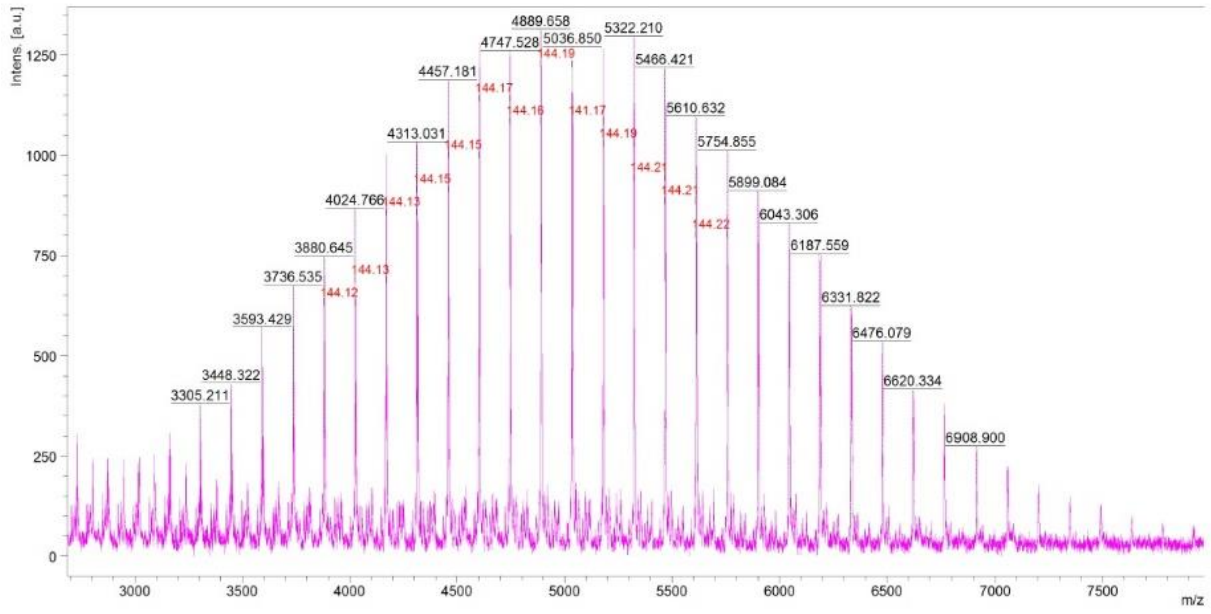
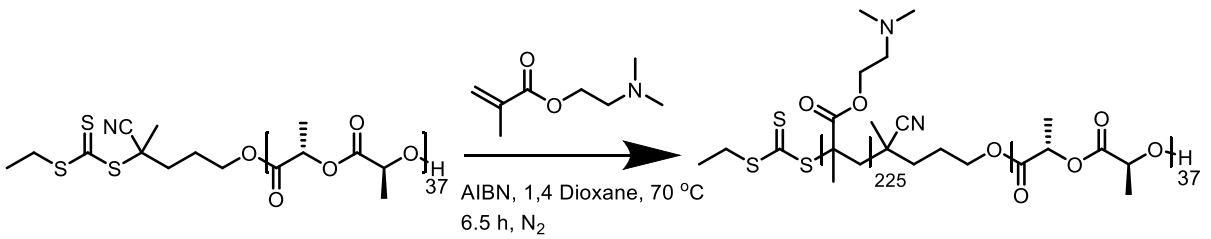


Figure 2.3. Maldi-TOF mass spectroscopy of poly(L-lactide)$_{37}$ in dithranol matrix with THF as solvent

Matrix-assisted laser desorption ionisation time of flight (MALDI-ToF) mass spectrometry was consistent with the expected molar mass and showed minimal transesterification only (Fig. 2.3).

2.2.2 Synthesis of positively charged diblock copolymer PDMAEMA-b-PLLA

Amphiphilic diblock copolymer PDMAEMA-b-PLLA was synthesised using a combination of ring-opening polymerisation (ROP) of L-lactide and reversible addition-fragmentation chain transfer (RAFT) polymerisation of DMAEMA (Scheme 7). A dual-headed ROP initiator and chain transfer agent was chosen specifically for the controlled RAFT polymerisation of DMAEMA, where the tertiary carbon R group of this chain transfer agent is more suitable for the polymerisation of methacrylate monomers.



Scheme 7. Reaction scheme of poly(L-lactide)$_{37}$ -b-poly(N,N-dimethylaminoethyl methacrylate)$_{225}$ diblock copolymers.

As such, detailed procedures and characterisation data is given for these polymers. A summary of the prepared polymers can be found in table 1. $PLLA_{37}$, (95.6 mg, 17.6 µmol), N,N-dimethylaminoethyl methacrylate, (1000 mg, 6360 µmol) and AIBN (28.9 µL of a 10 mg mL^{-1} solution in 1,4-dioxane) were dissolved in 1,4-dioxane (2.14 mL) before transferring to a dried ampoule under nitrogen (Scheme 7). After three freeze-pump-thaw cycles, the solution was sealed under nitrogen and heated for 6 hours at 70 °C for 60% conversion. The reaction was quenched in liquid nitrogen and purified by precipitation three times into cold ice-cold n-hexane. The resultant pale yellow solid was dried in vacuum before use. After 6.5 hours, the conversion indicated by NMR analysis was 63 %. The purified polymer had a DP of 225 of the DMAEMA block, and an overall *M*n of 41 kDa as calculated using the known ^{1}H NMR PLLA signals (Fig. 2.4). The *M*n of 32 kDa is given by SEC analysis with THF as eluent. There is a discrepancy between the SEC and NMR result, that as previously mentioned, can be attributed to the PMMA standards used for SEC calibration. The block copolymer had a polydispersity of 1.41 with good overlap of the RI and UV (λ = 309 nm) traces, showing retention of the RAFT end group (Fig. 2.5). A clear shift from the PLLA-macroCTA can be observed, confirming quantitative conversion of the macroinitiator into the block copolymer with no homopolymer remaining.

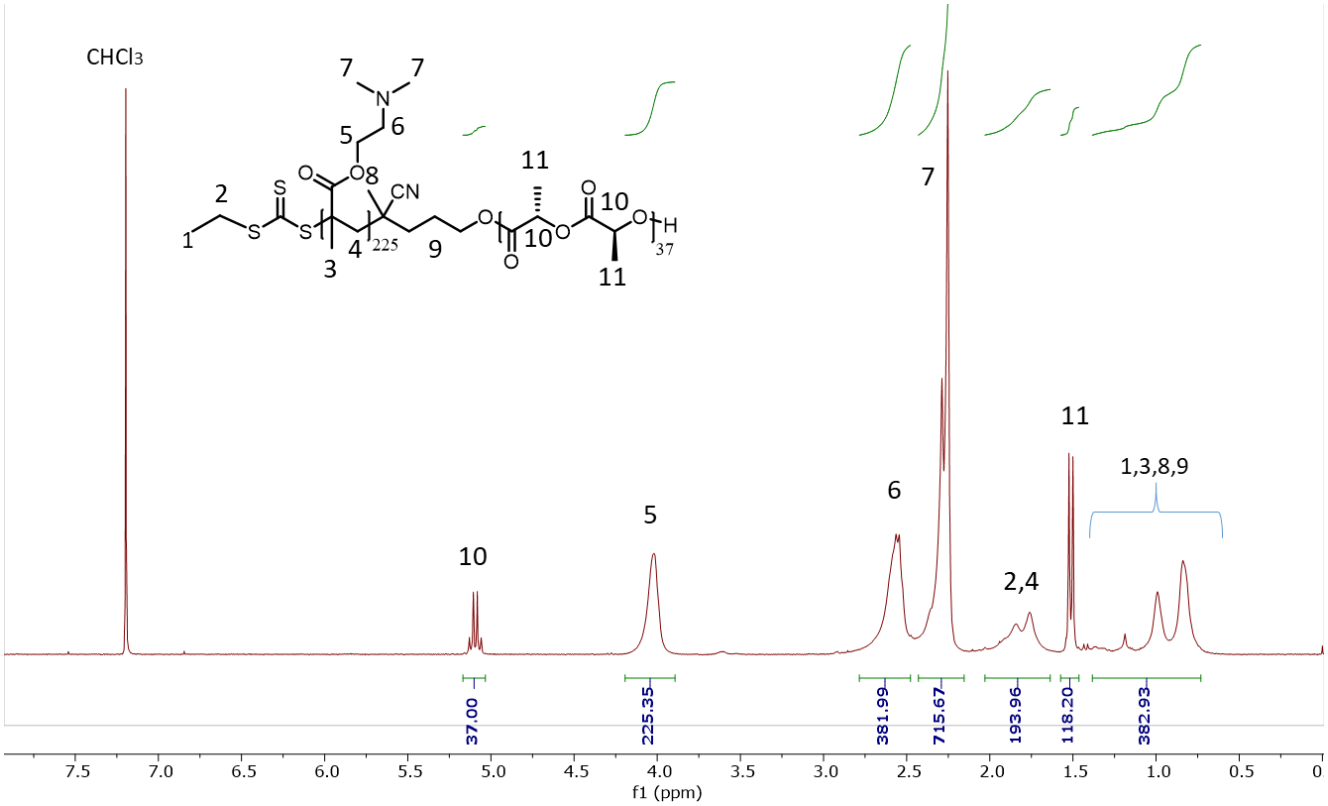


Figure 2.4. ^{1}H NMR spectrum ($CDCl_3$, 300 MHz) of poly(L-lactide)$_{37}$ -b-poly(N,N-dimethylaminoethyl methacrylate)$_{225}$ diblock copolymers.

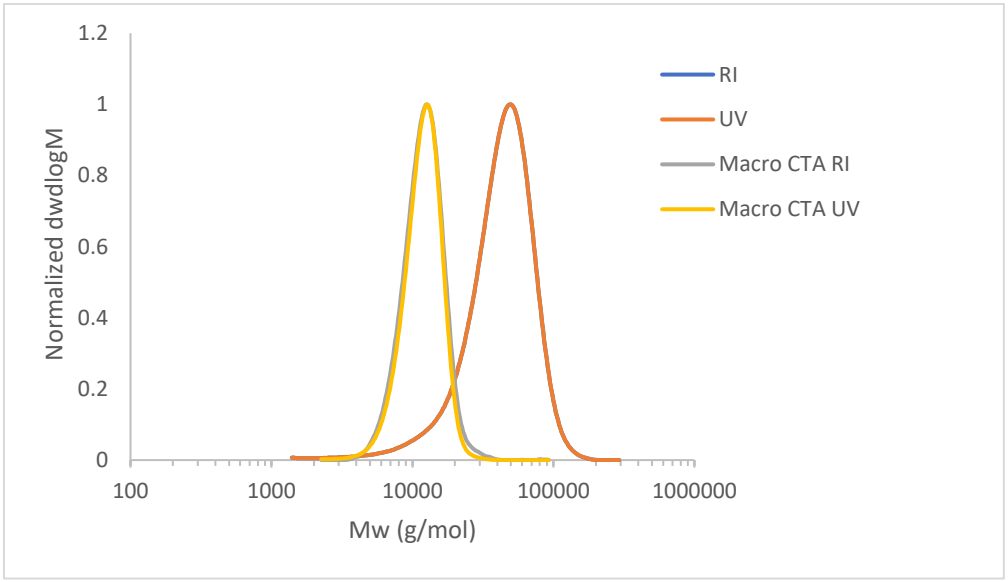
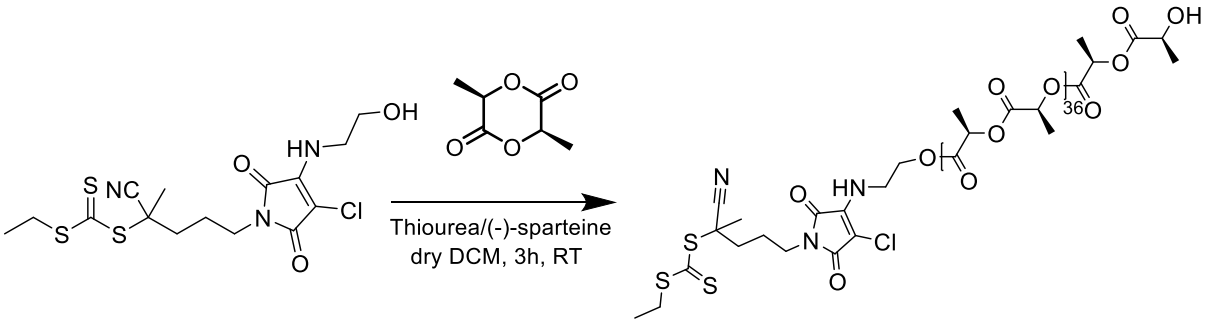


Figure 2.5. Representation of Molecular weight distribution from THF GPC of poly(L-lactide)$_{37}$-b-poly(N,N-dimethylaminoethyl methacrylate)$_{225}$ diblock copolymers (λ = 309 nm).

After the successful synthesis of the poly(L-lactide)$_{37}$-b-poly(N,N-dimethylaminoethyl methacrylate)$_{225}$ diblock copolymer, which indicated control over the ROP and RAFT synthetic techniques, the same process was repeated with the addition of a dichlomaleimide moiety to the previously synthesized CTA, in order to create an aminochloromaleimide (ACM) fluorescent probe (see experimental) which has been reported to have great stability and fluorescence properties.[134]

Synthesis of fluorescent with ACM probe Macro-CTA (ROP of L-lactide of fluorescent CTA)

As previously reported, the standardized ROP of L-lactide was carried out in a nitrogen-filled glove box with the same conditions as above with the only difference being the fluorescent CTA (Scheme 8) . The reaction reached full conversion after 3 hours, and produced a polymer with DP of 36 as targeted and an *M*n of 5.8 kDa as calculated by ^{1}H NMR end-group analysis (Fig. 2.6). Chloroform SEC analysis revealed an M_n of 11 kDa and a polydispersity $Đ_M$ of 1.11 calculated from the refractive index data (Fig. 2.7). A second smaller peak was appearing, but it was identified as trapped solvent within the crystalline polymer. As with the non-fluorescent polymer, the discrepancy between the *M*n by size exclusion chromatography (SEC) analysis of 11 kDa and NMR analysis can be explained by comparison to the poly(methyl methacrylate) standards used for calibration.



Scheme 8. ROP of L-Lactide with fluorescent initiator

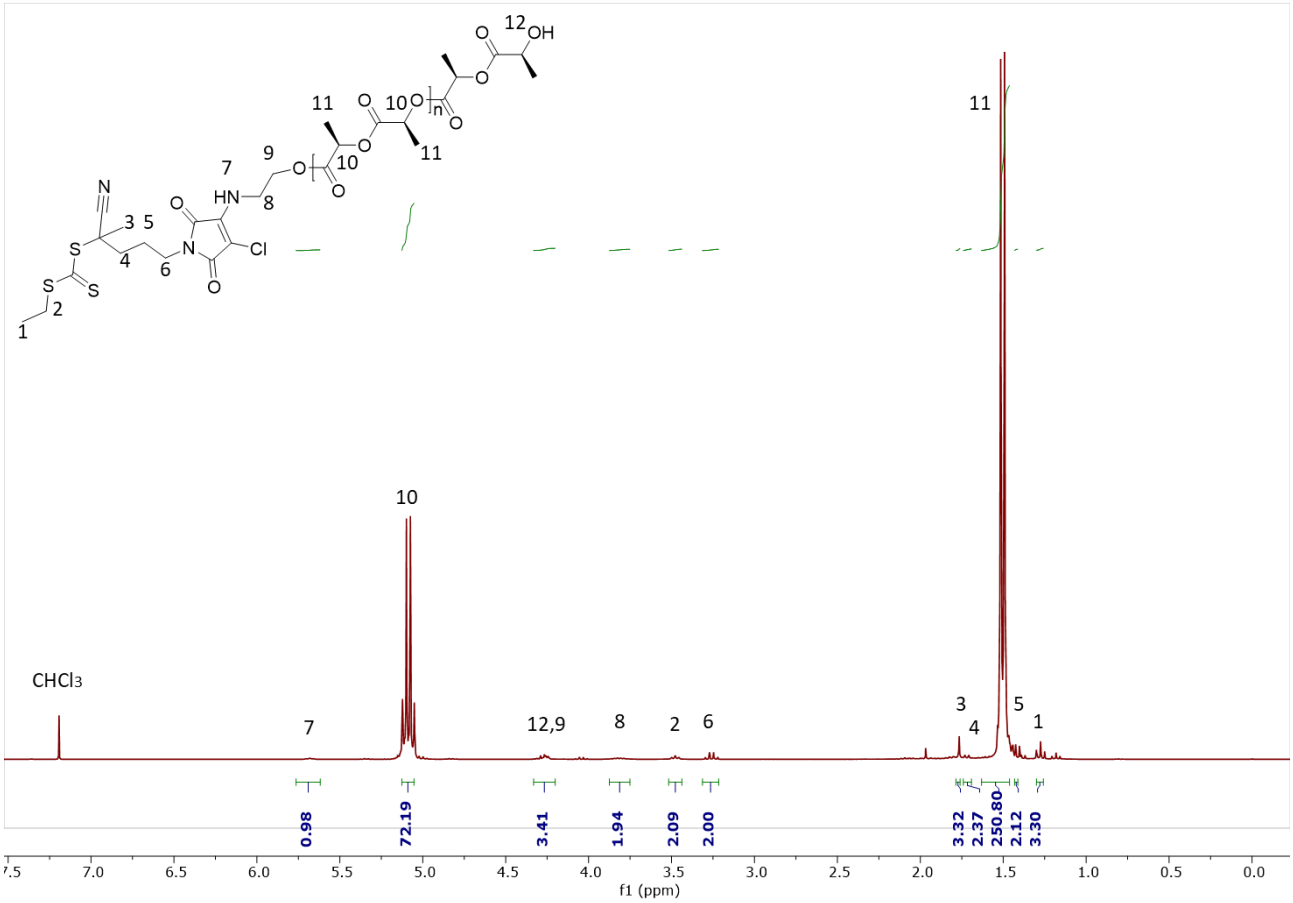


Figure 2.6. ^{1}H NMR spectrum ($CDCl_3$, 300 MHz) of fluorescent Macro CTA

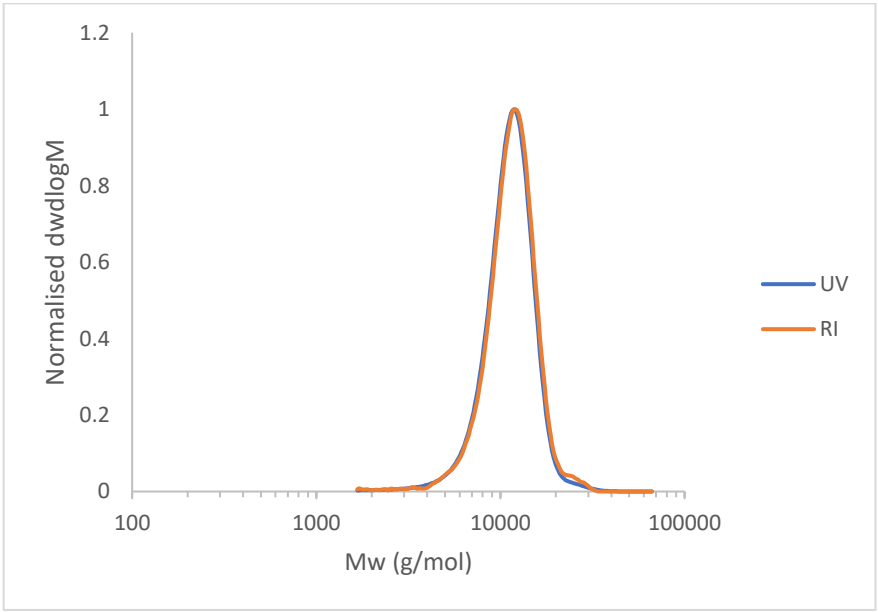


Figure 2.7. Representation of Molecular weight distribution from Chloroform GPC of fluorescent Macro CTA Poly(L-lactide)$_{36}$ (λ=309 nm)

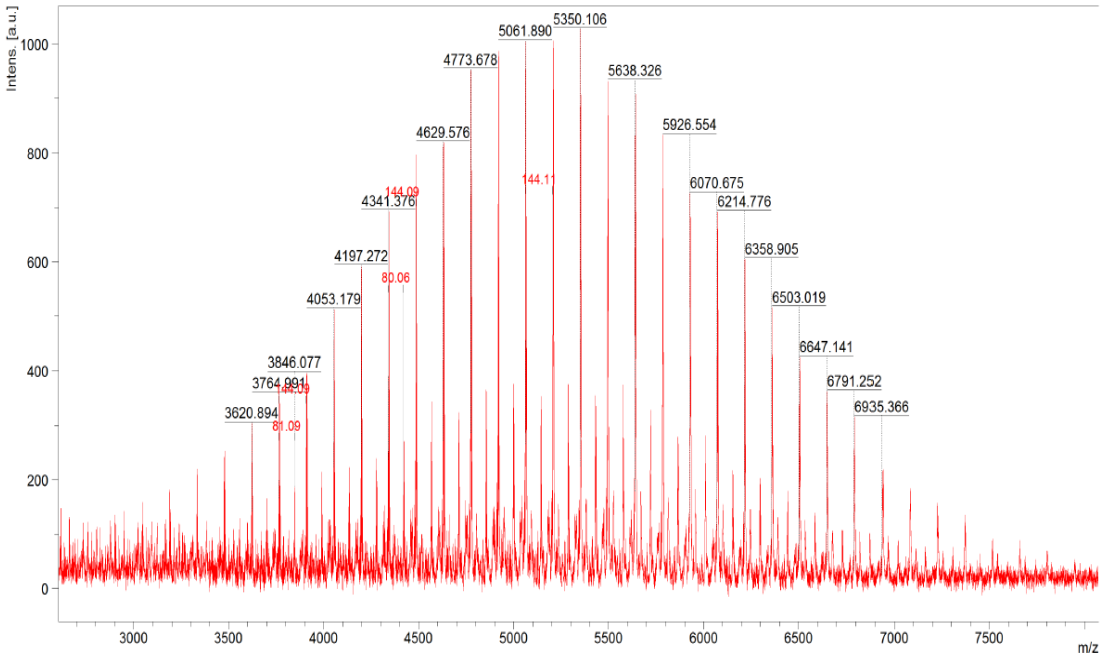


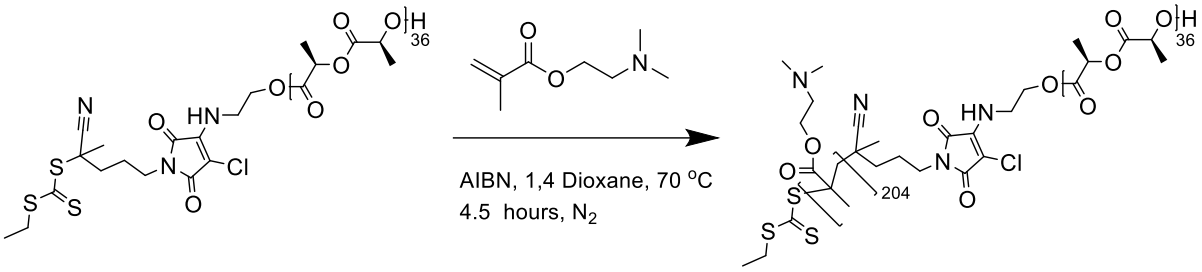
Figure 2.8 MALDI-TOF analysis of fluorescent Macro CTA Poly(L-lactide)$_{36}$

As presented by figure 2.8, MALDI-TOF analysis of the fluorescent Macro CTA revealed atomic distances of 144.11 indicative of lactide repeating units, but also of 80 which indicates transesterification in a scale of approximately 15%. However, the level of transesterification was low, and was hypothesized as not likely to affect the next synthetic step.

RAFT Synthesis of poly(L-lactide)$_{36}$ -b-poly(N,N-dimethylaminoethyl methacrylate)$_{204}$ fluorescent block copolymers

The PLLA macroinitiator was then employed for the RAFT polymerization of DMAEMA, using 1,4-dioxane at 70 °C with AIBN as the radical initiator (Scheme 9). RAFT polymerization of DMAEMA was carried out and after 4.5 hours, the conversion indicated by NMR analysis was 55.6%. The purified polymer had a DP of 204, and a *M*n of 37.8 kDa as calculated using the known PLLA ^{1}H NMR signals(Fig 2.9). This is in good agreement with the *M*n of 34.8 kDa as given by SEC analysis with chloroform as eluent. The final block copolymer polydispersity was 1.34 with good overlap of the RI and UV (λ = 309 nm) traces, showing retention of the RAFT end group (Fig. 2.10). A small shoulder was observed in the UV trace, which is likely a small amount of homopolymer within the polymerization, however was only minimal and so

it is not likely to affect the polymer properties and the self-assembly further. The polydispersity given by the UV detector was 1.41, in comparison with the RI which gave a polydispersity of 1.34.



Scheme 9. Reaction scheme of poly (L-lactide)-b-poly (N,N-dimethylaminoethyl methacrylate) fluorescent diblock copolymers.

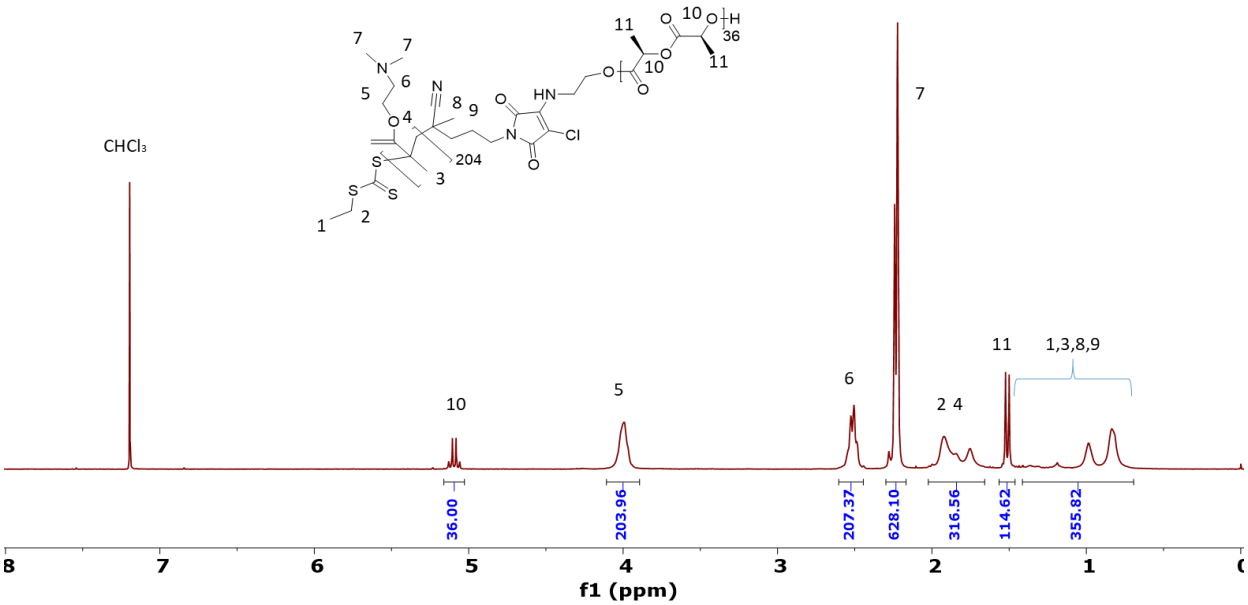


Figure 2.9. ^{1}H NMR spectrum ($CDCl_3$, 300 MHz) of fluorescent $PLLA_{36}$-b-$PDMAEMA_{204}$

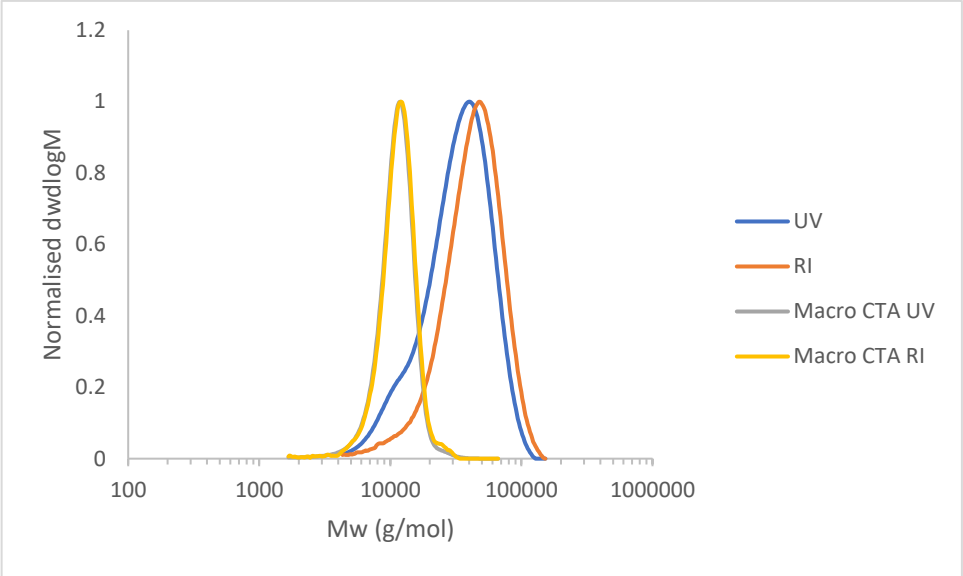


Figure 2.10. Representation of Molecular weight distribution from chloroform SEC of poly(L-lactide)$_{36}$-b-poly(N,N-dimethylaminoethyl methacrylate)$_{204}$ diblock copolymers. (λ=309 nm)

Table 1 below provides information of all the diblock copolymers synthesized with the positively charged PDMAEMA corona. The rest of the polymers were synthesized in a similar manner and their details can be found in the experimental section.

Table 1. Table of positively charged polymers and their characteristics

Corona	Polymer Name	DP	M_n (kDa)	M_w (kDa)	$Đ_M$	Ratio Core:corona	Fluorescence	Core
DMAEMA	P1	204	35	31	1.31	1:6	Yes	PLLA
DMAEMA	P2	225	32	34	1.41	1:6	No	PLLA
DMAEMA	P3	200	25	31	1.20	1:6	Yes	PDLLA
DMAEMA	P4	199	26	34	1.27	1:6	No	PDLLA

2.2.3 Self-assembly of block copolymers with positive charge

After the synthesis and characterisation of the diblock copolymers necessary, it is time to explore their ability to self-assemble into a potential drug delivery carrier. In order to optimize the nanoparticle system different methods was employed. As previously mentioned in ***Chapter 1***, three different methods will introduced different characteristics and they will promote a different thermodynamic state in each assembly. Target of this

study is to optimize the self-assembly of the diblock copolymers in order to get the smaller size nanoparticles as it is required for the drug delivery application that it is indented to.

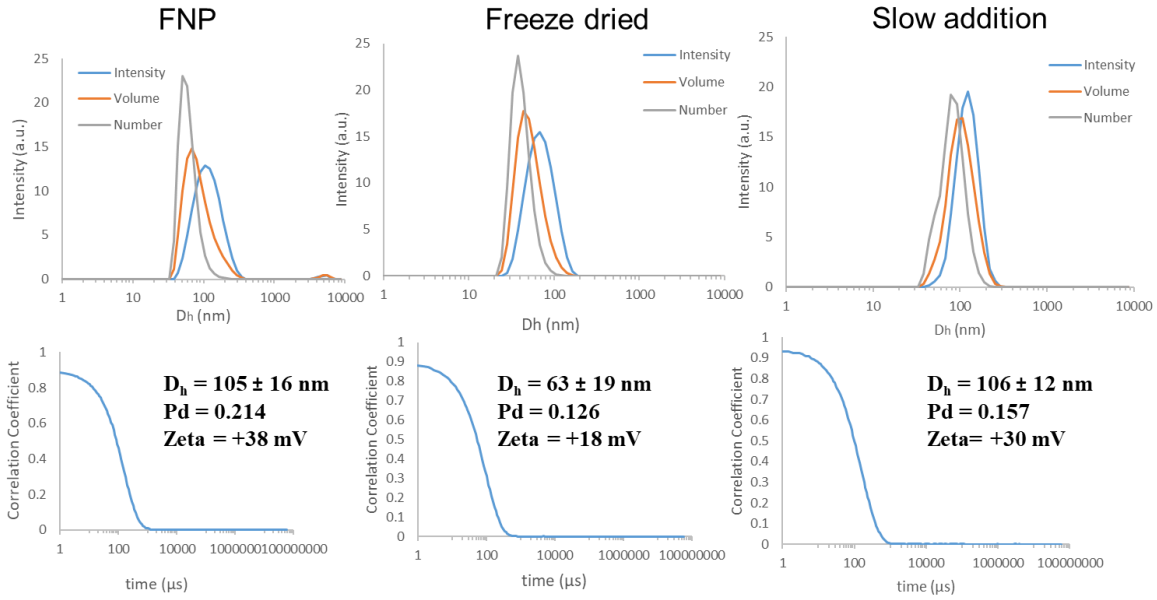


Figure 2.11 DLS data of self-assembly of P2 in DMF with flash nanoprecipitation, freeze drying, slow addition. (errors bar represent standard deviation)

The P2 (2 mg) was dispersed in DMF 1mL and then 1 mL of distilled water was added via pipetting (FNP) or inserted slowly with a syringe pump 0.5 mL/hr (slow addition). Figure 2.11, presents P2 nanoparticles arising from different methods. FPN and slow addition indicate similar hydrodynamic diameter after the dialysis. A small amount of the slow addition formulation was freeze dried and redispersed at 1 mg/mL concentration and provided with a size of 63 nm as depicted in figure 2.11. Particle aggregation or clustering may be interfered with by freeze-drying. Due to the attraction interactions that exist between the particles when they are scattered in a liquid, aggregates may develop. However, the solvent is eliminated during freeze-drying, and the particles are immobilised in a solid matrix. Smaller apparent sizes can occur from the dispersion of individual particles caused by this immobilisation, which can stop future aggregation. Another reason, that phenomenon occurred could be that the dispersion of particles in the dry state can be improved by freeze-drying. Agglomerates can be dispersed and particle homogeneity can be improved by the procedure. Due to their more even distribution across the sample, the particles may look smaller due to the better dispersion.

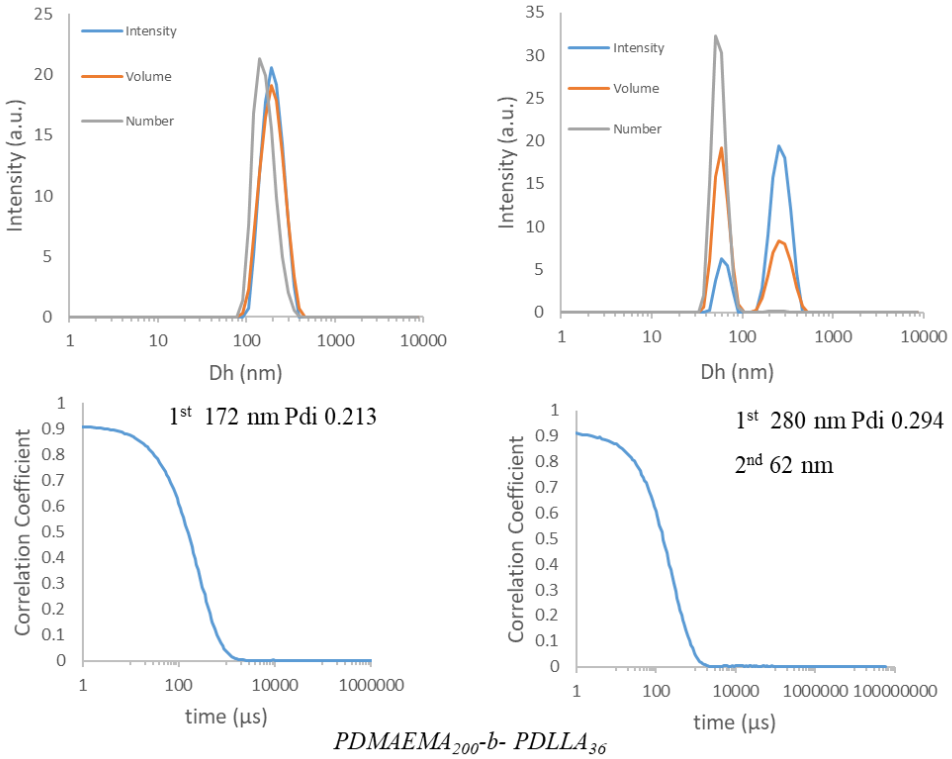


Figure 2.12 DLS data of P3 FNP(left), after freeze dry (right)

Same results as before tried to be recreated with P3 polymer and a flash nanoprecipitation was conducted with DMF solvent at 1 mg/mL and dialysed against water 18.2 MΩ for 3 days. After dialysis a sample was taken and was freeze dried. Unfortunately, after redispersion the same results did not repeat. An explanation could be that after the freeze drying process the nanoparticles collapse and reorganize a new when they are redispersed in the new solution. Also, not all nanoparticles may redisperse equally following reconstitution after freeze-drying. While some nanoparticles may stay in their aggregated or agglomerated states, others may separate into separate particles. The size distribution analysis may reveal two populations as a result of this insufficient redispersion.[160] The synthesized particles of P3 after FNP were analysed through TEM, to compare the sizes. The TEM data in figure 2.13 depict a size of 46 nm and not 172 nm that the DLS had reported. TEM is a dry technique, and it can shrink the NPs. Also, DLS is calculating the hydrodynamic diameter is a more dynamic system that will have a lot interactions like aggregations, especially in a charged environment.

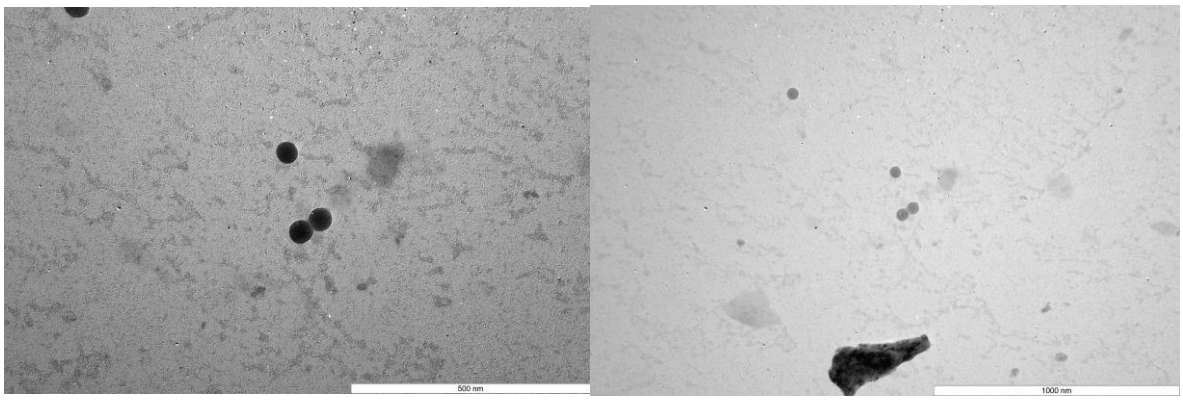


Figure 2.13. TEM DATA of P3 after FNP (sample of 20),scale bar 500 nm (left), scale bar 1000 nm (right)

Continuing with imaging techniques P1 and P2 were self-assembled with FNP with the standard protocol with DMF solvent. From figure 2.14 below the P1 polymer presents bigger D_h= 149 nm even though it has smaller corona and core than the counterpart P2 that does not carry a fluorophore. DLS data and AFM data of P2 are in good agreement, and the difference between the D_h= 105 nm and AFM=80 nm is most likely because AFM is a dry technique. 80 nm is the size depicted through AFM for the P1 too.

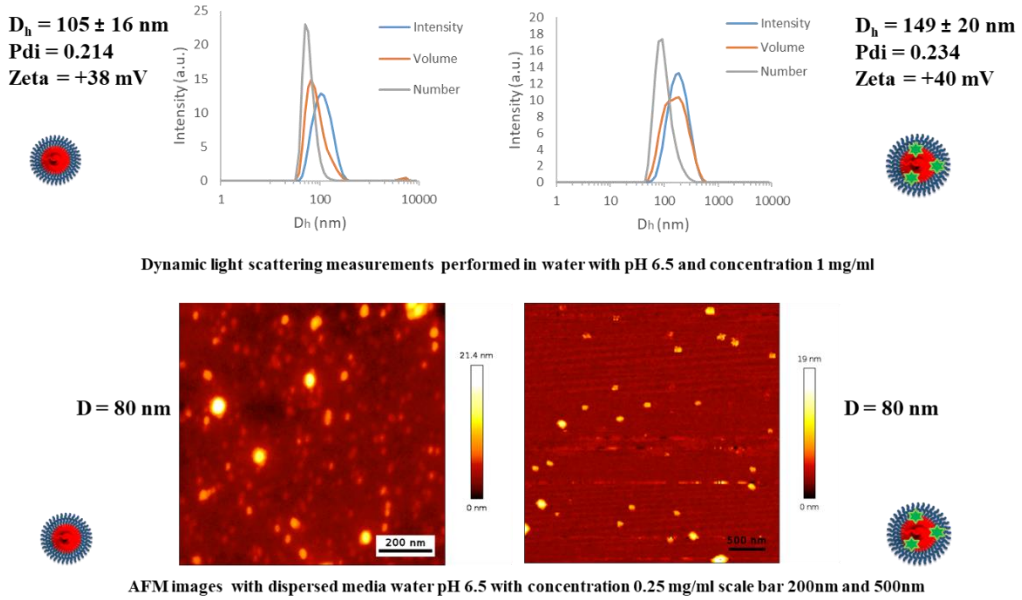


Figure 2.14 DLS and AFM data of a,c) P2 and b,d) P1 after FNP (errors represent standard deviation)

After the examination of P1 and P2 with DLS and AFM a small quantity of their solution was taken and was freeze dried to check if the crystalline PLLA core in these nanoparticles helps to stabilize the formulation.

Table 2. Freeze drying effect of P1 and P2 after FPN

Particles	Size	Pd	Zeta	Temperature
P1	65 nm	0.261	+38 mV	25°C
P2	86 nm	0.177	+42 mV	25°C

During the lyophilization process, the PLLA crystalline core could initially provide the nanoparticles structural with support.[161] However, as the solvent is removed, the nanoparticles desiccate, potentially causing shrinkage or collapse. This may result in a smaller size of the nanoparticles post-lyophilization, indicating deformation. While the stable crystalline core can help preserve the overall structure to some extent, it may not fully prevent nanoparticle deformation or aggregation. Table 2 above shows that the lyophilized samples have reduced in size but preserve the charges.

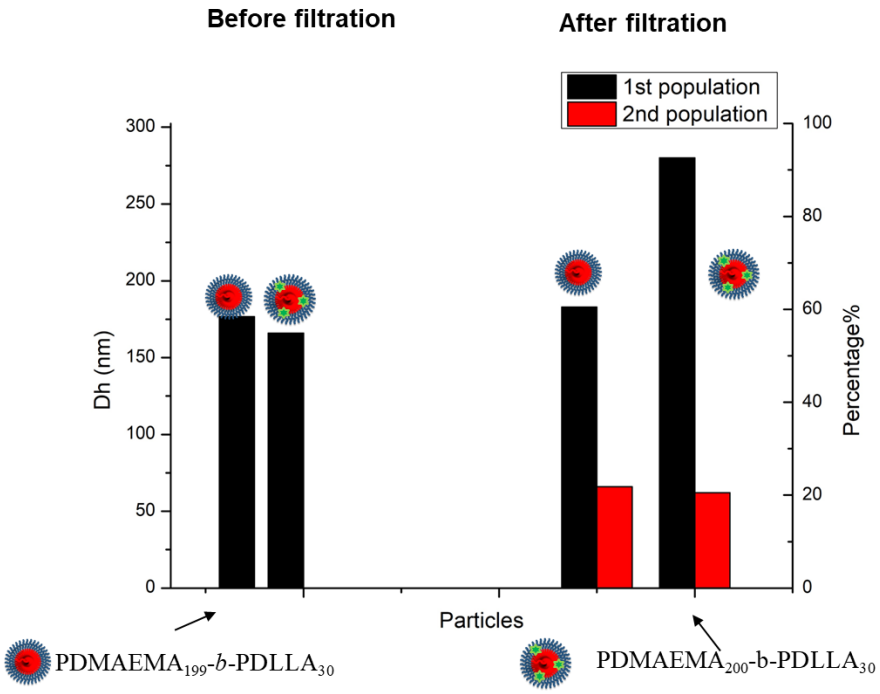


Figure 2.15 Microfluidics of P3 and P4 and filtration effect (1st population in black and 2nd population in red)

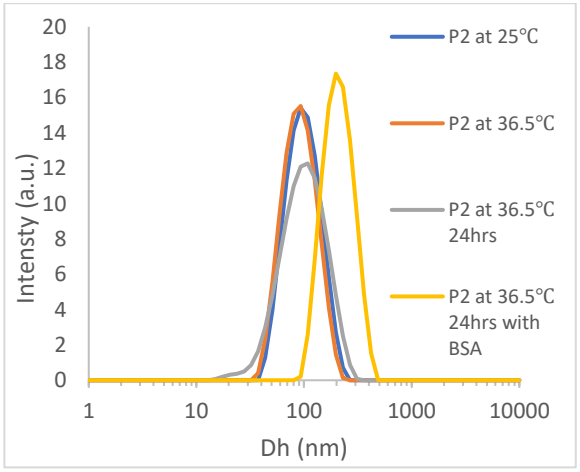
A microfluidics flow reactor was utilized in order to optimize the NPs. The P3 and P4 (2mg) were dissolved in 1 mL DMF and introduced into a 3 mL syringe and placed into the syringe pump. Similarly a water syringe was filed with 1mL water and also placed into the syringe pump. Two PFTE tubing were placed and secured on the nostrils of the syringes. The flow rate was set to 1mL/minute. The syringes were moving and pushed the solutions into the tubing and into the vial. After the procedure the NPs were left stirring for 2 hours before they were dialysed. Figure 2.15 presents their sizes after the dialysis which were 163 nm for P4 and 152 nm for P3 with polydispersity 0.107 and 0.248 respectfully. After the formation of the NPs they were passed through a 0.22 μm filter and two different populations were found in the DLS in terms of their size. A smaller population of around 20 nm appeared in both solutions with the difference that the P4 1st population did not change size, but P3 formed aggregations of 280 nm. A sample of nanoparticles could be made up of a variety of particles with various characteristics or sizes. Due to the preferential retention or passing of specific nanoparticle subpopulations based on their size or properties during the sample's passage through a filter, separate populations may arise. The polymer chains in the system have a tendency to agglomerate after nanoparticles formation in order to lower their free

energy. Larger particle sizes may emerge from phase separation or aggregation if the polyester core is insufficiently soluble in the solvent or has poor compatibility with PLLA.

2.2.4 Self-assembly in biological media of positively charge NPs

The human body produces various proteins in order to regulate the basic necessary functions. As the particles are developed as an intravenous carrier, the interaction between the self-assembled NPs and protein models must be investigated. Initially, these experiments were performed with the PDMAEMA corona particles. For these experiments, firstly the stability of the spherical micelles in body temperature of 36.5 ℃ was verified over 24 hours. The freeze dried particles were redispersed in water and examined over a 24 hour period in 25℃ and 36.5 ℃. From figure 2.16 there were no size change between the 25℃ and the after 24 hours at 36.5 ℃ sample. Continuing with the experiment a 4 mg/mL bovine serum albumin (BSA) solution was introduced to the developed P1 with and P2 without fluorescence. Their interactions were monitored with DLS measurements over a 24 hour period. An excess of BSA was used in order to mimic the conditions that the potential drug carrier may encounter in the body. The molar ratio chosen for this was 4:1 BSA: positively charged NPs. The DLS measurements below confirm an immediate interaction of the P1 and P2 particles with the negatively charged BSA.

A)



B)

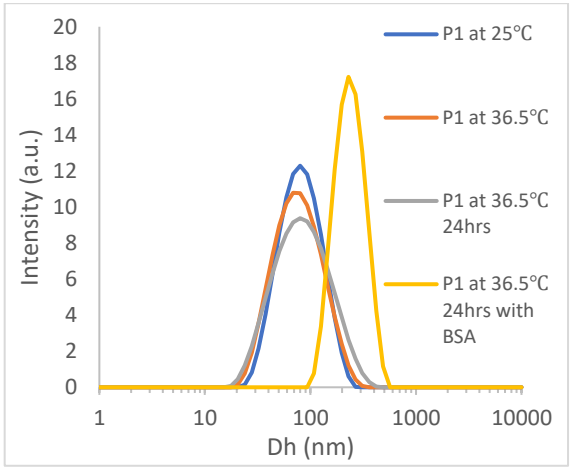


Figure 2.16.DLS results of (A) P2 (B) P1 spheres in different temperatures of 25℃, 36.5℃, 36.5℃ for 24hrs and 36.5℃ for 24hrs with BSA 4mg/ mL.

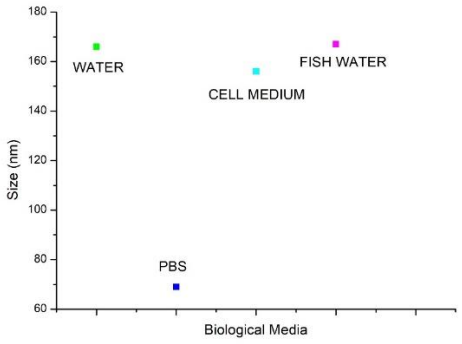
As it is demonstrated by figure 2.16, the PDMAEMA-b-PLLA spheres exhibit stability in body temperature over 24 hours. From figure 2.16 B) the P1 NPs appear to have higher PD=0.261 than the non-fluorescent P2 in figure 2.16 A) PD = 0.177. However, after addition of the solution of negatively charge BSA 4 mg/mL there is a change of the particle size and zeta potential, as the BSA forms electrostatic interactions with the protonated amino groups of the DMAEMA corona leading to aggregation as can be seen above. For the non-fluorescent P2 the D_h shifted from 84 ± 3 nm to 196 ± 5 nm and for the fluorescent P1 the D_h from 64 ± 3nm exhibited an increase to 223 ± 6 nm. The zeta potential indicated a change after the negatively charged protein addition. The P2 from a zeta potential of +42 mV had a decrease to -20 mV. Similarly the fluorescent P1 NPs had initially a zeta of +38 mV and then -17 mV. That was a reasonable change since the amount of BSA protein added was a 4 time bigger than the NPs in the system and after the protein corona formulation, the electrophoretic mobility, changed due to excess protein in the solution.

Finally, the particles were assessed for their stability in various biologically-relevant medium for *in vitro* testing, such as salts like PBS and cell culture medium and fish water for *in vivo* experiments in zebrafish. The cell culture medium selected was Dulbecco's Modified Eagle Medium (DMEM), phenol red free with pH=7.4, for *in vitro* assay experiments. The fish water is composed of de-chlorinated tap water at 26 ^{o}C -29^{o}C, with pH= 7-8 and conductivity 200–3000 micro-Siemens. The inclusion of fish water experiments is indispensable, as it allows for the assessment of zebrafish viability under in vivo conditions, crucial for elucidating the biocompatibility of NPs. Evaluating zebrafish viability in fish water is pivotal for gaining insights into the interaction dynamics between nanoparticles and living organisms within authentic environmental contexts. Through the execution of in vivo experiments in zebrafish exposed to fish water, our objective is to conduct a comprehensive evaluation of NP biocompatibility and potential toxicological effects, thereby providing valuable insights into their applicability for biomedical purposes. The self-assembly of the diblock $PDMAEMA_{200}$-b-$PDLLA_{30}$ with fluorescent probe was investigated by direct flash nanoprecipitation into different systems. The polymer was dissolved in acetone and added into the following solutions while stirring at 550 rpm: water, PBS, BSA 4 mg/mL, fish water and cell medium.

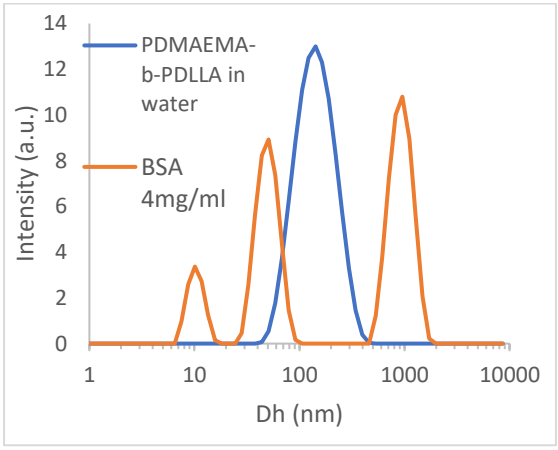
The samples were left stirring overnight for the acetone to evaporate, and then characterised with DLS and AFM at 1 mg/mL.

Table 3. DLS measurements of $PDMAEMA_{200}$-b-$PDLLA_{30}$ with ACM probe self-assembled in different systems.

Samples	D_h (nm) (by intensity)	Pdi	Size (nm) by AFM
Water	166	0.188	113 (with aggregates around 400 nm)
PBS	69	0.241	-
BSA 4 mg/mL	10, 50, 946	0.532	200 (protein-particle aggregates), 1µm cluster
Fish water	155	0.270	154 nm with aggregates around 400 & 300 nm)
Cell medium	167	0.299	Multiple populations 10 & 20 nm, 200 & 500 nm



A)



B)

Figure 2.17. A) D_h sizes of $PDMAEMA_{200}$-b-$PDLLA_{30}$ with ACM probe in various biological media B) DLS measurements of $PDMAEMA_{200}$-b-$PDLLA_{30}$ with ACM probe self-assembled in BSA 4 mg/mL

From figure 2.17 A, is shown that the addition of salts (PBS) stabilizes the charges in the solution and breaks apart some of the aggregation compared with dissolving in water. Overall, the rest of the biological media appear to have similar hydrodynamic radius as presented in table 3. Fish water contains a variations of salts but apparently it does not have the same effect as the PBS as depicted. The more interesting result is from the addition of BSA 4 mg/mL, where three populations appear to be forming. Around 10 nm is the excess BSA, and around 900 nm are the aggregations of particles and BSA because of the opposite charges, however around 50 nm could be NPs with BSA acting as a surfactant.

The same behaviour was verified by AFM results.

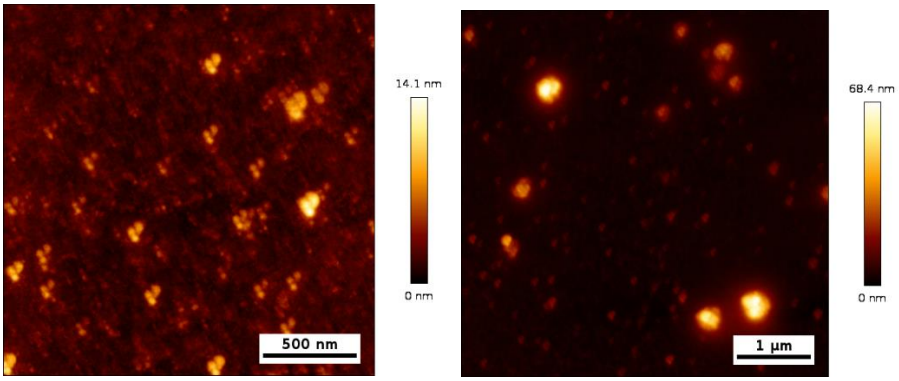


Figure 2.18. AFM images of 1 mg/mL (left) and 0.25 mg/mL (right) of the water self-assembled diblock PDMAEMA$_{200}$-b-PDLLA$_{30}$

The water sample was measured at 1 mg/mL and afterwards at 0.25 mg/mL in order to get a clearer image. Figure 2.18 depicts aggregated particles around 400 nm and around 100 nm, which are thought to be aggregated particles of around 45 nm. (The numbers were calculated using imageJ software of a sample of 100)

Due to salts within the medium, no clear AFM images were able to be obtained for the PBS, fish water and cell culture medium. In the BSA 4 mg/mL solution the protein corona formation was observed, as depicted in figure 2.19, a 1 µm cluster of aggregates, as well as another population around 100 nm, and verification of the population of 50 nm that appears in the DLS measurements.

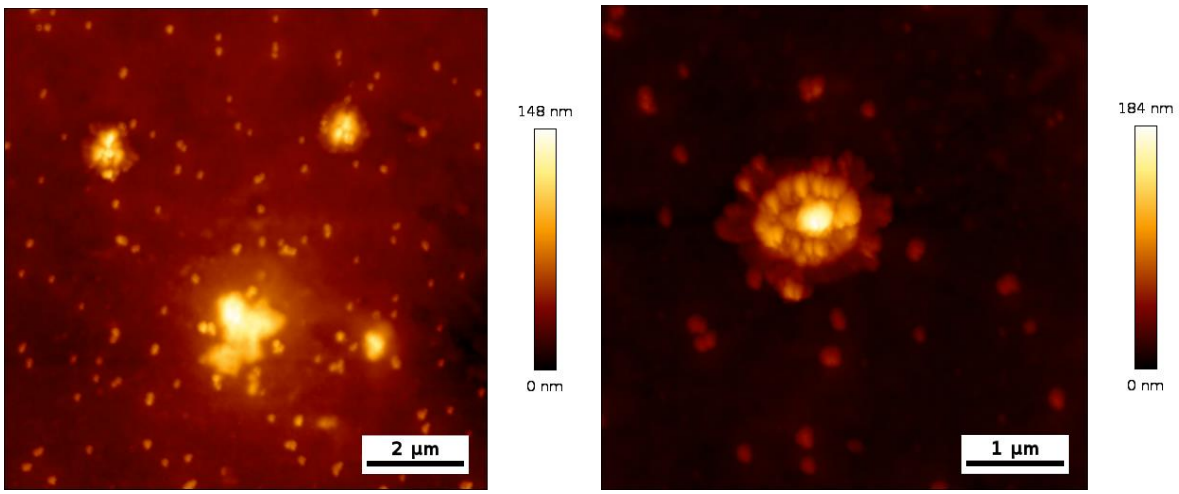
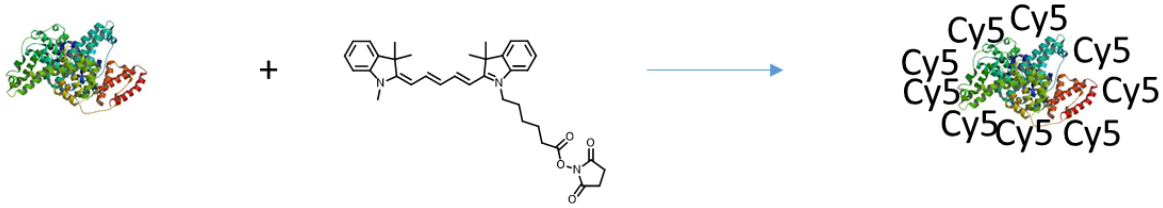


Figure 2.19. Protein corona formation of PDMAEMA$_{200}$-b-PDLLA$_{30}$ particles at 2 µm (left) and at 1 µm (right).

As it can be observed from figure 2.19, various layers of BSA deposit on top of the particles and form aggregates. The core from the image of 1 µm scale bar appears to 229 nm with first layer of 200 nm and second layer of 230 nm, which suggest the formation of clusters of particles that are interacting with BSA and have achieved sizes of 200 nm. In total the diameter of the protein corona formation on P3 appears to be 1000 nm. Differentiation exist depending on the concentration of the protein interacting with NPs. Further studies need to be conducted to verify the existence of the protein corona on the positively charged NPs, like confocal microscopy. Confocal microscopy provides spatial information about the distribution of proteins on the surface of nanoparticles. This enables researchers to determine whether proteins are uniformly or preferentially adsorbed onto the nanoparticles, which can impact their biological behaviour and efficacy. Furthermore, confocal microscopy allows for the direct visualization of interactions between proteins and nanoparticles. By fluorescently labelling proteins or nanoparticles, researchers can observe the formation and composition of the protein corona on the NPs and can confirm the protein corona via colocalization.

Confocal studies for the PDMAEMA$_{200}$-b-PDLLA$_{30}$ & BSA- Cy5 interactions

In order to proceed with the confocal microscopy experiments, both the NPs and the model BSA protein need to have independent excitations. PDMAEMA$_{200}$-b-PDLLA$_{30}$, already carries the ACM fluorophore in the intermediate position in the NP formulation, which excites at emission λ_{max}= 500 ± 8 nm and excitation λ_{max} = 375 ± 3 nm as calculated through fluorescent spectroscopy. In order for the BSA model protein to be visible a small Cy5-NHS ester fluorophore was utilised and tagged to the primary and secondary amines carried by the BSA protein. Scheme 10 below represents the reaction.

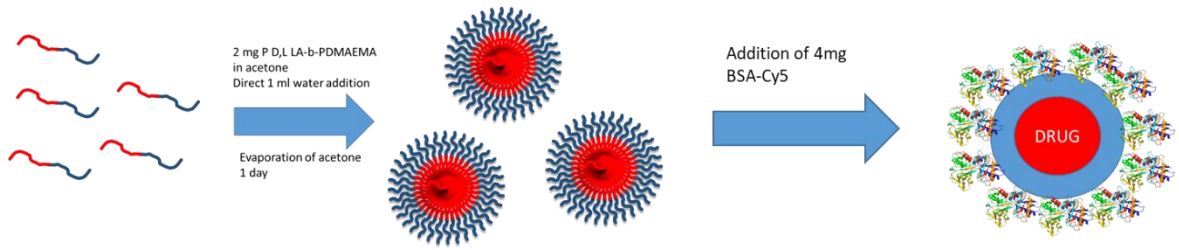


Scheme 10. Attachment of Cy5 ester dye to BSA.

The Cy5 NHS ester dye was dissolved in DMSO 100 µl, that was added dropwise to the system of 8 mg BSA dissolved in 900 µl sodium bicarbonate. By following protocol, the Cy5 ester dye was left to bind to the amino groups of the BSA while stirring for 3 days (8:1). Afterwards, the cleaning process was conducted with spin filtration with a 3 kDa membrane to remove the excess of the unreacted dye and the substance was freeze dried.

For the protein corona experiment a molar ratio of 1:4 positively charged NPs: BSA was implemented. BSA (66 kDa) has double the molecular weight of the polymer (33 kDa) in use. Thus at 2 mg of polymer , 4 mg of BSA-Cy5 was added.

Different protocols for the self-assembly of the positively charged nanoparticles were followed. The reason behind those separate experiments is to verify the protein corona effect in different conditions.



Scheme 11. Self-assembly of spherical particles and afterwards addition of BSA-Cy5.

A) Spherical self-assembly with flash nanoprecipitation with water and after addition of 4 mg of BSA-Cy5 (Scheme 11).

Firstly the examination of the positively charged nanoparticles, was conducted in order to investigated the coating formed by the protein corona effect.

The characterization of the DLS (figure 2.20) for experiment A, the self-assembly produced a size of 282 nm with PDI 0.195 of NPs before the addition and 271 nm with PDI 0.221 after the addition of the BSA-Cy5. The self-assembly was conducted with FNP with acetone as solvent for the diblock copolymer P4. The acetone was removed from the solution via evaporation after a day stirring at 500 rpm. After the purification of the P4 NPs the addition of the BSA-Cy5 did not indicated in increase in the D_h as expected.

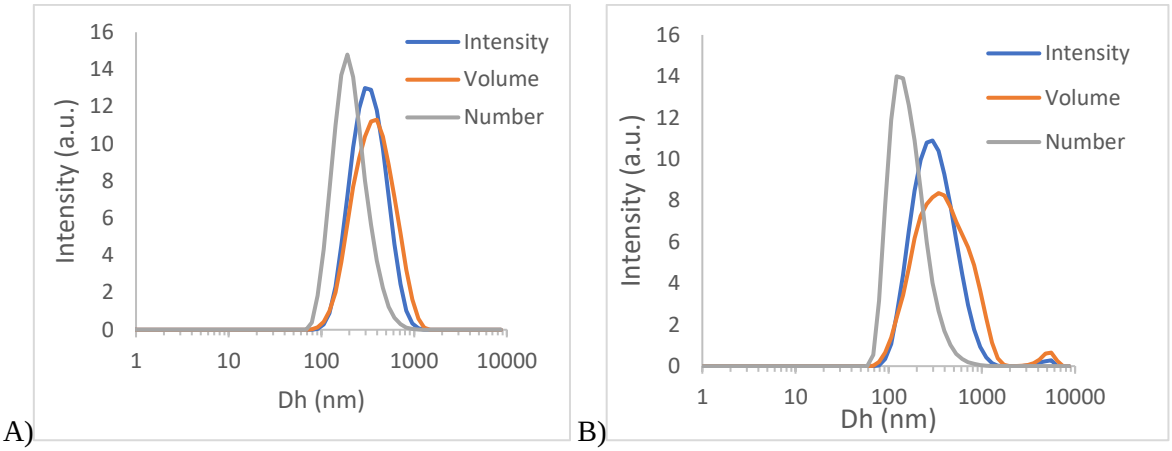


Figure 2.20. DLS graphs of A) Self-assembled P4 with FNP in Acetone B) Protein corona addition to P4 NPs

No significant difference in size with the DLS (figure 2.20) was observed before and after the addition of BSA-Cy5, which raises concern since we should be able to see a clear size increase. Perhaps that can be attributed to the occupied amino groups of the BSA, since they cannot interact anymore with the corona leaving only the electrostatic properties to prevail and lead to the formation of a coated particle.

Because 4 mg/mL is an excess of dye and it can affect our system, a quantity of the particles was dialyzed against 18.2 MΩ water for 3 days and the following confocal images were acquired with concentration 0.05 mg/mL.

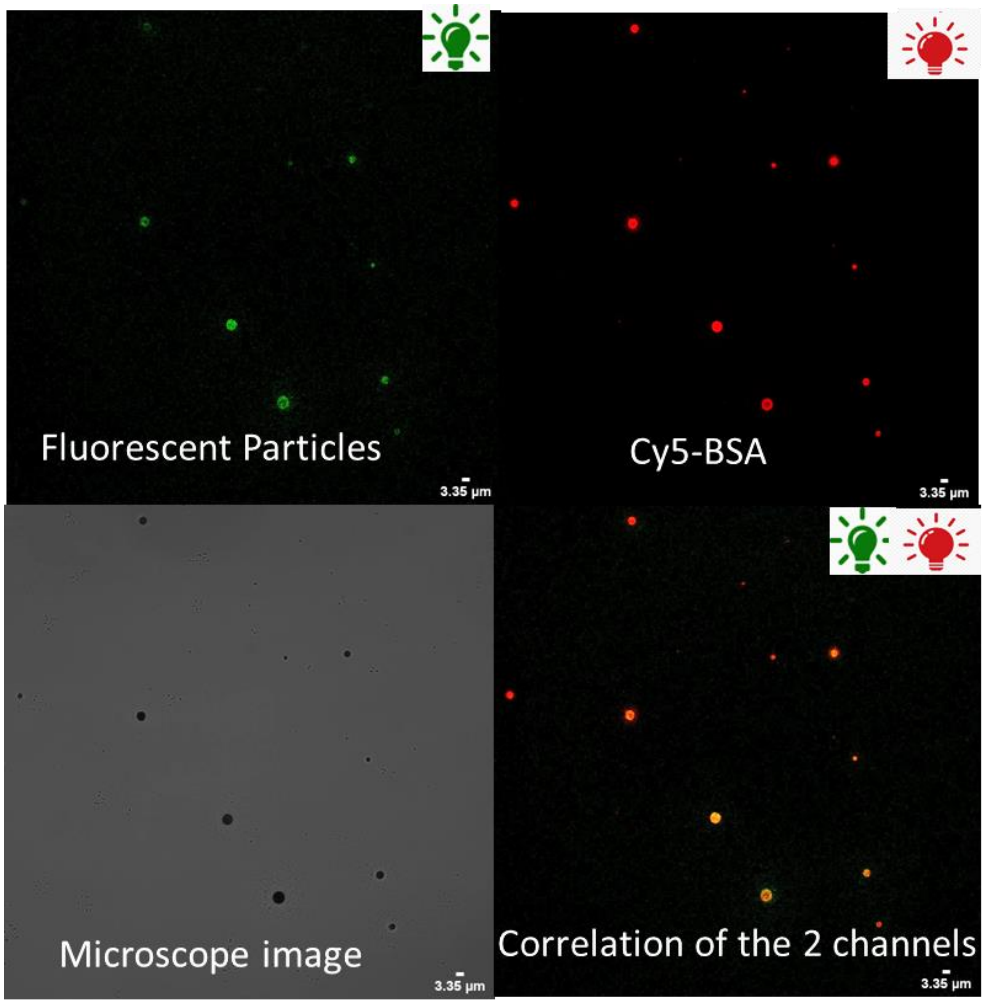
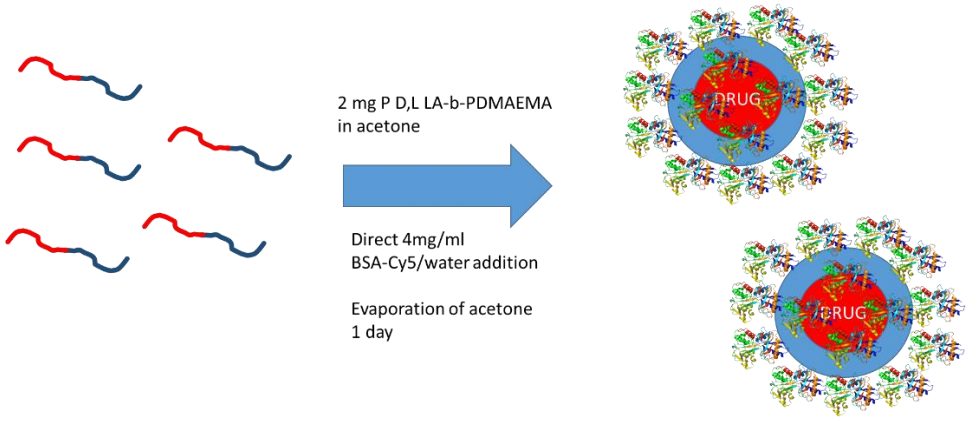


Figure 2.21. Self-assembly of spherical particles and afterwards addition of BSA-Cy5 DIALYZED ACM probe channel (up left), Cy5 channel(up right), both channels (down)

More images were acquired in order to confirm the correlation between BSA and our positively charged particles. Figure 2.21 above is providing information about the electrostatic interactions between the positively charged P4 NPs and the negatively charge BSA. The colocalization of both channels suggest that BSA molecules interact with the positively charged NPs and has been deposited on top of our nanoparticles. The corelation channel emits orange colour that is the outcome colour or red and green (red+green= orange). It is visible that the morphologies are spherical and have thinner outer layer of BSA deposited on top of them. That should be the effect of a hard corona formation since the sample was dialysed prior to imaging. The hard corona suggests strong interactions between BSA and NPs like electrostatic interactions.

B) Direct self-assembly with of 4mg/mL of BSA-Cy5/water solution by flash nanoprecipitation



Scheme 12. Direct Self-assembly of spherical particles with addition of 4mg/mL BSA-Cy5

Experiment B was explored by the formation of the particles directly by addition of the protein in the system. This method can indicate if the electrostatic interactions can prevail in the self-assembly leading to bigger aggregations and about the ability of BSA due to the favourable electrostatic interactions to create a variation of sizes. The self-assembly was executed as previously by dissolving P4 in acetone and in this instance adding the solution of the BSA-Cy5 dissolved in distilled water.

The size acquired from the DLS before (figure 2.22 A) and after the dialysis (figure 2.22 B) of a certain quantity. The size for the self-assembly with 4 mg/mL BSA was found to be 160 nm with Pd 0.109 and after the dialysis of the excess protein was 258 nm with Pd 0.153. The above result revealed that a smaller size was achieved by the direct addition of protein. That could be attributed to the excess amount of the protein acting as a surfactant in the solution for the polymers, but on this matter further investigation through ITC would be needed to verify the above statement.

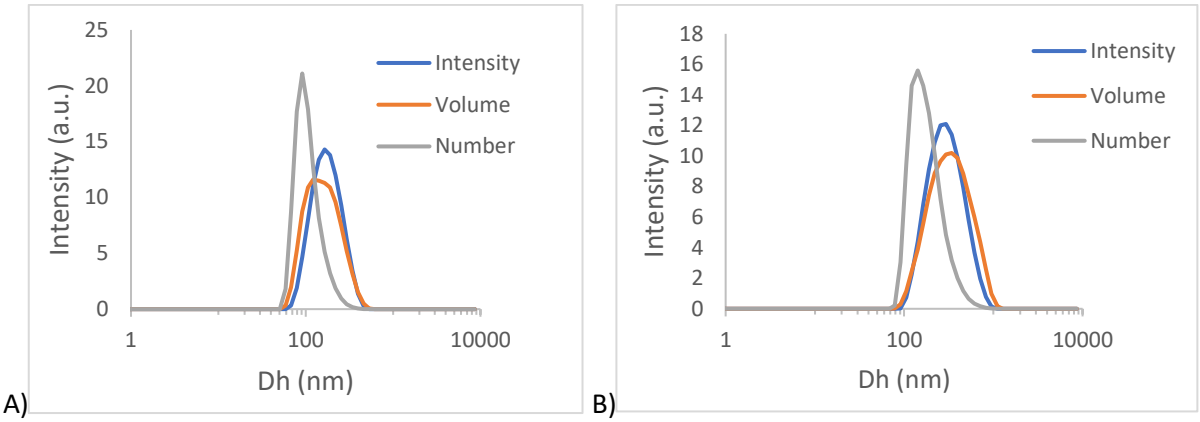


Figure 2.22. A)DLS measurements of $PDMAEMA_{200}$-b-$PDLLA_{30}$ self-assembled with 4 mg/mL BSA-Cy5, B) Dialysed sampled with the excess of BSA-Cy5 removed .

Confocal results for the experiment B with concentration 0.01 mg/mL (the solution had a very intense dye that's why it was dissolved) reveal the coating of the nanoparticles none the less, but their morphology was affected due to the excess of the BSA solution.

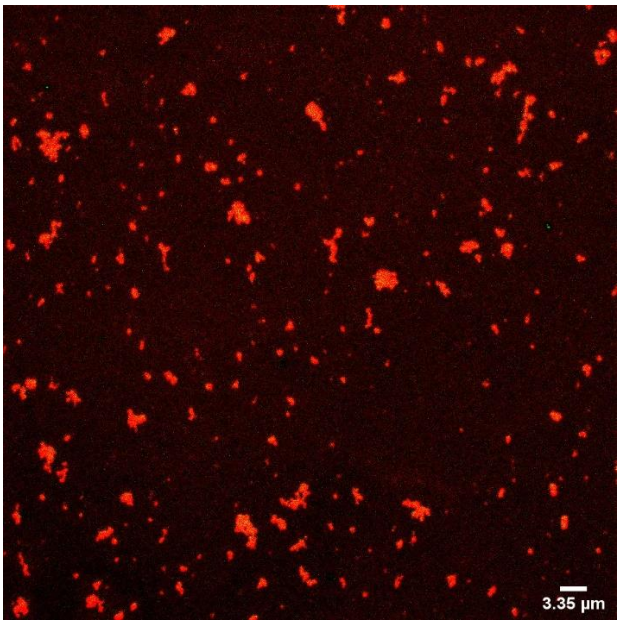


Figure 2.23. Self-assembly of spherical particles with 4mg/mL addition of BSA-Cy5 overlap of channels (green+red).

The overlap of the 2 channels has bigger intensity due to the excess of the dye Cy5 that is attached to the BSA. The red dominant colour is clearly more visible and even though trials to increase the magnitude were conducted in order to observe the ACM which was through the experiments appearing to be weaker, with less intensity. The alteration of the shape was observed in all the areas of the non-dialysed sample as depicted in figure 2.24 above. This is

attributed to the excess of the BSA protein and the formation of a soft protein corona. Dialyzed samples appear to be perfect spheres mostly with sometimes good correlation of both channels and sometimes not. Examples are exhibited below.

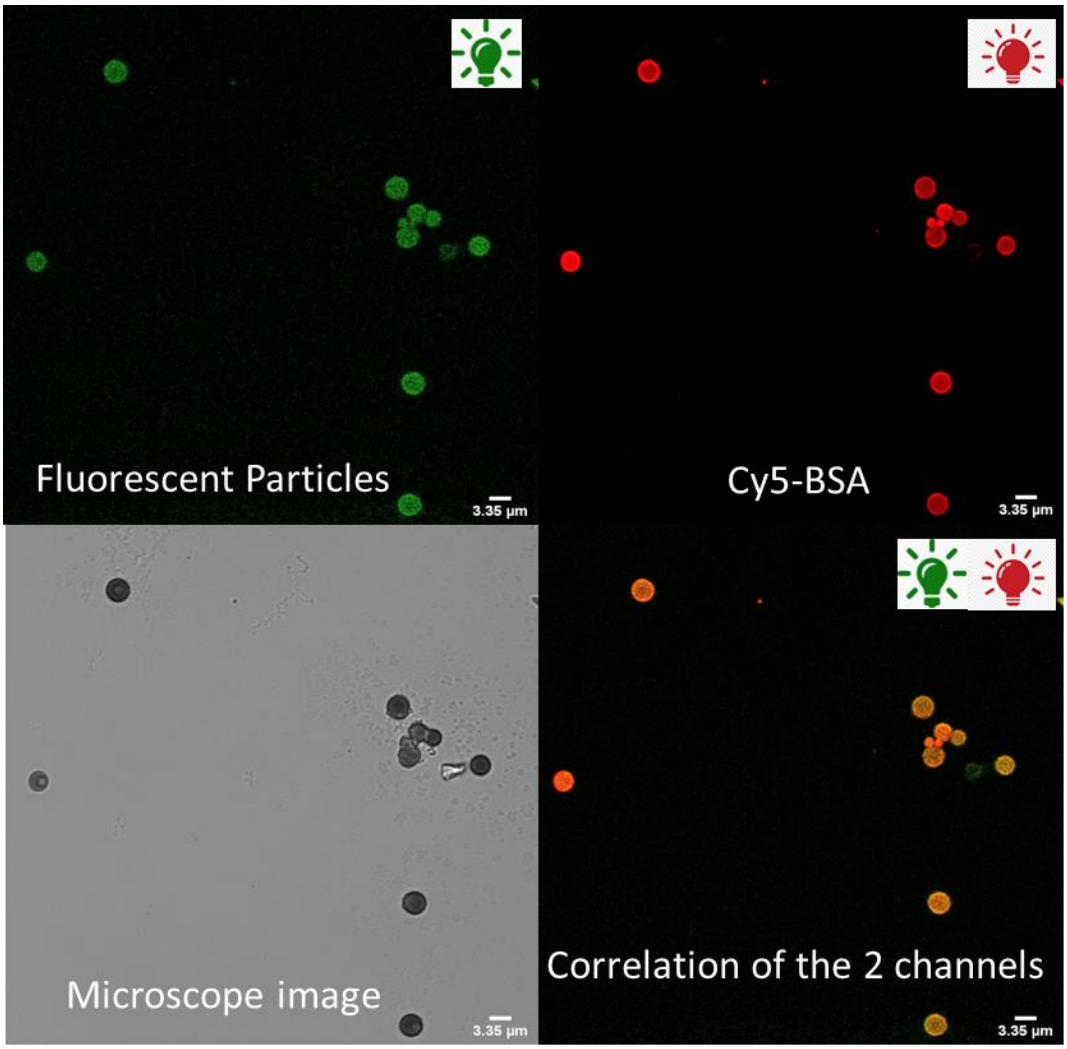


Figure 2.24. Self-assembly of spherical particles with 4mg/mL addition of BSA-Cy5 after DIALYSIS. ACM probe channel (up left), Cy5 channel (up right), no channel (down left), and both channels (down right) area 3

In the figure 2.24 above the overlap of both channels appears better after the dialysis and the removal of the overwhelming soft corona. This provides evidence to the prior assumption that a clearer formation was achieved through dialysis of an outer homogeneous layer of BSA all around the particle. It could be also the amount of encapsulation in this case is lower, so only the coverage of BSA on the particle with less intensity was witnessed.

The above image if enlarged (below) we can clearly see smaller formations of around 200 nm in the solution as well.

ITC for protein corona verification

ITC capitalises on the enthalpic effect caused by proteins adsorbing on nanoparticles solution. This approach provides some direct thermodynamic information that is not feasible on planar surfaces. Numerous research has been conducted as a result of this abundant benefit of ITC for the investigation of protein adsorption.

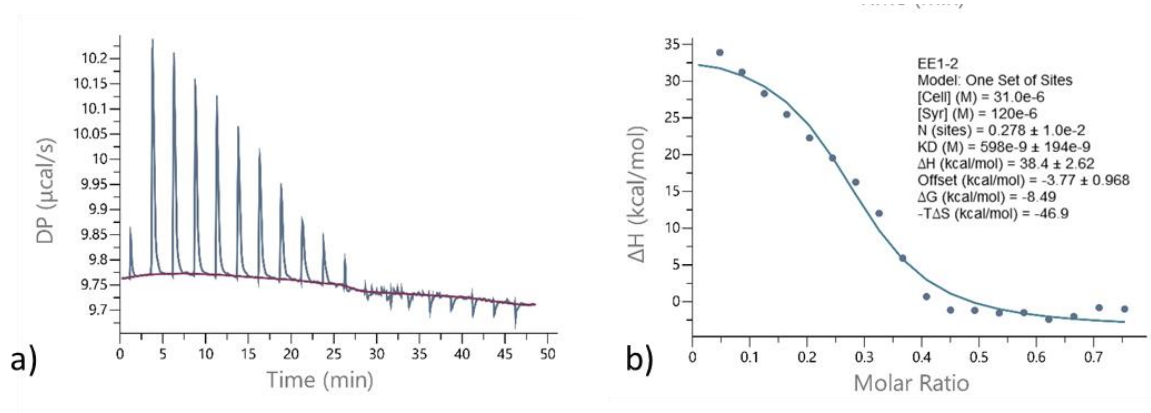


Figure 2.25. ITC experiment of BSA protein attaching to $PDMAEMA_{204}$-b-$PLLA_{30}$ nanoparticles

From figure 2.25 above, the value of N (stoichiometry) represents the typical number of binding sites present on each particle or molecule. N in this case is 0.278, indicating that fewer than one BSA molecule binds to each PDMAEMA-PLLA nanoparticle on average. Even though molecular ratio selected for the examination 2:8 nanoparticles: BSA, so the BSA proteins should overpowering the system equilibrium as suggested from the confocal images above.

PDMAEMA-PLLA nanoparticles and BSA have an equilibrium binding affinity that is represented by the dissociation constant, or K_D. A higher binding affinity is indicated by a lower K_D value. The K_D in the findings is 589 x 10^{-9} M, which points to a strong interaction between the nanoparticles and BSA.

The interaction between the nanoparticles and BSA in this experiment is accompanied by an endothermic process, as indicated by the ΔH= 38.4 (kcal/mol) H value (heat is absorbed).

The free energy ΔG, indicates how spontaneously the binding reaction occurred. Positive, unplanned interactions are indicated by a negative G score. Here ΔG value of -8.49 (kcal/mol) indicates that the binding of the nanoparticles to BSA is thermodynamically advantageous. Entropy change is a measure of how much unpredictability a system contributes to the binding process. The -TΔS result in this case is -46.9(kcal/mol),thus the -ΔS will be positive ,which indicates that there was less unpredictability in the system before binding. This may occur whenever a complex form develops due to increased molecular disarray, flexibility, or conformational changes.

Overall, the findings indicate that the PDMAEMA-PLLA nanoparticles and BSA interact in a rather strong and thermodynamically advantageous way. The positive ΔH value denotes an endothermic reaction, whereas the negative ΔG value suggests that the binding is spontaneous. Entropy (-TΔS) decrease suggests a more ordered binding state.

2.2.5 Self-assembly of block copolymers with neutral charged

A library of neutrally charged polymers were synthesized and then self-assembled into nanoparticle structures. The size of the nanoparticles tried to be optimized, to obtain small size NPs which should be able to permeate through the BBB.

Table 4. Library of neutrally charged diblock copolymers.

Corona	DP	M_n (kDa)	M_w(kDa)	$Đ_M$	Ratio Core:corona	Fluorescence	Core
TEGA	82	9	10	1.18	1:2	Yes	PLLA
TEGA	63	15	20	1.23	1:2	No	PLLA
DMA	87	15	19	1.10	1:3	No	PLLA
DMA	138	20	29	1.49	1:3	Yes	PLLA
DMA	69	4	5	1.24	1:2	Yes	PLLA
DMA	527	52	71	1.38	1:13	Yes	PLLA
NIPAM	111	13	17	1.33	1:3	No	PLLA
NIPAM	135	12	18	1.52	1:3	Yes	PLLA
TEGA	28	9	10	1.18	1:1	Yes	PDLLA
TEGA	42	15	20	1.37	1:1	No	PDLLA
TEGA	65	15	20	1.30	1:2	No	PDLLA
DMA	57	15	19	1.23	1:2	Yes	PDLLA
DMA	114	18	21	1.12	1:3	No	PDLLA
NIPAM	85	8	9	1.19	1:3	Yes	PDLLA
NIPAM	119	19	23	1.19	1:3	No	PDLLA

A series of neutrally charged nanoparticles were self-assembled via flash nanoprecipitation. The common self-assembly protocol was neutrally charged polymer (2mg) in 1 mL of DMF solvent and 1 mL distilled water with intense stirring at 550 rpm.

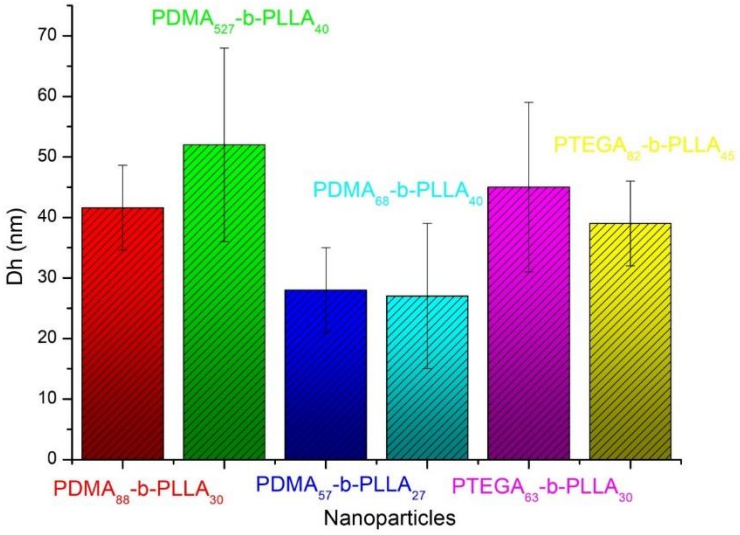


Figure 2.26. Comparison of different nanoparticle size prepared by flash nanoprecipitation of neutrally charged polymers (error bars represent standard deviation of 3 consecutive runs of 100 measurements)

On the above figure 2.26 it is portrayed the small nanoparticles that were produced with flash nanoprecipitation and polydispersity below 0.2. PDMA-b-PLLA polymer with a variety of core : corona ratios. $PDMA_{527}$-b-$PLLA_{40}$ exhibits the largest D_h =52 nm, followed by $PDMA_{88}$-b-$PLLA_{30}$ that has the second highest D_h=42 nm , and the $PDMA_{57}$-b-$PLLA_{27}$ with $PDMA_{68}$-b-$PLLA_{40}$ have approximate sizes since they are having similar ratios at 2:1 and 1.7:1 accordingly. The last 2 polymers though appear to have different lengths in the PLLA, and yet they still are the same size. That can lead to the conclusion that the length of the core would not influence the self-assembly as much as the corona: core ratio. The above assumption though would be wrong since PLLA plays important role in the polymer self-assembly. The kinetics and thermodynamics of the self-assembly process can be affected by the length of the core. Longer cores could require special circumstances or assembly kinetics that are slower to produce the desired structures. The balance between the enthalpic and entropic contributions to self-assembly can be affected by the length of the core thermodynamically, which will alter the stability and phase behaviour of the system.[162]

In figure 2.26 PTEGA nanoparticles appear to be monodisperse and small sizes. But in reality, flash nanoprecipitation will dictate the self-assembly based on the thermodynamics of the solution and since there is a human factor involved in the precipitation the results can

change. In table 5 below shows an extensive study of various solvents, temperatures and filtration parameters that influence the outcome of flash nanoprecipitation every time.

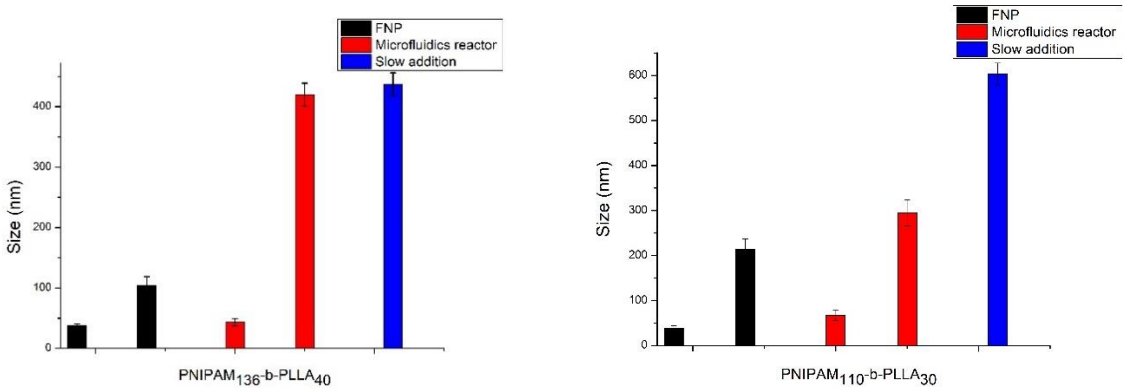
Table 5. PTEGA-b-PLLA flash nanoprecipitation factor

SAMPLE	SOLVENT	SIZE	Pd	ZETA	CONCETR	FILTERS
$PTEGA_{63}$-b-$PLLA_{36}$	Acetone	46, 390	0.356	-	1 mg/mL	0.22 µm
	Acetone	144	0.172	-	1 mg/mL	0.22 µm
	WATER	117	0.265	-	1 mg/mL	NO
	WATER	102	0.167	-	1 mg/mL	0.22 µm (1)
	WATER	100	0.154	-	1 mg/mL	0.22 µm (2)
	WATER AT 80°C	70	0.157	-19	1 mg/mL	0.22 µm
	WATER AT 80°C	67	0.123	-19	1 mg/mL	0.22 µm (2)
	WATER AT 80°C	69	0.127	-	0.5 mg/mL	0.22 µm
	WATER AT 80°C	70	0.114	-13	0.1 mg/mL	0.22 µm
	DMSO	142	0.051	-	1 mg/mL	NO
	DMSO	141	0.195	-9.1	1 mg/mL	0.22 µm
	DMF	40,200	0.375	-	1 mg/mL	NO
	DMF	44,239	0.232	-7.7	1 mg/mL	0.22 µm
	DMF	41, 4268	0.197	- 7.7	1 mg/mL	0.22 µm (2)

Solvent appears to have a great effect on the system. As discussed in ***Chapter 1***, amphiphilic block copolymers, that are formed of solvophilic and solvophobic blocks, can spontaneously self-assemble in solvents that are selective for one of the copolymer's blocks. In this case the lead energetically unfavourable interactions for one of the two blocks. Due to that fact aggregation are forming to the solution that was kinetically entrapped since it did not have time to reorganise. That effect is apparent here when DMF is used as a solvent system.

Temperature also plays an important role in the flash nanoprecipitations, as can be seen above the direct dissolution with water can lead to formulations at 100 nm. But temperature of the water rises at 80 ℃ it gives more energy to the system to decrease the hydrodynamic radius at 70 nm. Concentration is also one of the factors that was examined with concentrations at water dissolution 1 mg/mL, 0.5 mg/mL and 0.1 mg/mL. $PTEGA_{63}$-b-$PLLA_{30}$ does not appear to change, since perhaps has already reached an equilibrium in these concentrations. Perhaps if we had studied a saturation concentration that would have changed. Lastly, an effort to verify if the filtrations influence the system was executed, since filtrations can create movement and rearrangement of particles. In the DMSO system, an elevation in the polydispersity can be observed because of the rearrangement, but the opposite appears to be happening in the DMF system.

Proceeding, various self-assembly processes have been tested but not with all the methods provided from **Chapter 1**. FNP, Slow addition and microfluidics reactor have their advantages and disadvantages. Herein, it is demonstrated how each method establishes a thermodynamic system.



a) b)

Figure 2.27. Comparison of different self-assembly methods with PNIPAM diblock copolymers, a) $PNIPAM_{136}$-$PLLA_{40}$ self-assembly, b) $PNIPAM_{110}$-$PLLA_{30}$ self-assembly with FNP (black), microfluidics reactor (red), slow addition (blue) (errors bar represent standard deviation)

FNP seems to provide the smallest particle sizes due to kinetic entrapment. Overall, the samples created with all the methods had very big polydispersity. From figure 2.27 it is observed that the microfluidics reactor is closer to the FNP in sizes formations. Slow addition exhibits aggregations at 450 nm and at 600 nm for $PNIPAM_{136}$-b-$PLLA_{40}$ and $PNIPAM_{110}$-b-

$PLLA_{30}$ accordingly. The microfluidics reactor created small and big populations, and it seems like it is creating a larger second population than FNP. FNP made a small population of 37 nm and 26 nm, but also 120 nm and 230 nm for $PNIPAM_{136}$-b-$PLLA_{40}$ and $PNIPAM_{110}$-b-$PLLA_{30}$ accordingly. For this nanoparticle model system appears that FPN created the smallest formulations.

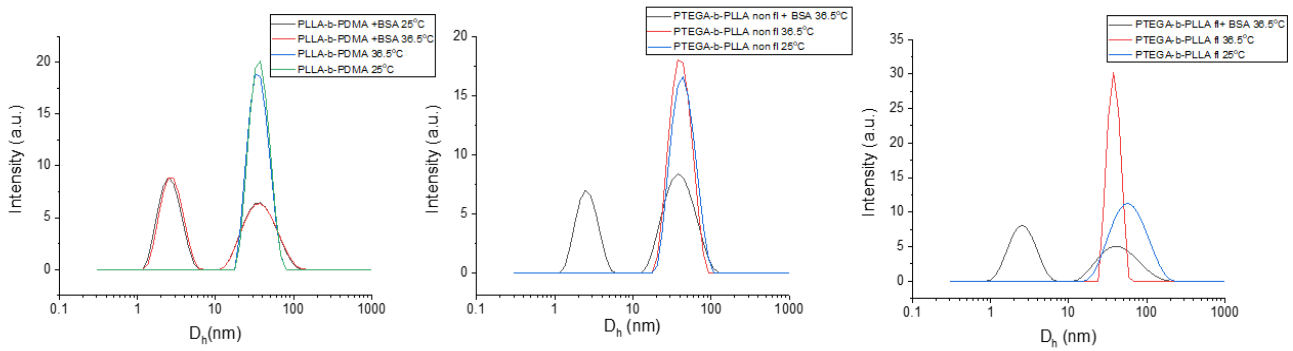


Figure 2.28 DLS measurements of $PDMA_{87}$-b-$PLLA_{30}$, $PTEGA_{63}$-b-$PLLA_{36}$ (non fl) & $PTEGA_{82}$-b-$PLLA_{45}$ (fl) at 25°C, 36.5°C and with BSA at 36.5°C

For NPs that have purpose for drug delivery and biological applications, stability testing in various temperatures and with biomolecules are crucial. To test this, the NPs were incubated for a day at 36.5 ℃ and then were measured to validate their size. Figure 2.28 verifies that the nanoparticles are stable at 36.5 ℃, even though $PTEGA_{82}$-b-$PLLA_{45}$ (fl) present a broader distribution. Next the NPs were incubated with BSA as model protein with 4:1 molar ratio at 36.5 ℃. All neutrally charged NPs do not appear to form any connections with the BSA and the sizes remained the same. There was no association or interaction between the BSA model protein and the neutrally charged NPs. Below in table there are the hydrodynamic diameter sizes as provided by the DLS measurements above.

Table 6. Stability of neutrally charged NPs in different temperature and protein corona examination.

Samples	Size at 36.5℃	Size at 25℃	Sizes with BSA at 36.5 ℃	BSA	PD
PLLA-b-PDMA	36 nm	40 nm	40 nm	3 nm	0.157
PLLA-b-PTEGA non fl	42 nm	45 nm	42 nm	3 nm	0.208
PLLA-b-PTEGA fl	38 nm	65 nm	49 nm	3 nm	0.209

ZEBRAFISH STUDIES

Zebrafish are widely utilized as model organisms in biomedical research due to their genetic and physiological similarity to humans. Therefore, assessing the viability of zebrafish in fish water is essential for understanding how the nanoparticles interact with living organisms in their natural environment. By conducting *in vivo* experiments in zebrafish exposed to fish water, we aim to evaluate the biocompatibility and potential toxic effects of the nanoparticles under conditions that closely mimic physiological settings. This comprehensive approach allows us to assess the safety and suitability of the nanoparticles for biomedical applications. Toxicity evaluation of $PLLA_{30}$-b-$PDMA_{88}$ spherical nanoparticles was carried out in zebrafish by a collaborator in Queen Mary University of London Dr. Roberta Bilardo. These materials were tested in terms of both acute and chronic toxicity. The size after the addition of fish water was measured to be stable for 24 hours at 68 nm.

In order to evaluate acute toxic effects, 8-cell stage embryos were placed individually into the wells of a 48-well plate and exposed for 1 hour to NPs' suspensions of concentration 0.5 mg/mL or 0.1 mg/mL. They were investigated for morphological changes or death every 24 hours.

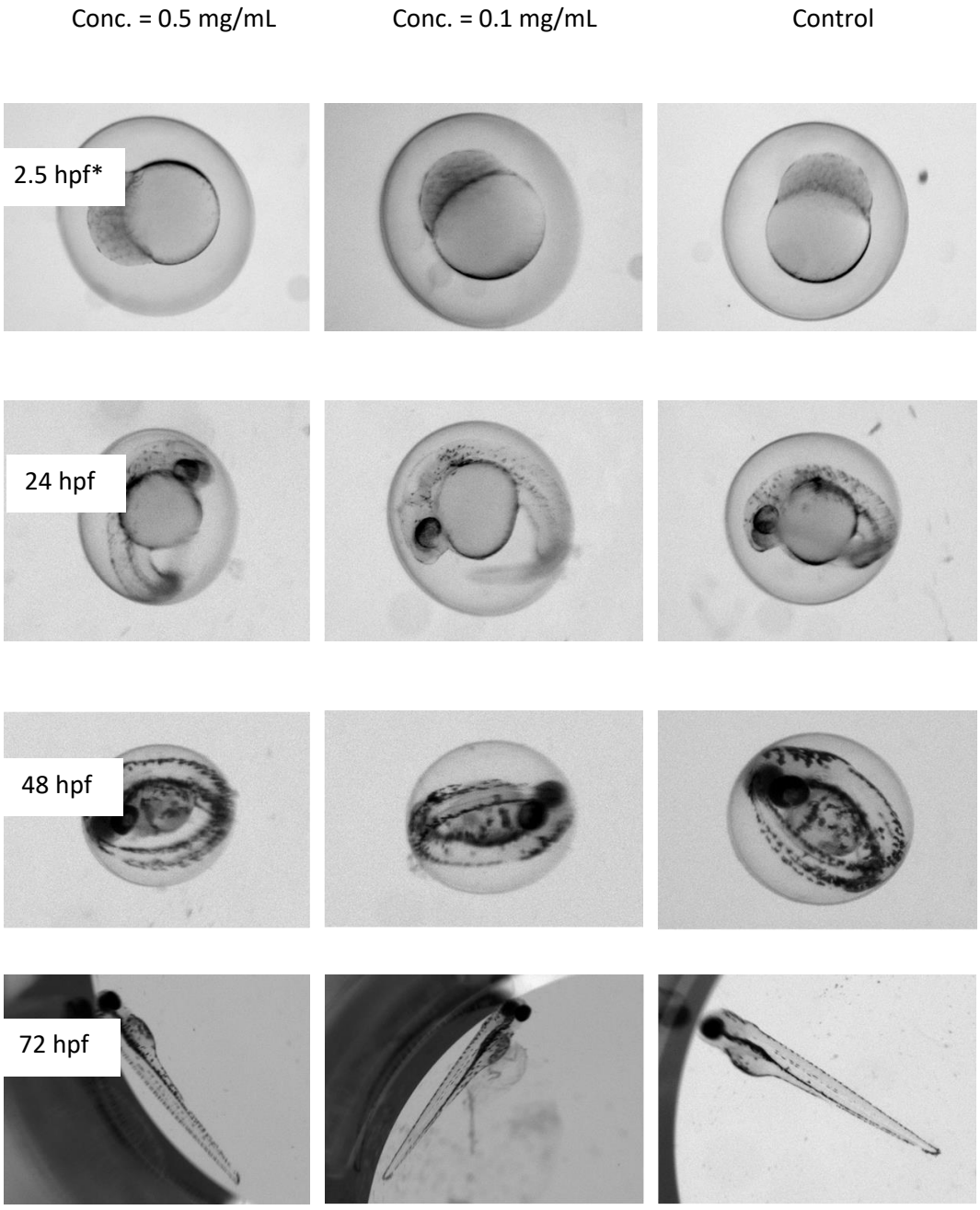


Figure 2.2.29. Zebrafish studies of acute toxicity of $PDMA_{88}$-b-$PLLA_{30}$

Neither deformities nor dead embryos were found as a result of the exposure to these nanoparticles' suspensions. However, in comparison with both the control fish and the embryos immersed into the suspension of concentration equal to 0.1 mg/mL, a delay in hatching was noticed in case of embryos exposed to the highest quantity of nanoparticles (i.e. suspensions with concentration 0.5 mg/mL).

Chronic toxicity was evaluated by exposing embryos at 8-cell-stage (2.5 hpf) to nanoparticles' suspensions of concentration equal to 0.5 mg/mL and 0.1 mg/mL for a longer period. Also for this study, embryos were checked for evident morphological damage and death every 24 hours.

[* hours post fertilisation]

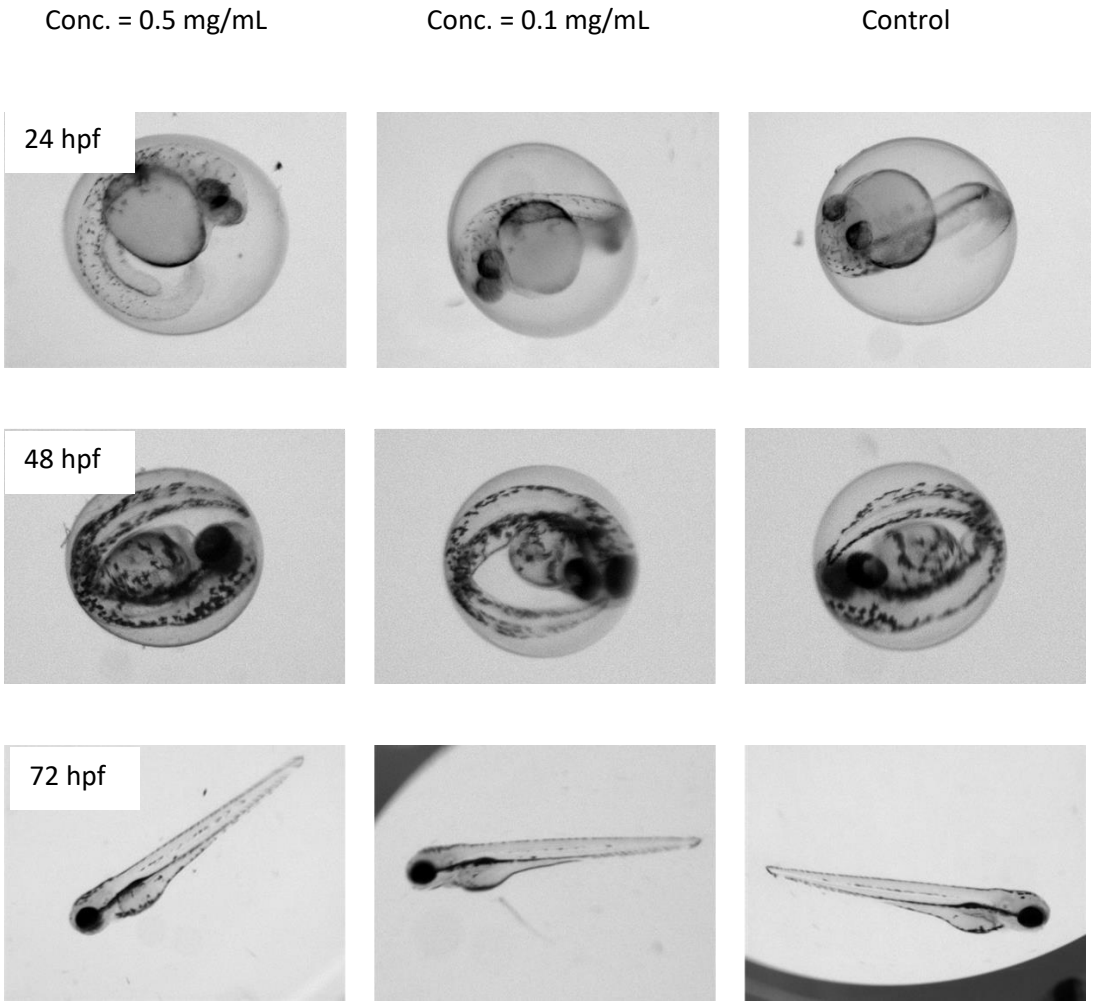


Figure 2.2.30. Chronic toxicity in zebrafish of $PDMA_{88}$-b-$PLLA_{30}$ nanoparticles

All the embryos exposed to nanoparticles were alive after 72 hours of exposure and did not show any sign of toxicity. In accordance with what had been observed for acute toxicity testing, fish immersed into suspensions with higher concentration of nanoparticles showed more difficulties in hatching. However, after mechanical dechorionation, they did not display any deformity.

The PLLA-b-PDMAEMA spherical nanoparticles were also examined for their toxicity after being subjected to dialysis in fish water for 3 days. Unfortunately, the embryos were deceased within the first 2.5 hours indicating toxicity of the NPs.

2.2.6 Self-assembly of block copolymers with negative charged

For the negatively charged diblock copolymers a new polymer was synthesized through a RAFT polymerization with the macro CTA $PLLA_{30}$. The RAFT polymerization of *tert*-butyl acrylate was performed. The polymerization was carried out in a 10 mL ampoule containing a magnetic stir bar and fitted with a rubber septum. The monomer, tBA (399 mg, 3118 µmol), was added to the vial containing the PLLA macro CTA (25 mg, 5.4 µmol, tBA/CTA = 571) in chloroform (0.5 mL). The initiator, AIBN (0.9 mg, 0.55 µmol, AIBN/CTA = 0.10), was finally added and 3 cycles freeze pump thaw were executed for 10 minutes per cycle, as the degassing method. After stirring for 5 hours in a 70 °C, the solution appeared to be viscous and was quenched by freezing the solution. An aliquot was removed and dissolved in $CDCl_3$ to determine the monomer conversion through ^1H NMR analysis [monomer conversion = 85% , DP= 486 by comparison of the ^1H NMR signals of the vinylic monomer (6.29, 6.04, and 5.72 ppm, 3H, integration = 1.00) to the methine polymer backbone signal (2.36–2.10 ppm, 1H, integration = 6.60)] (see experimental).

The characterization data of the polymer (with SEC and NMR) are stated in Table 7.

Table 7. Poly(tetr-Butyl Acrylate)$_{486}$-b-P(L-lactic acid)$_{30}$ characterization

Corona	DP	M_n (kDa)	M_w(kDa)	$Đ_M$	Ratio Core:corona	Fluorescence	Core
tBA	486	19	22	1.15	1:16	No	PLLA

To self-assemble this diblock copolymer a variation of a previously established protocol was followed.[163] Instead of slow addition the protocol of flash nanoprecipitation was adopted and was tested with a variation of solvents and it can be seen below. $PLLA_{30}$-*b*-$PtBA4_{86}$ (10 mg) was dissolved in solvent of choice (5 mL). Distilled water 5 mL was mixed with acetic acid (3.36 µl, 58.7 µmol) and introduced with a pipette in the system. The solution was dialysed for 3 days against water 18.2 MΩ.

Table 8. Data obtained from flash nanoprecipitation of PTBA-b-PLLA with various solvents

Polymer	Size (nm)	Polydispersity	Method	Solvent
PAA_{486}-b-$PLLA_{30}$	512	0.288	FNP	DMSO
PAA_{486}-b-$PLLA_{30}$	1st 131	0.095	FNP	THF
PAA_{486}-b-$PLLA_{30}$	1st 230	0.263	FNP	DMF
PAA_{486}-b-$PLLA_{30}$	1st 159 2nd 17	0.423	FNP	DMSO, anhydrous sodium carbonate
PAA_{486}-b-$PLLA_{30}$	1st 129 2nd 11	0.269	FNP	THF, NaCl 0.1 M

PAA_{486}-b-$PLLA_{30}$ (11.6 mg) in 2mL water and 0.5 mL THF with 13.6 µl TFA. The nanoparticles were dialysed against water and the following was acquired through AFM. Figure 2.31 is providing sizes of 200nm-500nm. The sample was found to be too polydisperse, PD>0.2 ,based on the various sizes calculated through ImageJ and DLS data.

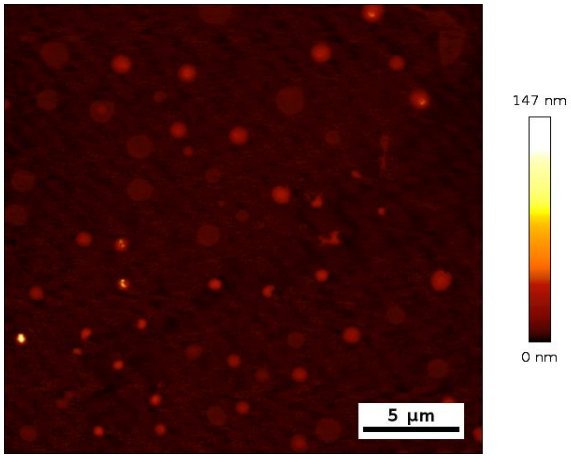


Figure 2.31. AFM image of PAA_{486}-b-$PLLA_{30}$

Since the negatively charged NPs appears to be polydisperse and agglomerating, is not a viable candidate for BBB permeation, thus no protein corona studies will be conducted with this NP system.

2.3 Conclusions

In conclusion, different diblock copolymers were synthesized through controlled RAFT polymerization and characterized. After the assembly into nanoparticles they were examined with multiple techniques like DLS, zeta, TEM and AFM to examine the characteristics of the nanoparticle. Herein three different self-assembly techniques and their effect on the NPs formulation have been demonstrated. FNP and microfluidic reactor are fast and scalable, but they tend to make two different size populations because of the kinetic entrapment in the solutions. Positive, neutral and negative charged particles were synthesized, characterized and optimized. An evaluation of the protein corona formation was conducted with a 4:1 BSA : polymer molar ratio. While the neutral particles remain unaffected with addition of the negatively charged BSA, the positively charged nanoparticles exhibited an increase in the hydrodynamic radius from 60 nm to 223 nm. AFM measurements revealed protein-nanoparticles agglomeration due to their electrostatic interactions. Confocal studies verified the colocalization that positively charged NPs interact with negatively charged protein, and ITC confirmed that this is a strong interaction. Finally, zebrafish experiments were conducted and confirmed that positively charged NPs are cytotoxic but the neutrally charged particles are viable.

APENDIX I

2.4 Materials & Methods

Materials

Chemicals and solvents were purchased from Aldrich, Fisher, Acros, and Alfa Aesar.1,4-Dioxane and DMAEMA were purified by passing through basic alumina before use. L-lactide and DL-lactide was purified and reduced in dry toluene and dry dichloromethane and after it was sublimed twice before being stored in a glove box. DBU was dried over calcium hydride and distilled before use. 2,2'-azo-bis(isobutyronitrile)AIBN was recrystallized twice from methanol and stored in the dark at 4 °C. Toluene, dichloromethane and tetrahydrofuran were dried using solvent drying towers under a dry N_2 atmosphere.

^{1}H NMR & ^{13}C NMR spectroscopy

^{1}H NMR experiments were performed either on a Bruker DPX-400 spectrometer at 400 MHz or a Bruker DPX-300 spectrometer at 300 MHz using deuterated chloroform. Chemical shifts are reported in parts per million (ppm) downfield from trimethylsilane (0 ppm). All spectra were obtained at 25 °C.

Size Exclusion Chromatography

Size exclusion chromatography (SEC) measurements in chloroform were performed on a Varian 390-LC-Multi detector suite fitted with differential refractive index (DRI) and photodiode array (PDA) detectors equipped with a guard column (Varian Polymer Laboratories PLGel 5 µm (50 × 7.5 mm)) and two mixed-D columns (Varian Polymer Laboratories PLGel 5 µm (300 × 7.5 mm)) using THF with 2% triethylamine eluent at a flow rate of 1.0 mL min-1. SEC measurements in chloroform were performed on a Varian 390-LC-Multi detector suite system fitted with RI and ultraviolet (UV) detectors (λ = 309 nm) equipped with a PLGel 3 µm (50 × 7.5 mm) guard column and two PLGel 5 µm (300 × 7.5 mm) mixed-D columns using chloroform with 0.5% trimethylamine at 40 °C as the eluent at a

flow rate of 1.0 mL min^{-1}. SEC data was calibrated against PS or PMMA standards and analysed using Cirrus v3.3 software.

Dynamic Light Scattering (DLS)

Hydrodynamic diameters (D_h) of particles were determined by dynamic light scattering (DLS) using a Malvern Zetasizer Nano ZS fitted with a 4 mW He-Ne 633 nm laser module at 25 °C. Measurements were carried out at a detection angle of 173° (back scattering) and the data was analysed using Malvern DTS 7.03 software. All determinations were repeated 5 times. D_h was calculated using the Stokes-Einstein equation where particles are assumed to be spherical. For cylindrical particles, DLS can be used to detect multiple populations and obtain dispersity information.

Zeta potential

Zeta potentials were measured using a Malvern Zetasizer Nano. The zeta potentials of particles in suspension at pH 6.5 were obtained by measuring the electrophoretic movement of the particles under an applied electric field at 25 °C. All determinations were repeated 3 times.

Fluorescence Spectroscopy

Steady-state fluorescence spectra of emission and excitation were recorded using an Edinburgh Instruments FS5 Spectrofluorometer. Quartz cells 3.5 mL cuvettes with screw caps and four polished sides (Starna Cell, Type: 3/Q/10), were used for fluorescence measurements. The analysis was conducted in Fluoracle (Edinburgh Instruments) and Origin 2019 (Origin Labs).

MALDI-TOF

Matrix-assisted laser desorption/ionization (MALDI) was conducted with a Bruker Ultraflextreme MALDI to show molecular weight distribution of the polymer molecules instrument that fragment easily specifically for the detergent size polymers, 1-30kDa.The matrix used for all measurements is Dithranol .

Methods

Synthesis of 2-cyano-5-hydroxypentan-2-yl ethyl carbonotrithioate (CPET)

The RAFT chain transfer agent was synthesized in a three step reaction process as depicted in figure 2.4.1 to yield the final CTA (2-cyano-5-hydroxypentan-2-yl ethyl carbonotrithioate). The first step was a nucleophilic addition of ethanethiolate to carbon disulfide, while the second was a radical reaction with the initiator ACVA to form the intermediate CTA. Finally the last step was a simple reduction of 4-cyano-4-(((ethylthio)carbonothioyl)thio)pentanoic acid with borane to yield the terminal hydroxyl .

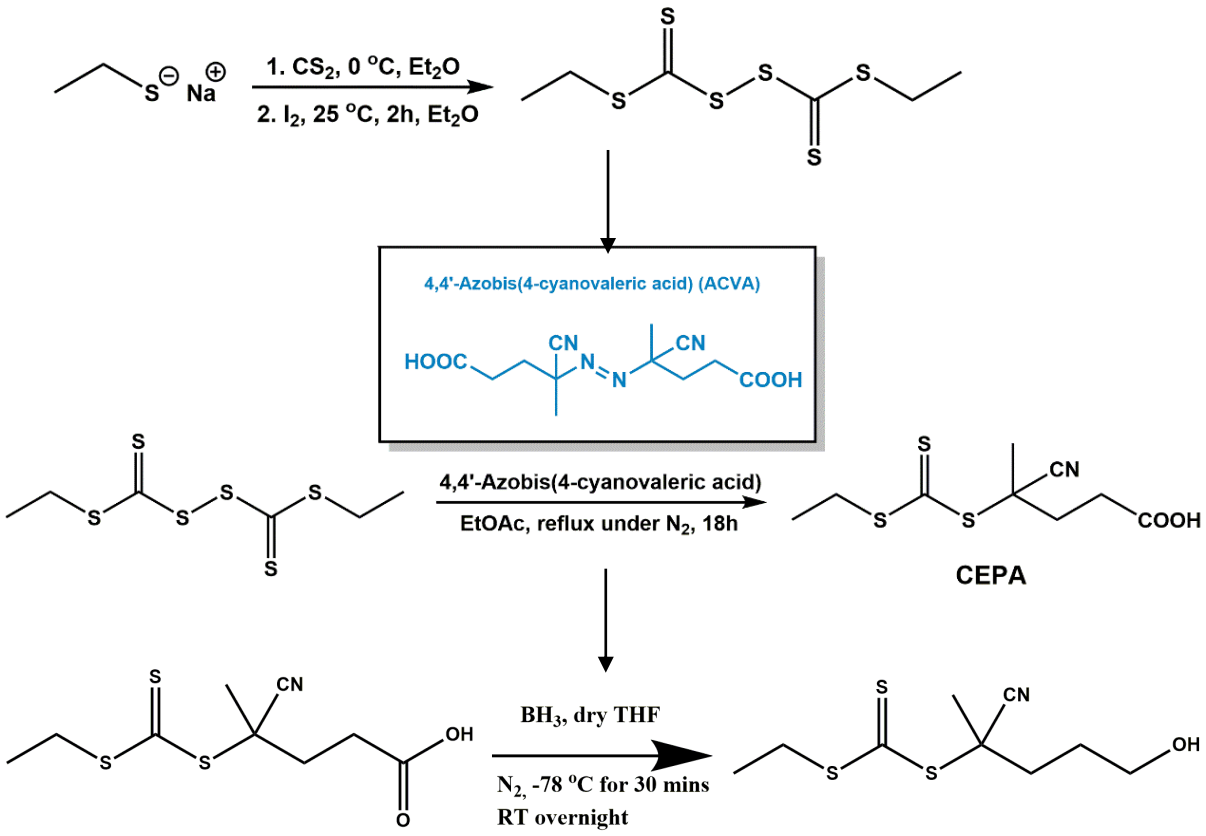
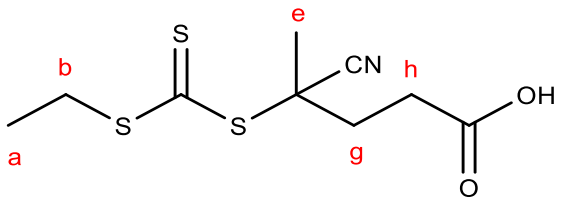


Figure 2.4.1. Synthesis of 2-cyano-5-hydroxypentan-2-yl ethyl carbonotrithioate (CEP) RAFT-agent initiator

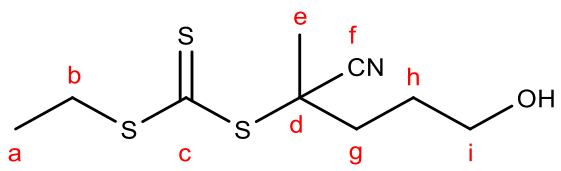
Synthesis of 4-cyano-4-(((ethylthio)carbonothioyl)thio)pentanoic acid (CEPA)



To an oven-dried round bottom flask, sodium ethanethiolate (10 g, 119 mmol) was added followed by the addition of dry diethyl ether (500 mL) with the resulting solution cooled to 0 °C. Carbon disulfide (7.74 mL, 131 mmol) was subsequently added dropwise over 10 min producing a thick yellow precipitate of sodium *S*-ethyl trithiocarbonate. After 2 h of stirring at room temperature, solid iodine (15.1 g, 59.4 mmol) was added. After 2 h of stirring at room temperature, the reaction mixture was washed with sodium thiosulphate solution (1 M, 3 x 250 mL), deionized water (3 x 250 mL) and finally with brine (250 mL). The organic layer was dried over $MgSO_4$ and evaporated to leave a residue of bis-(ethyl-sulfanylthiocarbonyl) disulfide (11.4 g, quantitative).

A solution of 4,4'-azobis(4-cyanovaleric acid) (ACVA) (17.5 g, 62.3 mmol) and bis-(ethyl-sulfanylthiocarbonyl) disulfide (11.4 g, 41.5 mmol) in ethyl acetate (500 mL) was refluxed for 18 h. After removal of ethyl acetate *in vacuo*, purification was carried out using silica column chromatography (petroleum ether 40/60:dichloromethane = 1:1) affording 4-cyano-4-(((ethylthio)carbonothioyl)thio)pentanoic acid (CEPA) as an orange red oil (6.97 g, 26.5 mmol, 64%). ^{1}H NMR (400 MHz, $CDCl_3$): δ (ppm) 3.34 (q, 2H, $^3J_{H\text{-}H}$ = 7.6 Hz, H_b), 2.68 (t, 2H, $^3J_{H\text{-}H}$ = 7.6 Hz, H_h), 2.3-2.6 (m, 2H, H_g), 1.88 (s, 3H, H_e), 1.35 (t, 3H, $^3J_{H\text{-}H}$ = 7.6 Hz, H_a).

Synthesis of 2-cyano-5-hydroxypentan-2-yl ethyl carbonotrithioate (CPET)



To a flame-dried round bottom flask, 4-cyano-4-(((ethylthio)carbonothioyl)thio)pentanoic acid (CEPA) (10 g, 38 mmol) was added followed by the addition of dry tetrahydrofuran (250 mL) with the resulting solution cooled to -78 °C. 1 M borane tetrahydrofuran complex solution (40 mL, 39.9 mmol) was subsequently added dropwise over 30 min. Reaction mixture was left to stir for 1 h, after which the cooling bath was removed and the reaction stirred overnight at ambient temperature under a nitrogen atmosphere. After 24 h of stirring, methanol (100 mL) was added in five portions and stirred for 10 min after each addition or until no further bubbling was observed. After removal of tetrahydrofuran and methanol *in vacuo*, the organic residue was dissolved in diethyl ether (250 mL) and washed with saturated $NaHCO_3$ solution (3 x 250 mL) and then with brine (250 mL). Further extraction using diethyl ether from the collected aqueous layers was carried out. Combined organic layers were dried over $MgSO_4$, filtered and evaporated to dryness. Purification was carried out using silica column chromatography (ethyl acetate 50/50:hexane = 1:1) affording 2-cyano-5-hydroxypentan-2-yl ethyl carbonotrithioate (CPET) as an orange red oil (5.64 g, 22.6 mmol, 60%). ^{1}H NMR (300 MHz, $CDCl_3$): δ (ppm) 3.72 (t, 2H, $^3J_{H\text{-}H}$ = 6 Hz, H_i), 3.34 (q, 2H, $^3J_{H\text{-}H}$ = 7.5 Hz, H_b), 2.0-2.4 (m, 2H, H_g), 1.89 (s, 3H, H_e), 1.78-1.88 (m, 2H, H_h), 1.35 (t, 3H, $^3J_{H\text{-}H}$ = 7.5 Hz, H_a). ^{13}C NMR (75 MHz, $CDCl_3$): δ (ppm) 217.4 (C_c), 119.5 (C_f), 61.7 (C_i), 46.9 (C_d), 35.7 (C_g), 31.3 (C_b), 27.9 (C_h), 24.9 (C_e), 12.8 (C_a).

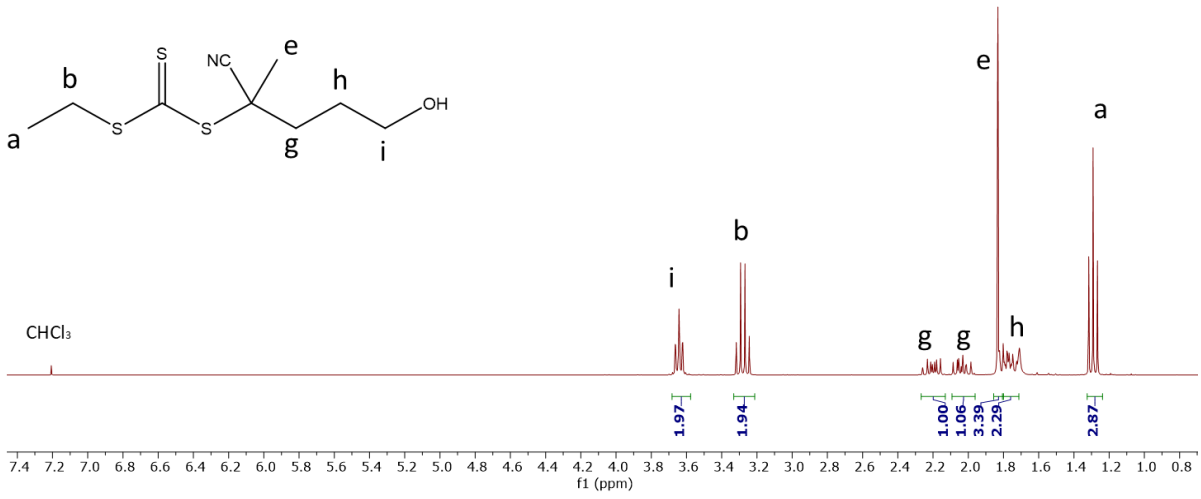


Figure 2.4.2. ^{1}H NMR (300MHz, $CDCl_3$) 2-cyano-5-hydroxypentan-2-yl ethyl carbonotrithioate (CEP) RAFT-agent initiator

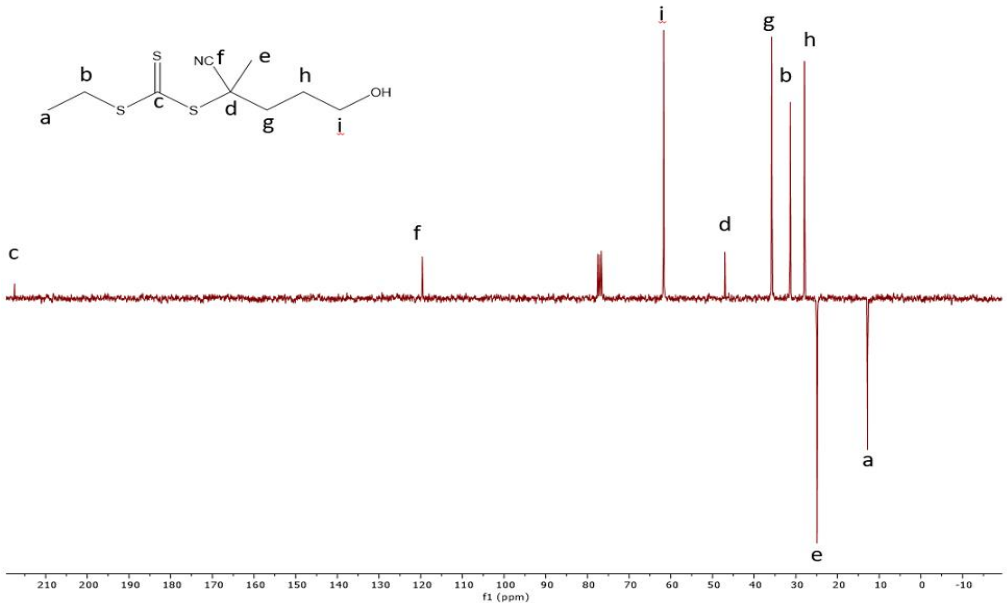


Figure 2.4.3. ^{13}C NMR of 2-cyano-5-hydroxypentan-2-yl ethyl carbonotrithioate (CEP) RAFT-agent initiator

Synthesis of poly(L-lactide) and poly(D,L-lactide)

In a nitrogen-filled glove box, a solution of 1,8-Diazabicyclo(5.4.0)undec-7-ene (DBU)(2.80 mg, 0.0184mmol) and 2- cyano-5-hydroxypentan-2-yl ethyl carbonotrithioate (12.7 mg, 0.0511 mmol) in dry CH_2Cl_2 (1 mL) were added to a solution of L-lactide (265.2 mg, 1.84 mmol) or D,L-lactide (265.2 mg, 1.84 mmol) in dry CH_2Cl_2 (1 mL). After stirring for 4 minutes at room temperature, the solution was removed from the glove box and precipitated two times into ice-cold n-hexane and one time into diethyl ether. The resultant yellow polymer was filtered and dried under vacuum for two days. Mn, NMR = 5.6 kDa,, DP = 37, Mn SEC =11 kDa, ,ÐM = 1.12. ^1H NMR (CDCl3): δ (ppm) 5.30 (q, 74H, $^3J_{H-H}$ = 7.0 Hz, $OCH(CH_3)CO$) 4.31 (q, 1H $^3J_{H-H}$ = 7.0 Hz, $CH(CH_3)OH$), 4.22 (t, 2H, OCH_2) 3.37 (t, 2H, $^3J_{H-H}$ = 6.3 Hz, SCH_2) 1.75 (s, 3H, $(CN)CCH_3$) 1.20- 1.30 (m, 4H, C_2H_4) 1.60 (d, 226H, $^3J_{H-H}$ = 7.0 Hz, CH_3CHO)), 1.27 (t, 3H, $^3J_{H-H}$ = 7.40 Hz, CH_3CH_2S).

Synthesis of poly(L-lactide)37-b-poly(N,N-dimethylaminoethyl methacrylate)225

$PLLA_{37}$, (95.6 mg, 17.6 µmol), N,N-dimethylaminoethyl methacrylate, (1000 mg, 6360 µmol) and AIBN (28.9 µL of a 10 mg mL-1 solution in 1,4-dioxane) were dissolved in 1,4-dioxane (2.14 mL) before transferring to a dried ampoule under nitrogen. After three freeze-pump-thaw cycles, the solution was sealed under nitrogen and heated for 6 hours at 70 °C for 60% conversion. The reaction was quenched in liquid nitrogen and purified by precipitation three times into cold ice-cold n-hexane. The resultant pale yellow solid was dried in vacuo before use. Mn, NMR = 35 kDa, DP = 225. Mn, SEC = 32 kDa, ĐM = 1.41. ^{1}H NMR (CDCl3): δ (ppm) 5.16 (q, 37H, $^{3}J_{H-H}$ = 6.9 Hz, OC*H*(CH3)CO) 4.05 (br s, 225 H, OC*H2*CH2N) 2.56 (br s, 382H, C*H2*N(CH3)2) 2.28 (s, 716H, N(C*H3*)2) 1.75-2.05 (br d, 196H, (CH3)CC*H2*, C*H2*S) 1.75 (d, 119H $^{3}J_{H-H}$ = 6.9 Hz, C*H3*CHO) 1.05-0.75 (m, 383H, C*H3*C(CN)C3*H6*, C*H3*CH2S, (C*H3*)CCH2).

Synthesis of 5-(3-chloro-4-((2-hydroxyethyl)amino)-2,5-dioxo-2,5-dihydro-1H-pyrrol-1-yl)-2-cyanopentan-2-yl ethyl carbonotrithioate (fluorescent CTA)

A two step process was used in order to synthesize the 5-(3-chloro-4-((2-hydroxyethyl)amino)-2,5-dioxo-2,5-dihydro-1H-pyrrol-1-yl)-2-cyanopentan-2-yl ethyl carbonotrithioate initiator. After the synthesis of the 2-cyano-5-hydroxypentan-2-yl ethyl carbonotrithioate and the dichloromaleimide precursors, a mitsunobu reaction [164] was performed. The reaction (Fig. 2.4.4) was conducted using air sensitive techniques and the ^{1}H NMR (Fig. 2.4.6) and ^{13}C NMR (Fig. 2.4.7) confirmed the existence of a pure product.

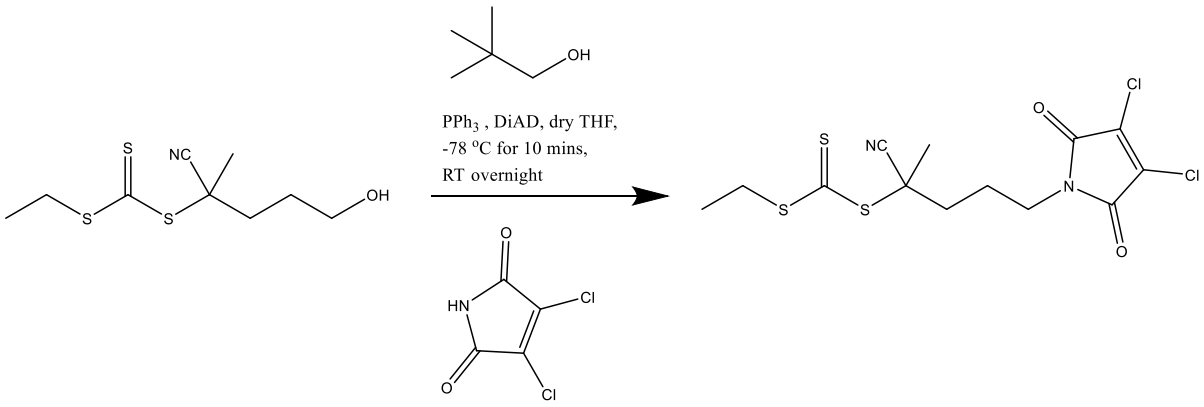


Figure 2.4.4. Synthesis of 2-cyano-5-(3,4-dichloro-2,5-dioxo-2,5-dihydro-1H-pyrrol-1-yl)pentan-2-yl ethyl carbonotrithioate

The last step to produce the fluorescent CTA was a substitution of one chloro group with a 2-aminoethanol group, in order to provide the terminal hydroxyl group that can initiate the ROP. The reaction (Fig. 2.4.4) was monitored with TLC and was terminated after one hour to ensure the monosubstituted product of the final product is provided (Fig. 2.4.5) confirming the successful synthesis.

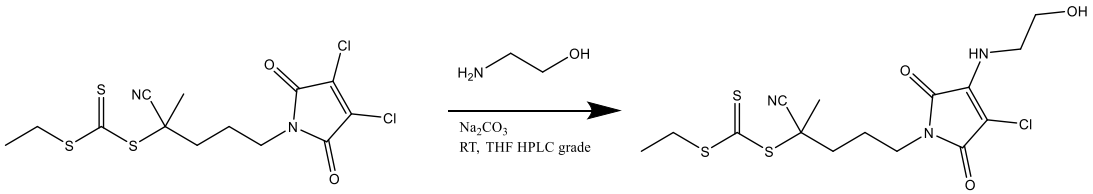
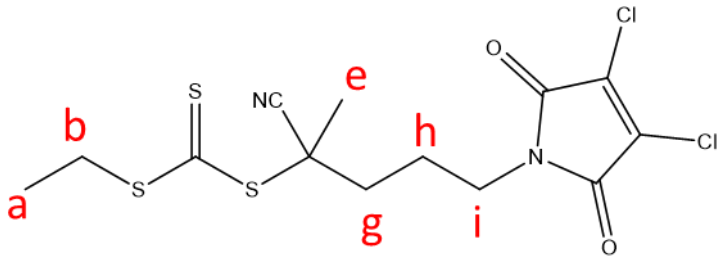


Figure 2.4.5. Synthesis of fluorescent CTA

Synthesis 2-cyano-5-(3,4-dichloro-2,5-dioxo-2,5-dihydro-1H-pyrrol-1-yl)pentan-2-yl ethyl carbonotrithioate (intermediate fluorescent CTA CPET-DCM)



To a flame-dried round bottom flask, triphenylphosphine (3.16 g, 12.05 mmol) was added followed by the addition of dry tetrahydrofuran (150 mL) and the resulting solution cooled to -78 °C. Diisopropyl azodicarboxylate (DIAD) (2.40 mL, 12.05 mmol) was added dropwise over 2-3 min. Reaction mixture was stirred for 5 min after which 2-cyano-5-hydroxypentan-2-yl ethyl carbonotrithioate (CPET) (3 g, 12.05 mmol) dissolved in dry tetrahydrofuran (25 mL) was added using air sensitive techniques and stirred for 5 min. Neopentyl alcohol (0.53 g, 6.025 mmol) was added and the reaction mixture left to stir for 10 min. Dibromomaleimide (2 g, 12.05 mmol) was then added to the reaction mixture. Resulting suspension was allowed to remain at -78 °C for 10 min before the cooling bath was removed and the reaction was stirred overnight at ambient temperature under a nitrogen atmosphere. After removal of tetrahydrofuran *in vacuo*, purification was carried out using silica column chromatography (dichloromethane:petroleum ether 40/60 = 2:1) affording 2-cyano-5-(3,4-dichloro-2,5-dioxo-2,5-dihydro-1*H*-pyrrol-1-yl)pentan-2-yl ethyl

carbonotrithioate (CPET-ACM) as an orange red oil (3.5 g, 8.8 mmol, 70 %). ^{1}H NMR (300 MHz, $CDCl_3$): δ (ppm) 3.68 (t, 2H, $^{3}J_{H\text{-}H}$ = 6.9 Hz, H_i), 3.33 (q, 2H, $^{3}J_{H\text{-}H}$ = 7.5 Hz, H_b), 2.0-2.3 (m, 2H, H_g), 1.92 (q, 2H, $^{3}J_{H\text{-}H}$ = 6.9 Hz, H_h), 1.84 (s, 3H, H_e), 1.35 (t, 3H, $^{3}J_{H\text{-}H}$ = 7.5 Hz, H_a). ^{13}C NMR (75 MHz, $CDCl_3$): δ (ppm) 217.0 (C_c), 163.8 (C_j), 129.5 (C_k) 119.1 (C_f), 46.5 (C_d), 38.8 (C_i), 35.8 (C_g), 31.4 (C_b), 24.8 (C_e), 24.0 (C_h), 12.7 (C_a).

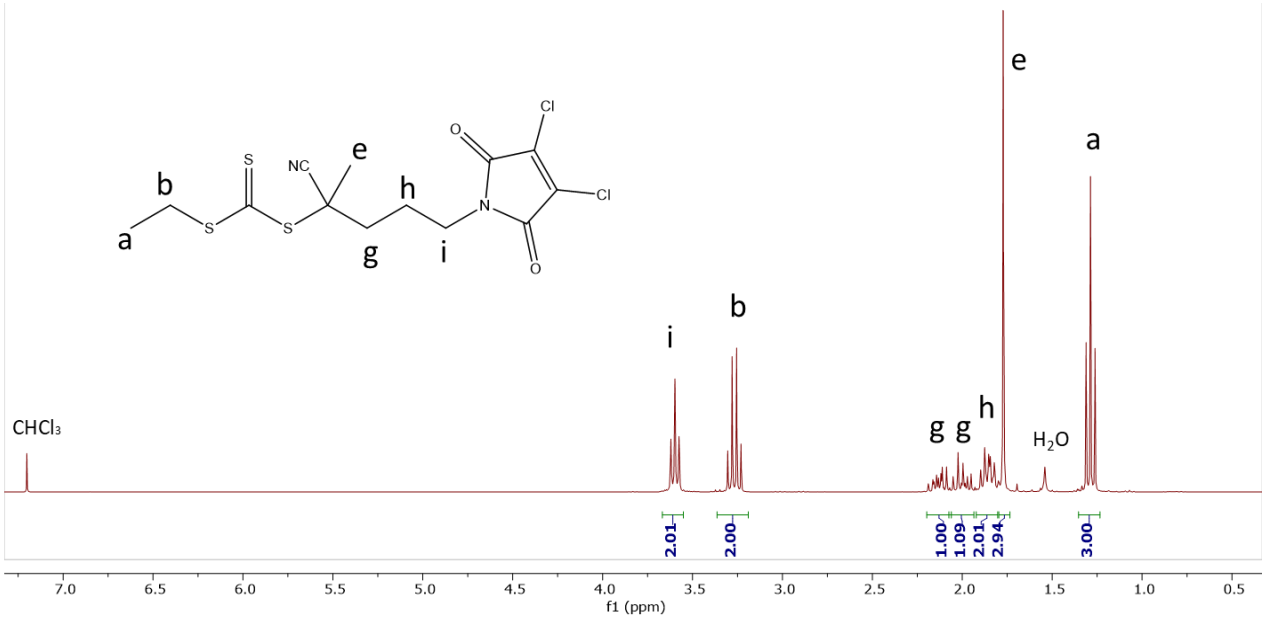


Figure 2.4.6. ^{1}H NMR (300MHz, $CDCl_3$) spectrum of 2-cyano-5-(3,4-dichloro-2,5-dioxo-2,5-dihydro-1H-pyrrol-1-yl)pentan-2-yl ethyl carbonotrithioate

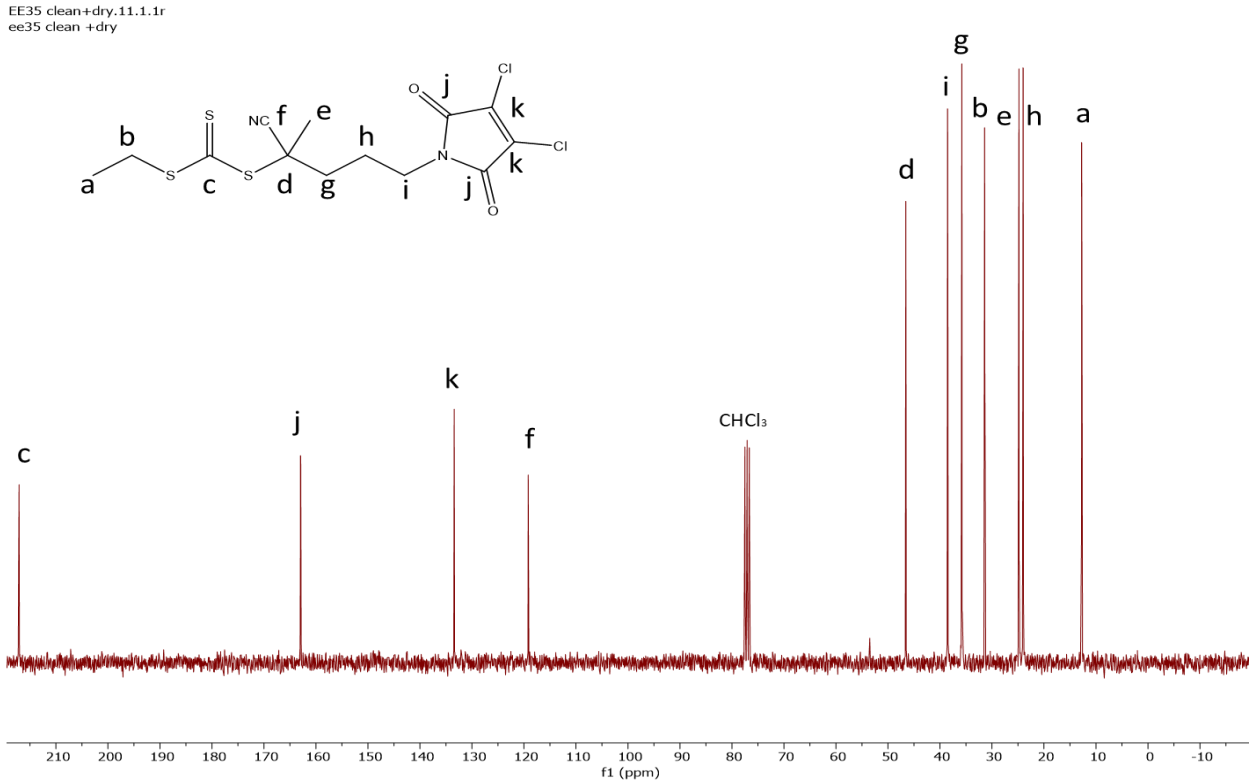
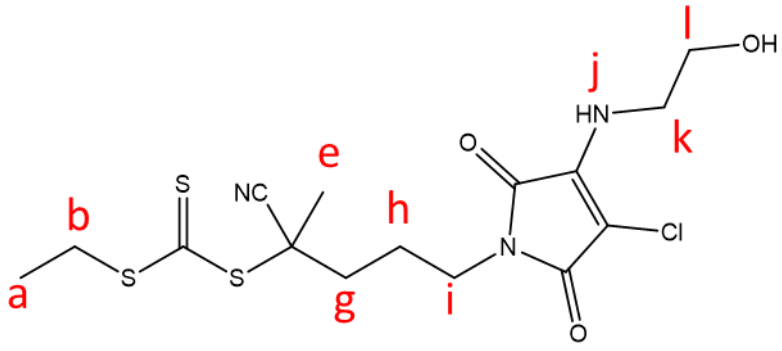


Figure 2.4.7. ^{13}C NMR spectrum of 2-cyano-5-(3,4-dichloro-2,5-dioxo-2,5-dihydro-1H-pyrrol-1-yl)pentan-2-yl ethyl carbonotrithioate

Synthesis of 5-(3-chloro-4-((2-hydroxyethyl)amino)-2,5-dioxo-2,5-dihydro-1H-pyrrol-1-yl)-2-cyanopentan-2-yl ethyl carbonotrithioate (fluorescent CTA)



To a suspension of Na_2CO_3 (1.03 g, 9.70 mmol) and 2-cyano-5-(3,4-dibromo-2,5-dioxo-2,5-dihydro-1*H*-pyrrol-1-yl)pentan-2-yl ethyl carbonotrithioate (CPET-DCM) (3.5 g, 8.82 mmol) in tetrahydrofuran (150 mL), 2-aminoethanol (0.560 mL, 9.26 mmol) was added. Reaction mixture was stirred at room temperature with the conversion of CPET-DCM monitored by thin layer chromatography. After 1 hour, tetrahydrofuran was removed *in vacuo* and the organic residue dissolved in dichloromethane (250 mL) and washed with deionized water (3 x 250 mL) and brine (1x250mL). Organic layer was dried over $MgSO_4$, filtered and

evaporated to dryness. Purification was carried out using silica column chromatography (ethyl acetate: hexane 40/60 = 2:1) affording 5-(3-chloro-4-((2-hydroxyethyl)amino)-2,5-dioxo-2,5-dihydro-1H-pyrrol-1-yl)-2-cyanopentan-2-yl ethyl carbonotrithioate (CPET-ACM) as an orange red oil (2 g, 4.73 mmol, 50 %). ^{1}H NMR (300 MHz, $CDCl_3$): δ (ppm) 5.28 (d, 1H, $^{3}J_{H\text{-}H}$ = 8.7 Hz, H_n), 4.41 (ds, 1H, $^{3}J_{H\text{-}H}$ = 6.6 and 8.7 Hz, H_o), 3.56 (t, 2H, $^{3}J_{H\text{-}H}$ = 6.6 Hz, H_i), 3.33 (q, 2H, $^{3}J_{H\text{-}H}$ = 7.5 Hz, H_b), 1.95-2.25 (m, 2H, H_g), 1.7-1.95 (m, 2H, H_h), 1.84 (s, 3H, H_e), 1.25-1.4 (m, 9H, H_a and H_p). ^{13}C NMR (75 MHz, $CDCl_3$): δ (ppm) 217.1 (C_c), 167.7 (C_j), 166.0 (C_k) 142.2 (C_l and C_m) 119.2 (C_f), 46.6 (C_o), 44.8 (C_d), 37.7 (C_i), 36.0 (C_g), 31.3 (C_b), 24.8 (C_e), 24.1 (C_h), 23.7 (C_p) 12.7 (C_a).

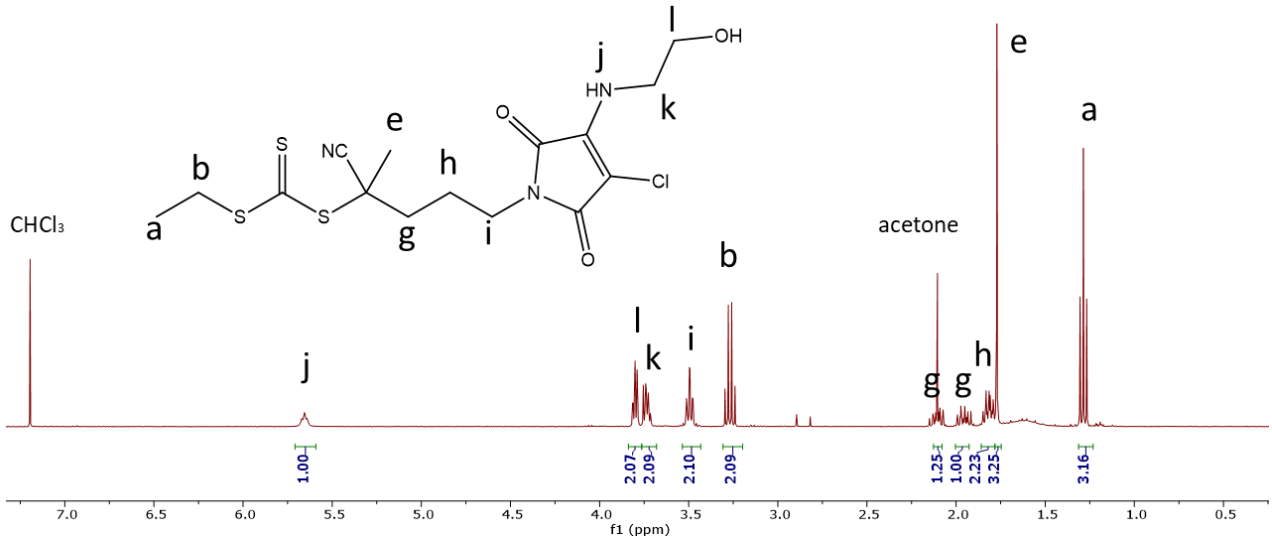


Figure 2.4.8. ^{1}H NMR (300MHz, $CDCl_3$) spectrum of 5-(3-chloro-4-((2-hydroxyethyl)amino)-2,5-dioxo-2,5-dihydro-1H-pyrrol-1-yl)-2-cyanopentan-2-yl ethyl carbonotrithioate (fluorescent CTA)

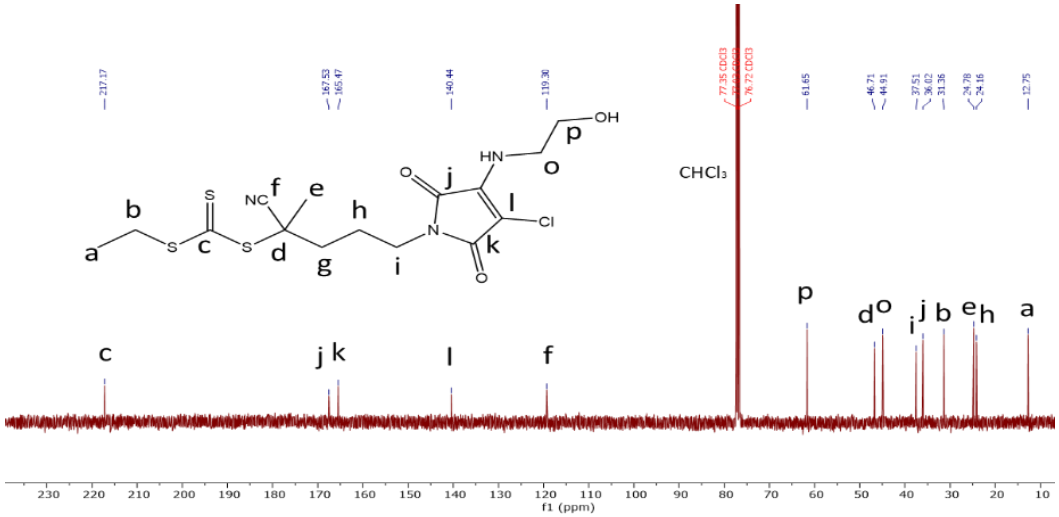


Figure 2.4.9. ^{13}C (DOWN) spectrum of 5-(3-chloro-4-((2-hydroxyethyl)amino)-2,5-dioxo-2,5-dihydro-1H-pyrrol-1-yl)-2-cyanopentan-2-yl ethyl carbonotrithioate (fluorescent CTA)

Synthesis of poly(L-lactide) and poly(D,L-lactide) with fluorescent ACM probe

A typical ROP polymerization as previously described was conducted. The only difference is the CTA with the ACM probe adjusted. Mn, NMR = 5.8 kDa,, DP = 36, Mn SEC =11 kDa, ,ÐM = 1.11. ^{1}H NMR (CDCl3): δ (ppm) 5.68 (br t , 1H, *H*NCH$_2$), 5.30 (q, 72 H, $^{3}J_{H\text{-}H}$ = 7.06 Hz, OC*H*(CH$_3$)CO) 4.28 (m, 3H,CH$_2$C*H*$_2$OCO + C*H*(CH$_3$)OH), 3.81(br m,2H, HNC*H*$_2$CH$_2$), 3.48 (t, 2H, , $^{3}J_{H\text{-}H}$ = 6.53 Hz, SC*H*$_2$) 3.26 (q, 2H, $^{3}J_{H\text{-}H}$ = 7.57 Hz, CH$_2$C*H*$_2$NCO) 1.77 (s, 3H, (CN)CCH$_3$) 1.75-1.60(d, 2H, $^{3}J_{H\text{-}H}$ = 7.09 Hz, CH$_3$C*H*$_2$CH$_2$), 1.50 (d, 250H, $^{3}J_{H\text{-}H}$ = 7.12 Hz, CH$_3$CHO), 1.43 (m, 2H, CH$_2$C*H*$_2$CH$_2$N), 1.27 (t, 3H, $^{3}J_{H\text{-}H}$ = 7.40 Hz, C*H*$_3$CH$_2$S).

The ROP of L-lactide & DL- lactide was carried out in a nitrogen-filled glove box to avoid any unwanted initiation from water in the atmosphere with 1,8-Diazabicyclo(5.4.0)undec-7-ene (DBU) as a catalyst and the bifunctional initiator with the ACM probe attached.

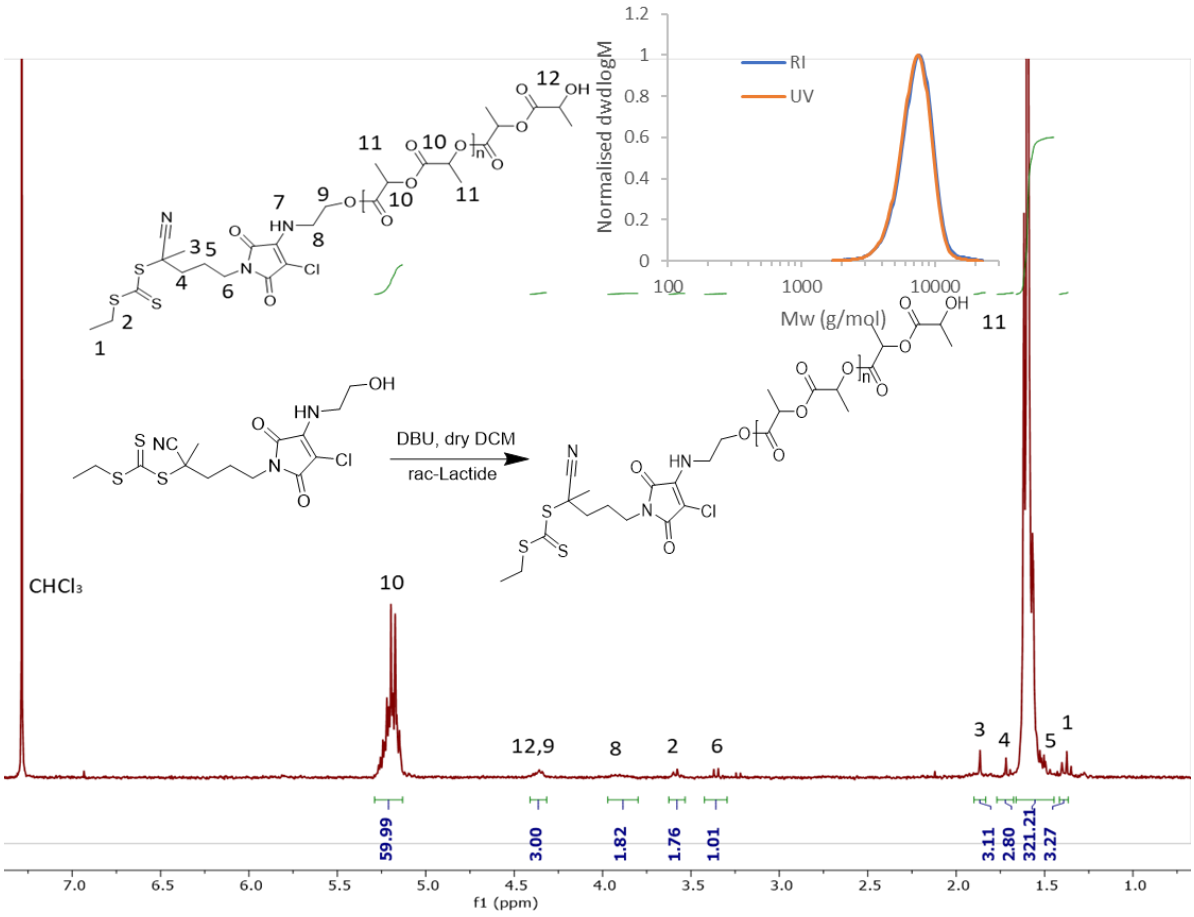


Figure 2.4.10.Scheme of ROP of DL-Lactide and ^{1}H NMR (300MHz, $CDCl_3$) and $CHCl_3$ GPC characterization

The reaction was terminated and purified via multiple precipitations to yield a yellow powder. The DP acquired from the NMR is 30 as calculated by end-group analysis and the dispersity $Đ_M$= 1.08 with a M_n of 7 kDa was provided by the chloroform GPC.

Synthesis of poly(L-lactide)$_{36}$-b-poly(N,N-dimethylaminoethyl methacrylate)$_{204}$ with fluorescent ACM probe

A typical RAFT polymerization was conducted as previously described with the only difference being the reaction time instead of 6 hours to 4 hours and 30 minutes. The conversion reached was 55.6 %. Mn, NMR = 37.8 kDa, DP = 206. Mn, SEC = 34.8 kDa, ĐM = 1.34. ^{1}H NMR (CDCl3): δ (ppm) 5.18 (q, 36H, $^{3}J_{H-H}$ = 7.04 Hz, OC*H*(CH3)CO) 4.09 (br s, 206H, OC*H2*CH2N) 2.59 (br t, 211H, C*H2*N(CH3)2) 2.32 (d, 634H, N(C*H3*)2) 2.00-1.84 (br d, 327H, (CH3)CC*H2*, C*H2*S) 1.60 (d, 114 H, 3JH-H = 7.02 Hz, C*H3*CHO) 1.59-0.90 (m, 346H, C*H3*C(CN)C3*H6*, C*H3*CH2S, (C*H3*)CCH2).

Similarly the other polymers with various corona chemistries were synthesised.

Table 9. Synthesis of diblock copolymers with different corona chemistry with crystalline (PL LA) core and amorphous (PDLLA) core

Corona	DP	M_n (kDa)	M_w(kDa)	$Đ_M$	Ratio Core:corona	Fluorescence	Core
DMAEMA	204	35	31	1.31	1:6	Yes	PLLA
DMAEMA	225	32	34	1.41	1:6	No	PLLA
DMAEMA	124	26	36	1.39	1:3	Yes	PLLA
TEGA	82	9	10	1.18	1:2	Yes	PLLA
TEGA	63	15	20	1.23	1:2	No	PLLA
TEGA	482	17	41	2.37	1:16	No	PLLA
TEGA	675	22	67	3.02	1:16	Yes	PLLA
TEGA	270	28	43	1.53	1:6	Yes	PLLA
DMA	87	15	19	1.10	1:3	No	PLLA
DMA	69	TBC	TBC	TBC	1:2	Yes	PLLA
DMA	527	52	71	1.38	1:13	Yes	PLLA
NIPAM	22	12	13	1.09	1:1	No	PLLA
NIPAM	119	10	11	1.08	1:4	No	PLLA
NIPAM	168	12	13	1.11	1:5	Yes	PLLA
NIPAM	111	13	17	1.33	1:3	No	PLLA
NIPAM	135	12	18	1.52	1:3	Yes	PLLA
tBA	486	19	22	1.15	1:16	No	PLLA
tBA	299	7	16	2.34	1:7	Yes	PLLA
DMAEMA	200	25	31	1.20	1:6	Yes	PDLLA
DMAEMA	199	26	34	1.27	1:6	No	PDLLA
TEGA	28	9	10	1.18	1:1	Yes	PDLLA
TEGA	42	15	20	1.37	1:1	No	PDLLA
TEGA	65	15	20	1.30	1:2	No	PDLLA
DMA	57	15	19	1.23	1:2	Yes	PDLLA
DMA	114	18	21	1.12	1:3	No	PDLLA
NIPAM	85	8	9	1.19	1:3	Yes	PDLLA

NIPAM	**119**	**19**	**22**	**1.19**	**1:3**	**No**	**PDLLA**

Below the polymerisation and characterisation of the polymers is depicted.

PDMAEMA$_{200}$-b-P$_{D,L}$LA$_{30}$

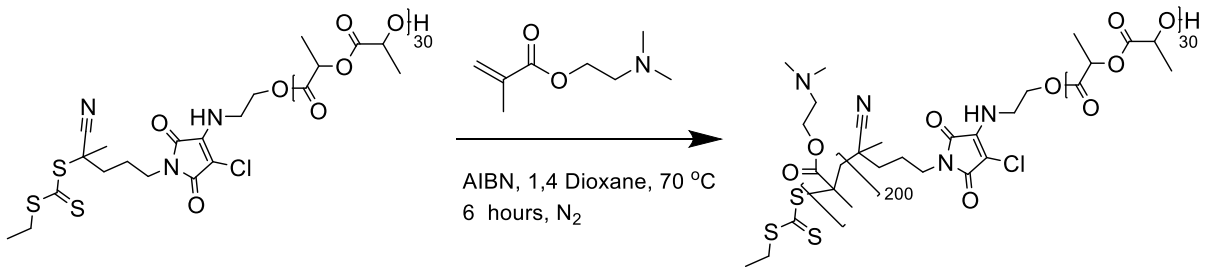


Figure 2.4.11. Synthesis of diblock PDMAEMA$_{200}$-b-PDLLA$_{30}$ with fluorescent probe

Comments: Freeze-pump-thaw technique was used to degas the solution, by doing at least 4 cycles. The polymers precipitated in hexane afterwards.

^{1}H NMR

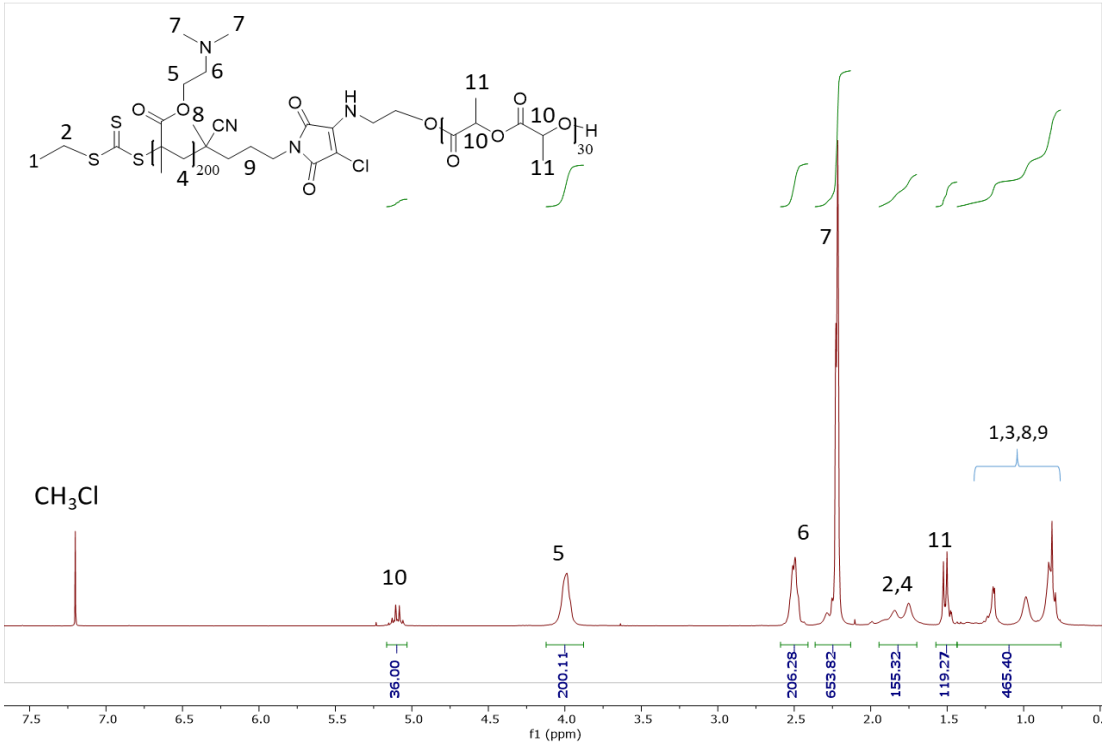


Figure 2.4.12. ^{1H} NMR spectrum of PDMAEMA$_{200}$-b-PD,LLA$_{30}$ with fluorescent probe

The NMR spectrum presents the degree of polymerization (DP) to be 200 as calculated by peak 5 which corresponds to 2 protons, as peak 10.

<u>$CHCl_3$ GPC</u>

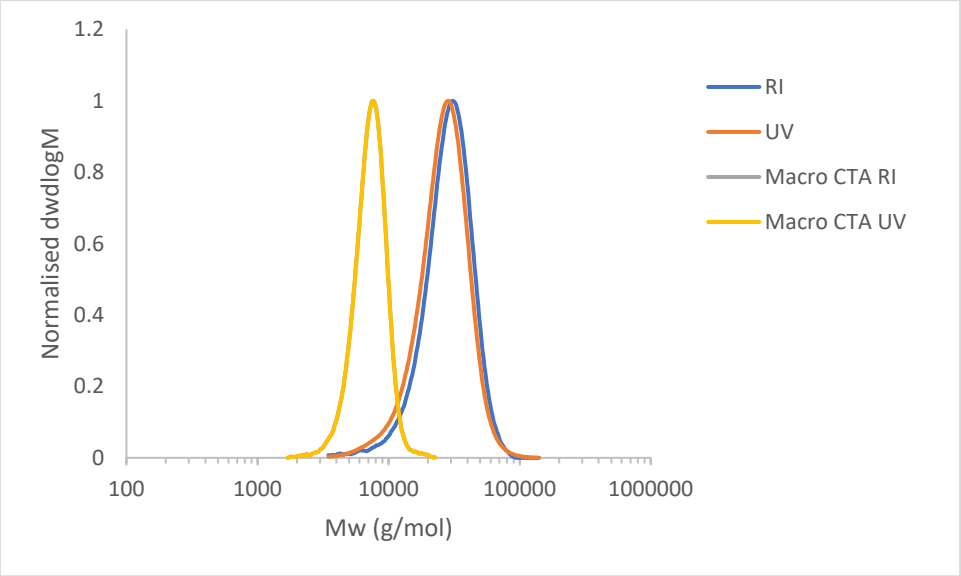


Figure 4.13. Representation of Molecular weight distribution from chloroform GPC (λ=309 nm) of $PDMAEMA_{200}$-b-$P_{DL}LA_{30}$

SEC analysis revealed a M_n of 25 kDa and a dispersity $Đ_M$ = 1.2 calculated from the refrective index data.

$PDMAEMA_{199}$-b-$P_{DL}LA_{36}$

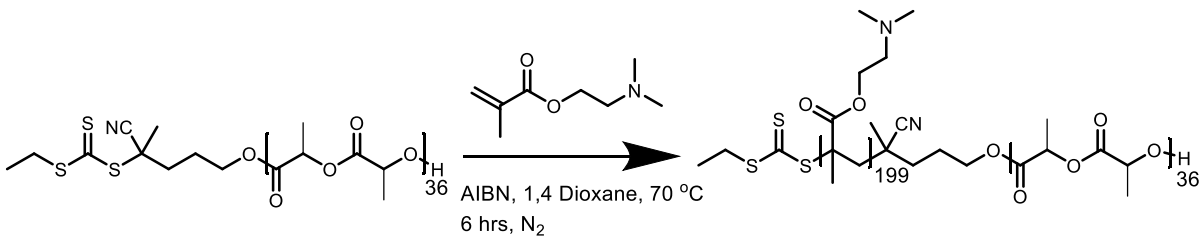


Figure 4.14. Synthesis of diblock $PDMAEMA_{199}$-b-$PDLLA_{36}$

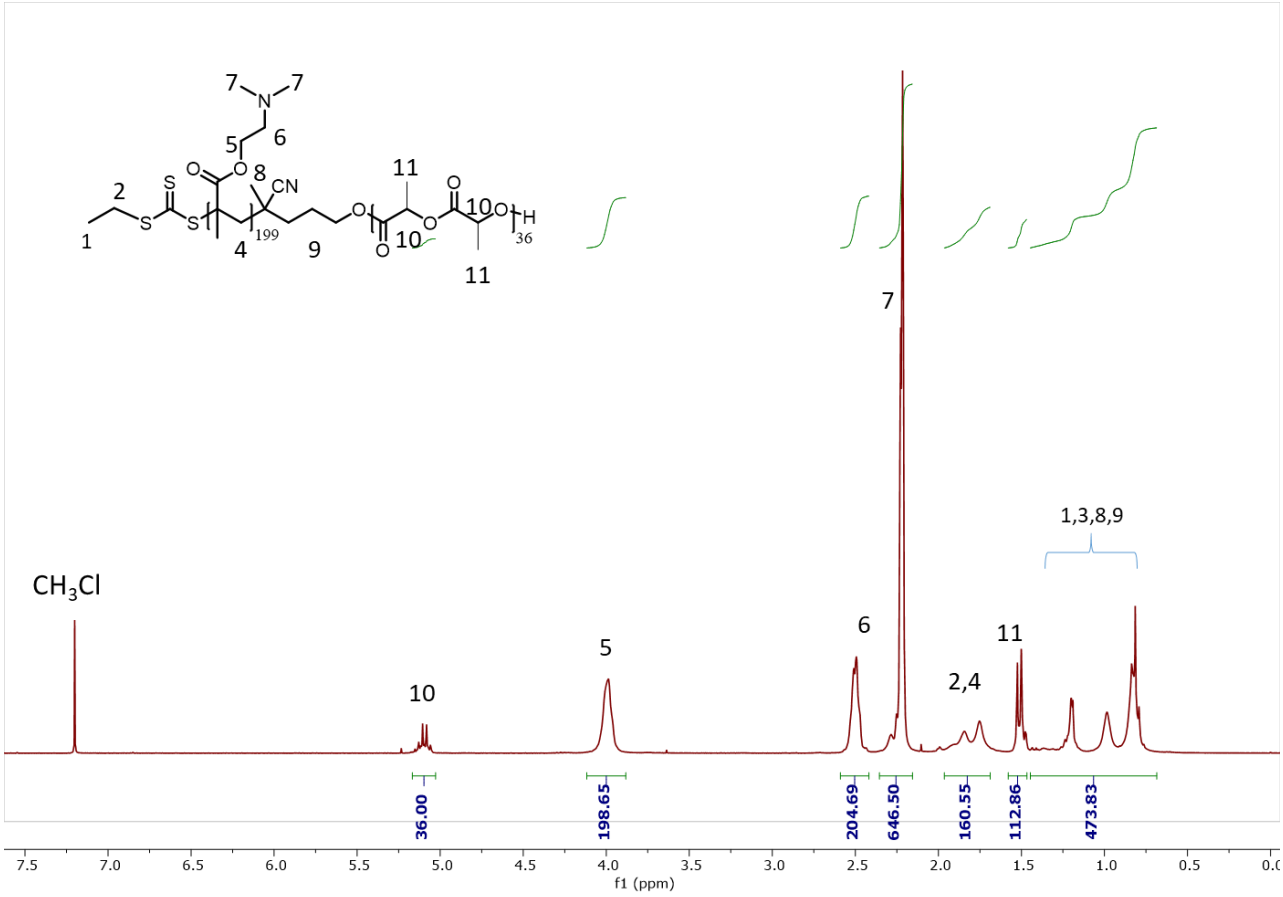


Figure 4.15. ^{1}H NMR (300MHz, $CDCl_3$) of diblock $PDMAEMA_{199}$-b-$P_{D,L}LA_{36}$

The NMR spectrum presents the degree of polymerization (DP) to be 199 as calculated by peak 5 which corresponds to 2 protons, as peak 10.

CHCl$_3$ GPC

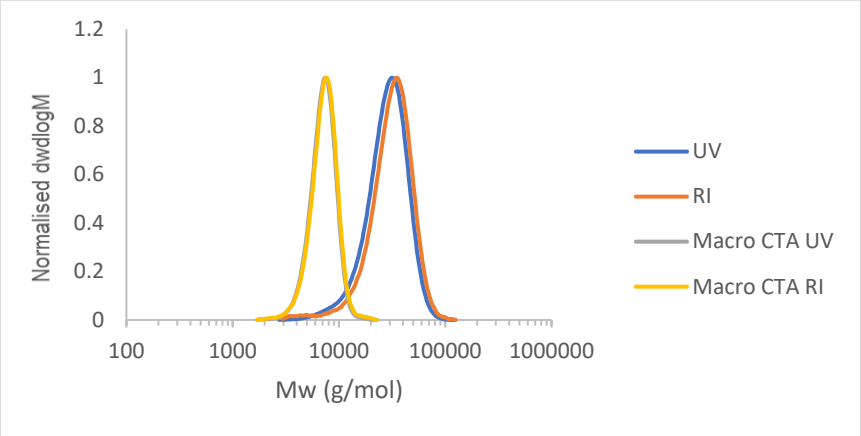


Figure 4.16. Representation of Molecular weight distribution from chloroform GPC (λ=309 nm) of PDMAEMA$_{199}$-b-PDLLA$_{36}$

SEC analysis revealed a M_n of 26 kDa and a dispersity $Đ_M$ = 1.27 calculated from the refrective index data.

PTEGA$_{28}$-b-PD,LLA$_{30}$

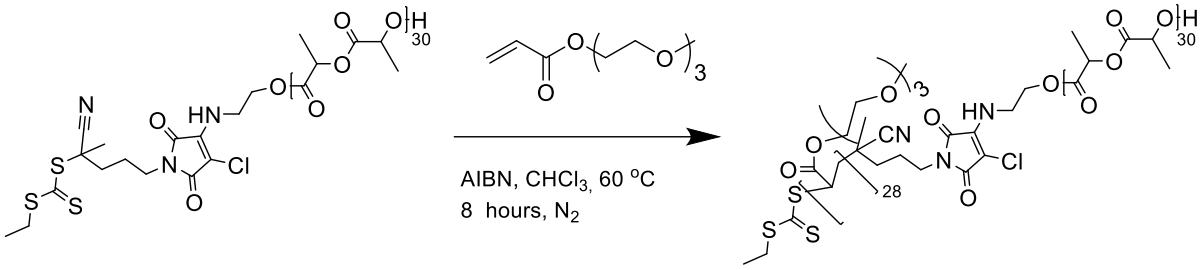


Figure 4.17 Synthesis of diblock PTEGA$_{28}$-b-PD,LLA$_{30}$

Comments: Freeze-pump-thaw technique was used to degas the solution, by doing at least 4 cycles. The polymers precipitated in hexane afterwards. The conversion was 35% very low after 8 hours while aiming for 80% conversion. The NMRs of all the materials though appear to be normal.

^{1}H NMR

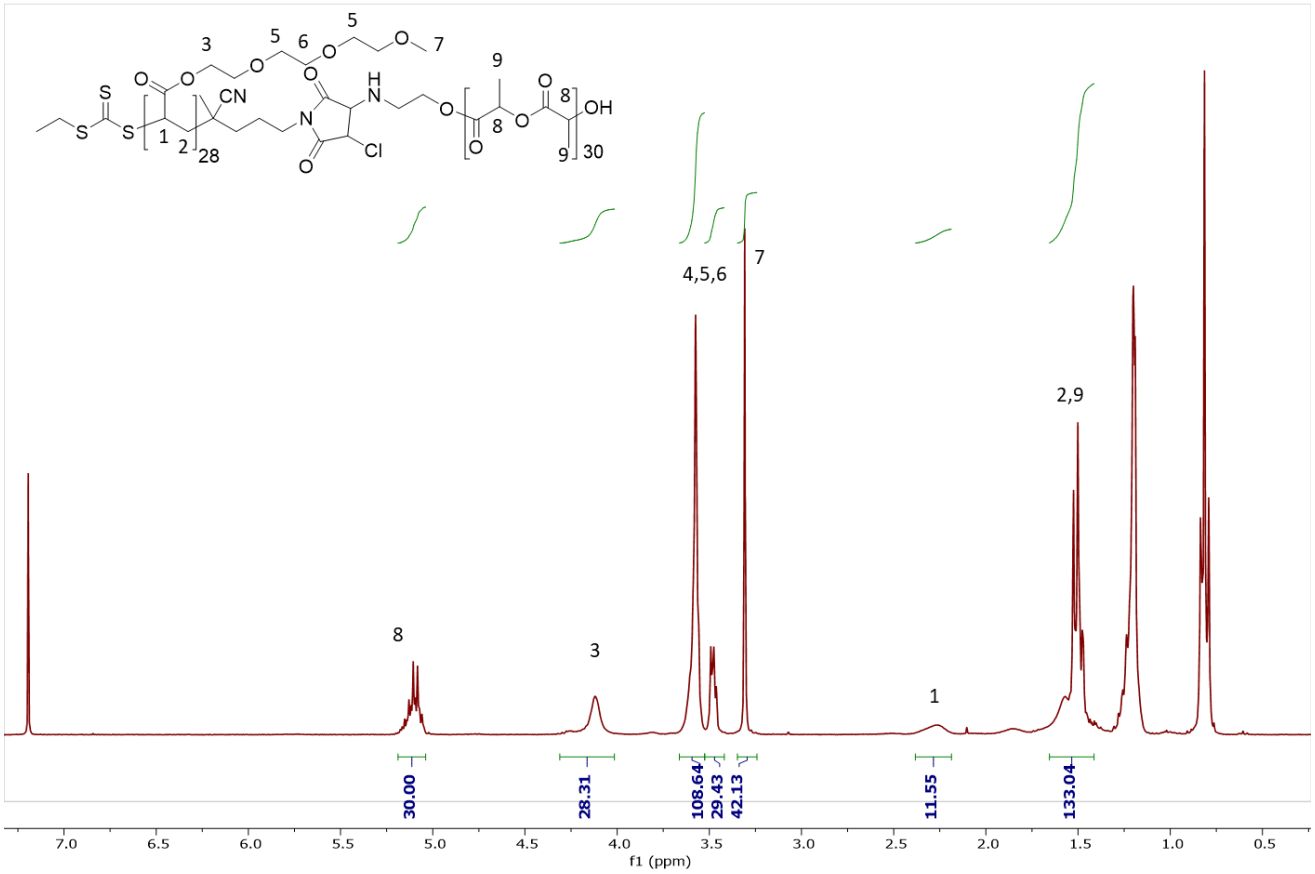


Figure 4.18. ^{1}H NMR (300MHz, $CDCl_3$) of diblock $PTEGA_{28}$-b-$P_{D,L}LA_{30}$ with fluorescent probe

The NMR spectrum presents the degree of polymerization (DP) to be 28 as calculated by peak 3 which corresponds to 2 protons, as peak 8.

<u>$CHCl_3$ GPC</u>

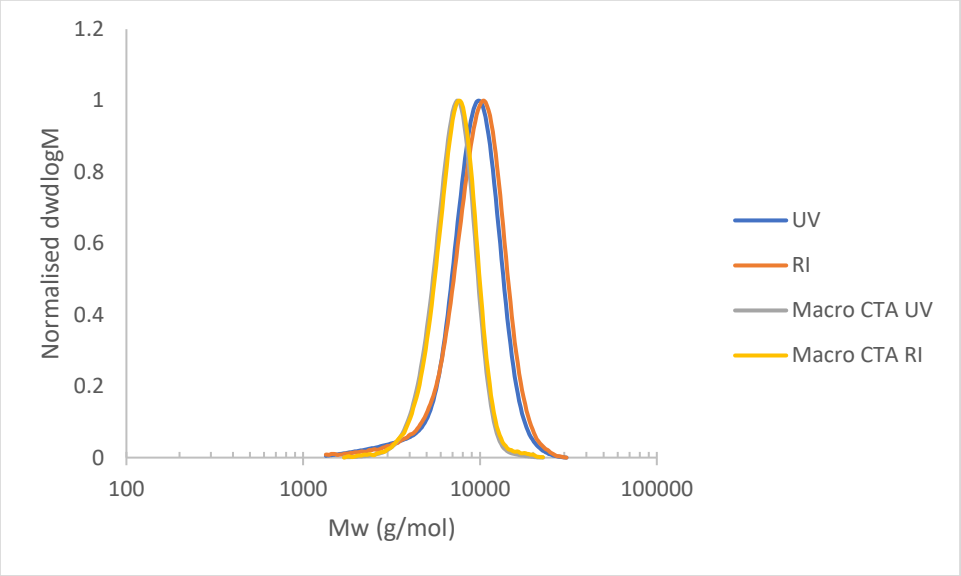


Figure 4.19. Representation of Molecular weight distribution from chloroform GPC (λ=309 nm) of $PTEGA_{28}$-b-$P_{D,L}LA_{30}$ with fluorescent probe

SEC analysis revealed a M_n of 9 kDa and a dispersity $Đ_M$ = 1.18 calculated from the refrective index data.

$PTEGA_{65}$-b-$P_{D,L}LA_{36}$

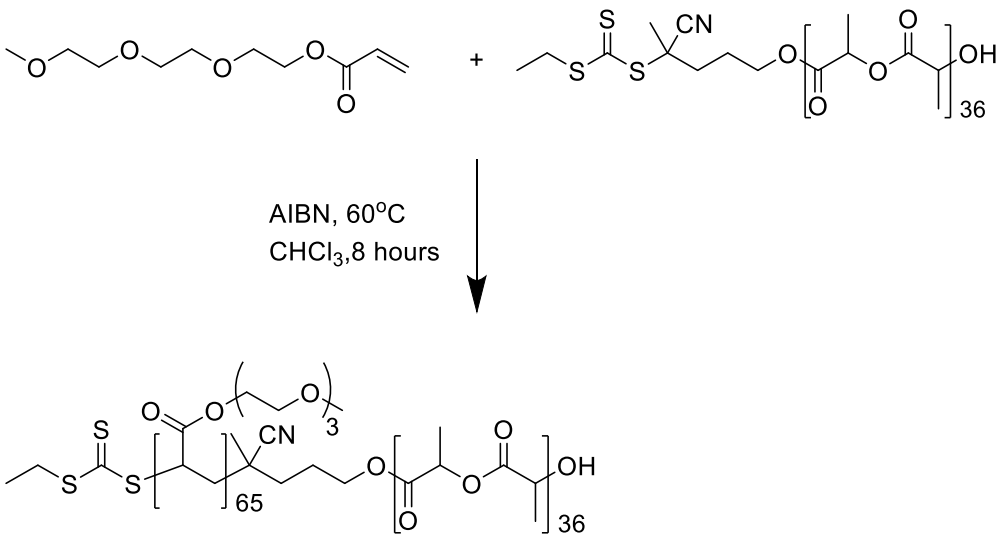


Figure 4.20. Synthesis of $PTEGA_{65}$ -b-$P_{D,L}LA_{36}$

Comments: Freeze-pump-thaw technique was used to degas the solution, by doing at least 4 cycles. The polymers precipitated in hexane afterwards. The conversion aiming for 80% conversion and from the crude NMR was calculated to be 88%, but the traces of chloroform GPC indicate the existence of homopolymer. The NMRs of all the materials though appear to be normal.

^{1}H NMR

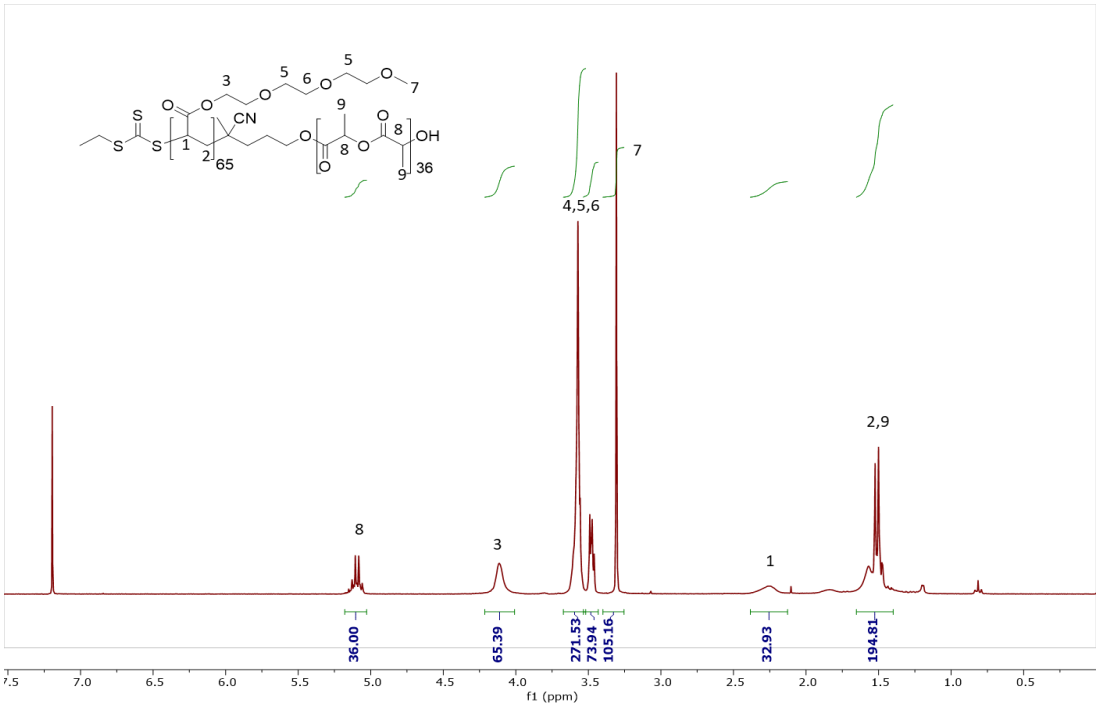


Figure 4.21. ^{1}H NMR (300MHz, $CDCl_3$) of diblock $PTEGA_{65}$-b-$P_{D,L}LA_{36}$

The NMR spectrum presents the degree of polymerization (DP) to be 65 as calculated by peak 3 which corresponds to 2 protons, as peak 8.

$\underline{CHCl_3\ GPC}$

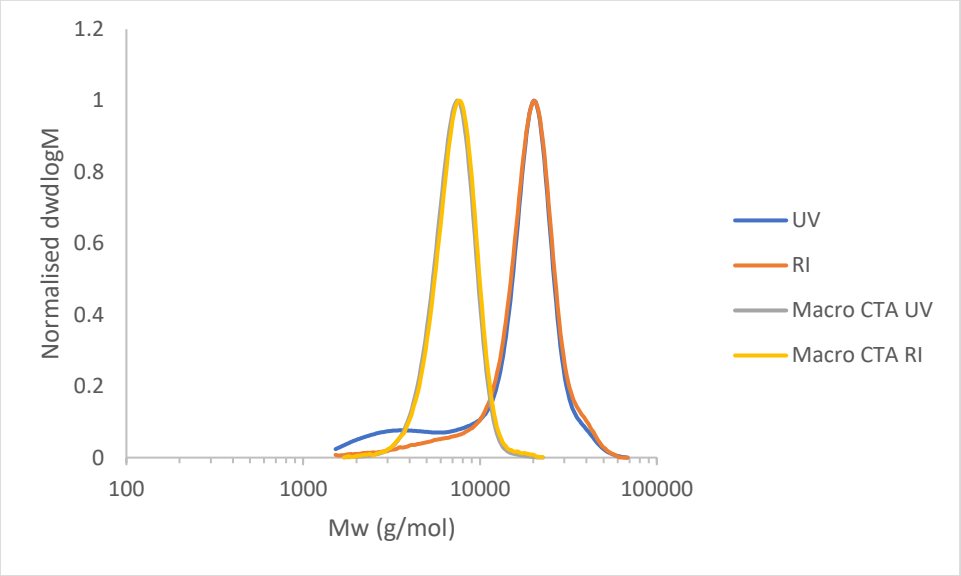
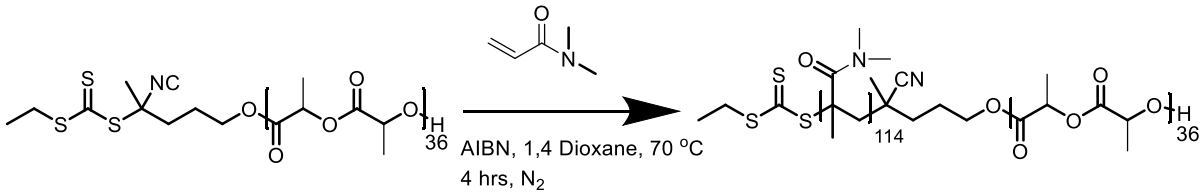


Figure 4.22. Representation of Molecular weight distribution from chloroform GPC (λ=309 nm) of $PTEGA_{65}$-b-$P_{D,L}LA_{36}$

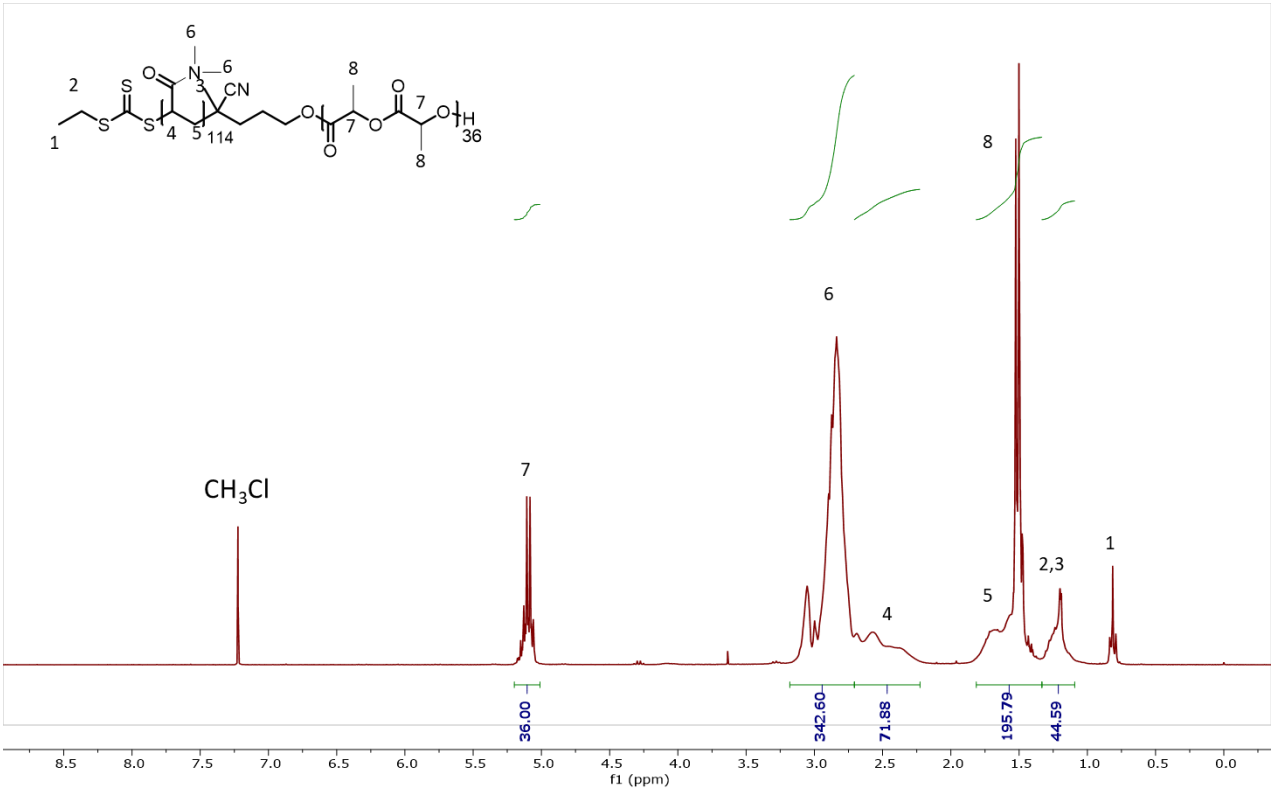
SEC analysis revealed a M_n of 15 kDa and a dispersity $Đ_M$ = 1.30 calculated from the refrective index data. UV trace depicts a shoulder of homopolymer.

$PDMA_{114}$-b-$P_{D,L}LA_{36}$



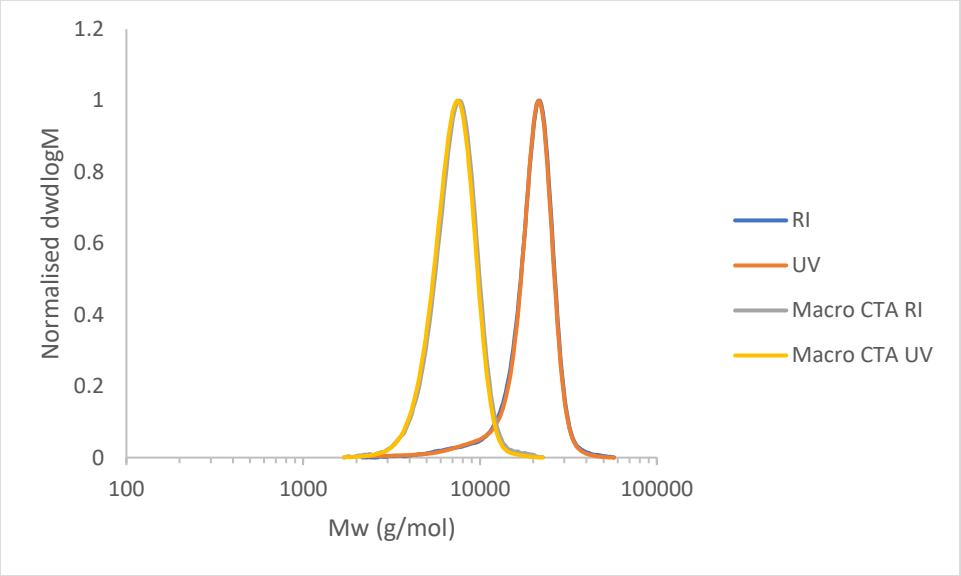
Comments: Freeze-pump-thaw technique was used to degas the solution, by doing at least 4 cycles. The polymers precipitated in hexane afterwards.

^{1}H NMR



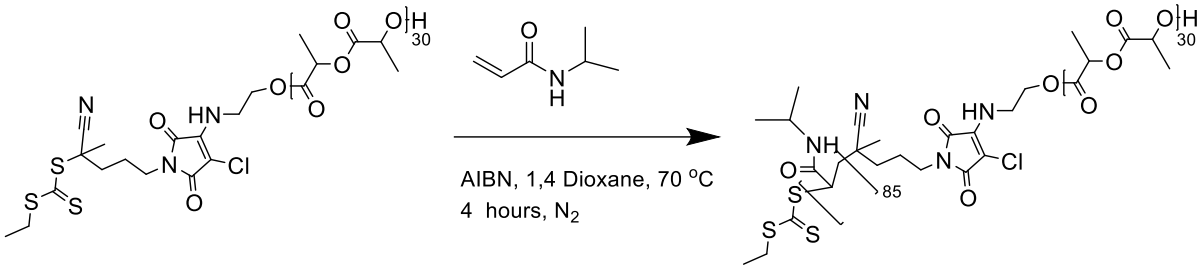
The NMR spectrum presents the degree of polymerization (DP) to be 114 as calculated by peak 6 which corresponds to 6 protons.

<u>$CHCl_3$ GPC</u>



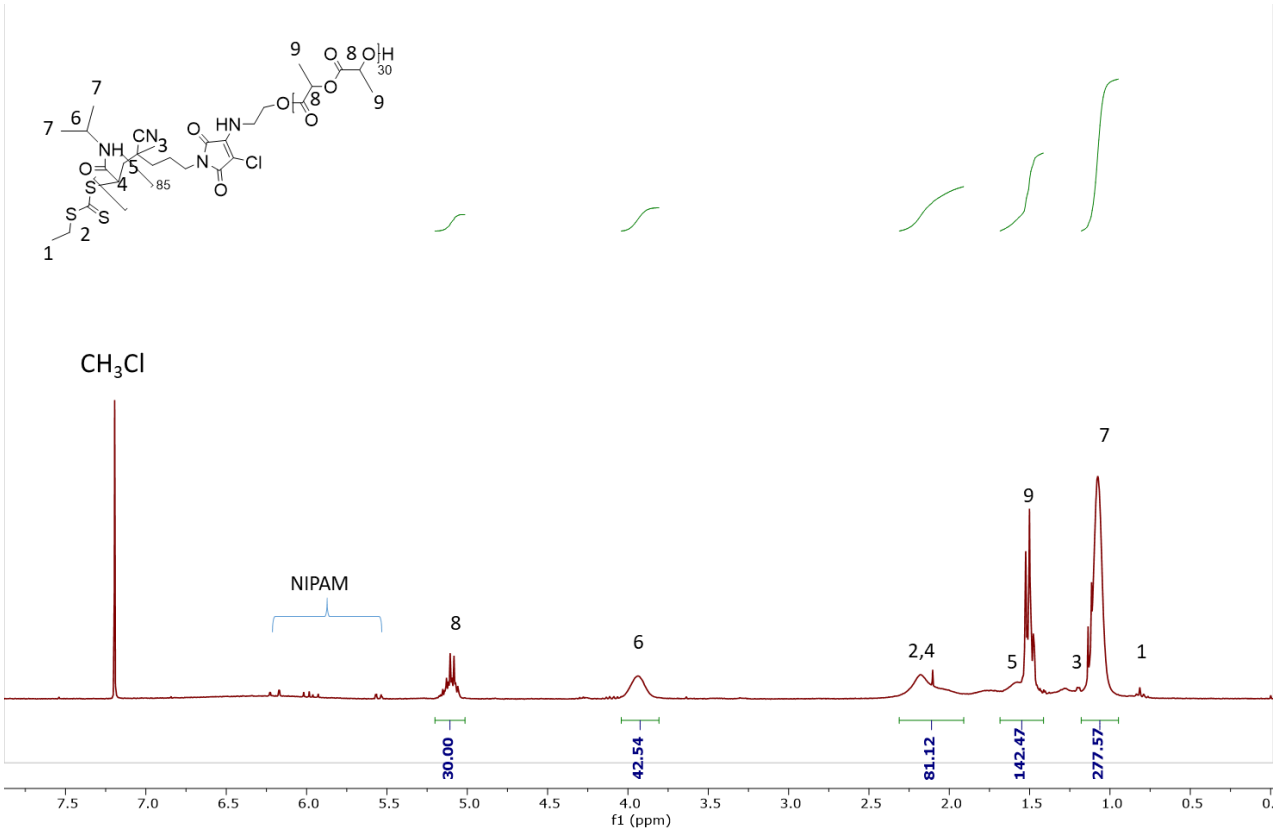
SEC analysis revealed a M_n of 18 kDa and a dispersity $Đ_M$ = 1.12 calculated from the refrective index data.

$PNIPAM_{85}$-b-$P_{D,L}LA_{30}$



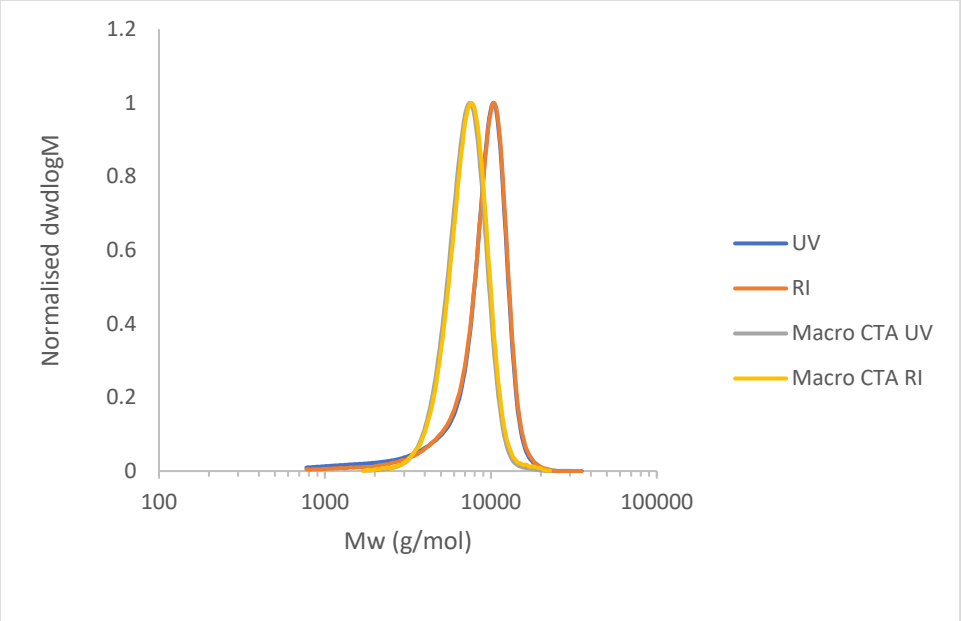
Comments: Freeze-pump-thaw technique was used to degas the solution, by doing at least 4 cycles. The polymers precipitated in hexane afterwards.

^{1}H NMR



The NMR spectrum presents the degree of polymerization (DP) to be 85 as calculated by peak 6 which corresponds to 1 proton. More precipitations are of need since we can still see monomer in the NMR.

<u>$CHCl_3$ GPC</u>



SEC analysis revealed a M_n of 8 kDa and a dispersity $Đ_M$ = 1.19 calculated from the refrective index data.

PD,LLA$_{57}$-b-PDMA$_{27}$

Synthesis as previously mentioned

^{1}H NMR

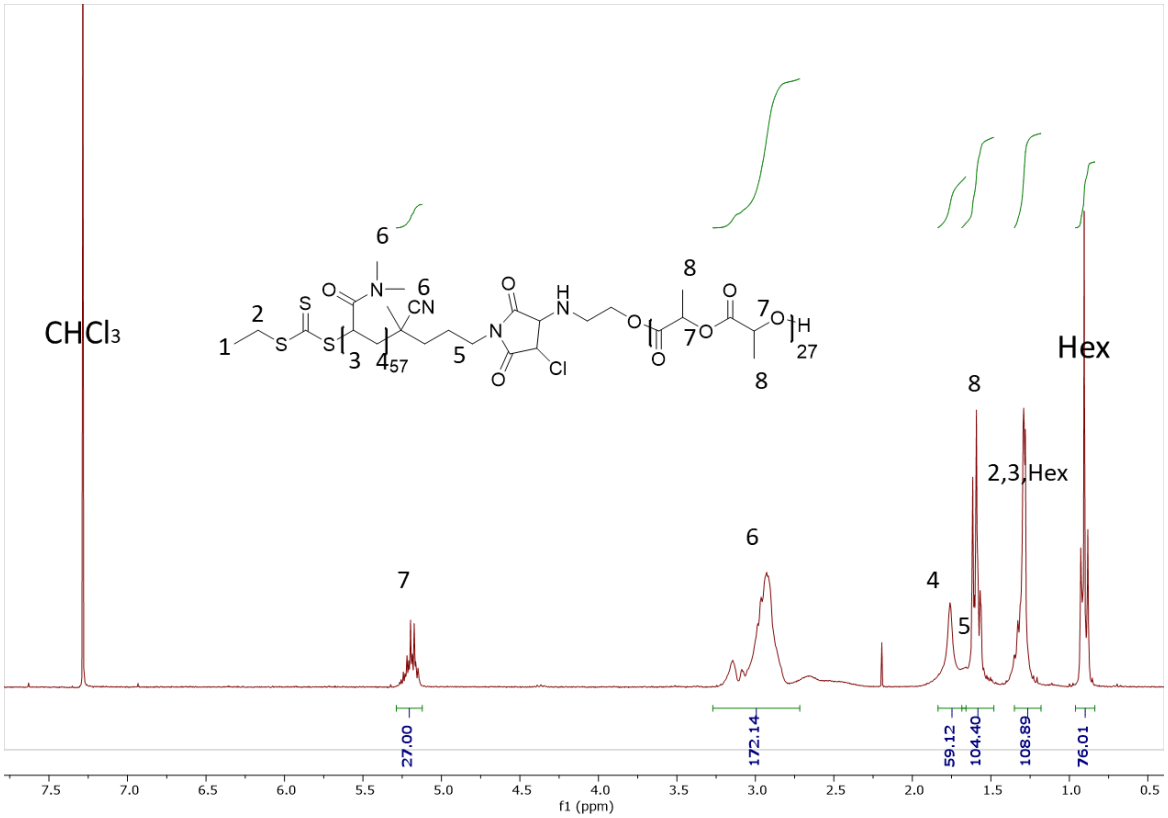


Figure 4.23 ^{1}H NMR (300MHz, $CDCl_3$) of clean. poly(D, L-lactide)27-b-poly(N,N-dimethylacrylamide)57 diblock copolymers

The NMR spectrum presents the degree of polymerization (DP) to be 57 as calculated from peak 6 which corresponds to 6 protons and from peak 7 which corresponds to 2 protons from our Macro CTA PDLLA.

$\underline{CHCl_3\ GPC}$

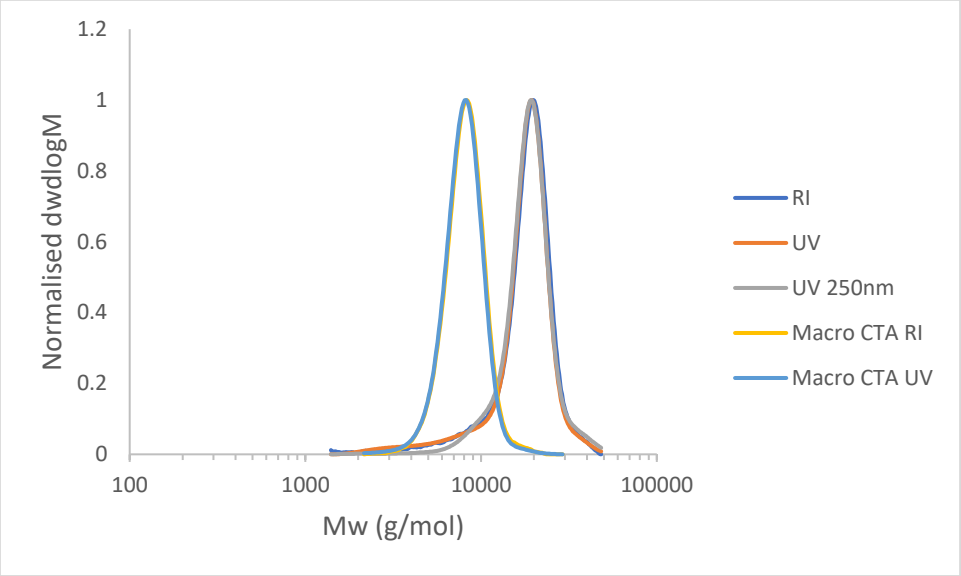


Figure 4.24.Representation of Molecular weight distribution from chloroform GPC (λ=309 nm) of poly(D, L-lactide)$_{27}$-b-poly(N,N-dimethylacrylamide)$_{57}$ diblock copolymers

SEC analysis revealed a M_n of 15 kDa and a dispersity $Đ_M$ = 1.23 calculated from the refrective index data.

$P_{DL}LA_{27}$-b- $PTEGA_{47}$ with ACM probe

Synthesis as previously mentioned.

^{1}H NMR

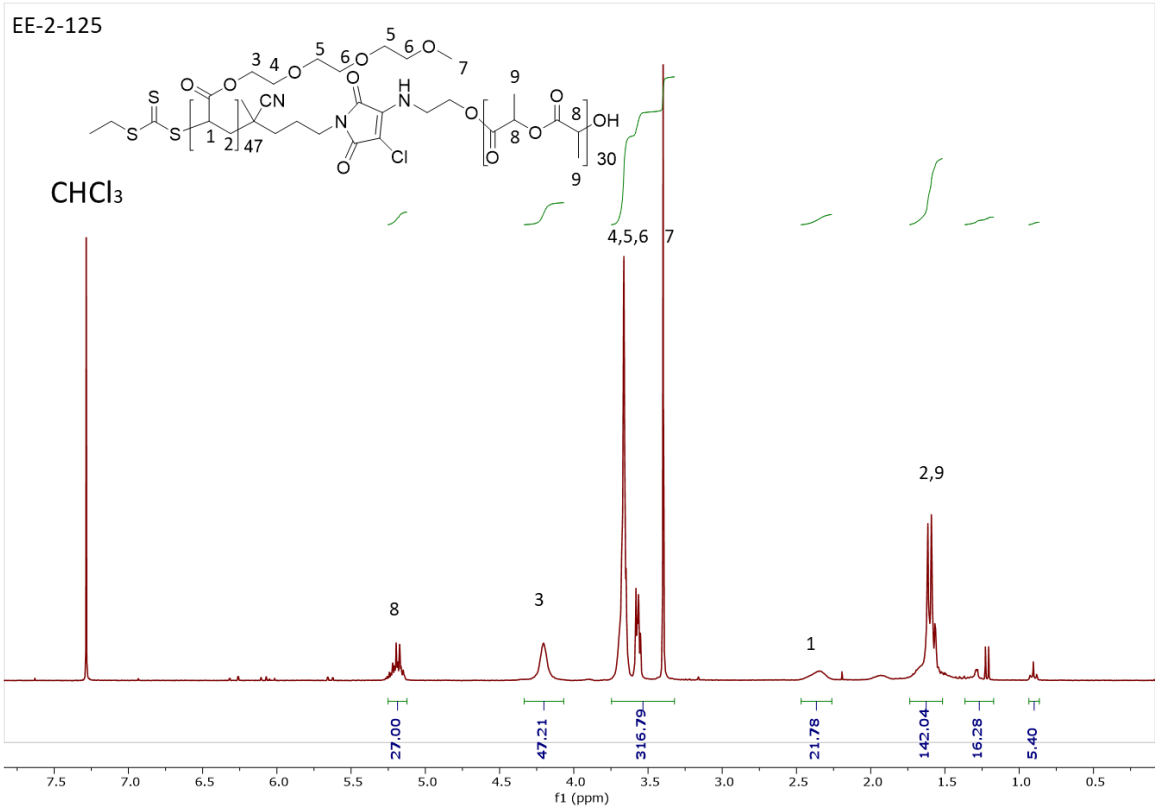


Figure 4.25. ^{1}H NMR (300MHz, $CDCl_3$) of clean. poly(D, L-lactide)$_{27}$-b-poly(TEGA) diblock copolymer.

The NMR spectrum presents the degree of polymerization (DP) to be 47 as calculated from peak 3 which corresponds to 2 protons and from peak 8 which corresponds to 2 protons from our Macro CTA PDLLA.

$CHCl_3$ GPC

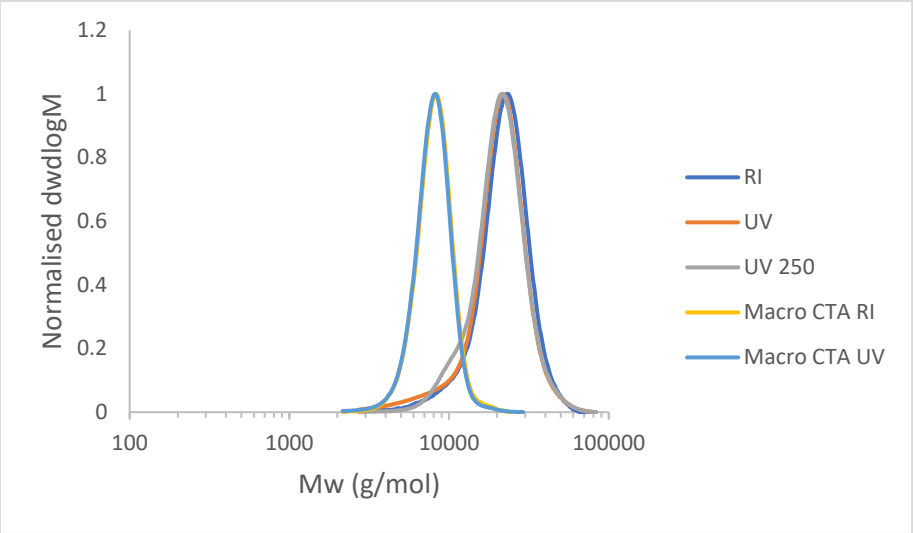
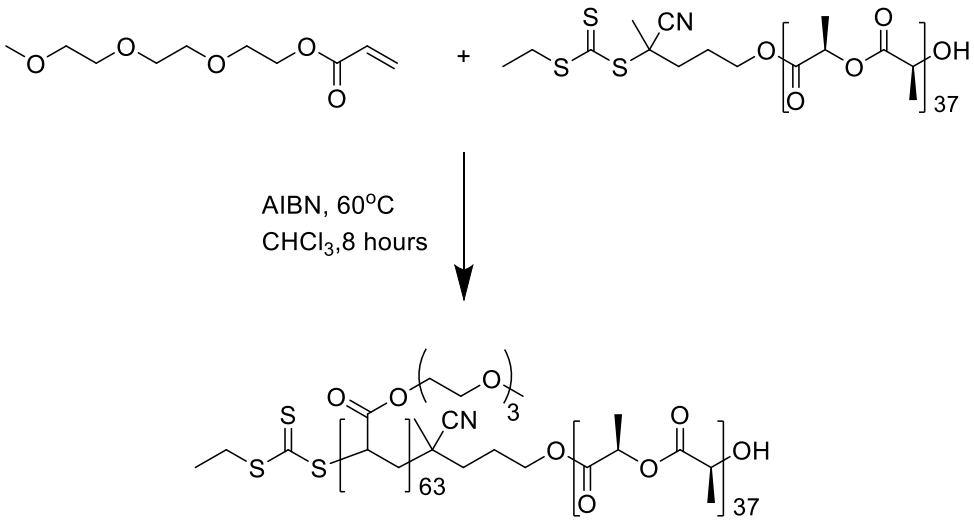


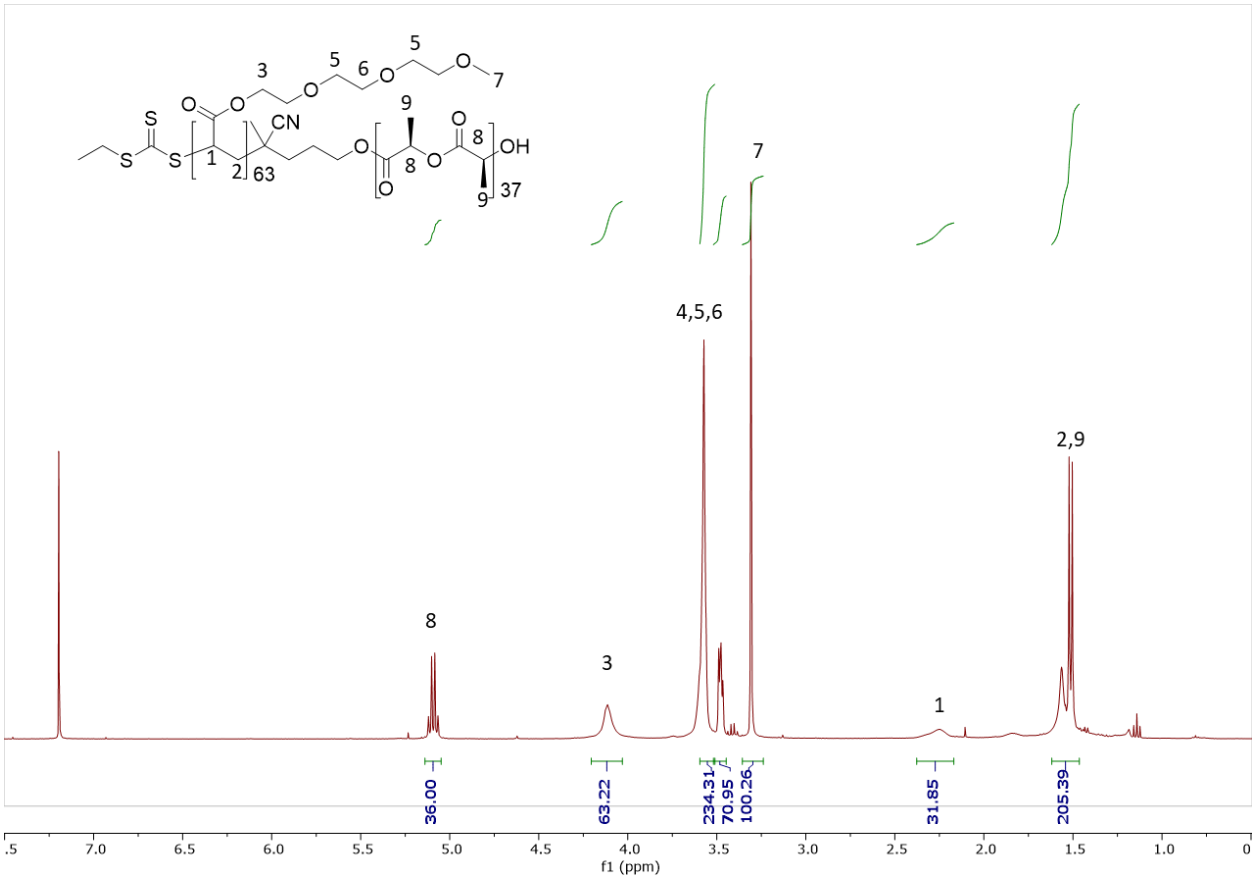
Figure 4.26. Representation of Molecular weight distribution from chloroform GPC (λ=309 nm) of poly(D, L-lactide)$_{27}$-b-poly(TEGA)$_{47}$ diblock copolymers

SEC analysis revealed a M_n of 15 kDa and a dispersity $Đ_M$ = 1.17 calculated from the refrective index data. Self-assembly and fluorescence studies will be conducted with the above diblock.

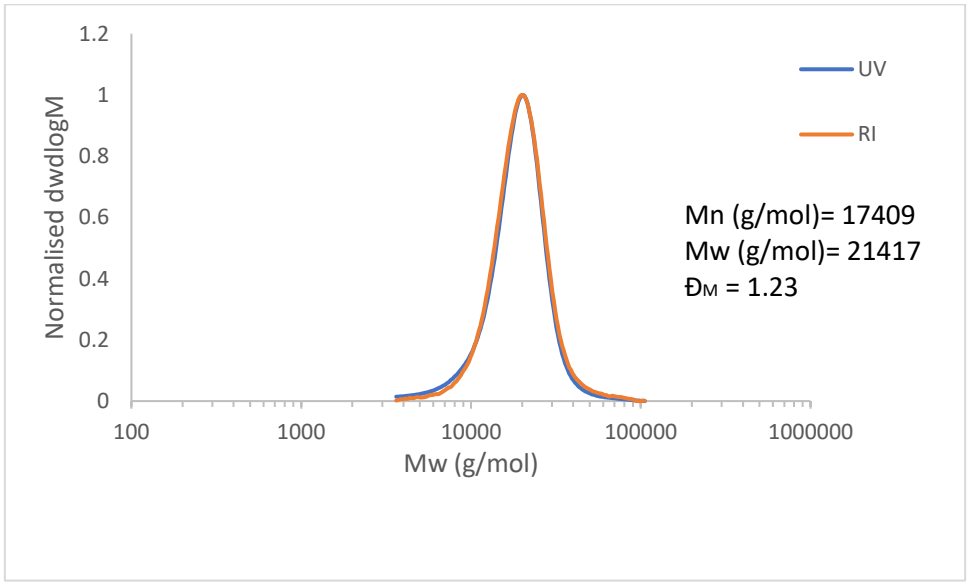
PTEGA$_{63}$-b-PLLA$_{37}$



CLEAN ^{1}H NMR



$CHCl_3$ GPC



PLLA$_{30}$-b-PDMA$_{87}$

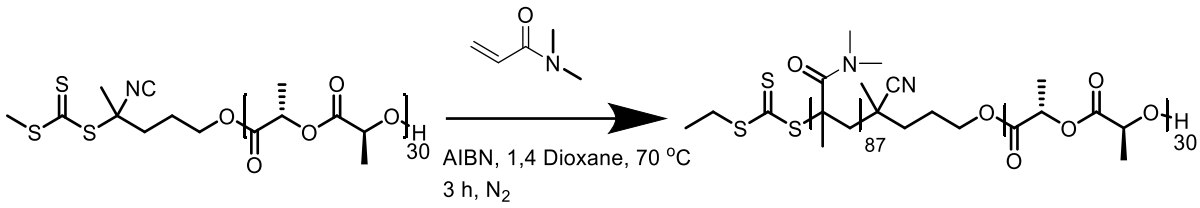


Figure 4.27.RAFT polymerization

The conversion aimed was 60% from crude NMR we get a conversion of 58%.

Reaction	Time	DP	Conversion	Mn(kDa)	Mw(kDa)	$Đ_M$
PLLA$_{30}$-b-PDMA$_{87}$ (EE88)	3 hrs	87	58 %	26	28	1.1

CLEAN ^{1}H NMR

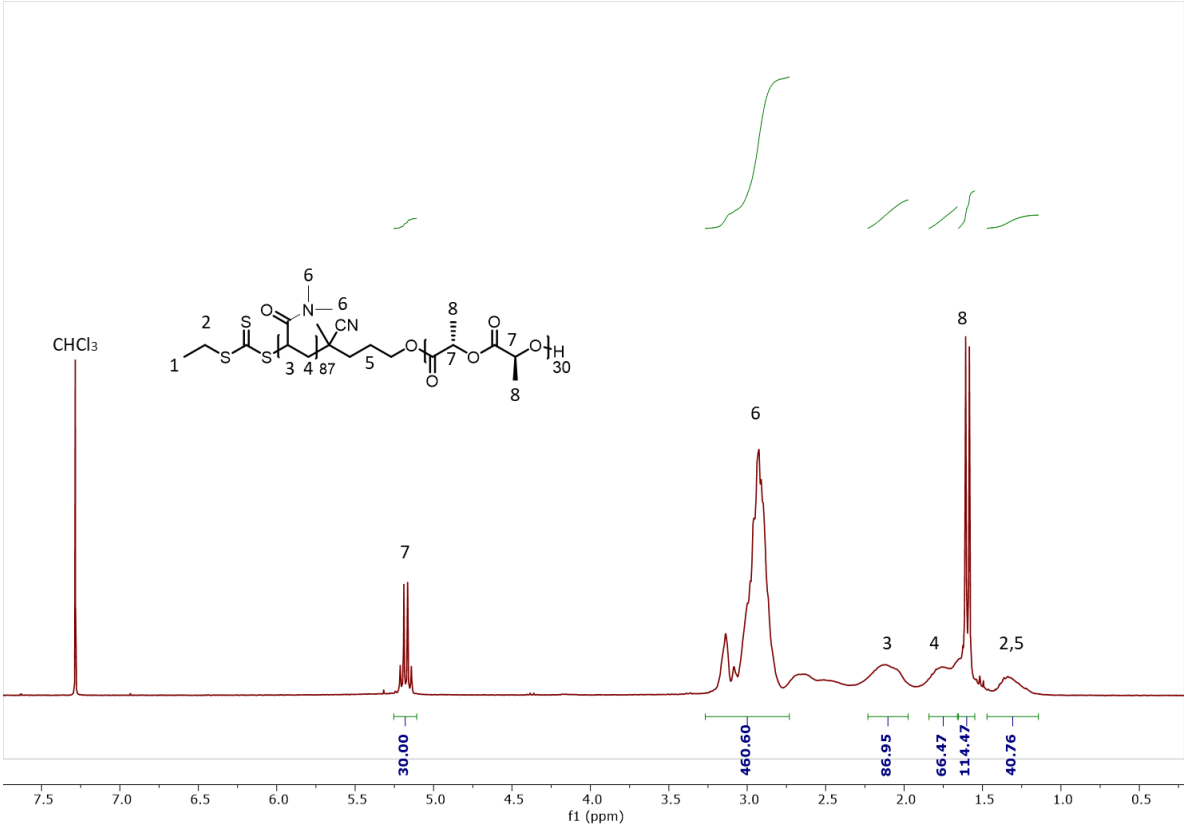


Figure 4.28. ^{1}H NMR spectra (300MHz) of clean PLLA$_{30}$-b-PDMA$_{87}$

$\underline{CHCl_3\ GPC}$

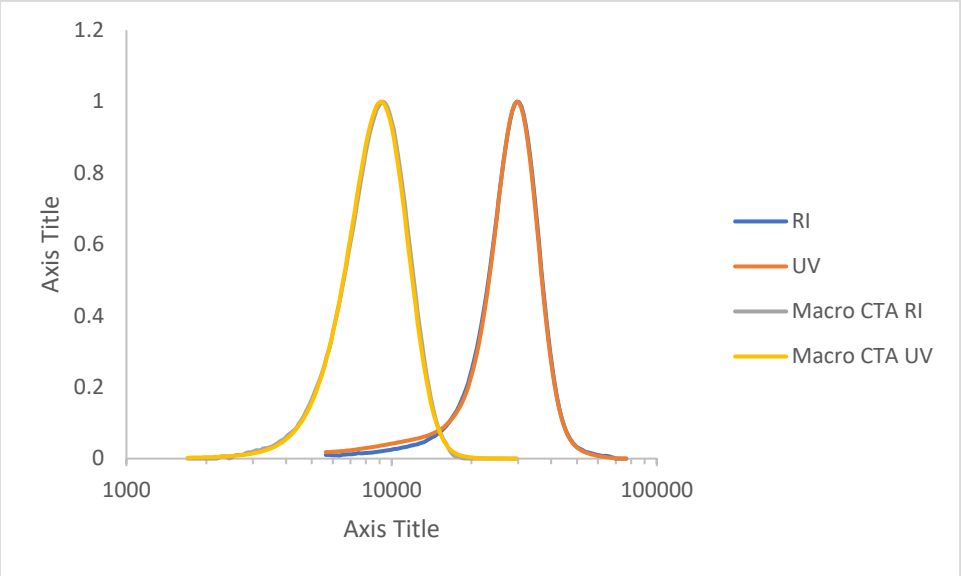


Figure 4.29. Representation of Molecular weight distribution from chloroform GPC (λ=309 nm) of poly(L-lactide)$_{30}$-b-poly(N,N-dimethylacrylamide)$_{87}$ diblock copolymers

Typical self-assembly with flash nanoprecipitation of diblock copolymers

18.2 MΩ·cm water (1 mL) was added at to a solution of diblock copolymer (2 mg) dissolved in good solvent (1 mL) using flash nanoprecipitation method while stirring intensively at 550 rpm. The solution was sealed in a 7mL vial and left stirring overnight. Afterwards the particle dispersion was dialyzed against 18.2 MΩ·cm water for 3 days (MWCO = 6-8 kDa).

Self-assembly with microfluidics system of diblock copolymers

In a syringe pump device two 1mL syringes were loaded with one containing 1mL 18.2 MΩ·cm water and the other containing a solution of dissolved diblock copolymer (2 mg) in a good solvent . The contained of both syringes was pushed through the polyethylene tubing in ratio of 1mL/min or 2mL/min.The final eluent was collected in a 7mL vial . The solution was left stirring for 2 hours before dialysed against 18.2 MΩ·cm water to remove the organic solvent for 3 days. (MWCO = 6-8 kDa).

Slow addition self-assembly of diblock copolymers

18.2 MΩ·cm water (1 mL) was added at to a solution of diblock copolymer (2 mg) dissolved in good solvent (1 mL) using a peristaltic pump at 0.5 mL hr-1. The solution was dialysed against 18.2 MΩ·cm water (MWCO = 3.5 kDa).

2.5 References

1. N. Poovaiah, Z. Davoudi, H. Peng, B. Schlichtmann, S. Mallapragada, B. Narasimhan and Q. Wang, *Nanoscale*, 2018, **10**, 16962-16983.
2. M. D. Sweeney, Z. Zhao, A. Montagne, A. R. Nelson and B. V. Zlokovic, *Physiol Rev*, 2019, **99**, 21-78.
3. E. Zenaro, G. Piacentino and G. Constantin, *Neurobiol Dis*, 2017, **107**, 41-56.
4. M. D. Sweeney, A. P. Sagare and B. V. Zlokovic, *Nat Rev Neurol*, 2018, **14**, 133-150.
5. J. Baskin, J. E. Jeon and S. J. G. Lewis, *Journal of Neurology*, 2021, **268**, 1981-1994.
6. W. M. Pardridge, *Expert Opinion on Drug Delivery*, 2016, **13**, 963-975.
7. A. Mishra, R. Kumar, J. Mishra, K. Dutta, P. Ahlawat, A. Kumar, S. Dhanasekaran, A. K. Gupta, S. Sinha, D. K. Bishi, P. K. Gupta and S. Nayak, *Journal of Drug Delivery Science and Technology*, 2023, **86**, 104694.
8. D. E. Nayab, F. U. Din, H. Ali, W. A. Kausar, S. Urooj, M. Zafar, I. Khan, K. Shabbir and G. M. Khan, *J Nanobiotechnology*, 2023, **21**, 477-493.
9. A. Janesick, S. C. Wu and B. Blumberg, *Cellular and Molecular Life Sciences*, 2015, **72**, 1559-1576.
10. S. L. B. Oliveira, M. M. Pillat, A. Cheffer, C. Lameu, T. T. Schwindt and H. Ulrich, *Cytometry Part A*, 2013, **83A**, 76-89.
11. B. Srinageshwar, M. Florendo, B. Clark, K. Johnson, N. Munro, S. Peruzzaro, A. Antcliff, M. Andrews, A. Figacz, D. Swanson, G. L. Dunbar, A. Sharma and J. Rossignol, *Pharmaceutics*, 2020, **12**, 619-631.
12. Y. Zhou, Z. Peng, E. S. Seven and R. M. Leblanc, *Journal of Controlled Release*, 2018, **270**, 290-303.
13. H. Luo and E. V. Shusta, *Pharmaceutics*, 2020, **12**, 1085.
14. C. W. Fong, *The Journal of Membrane Biology*, 2015, **248**, 651-669.
15. C. Saraiva, C. Praça, R. Ferreira, T. Santos, L. Ferreira and L. Bernardino, *Journal of Controlled Release*, 2016, **235**, 34-47.

16. R. G. R. Pinheiro, A. J. Coutinho, M. Pinheiro and A. R. Neves, *Int J Mol Sci*, 2021, **22**, 11654-11666.
17. D. Wu, Q. Chen, X. Chen, F. Han, Z. Chen and Y. Wang, *Signal Transduction and Targeted Therapy*, 2023, **8**, 217-230.
18. C. Jiang, Y. Zhou, R. Chen, M. Yang, H. Zhou, Z. Tang, H. Shi and D. Qin, *Pharmaceutics*, 2023, **15**, 2669-2678.
19. P. K. Pandey, A. K. Sharma and U. Gupta, *Tissue Barriers*, 2016, **4**, e1129476.
20. Y. Zhou, Z. Peng, E. S. Seven and R. M. Leblanc, *J Control Release*, 2018, **270**, 290-303.
21. A.-C. Lussint, *Fluids and Barriers of the CNS*, 2012, **23**, 21-32.
22. D. J. Begley, *Pharmacology & Therapeutics*, 2004, **104**, 29-45.
23. C. Saraiva, *Journal of Controlled Release*, 2016, **235**, 34-47.
24. T. Patel, *Adv Drug Deliv Rev*, 2012 May 15, **64**, 701-705.
25. D. M. Teleanu, C. Chircov, A. M. Grumezescu, A. Volceanov and R. I. Teleanu, *Pharmaceutics*, 2018, **10,** 269-285.
26. T. T. Zhang, *Biomaterial Science*, 2016, **4**, 119-129.
27. E. Nance, *J Control Release*, 2014, **189**, 123-132.
28. D. M. Teleanu, C. Chircov, A. M. Grumezescu, A. Volceanov and R. I. Teleanu, 2018, **10**, 269-285.
29. V. Cena, *Nanomedicine*, 2018, **13**, 1513-1516.
30. X. Dong, *Theranostics*, 2018, **8**, 1481-1493.
31. R. L. Roberts, R. E. Fine and A. Sandra, 1993, **104**, 521-532.
32. L. Aloe, P. Bianchi, A. De Bellis, M. Soligo and M. L. Rocco, *Neural Regen Res*, 2014, **9**, 1025-1030.
33. P. Rivera-Gil, *Accounts of chemical research*, 2013, **46**, 743–749.
34. T. C. H Ou , Y. Zhang *Acta Biomater*, 2018, **65**, 339–348
35. Y. W. Yating Zhao, Fu Ran, Yu Cui, Chang Liu, Qinfu Zhao, Yikun Gao, Da Wang & Siling Wang, *Scientific Reports*, 2017, **7**.
36. X. Li, *Journal of Drug Targeting*, 2016, **25**, 17–28.
37. C. M. Plummer, L. Li and Y. Chen, *Macromolecules*, 2023, **56**, 731-750.
38. E. Balla, V. Daniilidis, G. Karlioti, T. Kalamas, M. Stefanidou, N. D. Bikiaris, A. Vlachopoulos, I. Koumentakou and D. N. Bikiaris, *Polymers (Basel)*, 2021, **13**, 1822-1835.
39. A. Peterson, R. Hador, M. Pink, Y. Popowski, M. Kol and W. B. Tolman, *Journal of the American Chemical Society*, 2022, **144**, 20047-20055.
40. J. O. C. de França, D. da Silva Valadares, M. F. Paiva, S. C. L. Dias and J. A. Dias, *Polymers (Basel)*, 2022, **14,** 2317-2329.
41. I. Nifant'ev and P. Ivchenko, *Polymers (Basel)*, 2019, **11**, 2078.
42. A. P. Dove, *ACS Macro Letters*, 2012, **1**, 1409-1412.
43. S. Perrier, *Macromolecules*, 2017, **50**, 7433-7447.
44. A. Postma, T. P. Davis, G. Moad and M. S. O'Shea, *Macromolecules*, 2005, **38**, 5371-5374.
45. N. P. Truong, G. R. Jones, K. G. E. Bradford, D. Konkolewicz and A. Anastasaki, *Nature Reviews Chemistry*, 2021, **5**, 859-869.
46. F. M. Winnik, A. R. Davidson, G. K. Hamer and H. Kitano, *Macromolecules*, 1992, **25**, 1876-1880.
47. E. M. Todd and S. C. Zimmerman, *Journal of the American Chemical Society*, 2007, **129**, 14534-14535.
48. M. H. Stenzel, *Chemical Communications*, 2008, DOI: 10.1039/B805464A, 3486-3503.
49. K. E. B. Doncom, L. D. Blackman, D. B. Wright, M. I. Gibson and R. K. O'Reilly, *Chemical Society Reviews*, 2017, **46**, 4119-4134.
50. Y. Mai and A. Eisenberg, *Chemical Society Reviews*, 2012, **41**, 5969-5985.
51. A. Blanazs, S. P. Armes and A. J. Ryan, 2009, **30**, 267-277.

52. J. K. Oh, *Polylactide (PLA)-based amphiphilic block copolymers: Synthesis, self-assembly, and biomedical applications*, 2011, **7**, 5096-5119.
53. N. Kamaly, B. Yameen, J. Wu and O. C. Farokhzad, *Chem Rev*, 2016, **116**, 2602-2663.
54. Y. Li and D. Ju, in *Neurotoxicity of Nanomaterials and Nanomedicine*, eds. X. Jiang and H. Gao, Academic Press, 2017, **12,** pp. 285-329.
55. P. Bhargava, J. X. Zheng, P. Li, R. P. Quirk, F. W. Harris and S. Z. D. Cheng, *Macromolecules*, 2006, **39**, 4880-4888.
56. L. Zhang and A. Eisenberg, 1995, **268**, 1728-1731.
57. J. X. Zheng, H. Xiong, W. Y. Chen, K. Lee, R. M. Van Horn, R. P. Quirk, B. Lotz, E. L. Thomas, A.-C. Shi and S. Z. D. Cheng, *Macromolecules*, 2006, **39**, 641-650.
58. K. Kuperkar, D. Patel, L. I. Atanase and P. Bahadur, *Polymers (Basel)*, 2022, **14**.
59. Q. Tian, C. Fei, H. Yin and Y. Feng, *Progress in Polymer Science*, 2019, **89**, 108-132.
60. Y. H. A. Hussein and M. Youssry, *Materials (Basel)*, 2018, **11**.
61. A. Vardaxi, M. Kafetzi and S. Pispas, *Polymers (Basel)*, 2022, **14**.
62. N. J. Caggiano, S. K. Nayagam, L. Z. Wang, B. K. Wilson, P. Lewis, S. Jahangir, R. D. Priestley, R. K. Prud'homme and K. D. Ristroph, *Int J Pharm*, 2023, **640**, 122985.
63. X. Yan, J. Bernard and F. Ganachaud, *Advances in Colloid and Interface Science*, 2021, **294**, 102474.
64. J. Tao, S. F. Chow and Y. Zheng, *Acta Pharm Sin B*, 2019, **9**, 4-18.
65. J. He, X. Huang, Y.-C. Li, Y. Liu, T. Babu, M. A. Aronova, S. Wang, Z. Lu, X. Chen and Z. Nie, *Journal of the American Chemical Society*, 2013, **135**, 7974-7984.
66. W. S. Saad and R. K. Prud'homme, *Nano Today*, 2016, **11**, 212-227.
67. S. Damiati, U. B. Kompella, S. A. Damiati and R. Kodzius, *Genes (Basel)*, 2018, **9**,103-113.
68. B. G. Carvalho, B. T. Ceccato, M. Michelon, S. W. Han and L. G. de la Torre, *Pharmaceutics*, 2022, **14**,141-154.
69. B. Küçüktürkmen, W. Inam, F. Howaili, M. Gouda, N. Prabhakar, H. Zhang and J. M. Rosenholm, *Biosensors (Basel)*, 2022, **12,**181-190.
70. V. Uskoković, *Rev J Chem*, 2013, **3**, 271-303.
71. W. Xu, Y. Zheng and P. Pan, *Journal of Polymer Science*, 2022, **60**, 2136-2152.
72. R. M. Michell and A. J. Müller, *Progress in Polymer Science*, 2016, **54-55**, 183-213.
73. J. F. Kang, J. Zaccaro, A. Ulman and A. Myerson, *Langmuir*, 2000, **16**, 3791-3796.
74. P. J. Hurst, A. M. Rakowski and J. P. Patterson, *Nat Commun*, 2020, **11**, 4690.
75. M. Inam, J. C. Foster, J. Gao, Y. Hong, J. Du, A. P. Dove and R. K. O'Reilly, *Journal of Polymer Science Part A: Polymer Chemistry*, 2019, **57**, 255-259.
76. J. C. Foster, S. Varlas, B. Couturaud, Z. Coe and R. K. O'Reilly, *Journal of the American Chemical Society*, 2019, **141**, 2742-2753.
77. S. Ganda and M. H. Stenzel, *Progress in Polymer Science*, 2020, **101**, 101195.
78. W. Yu, M. Inam, J. R. Jones, A. P. Dove and R. K. O'Reilly, *Polymer Chemistry*, 2017, **8**, 5504-5512.
79. L. MacFarlane, C. Zhao, J. Cai, H. Qiu and I. Manners, *Chem Sci*, 2021, **12**, 4661-4682.
80. H. Phan, M. Cossutta, C. Houppe, C. Le Cœur, S. Prevost, I. Cascone, J. Courty, J. Penelle and B. Couturaud, *Journal of Colloid and Interface Science*, 2022, **618**, 173-184.
81. N. J. Warren and S. P. Armes, *Journal of the American Chemical Society*, 2014, **136**, 10174-10185.
82. M. S. Haider, M. M. Lübtow, S. Endres, S. Forster, V. J. Flegler, B. Böttcher, V. Aseyev, A. C. Pöppler and R. Luxenhofer, *ACS Appl Mater Interfaces*, 2020, **12**, 24531-24543.
83. P. P. Fu, Q. Xia, H. M. Hwang, P. C. Ray and H. Yu, *J Food Drug Anal*, 2014, **22**, 64-75.
84. A. Sharma, S. V. Madhunapantula and G. P. Robertson, *Expert Opin Drug Metab Toxicol*, 2012, **8**, 47-69.

85. J. M. Hillegass, A. Shukla, S. A. Lathrop, M. B. MacPherson, N. K. Fukagawa and B. T. Mossman, *Wiley Interdiscip Rev Nanomed Nanobiotechnol*, 2010, **2**, 219-231.
86. M. Niepel, M. Hafner, M. Chung and P. K. Sorger, *Curr Protoc Chem Biol*, 2017, **9**, 55-74.
87. S. J. Cameron, J. Sheng, F. Hosseinian and W. G. Willmore, *Int J Mol Sci*, 2022, **23**.
88. N. Lall, C. J. Henley-Smith, M. N. De Canha, C. B. Oosthuizen and D. Berrington, *Int J Microbiol*, 2013, **2013**, 420601.
89. Q. Mu, G. Jiang, L. Chen, H. Zhou, D. Fourches, A. Tropsha and B. Yan, *Chem Rev*, 2014, **114**, 7740-7781.
90. D. Docter, S. Strieth, D. Westmeier, O. Hayden, M. Gao, S. K. Knauer and R. H. Stauber, *Nanomedicine (Lond)*, 2015, **10**, 503-519.
91. V. H. Nguyen and B. J. Lee, *Int J Nanomedicine*, 2017, **12**, 3137-3151.
92. C. Weber, J. Simon, V. Mailänder, S. Morsbach and K. Landfester, *Acta Biomater*, 2018, **76**, 217-224.
93. W. Ma, L. Yang and L. He, *J Pharm Anal*, 2018, **8**, 147-152.
94. D. Hühn, K. Kantner, C. Geidel, S. Brandholt, I. De Cock, S. J. H. Soenen, P. Rivera_Gil, J.-M. Montenegro, K. Braeckmans, K. Müllen, G. U. Nienhaus, M. Klapper and W. J. Parak, *ACS Nano*, 2013, **7**, 3253-3263.
95. W. Huang, G. Xiao, Y. Zhang and W. Min, *Biomedicine & Pharmacotherapy*, 2021, **139**, 111541.
96. A. I. Khan, Q. Lu, D. Du, Y. Lin and P. Dutta, *Biochim Biophys Acta Gen Subj*, 2018, **1862**, 2779-2787.
97. J. Sargento-Freitas, S. Aday, C. Nunes, M. Cordeiro, A. Gouveia, F. Silva, C. Machado, B. Rodrigues, G. C. Santo, C. Ferreira, A. Amorim, S. Sousa, A. C. Gomes, M. Castelo-Branco, L. Ferreira and L. Cunha, *Neurology*, 2018, **90**, e127-e134.
98. J. Ahlawat, G. Guillama Barroso, S. Masoudi Asil, M. Alvarado, I. Armendariz, J. Bernal, X. Carabaza, S. Chavez, P. Cruz, V. Escalante, S. Estorga, D. Fernandez, C. Lozano, M. Marrufo, N. Ahmad, S. Negrete, K. Olvera, X. Parada, B. Portillo, A. Ramirez, R. Ramos, V. Rodriguez, P. Rojas, J. Romero, D. Suarez, G. Urueta, S. Viel and M. Narayan, *ACS Omega*, 2020, **5**, 12583-12595.
99. M. Heymans, R. Figueiredo, L. Dehouck, D. Francisco, Y. Sano, F. Shimizu, T. Kanda, R. Bruggmann, B. Engelhardt, P. Winter, F. Gosselet and M. Culot, *Fluids Barriers CNS*, 2020, **17**, 48-72.
100. I. Wilhelm and I. A. Krizbai, *Molecular Pharmaceutics*, 2014, **11**, 1949-1963.
101. A. Reichel, *Curr Drug Metab*, 2006, **7**, 183-203.
102. V. Berezowski, C. Landry, S. Lundquist, L. Dehouck, R. Cecchelli, M. P. Dehouck and L. Fenart, *Pharmaceutical Research*, 2004, **21**, 756-760.
103. R. Cecchelli, S. Aday, E. Sevin, C. Almeida, M. Culot, L. Dehouck, C. Coisne, B. Engelhardt, M. P. Dehouck and L. Ferreira, *PLoS One*, 2014, **9**, e99733.
104. S. Nakagawa, M. A. Deli, H. Kawaguchi, T. Shimizudani, T. Shimono, A. Kittel, K. Tanaka and M. Niwa, *Neurochem Int*, 2009, **54**, 253-263.
105. R. Booth and H. Kim, *Lab Chip*, 2012, **12**, 1784-1792.
106. M. Clemens-Hemmelmann, C. Kuffner, V. Metz, L. Kircher, U. Schmitt, C. Hiemke, R. Postina and R. Zentel, *Amphiphilic Copolymers Shuttle Drugs Across the Blood–Brain Barrier* Macromolecular bioscience, 2016.
107. C. Celia, D. Cosco, D. Paolino and M. Fresta, *Med Res Rev*, 2011, **31**, 716-756.
108. W. Zhang, A. Mehta, Z. Tong, L. Esser and N. H. Voelcker, *Adv Sci (Weinh)*, 2021, **8**, 2003937.
109. K. A. Woodrow, Y. Cu, C. J. Booth, J. K. Saucier-Sawyer, M. J. Wood and W. Mark Saltzman, *Nature Materials*, 2009, **8**, 526-533.
110. S. L. Demento, S. C. Eisenbarth, H. G. Foellmer, C. Platt, M. J. Caplan, W. Mark Saltzman, I. Mellman, M. Ledizet, E. Fikrig, R. A. Flavell and T. M. Fahmy, *Vaccine*, 2009, **27**, 3013-3021.

111. T. Patel, J. Zhou, J. M. Piepmeier and W. M. Saltzman, *Advanced Drug Delivery Reviews*, 2012, **64**, 701-705.
112. Y. Bai, F.-Y. Xie and W. Tian, *Chinese Journal of Polymer Science*, 2018, **36**, 406-416.
113. H. Liu, H. Chen, F. Cao, D. Peng, W. Chen and C. Zhang, *Polymers (Basel)*, 2019, **11**, 820.
114. A. Car, P. Baumann, J. T. Duskey, M. Chami, N. Bruns and W. Meier, *Biomacromolecules*, 2014, **15**, 3235-3245.
115. C. A. Figg, R. N. Carmean, K. C. Bentz, S. Mukherjee, D. A. Savin and B. S. Sumerlin, *Macromolecules*, 2017, **50**, 935-943.
116. N. Raval, D. Kalyane, R. Maheshwari and R. K. Tekade, in *Basic Fundamentals of Drug Delivery*, ed. R. K. Tekade, Academic Press, 2019, **5**, pp. 173-201.
117. J. C. Olivier, L. Fenart, R. Chauvet, C. Pariat, R. Cecchelli and W. Couet, *Pharm Res*, 1999, **16**, 1836-1842.
118. L. E. Freed, G. Vunjak-Novakovic, R. J. Biron, D. B. Eagles, D. C. Lesnoy, S. K. Barlow and R. Langer, *Bio/Technology*, 1994, **12**, 689-693.
119. Y. S. Yim, J.-s. Choi, G. T. Kim, C. H. Kim, T.-H. Shin, D. G. Kim and J. Cheon, *Chemical Communications*, 2012, **48**, 61-63.
120. Y. Zhu, C. Liu and Z. Pang, *Biomolecules*, 2019, **9**.
121. D. B. Vieira and L. F. Gamarra, *Int J Nanomedicine*, 2016, **11**, 5381-5414.
122. S. Whitelam and R. L. Jack, *Annu Rev Phys Chem*, 2015, **66**, 143-163.
123. P. J. Lu, E. Zaccarelli, F. Ciulla, A. B. Schofield, F. Sciortino and D. A. Weitz, *Nature*, 2008, **453**, 499-503.
124. R. Gutzler, L. Cardenas and F. Rosei, *Chemical Science*, 2011, **2**, 2290-2300.
125. C.-A. Palma, M. Bonini, T. Breiner and P. Samorì, *Advanced materials* 2009, **21**, 1383-1386.
126. W. Lu, in *Encyclopedia of Nanotechnology*, ed. B. Bhushan, Springer Netherlands, Dordrecht, 2012, DOI: 10.1007/978-90-481-9751-4_274, pp. 2371-2382.
127. M. C. Branco and J. P. Schneider, *Acta Biomater*, 2009, **5**, 817-831.
128. V. P. Torchilin, *Pharm Res*, 2007, **24**, 1-16.
129. D. Bennet and S. Kim, 2014, **8,**pp. 257-310.
130. D. J. Overstreet, H. A. Von Recum and B. L. Vernon, in *Injectable Biomaterials*, ed. B. Vernon, *Woodhead Publishing,* 2011, **6**, pp. 95-141.
131. K. M. Pustulka, A. R. Wohl, H. S. Lee, A. R. Michel, J. Han, T. R. Hoye, A. V. McCormick, J. Panyam and C. W. Macosko, *Molecular pharmaceutics*, 2013, **10**, 4367-4377.
132. X. Wang, P. Gao, Y. Yang, H. Guo and D. Wu, *Nature Communications*, 2018, **9**, 2772.
133. M. C. García, C. Aloisio, R. Onnainty and G. Ullio-Gamboa, in *Nanobiomaterials*, ed. R. Narayan, *Woodhead Publishing*, 2018, **9**, pp. 41-94.
134. Y. Xie, J. T. Husband, M. Torrent-Sucarrat, H. Yang, W. Liu and R. K. O'Reilly, *Chemical Communications*, 2018, **54**, 3339-3342.
135. A. B. Mabire, M. P. Robin, H. Willcock, A. Pitto-Barry, N. Kirby and R. K. O'Reilly, *Chemical Communications*, 2014, **50**, 11492-11495.
136. A. B. Mabire, M. P. Robin, W. D. Quan, H. Willcock, V. G. Stavros and R. K. O'Reilly, *Chem Commun (Camb)*, 2015, **51**, 9733-9736.
137. A. B. Mabire, M. P. Robin, W.-D. Quan, H. Willcock, V. G. Stavros and R. K. O'Reilly, *Chemical Communications*, 2015, **51**, 9733-9736.
138. R. Nicoară, M. Ilieș, A. Uifălean, C. A. Iuga and F. Loghin, *Applied Sciences*, 2019, **9**, 4789.
139. J. Wolfram, Y. Yang, J. Shen, A. Moten, C. Chen, H. Shen, M. Ferrari and Y. Zhao, *Colloids and Surfaces B: Biointerfaces*, 2014, **124**, 17-24.
140. M. P. Monopoli, C. Åberg, A. Salvati and K. A. Dawson, *Nature Nanotechnology*, 2012, **7**, 779-786.
141. S. Milani, F. Baldelli Bombelli, A. S. Pitek, K. A. Dawson and J. Rädler, *ACS Nano*, 2012, **6**, 2532-2541.

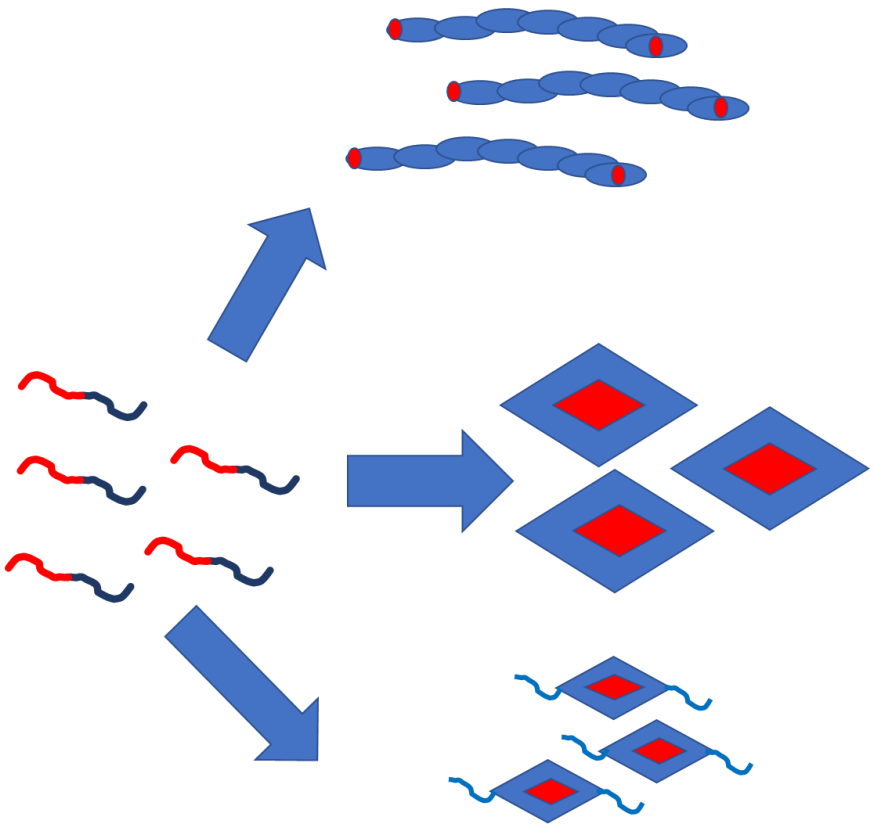
142. L. B. Nguyen VH, *Int J Nanomedicine*, 2017, **12**, 3137-3151.
143. T. Cedervall, I. Lynch, S. Lindman, T. Berggård, E. Thulin, H. Nilsson, K. A. Dawson and S. Linse, *Proceedings of the National Academy of Sciences*, 2007, **104**, 2050-2055.
144. F. Alexis, E. Pridgen, L. K. Molnar and O. C. Farokhzad, *Molecular Pharmaceutics*, 2008, **5**, 505-515.
145. Z. J. Deng, M. Liang, I. Toth, M. J. Monteiro and R. F. Minchin, *ACS Nano*, 2012, **6**, 8962-8969.
146. V. Mirshafiee, M. Mahmoudi, K. Lou, J. Cheng and M. L. Kraft, *Chemical Communications*, 2013, **49**, 2557-2559.
147. A. Kurtz-Chalot, C. Villiers, J. Pourchez, D. Boudard, M. Martini, P. N. Marche, M. Cottier and V. Forest, *Materials Science and Engineering: C*, 2017, **75**, 16-24.
148. A. Salvati, A. S. Pitek, M. P. Monopoli, K. Prapainop, F. B. Bombelli, D. R. Hristov, P. M. Kelly, C. Åberg, E. Mahon and K. A. Dawson, *Nature Nanotechnology*, 2013, **8**, 137-143.
149. Q. Dai, C. Walkey and W. C. Chan, *Angew Chem Int Ed Engl*, 2014, **53**, 5093-5096.
150. C.-Y. Sun, S. Shen, C.-F. Xu, H.-J. Li, Y. Liu, Z.-T. Cao, X.-Z. Yang, J.-X. Xia and J. Wang, *Journal of the American Chemical Society*, 2015, **137**, 15217-15224.
151. I. García, A. Sánchez-Iglesias, M. Henriksen-Lacey, M. Grzelczak, S. Penadés and L. M. Liz-Marzán, *Journal of the American Chemical Society*, 2015, **137**, 3686-3692.
152. F. Xu, M. Reiser, X. Yu, S. Gummuluru, L. Wetzler and B. M. Reinhard, *ACS Nano*, 2016, **10**, 1189-1200.
153. M. Inam, G. Cambridge, A. Pitto-Barry, Z. P. L. Laker, N. R. Wilson, R. T. Mathers, A. P. Dove and R. K. O'Reilly, *Chemical Science*, 2017, **8**, 4223-4230.
154. M. Inam, J. R. Jones, M. M. Pérez-Madrigal, M. C. Arno, A. P. Dove and R. K. O'Reilly, *ACS Central Science*, 2018, **4**, 63-70.
155. N. Petzetakis, A. P. Dove and R. K. O'Reilly, *Chemical Science*, 2011, **2**, 955-960.
156. N. Petzetakis, D. Walker, A. P. Dove and R. K. O'Reilly, *Soft Matter*, 2012, **8**, 7408-7414.
157. A. Pitto-Barry, N. Kirby, A. P. Dove and R. K. O'Reilly, *Polymer Chemistry*, 2014, **5**, 1427-1436.
158. L. Sun, A. Pitto-Barry, N. Kirby, T. L. Schiller, A. M. Sanchez, M. A. Dyson, J. Sloan, N. R. Wilson, R. K. O'Reilly and A. P. Dove, *Nature Communications*, 2014, **5**, 5746.
159. L. Sun, N. Petzetakis, A. Pitto-Barry, T. L. Schiller, N. Kirby, D. J. Keddie, B. J. Boyd, R. K. O'Reilly and A. P. Dove, *Macromolecules*, 2013, **46**, 9074-9082.
160. I. Andreana, V. Bincoletto, M. Manzoli, F. Rodà, V. Giarraputo, P. Milla, S. Arpicco and B. Stella, *Materials (Basel)*, 2023, **16,** 1212-1226.
161. E. Trenkenschuh and W. Friess, *European Journal of Pharmaceutics and Biopharmaceutics*, 2021, **165**, 345-360.
162. T. Chen, X. Zhao and Y. Weng, *Front Chem*, 2022, **10**, 1107620.
163. N. Petzetakis, M. P. Robin, J. P. Patterson, E. G. Kelley, P. Cotanda, P. H. Bomans, N. A. Sommerdijk, A. P. Dove, T. H. Epps, 3rd and R. K. O'Reilly, *ACS Nano*, 2013, **7**, 1120-1128.
164. M. Oyo and Y. Masaaki, 1967, **40**, 2380-2382.
165. R. Augustine, A. Hasan, R. Primavera, R. J. Wilson, A. S. Thakor and B. D. Kevadiya, *Materials Today Communications*, 2020, **25**, 101692.
166. L. Johnson, D. M. Gray, E. Niezabitowska and T. O. McDonald, *Nanoscale*, 2021, **13**, 7879-7896.
167. C. Zhu and J. Nicolas, *Biomacromolecules*, 2022, **23**, 3043-3080.
168. L. MacFarlane, C. Zhao, J. Cai, H. Qiu and I. Manners, *Chemical Science*, 2021, **12**, 4661-4682.
169. M. C. Arno, M. Inam, Z. Coe, G. Cambridge, L. J. Macdougall, R. Keogh, A. P. Dove and R. K. O'Reilly, *Journal of the American Chemical Society*, 2017, **139**, 16980-16985.
170. X. He, Y. He, M.-S. Hsiao, R. L. Harniman, S. Pearce, M. A. Winnik and I. Manners, *Journal of the American Chemical Society*, 2017, **139**, 9221-9228.
171. M. Brzeziński and T. Biela, *Polymer International*, 2015, **64**, 1667-1675.

172. G. C. Sosso, J. Chen, S. J. Cox, M. Fitzner, P. Pedevilla, A. Zen and A. Michaelides, *Chem Rev*, 2016, **116**, 7078-7116.
173. U. Tritschler, S. Pearce, J. Gwyther, G. R. Whittell and I. Manners, *Macromolecules*, 2017, **50**, 3439-3463.
174. E. Capuana, F. Lopresti, M. Ceraulo and V. La Carrubba, *Polymers (Basel)*, 2022, **14**, 1153
175. J. R. Finnegan, X. He, S. T. G. Street, J. D. Garcia-Hernandez, D. W. Hayward, R. L. Harniman, R. M. Richardson, G. R. Whittell and I. Manners, *Journal of the American Chemical Society*, 2018, **140**, 17127-17140.
176. H.-x. Lin, Z.-c. Lei, Z.-y. Jiang, C.-p. Hou, D.-y. Liu, M.-m. Xu, Z.-q. Tian and Z.-x. Xie, *Journal of the American Chemical Society*, 2013, **135**, 9311-9314.
177. N. Baig, I. Kammakakam and W. Falath, *Materials Advances*, 2021, **2**, 1821-1871.
178. A. Mattei, R. S. Hong, H. Dietrich, D. Firaha, J. Helfferich, Y. M. Liu, K. Sasikumar, N. S. Abraham, R. Miglani Bhardwaj, M. A. Neumann and A. Y. Sheikh, *Journal of Chemical Theory and Computation*, 2022, **18**, 5725-5738.
179. M. Karimi, P. S. Zangabad, F. Mehdizadeh, H. Malekzad, A. Ghasemi, S. Bahrami, H. Zare, M. Moghoofei, A. Hekmatmanesh and M. R. Hamblin, *Nanoscale*, 2017, **9**, 1356-1392.
180. S. Yadav, A. K. Sharma and P. Kumar, *Front Bioeng Biotechnol*, 2020, **8**, 127.
181. F. C. Meldrum and C. O'Shaughnessy, *Advanced Materials*, 2020, **32**, 2001068.
182. C. E. Ellis, J. D. Garcia-Hernandez and I. Manners, *Journal of the American Chemical Society*, 2022, **144**, 20525-20538.
183. Y. Fu and W. J. Kao, *Expert Opin Drug Deliv*, 2010, **7**, 429-444.
184. Y. Qiao and Y. Men, *Macromolecules*, 2017, **50**, 5490-5497.
185. W. Zhou, S. Z. D. Cheng, S. Putthanarat, R. K. Eby, D. H. Reneker, B. Lotz, S. Magonov, E. T. Hsieh, R. G. Geerts, S. J. Palackal, G. R. Hawley and M. B. Welch, *Macromolecules*, 2000, **33**, 6861-6868.
186. a. B. L. Stephen Z. D. Cheng, *Philosophical Transactions: Mathematical, Physical and Engineering Sciences*, 2003,**156**, 517–537.
187. J. Yang, T. Zhao, Y. Zhou, L. Liu, G. Li, E. Zhou and X. Chen, *Macromolecules*, 2007, **40**, 2791-2797.
188. C. Yang, Z.-X. Li and J.-T. Xu, *Journal of Polymer Science*, 2022, **60**, 2153-2174.
189. C. Park, C. De Rosa, L. J. Fetters and E. L. Thomas, *Macromolecules*, 2000, **33**, 7931-7938.
190. Y. Gong, W. Song, Y. Wu, D. Zhang, Y. Liu, Q. Zhao, M. He and X. Chen, *Polymers and Polymer Composites*, 2019, **28**, 77-88.
191. Y. Zhu, L. Han, H. Fan, M. Wang, R. Qi, Y. Zhao and F. He, *Macromolecules*, 2020, **53**, 3217-3223.
192. M. Awashra and P. Młynarz, *Nanoscale Advances*, 2023, **5**, 2674-2723.
193. M. Inam, J. R. Jones, M. M. Pérez-Madrigal, M. C. Arno, A. P. Dove and R. K. O'Reilly, *ACS Cent Sci*, 2018, **4**, 63-70.
194. E. G. Knox, M. R. Aburto, G. Clarke, J. F. Cryan and C. M. O'Driscoll, *Mol Psychiatry*, 2022, **27**, 2659-2673.
195. M. Brust, O. Aouane, M. Thiébaud, D. Flormann, C. Verdier, L. Kaestner, M. W. Laschke, H. Selmi, A. Benyoussef, T. Podgorski, G. Coupier, C. Misbah and C. Wagner, *Scientific Reports*, 2014, **4**, 4348-4369.
196. A. E. Nel, L. Mädler, D. Velegol, T. Xia, E. M. Hoek, P. Somasundaran, F. Klaessig, V. Castranova and M. Thompson, *Nat Mater*, 2009, **8**, 543-557.
197. M. Jiang, J. D. Olarte-Plata and F. Bresme, *The Journal of Chemical Physics*, 2022, **4,** 044701.
198. Q. Wei, T. Becherer, S. Angioletti-Uberti, J. Dzubiella, C. Wischke, A. T. Neffe, A. Lendlein, M. Ballauff and R. Haag, *Angewandte Chemie International Edition*, 2014, **53**, 8004-8031.
199. J. W. Chang, A. Armaou and R. M. Rioux, *The Journal of Physical Chemistry B*, 2021, **125**, 8075-8087.

200. M. Winiewska, E. Bugajska and J. Poznański, *PLoS One*, 2017, **12**, e0173260.
201. V. K. Srivastava and R. Yadav, in *Data Processing Handbook for Complex Biological Data Sources*, ed. G. Misra, Academic Press, 2019, **4**, pp. 125-137.
202. F. Villanueva-Flores, A. Castro-Lugo, O. T. Ramírez and L. A. Palomares, *Nanotechnology*, 2020, **31**, 132002.
203. M. Inam, G. Cambridge, A. Pitto-Barry, Z. P. L. Laker, N. R. Wilson, R. T. Mathers, A. P. Dove and R. K. O'Reilly, *Chem Sci*, 2017, **8**, 4223-4230.
204. C. Sinturel, M. Vayer, R. Erre and H. Amenitsch, *European Polymer Journal*, 2009, **45**, 2505-2512.
205. T. Vilgis and A. Halperin, *Macromolecules*, 1991, **24**, 2090-2095.
206. L. R. MacFarlane, X. Li, C. F. J. Faul and I. Manners, *Macromolecules*, 2021, **54**, 11269-11280.
207. Y. He, J.-C. Eloi, R. L. Harniman, R. M. Richardson, G. R. Whittell, R. T. Mathers, A. P. Dove, R. K. O'Reilly and I. Manners, *Journal of the American Chemical Society*, 2019, **141**, 19088-19098.
208. Z. Liu, H. Fan, W. Li, G. Bai, X. Li, N. Zhao, J. Xu, F. Zhou, X. Guo, B. Dai, E. Benassi and X. Jia, *Nanoscale*, 2019, **11**, 4751-4758.
209. Y. Chen, L. Wang, W. Chen, C. Zhong, S. Li, J. Shao, G. Li and H. Hou, *CrystEngComm*, 2022, **24**, 3903-3912.
210. J. Sun, Z. Hong, L. Yang, Z. Tang, X. Chen and X. Jing, *Polymer*, 2004, **45**, 5969-5977.
211. R. V. Castillo and A. J. Müller, *Progress in Polymer Science*, 2009, **34**, 516-560.
212. N. Petzetakis, M. P. Robin, J. P. Patterson, E. G. Kelley, P. Cotanda, P. H. H. Bomans, N. A. J. M. Sommerdijk, A. P. Dove, T. H. Epps, III and R. K. O'Reilly, *ACS Nano*, 2013, **7**, 1120-1128.
213. M. Jafari and F. Mehrnejad, *PLoS One*, 2016, **11**, e0165213.
214. P. Ferraboschi, S. Ciceri and P. Grisenti, *Antibiotics (Basel)*, 2021, **10**, 1534-1550
215. G. Bashiri, M. S. Padilla, K. L. Swingle, S. J. Shepherd, M. J. Mitchell and K. Wang, *Lab Chip*, 2023, **23**, 1432-1466.
216. N. J. Warren, O. O. Mykhaylyk, D. Mahmood, A. J. Ryan and S. P. Armes, *Journal of the American Chemical Society*, 2014, **136**, 1023-1033.
217. B. Charleux, G. Delaittre, J. Rieger and F. D'Agosto, *Macromolecules*, 2012, **45**, 6753-6765.
218. H. Phan, V. Taresco, J. Penelle and B. Couturaud, *Biomaterials Science*, 2021, **9**, 38-50.
219. N. J. W. Penfold, J. Yeow, C. Boyer and S. P. Armes, *ACS Macro Letters*, 2019, **8**, 1029-1054.
220. M. J. Derry, L. A. Fielding and S. P. Armes, *Progress in Polymer Science*, 2016, **52**, 1-18.
221. J. Wan, B. Fan and S. H. Thang, *Chem Sci*, 2022, **13**, 4192-4224.
222. P.-E. Millard, L. Barner, M. H. Stenzel, T. P. Davis, C. Barner-Kowollik and A. H. E. Müller, *Macromolecular Rapid Communications*, 2006, **27**, 821-828.
223. M. Y. Khan, M.-S. Cho and Y.-J. Kwark, *Macromolecules*, 2014, **47**, 1929-1934.
224. Y. Ma, P. Gao, Y. Ding, L. Huang, L. Wang, X. Lu and Y. Cai, *Macromolecules*, 2019, **52**, 1033-1041.
225. S. L. Brown, C. M. Rayner, S. Graham, A. Cooper, S. Rannard and S. Perrier, *Chem Commun (Camb)*, 2007, **21**, 2145-2147.
226. J. Yeow and C. Boyer, *Adv Sci (Weinh)*, 2017, **4**, 1700137.
227. L. D. Blackman, K. E. B. Doncom, M. I. Gibson and R. K. O'Reilly, *Polymer Chemistry*, 2017, **8**, 2860-2871.
228. W. M. Pardridge, *J Drug Target*, 2010, **18**, 157-167.
229. J. Kreuter, *J Microencapsul*, 2013, **30**, 49-54.
230. J. Samal, A. L. Rebelo and A. Pandit, *Adv Drug Deliv Rev*, 2019, **148**, 68-145.
231. T. Patel, J. Zhou, J. M. Piepmeier and W. M. Saltzman, *Adv Drug Deliv Rev*, 2012, **64**, 701-705.
232. M. Vert, Y. Doi, K.-H. Hellwich, M. Hess, P. Hodge, P. Kubisa, M. Rinaudo and F. Schué, *Pure and Applied Chemistry*, 2012, **84**, 377-410.

233. T. T. Zhang, W. Li, G. Meng, P. Wang and W. Liao, *Biomater Sci*, 2016, **4**, 219-229.
234. S. Aday, R. Cecchelli, D. Hallier-Vanuxeem, M. P. Dehouck and L. Ferreira, *Trends in Biotechnology*, 2016, **34**, 382-393.
235. C. D. Kuhnline Sloan, P. Nandi, T. H. Linz, J. V. Aldrich, K. L. Audus and S. M. Lunte, *Annu Rev Anal Chem (Palo Alto Calif)*, 2012, **5**, 505-531.
236. S. J. Parkinson, S. Tungsirisurp, C. Joshi, B. L. Richmond, M. L. Gifford, A. Sikder, I. Lynch, R. K. O'Reilly and R. M. Napier, *Nature Communications*, 2022, **13**, 7385-7399.
237. S. Varlas, R. Keogh, Y. Xie, S. L. Horswell, J. C. Foster and R. K. O'Reilly, *Journal of the American Chemical Society*, 2019, **141**, 20234-20248.
238. M. Weiss, J. Fan, M. Claudel, T. Sonntag, P. Didier, C. Ronzani, L. Lebeau and F. Pons, *Journal of Nanobiotechnology*, 2021, **19**, 5.
239. J. K. Patra, G. Das, L. F. Fraceto, E. V. R. Campos, M. d. P. Rodriguez-Torres, L. S. Acosta-Torres, L. A. Diaz-Torres, R. Grillo, M. K. Swamy, S. Sharma, S. Habtemariam and H.-S. Shin, *Journal of Nanobiotechnology*, 2018, **16**, 71.
240. H. Xu, S. Li and Y.-S. Liu, *Signal Transduction and Targeted Therapy*, 2022, **7**, 231.
241. S. Saha, N. Sachivkina, A. Karamyan, E. Novikova and T. Chubenko, *Biomedicines*, 2024, **12**.
242. H. Sun, C. Jiang, L. Wu, X. Bai and S. Zhai, *Front Bioeng Biotechnol*, 2019, **7**, 414.
243. P. Khanna, C. Ong, B. H. Bay and G. H. Baeg, *Nanomaterials (Basel)*, 2015, **5**, 1163-1180.
244. T. Kowada, H. Maeda and K. Kikuchi, *Chemical Society Reviews*, 2015, **44**, 4953-4972.
245. S. J. Byard, M. Williams, B. E. McKenzie, A. Blanazs and S. P. Armes, *Macromolecules*, 2017, **50**, 1482-1493.
246. D. Bartczak and A. G. Kanaras, *Langmuir*, 2011, **27**, 10119-10123.
247. L. D. Field, S. A. Walper, K. Susumu, E. Oh, I. L. Medintz and J. B. Delehanty, *Sensors*, 2015, **15**, 30457-30468.
248. A. S. Pitek, D. O'Connell, E. Mahon, M. P. Monopoli, F. B. Bombelli and K. A. Dawson, *PLOS ONE*, 2012, **7**, e40685.
249. K. Amornwachirabodee, S. Khramchantuk, P. Pienpinijtham, N. Israsena, T. Palaga and S. Wanichwecharungruang, *ACS Omega*, 2018, **3**, 6833-6840.
250. G. D. Byrne, D. Vllasaliu, F. H. Falcone, M. G. Somekh and S. Stolnik, *Molecular Pharmaceutics*, 2015, **12**, 3862-3870.
251. V. Capella, R. E. Rivero, A. C. Liaudat, L. E. Ibarra, D. A. Roma, F. Alustiza, F. Mañas, C. A. Barbero, P. Bosch, C. R. Rivarola and N. Rodriguez, *Heliyon*, 2019, **5**, e01474.
252. H. Yu, Y. Zou, Y. Wang, X. Huang, G. Huang, B. D. Sumer, D. A. Boothman and J. Gao, *ACS Nano*, 2011, **5**, 9246-9255.
253. S. Mazumdar, D. Chitkara and A. Mittal, *Acta Pharmaceutica Sinica B*, 2021, **11**, 903-924.
254. M. S. Khan, N. S. Dosoky and J. D. Williams, *Int J Mol Sci*, 2013, **14**, 21561-21597.
255. W. Au - Zhao, L. Au - Han, Y. Au - Bae and D. S. Au - Manickam, *JoVE*, 2019, DOI: doi:10.3791/58900, e58900.
256. X. Wang, J. Iqbal, D. Rahmat and A. Bernkop-Schnürch, *Int J Pharm*, 2012, **438**, 217-224.
257. F. Leve, D. P. Bonfim, G. Fontes and J. A. Morgado-Díaz, *Nanomedicine*, 2019, **14**, 1565-1578.
258. J. Gavard, *Cell Adh Migr*, 2014, **8**, 158-164.
259. A. Prlj, L. Vannay and C. Corminboeuf, *Helvetica Chimica Acta*, 2017, **100**, e1700093.
260. M. G. Paez-Segala, M. G. Sun, G. Shtengel, S. Viswanathan, M. A. Baird, J. J. Macklin, R. Patel, J. R. Allen, E. S. Howe, G. Piszczek, H. F. Hess, M. W. Davidson, Y. Wang and L. L. Looger, *Nature Methods*, 2015, **12**, 215-218.
261. S. B. Keel, R. Doty, L. Liu, E. Nemeth, S. Cherian, T. Ganz and J. L. Abkowitz, *Exp Hematol*, 2015, **43**, 469-478.e466.
262. B. Srinivasan, A. R. Kolli, M. B. Esch, H. E. Abaci, M. L. Shuler and J. J. Hickman, *J Lab Autom*, 2015, **20**, 107-126.
263. A. M. Butt, H. C. Jones and N. J. Abbott, *J Physiol*, 1990, **429**, 47-62.

CHAPTER 3-Crystallization Driven Self-assembly of Diblock Copolymers



3.1 Introduction

The literature has shown that size, morphology and surface charge of the nanoparticles are all key parameters for achieving efficient delivery to the CNS. Larger particles are unable to pass through the extracellular space in the brain, [23, 24] according to several studies, most notably Saraiva *et al.* [15, 23], which stated that only nanoparticles with diameters smaller than 100 nm can permeate the blood-brain barrier. In contrast, Cena *et al.* indicated that nanoparticles up to 200 nm diameter can be internalised by endocytosis [29] and can penetrate due to the enhanced permeability. [30]

Saraiva *et al.* also, demonstrated that rod-like nanoparticles have improved cellular uptake efficiency compared to other nanoparticle morphologies.[23] In contrast to this, Rivera *et al.* reported a comparison between spherical and rod-like nanoparticles of a similar size, where the nanospheres had the best cellular uptake [33]. Overall, creation of nanospheres requires a simpler synthetic route and allows more control over final size, but results in shorter blood circulation times [35]. Only a small number of studies have been conducted, investigating the effect of multiple structures according to their permeation ability of the BBB. Overall, elongated microstructures exhibit higher retention times than spherical nanoparticles, which may facilitate the endocytosis or transcytosis.[165]

When a block copolymer is dissolved in a solvent that is selective for one of the blocks, or when it is polymerized in a selective solvent for one of the blocks, self-assembly occurs.[166] The resultant micellar morphology is often determined by a balancing of energies associated with corona solvation and core block chain packing. Various morphologies can arise from the above process such as the design of closed structures like vesicles and cylinders which is considered common in comparison with more challenging 2D morphologies.[157] 2D nanomaterials have a high aspect ratio with free-standing sheet formation, that can be used as additives in tissue engineering applications.

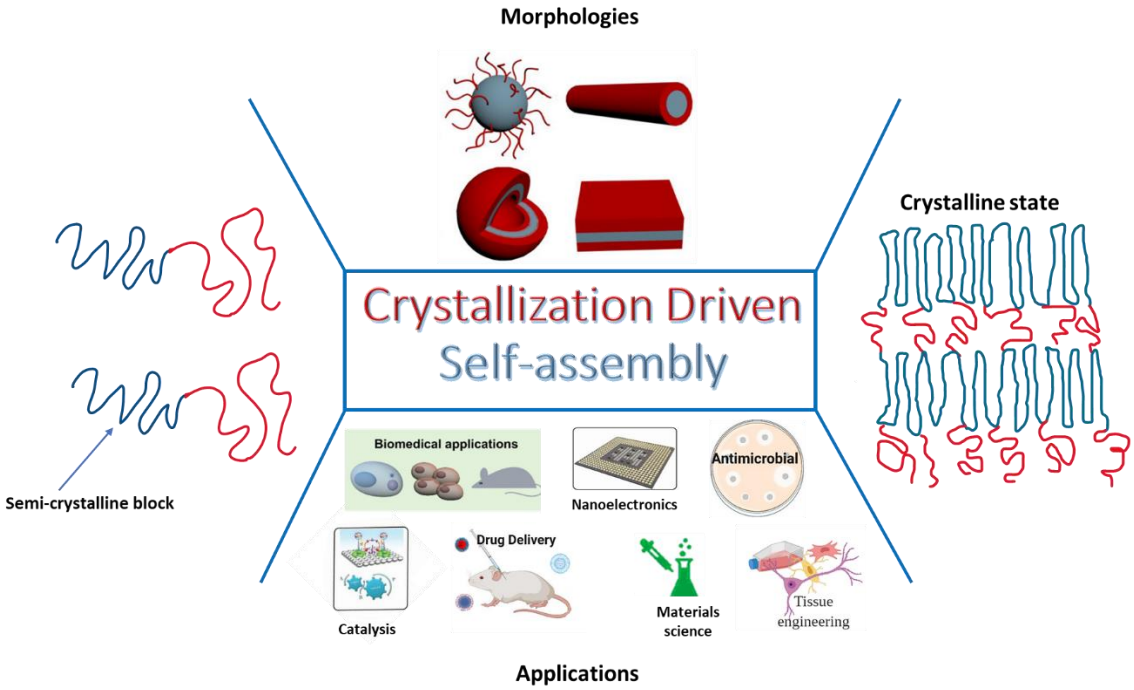


Figure 3.1.1. Crystallization Driven Self-Assembly (CDSA) morphologies and applications[167] (figure adapted with permission from C. Zhu *et al*)

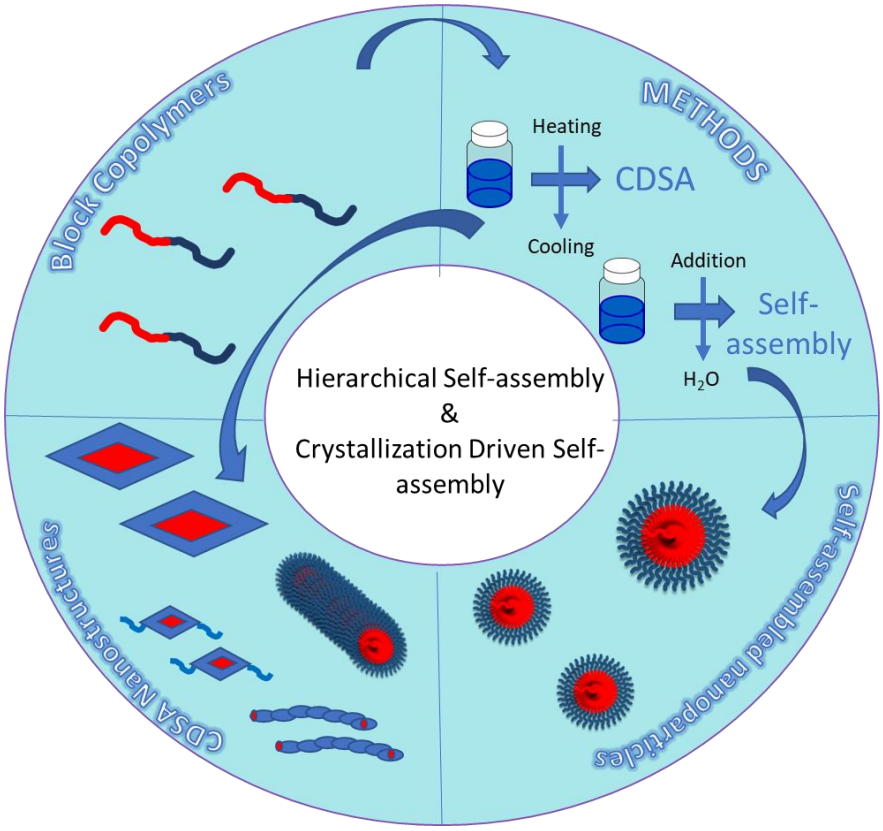
In the process known as crystallisation driven self-assembly (CDSA), molecules or nanoparticles spontaneously assemble into precise shapes under the control of a crystalline core. Due to its potential uses in a variety of domains, such as drug delivery, nanoelectronics, and materials science (Figure 3.1.1) this method has attracted a lot of attention recently.[168]

In systems where the hydrophobic core can undergo crystallization, there are driving forces for assemblies with low interfacial curvature, allowing access to different structures as a result of crystallisation-driven self-assembly (CDSA) [78, 158, 169] According to the balancing energies for corona solvation, chain packing of the core block, and the ratio between the blocks, the self-assembly of amphiphilic block copolymers with comparable solubility parameters will acquire distinctive properties and morphologies.[50, 51, 153, 154] Different morphologies have been accessed this way, from diamond-shaped platelets [153, 154] to wormLike cylinders or spherical micelles, all using the same crystalline core. [155-159] The morphology of the final assembly under specific conditions can be predicted by introducing charges at the polymer end groups. [153, 170] CDSA can be performed in solvents such as methanol, ethanol, [78, 153, 155, 156, 158] isopropanol,[170] acetone,[169] tetrahydrofuran (THF) and water,[158] and more recently the CDSA methodology has been explored in aqueous solutions

for PLA-based diblock copolymers.[156-159] Through optimization of the solvent and the ratio between the blocks, different sizes can be targeted.[153, 154] The size accrued varies according to the solubility parameter and the charges forming. [153, 155, 157, 158] The microstructures obtained can be used to encapsulate small molecules[171] and devised to release their cargo using internal or external stimuli, with a prolonged degradation time depending on the percentage of the core crystallinity. [53]

Reduction of supersaturation is the driving force for crystallisation in a solution which can occur via nucleation or crystal growth.[168] As the crystal develops, it captures the surrounding molecules, which subsequently position themselves to reduce the system's free energy.[172] Depending on the dimensions and shapes of the constituent parts as well as the properties of the system, this can lead to the production of a wide range of structures, such as spheres, cylinders, and sheets.[173]

In this section CDSA involves the self-assembly of nanoparticles with a semicrystalline PLLA core, which guides the formation of the crystal. As the PLLA crystal grows, it rearrange its chains towards a specific formation , leading to well-defined structures such as spheres, cylinders, and platelets (Scheme 3.1.13). The resulting structures exhibit a high degree of order and precision, which is critical for drug delivery applications where it is necessary to ensure that the drug molecules are delivered to the target site in a controlled manner.



Scheme 3.1.13. Hierarchical self-assembly and Crystallization Driven Self-assembly (CDSA)

Compared to conventional drug delivery methods, the combination of CDSA with biodegradable semi-crystalline polymers like PLLA has a number of benefits.[154] PLLA is a biodegradable polymer that has been extensively used in biomedical applications due to its favourable properties, such as high biocompatibility, low toxicity, and controlled degradation kinetics.[174] The size and shape of the produced structures can be considerably customised. [175] This is critical for drug delivery because size and shape can specifically control the drug release profile especially for a PLLA system. The molecular weight can indicate the degradation ratio, but also the shape can either prolong or minimize the degradation. By adjusting the parameters of the system, such as the concentration and temperature of the PLLA building blocks and the level of supersaturation, the size and shape of the arising structures can be readily controlled.[176]

CDSA can provide an environmentally friendly and sustainable method of medication administration by utilising biodegradable semi-crystalline polymers.[167] Release of encapsulated compounds can occur naturally by the simple hydrolysis of PLLA, a

biodegradable polymer into lactic acid, a naturally occurring metabolite in the human body.[174] As a result, it is possible to create a drug delivery system that releases the drug gradually over a certain time period, preventing the build-up of non-biodegradable residues in the body.

The capacity of CDSA to build structures with a high level of precision and order is one of its main benefits.[177] It is feasible to precisely regulate the size, form, and arrangement of the final structures by using the crystal as a template.[178] This degree of control is especially useful in applications like drug delivery, where it's crucial to make sure the drug molecules get to the right parts of the body.[179]

The adaptability of CDSA is another benefit. Many different molecules and nanoparticles, including organic compounds, inorganic particles, and biomolecules, can be assembled using this method.[180] Due to its adaptability, CDSA has the potential to be used in a variety of sectors, from materials science to biomedicine.

Controlling the size and shape of the generated structures is one of the difficulties of CDSA.[181] The system's conditions, such as the building block concentration and temperature, crystallisation rate, and supersaturation level, need to be carefully managed in order to achieve this.[181] The development of structures that are too small, too huge, or have irregular shapes may result if these conditions are not carefully regulated.

Another challenge of CDSA is scalability. While CDSA has shown great promise in the laboratory, it can be difficult to scale up the process to industrial levels.[182] This is because the conditions required for CDSA are often highly sensitive to small changes, and it can be difficult to achieve the same level of control over a large-scale system.[182]

In addition, employing biodegradable semi-crystalline polymers for CDSA has drawbacks. Controlling the rate of medication release from the system is one difficulty.[183] This needs careful adjustment of the structures' size, shape, and degree of crystallinity. Inconsistent drug release kinetics can undermine the effectiveness of the drug delivery system if these parameters are not optimised.[183]

3.1.2 Multilayer crystals

It has been reported that the leftover pieces of a crystalline lamella can serve as the nucleation sites for the growth of a second lamella layer in a process known as crystallization-driven self-assembly (CDSA). [184] Particularly when polymers are diffusing on top of the original crystal, this phenomena is important. A sufficiently long polymer chain can co-crystallize into two separate crystals that are close to one another, with the secondary lamella maintaining the orientation of the first layer.[185] The reason for this is that the crystalline regions act as a template or seed for the arrangement and alignment of nearby polymer chains. These chains can align and take on the same crystalline structure as the surface of the existing crystal as they diffuse and come into touch with it, essentially extending the crystal's growth in a layered fashion.[186]

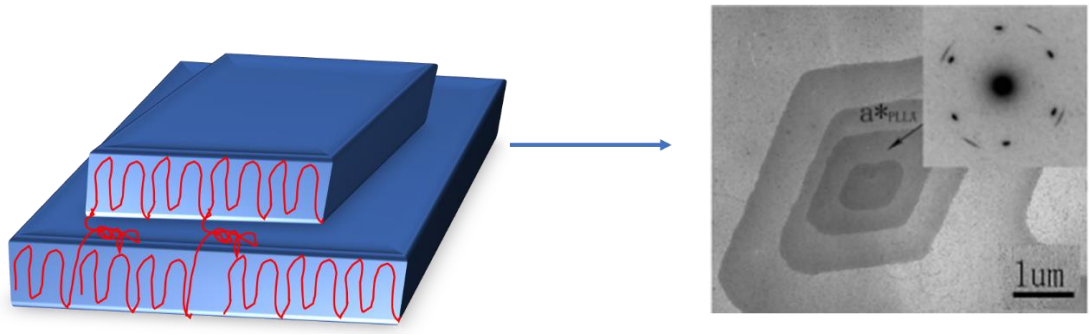


Figure 3.1.2 Schematic representation molecular ties forming a multilayer lamella and TEM data of PLLA crystal demonstrating the phenomenon[187, 188] adapted from Chen *et al* [187]

These secondary lamellae, which preserve the initial crystal's orientation, aid in the creation of multilayer structures and improve the overall crystalline order in the substance. This effect is seen in environments where lengthy polymer chains can diffuse and crystallise, resulting in the growth of numerous nearby, aligned-orientation crystal layers.[189]

The particular method and circumstances that lead to the development of secondary lamellae might differ depending on the kind of polymer system, the crystallisation environment, and the interactions between the polymer chains and the pre-existing crystal surface. Using experimental methods like in situ imaging or characterisation, researchers can learn a lot about how many neighbouring crystals form and develop in CDSA systems.

3.1.3 Edge and screw dislocations

Crystallinity can also expand to generate numerous crystal layers as a result of flaws in the formation of polymer single crystals, where crystal growth in one layer might spark growth in an adjacent layer. [190] The most frequently cited flaws are mechanisms for edge dislocation and screw dislocation.[188]

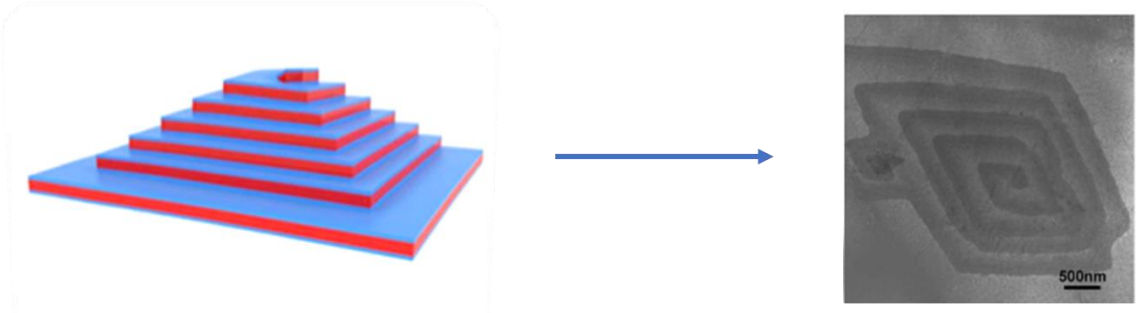


Figure 3.1.3. Schematic representation of screw dislocation[188, 191] and TEM micrograph depicting the screw dislocation of PLLA crystal presented by Chen and coworkers[187]

At the boundary or close to a crystal hole, an edge dislocation might happen, allowing alignment in nearby layers. When atoms or molecules are out of alignment or misplaced near a boundary or in close proximity to a crystal flaw or hole, an edge dislocation develops.[188] This misalignment enables the growth and alignment of adjacent layers, which promotes the increase of crystallinity. Additional crystal layers may emerge near the edge dislocation's nucleation point. The result of a screw dislocation is staggered crystal development, which is seen as many layers of spiral overgrowths where each layer is a separate crystal connected by the defect. A helical misalignment or distortion in the crystal lattice is what distinguishes a screw dislocation as a form of crystal defect. A screw dislocation causes the creation of staggered crystals, which are frequently seen as numerous layers of spiral-like overgrowths.[191] When layers are created in this way, each one is a different crystal that is joined together by a screw dislocation defect.

By offering sites for nucleation and encouraging the growth of adjacent layers, edge dislocations and screw dislocations can both aid in the production of numerous crystal

layers. These flaws function as sources of strain or distortion in the crystal lattice, which can promote crystallinity expansion and the formation of new crystal layers.

In conclusion, the type of their dislocation lines is the primary distinction between edge and screw dislocations. While screw dislocations have helical dislocation lines connected to a spiral-like distortion of the lattice, edge dislocations have linear dislocation lines connected to a step-like feature in the crystal structure.

Both kinds of dislocations have the potential to affect a material's mechanical and physical characteristics as well as a number of phenomena, including crystal development, plastic deformation, and material strength. For the purpose of researching the behaviour and characteristics of crystalline materials, it is essential to comprehend and characterise these dislocations.

In spite of these challenges, CDSA has shown considerable potential in a variety of applications, and research in this area is still developing. It is conceivable that in the future more applications of this procedure will contribute to various disciplines such as drug delivery and tissue engineering as our comprehension of the basic concepts of CDSA advances.

In conclusion, CDSA offers a potential approach for the development of sustainable and regulated drug delivery systems by utilising biodegradable semi-crystalline polymers, such as PLLA. More uses of this method in biomedicine are anticipated to emerge as research in the area develops, with potential advantages for patient care and the environment.

Based on this, the current work aimed to produce amphiphilic nanoparticles with various morphologies, different sizes and a biodegradable nature. Furthermore, the positive charge can be used to create electrostatic interactions with protein ligands. Finally, the core crystallinity can adjust and prolong the degradation time for efficient delivery, and therefore this system shows great promise for drug delivery and pharmaceutical applications to the brain. Saraiva et al demonstrated that the uptake and the encapsulation of nanoparticles

differs depending on the geometry. Cylinders specifically exhibit different retention times based on their size.[15] Other geometries are yet to be explored for BBB permeation, which creates a necessity for such a study. Herein we demonstrate that a variation of morphologies were synthesised and studied. PLLA's crystalline nature depending on the corona and the ratio between hydrophilic and hydrophobic copolymer has the potential of creating such shapes. The crystal that is predominately forming due to PLLA's ability is a diamond-shaped structure. Inam et al presented that same diamond-shaped morphology applies even with a DMAEMA corona as a hydrophilic part. Wei and associates by using a triblock copolymer system with PLLA as hydrophobic part exhibits similar structural behaviour but also demonstrates the morphological plasticity dependency on the core to corona ratio.[78]

3.2 Results and Discussion

3.2.1 Positively charged microstructures.

In ***Chapter 2*** spherical self-assemblies were developed in order to permeate the BBB. In this chapter the same diblock copolymers were developed with various morphologies and examined for their interactions with proteins. A simple comparison can help us address, which system is preferred for permeation through the BBB.

The interaction is promoted between negatively charged cell membranes and positive-charged PDMAEMA microstructures due to electrostatic interactions. The internalisation of the microstructures by cells may be facilitated by this electrostatic contact, improving cellular uptake. Effective cellular absorption, which is essential for therapeutic efficacy, makes this characteristic particularly attractive for drug delivery applications. The BBB has been measured to be negatively charged, thus potentially positively charged nanoparticles and microstructures have a chance to permeate passively. Although multiple studies have indicated that positively charged NPs can create cytotoxic effects in the cell lines.[192] PDMAEMA is a pH responsive polymer that has been used to improve stability of

nanoparticles and reduce their aggregation as well as provide controlled and targeted drug release.

The O'Reilly group has previously reported the synthesis of PDMAEMA-b-PLLA nanoparticles using CDSA.[193] PDMAEMA offers many advantages, so it would be exciting to explore its use in biomedical applications.

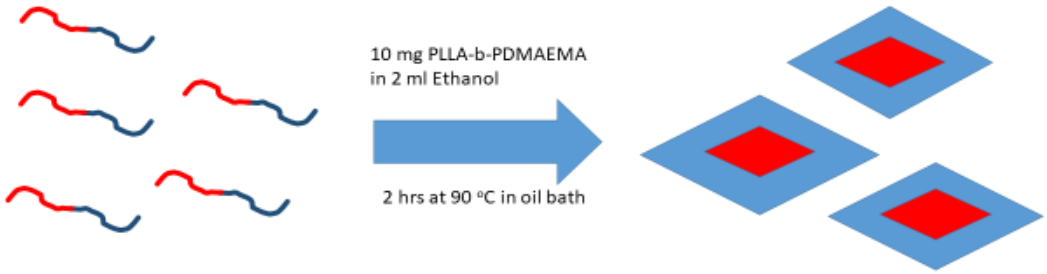
3.2.1.1 Positively charged diamond shaped nanoparticles

As previously reported (Chapter 2), diblock copolymers were synthesised with the purpose of permeating the BBB. The positively charged diblock copolymers that were selected to be examined can be found in table 3.2.1.

Table 3.2.1 PDMAEMA-b-PLLA diblock copolymers

Corona	DP	M_n (kDa)	M_w(kDa)	$Đ_M$	Ratio Core : Corona	Fluorescence	Core
DMAEMA	204	35	31	1.31	1:6	Yes	$PLLA_{36}$
DMAEMA	225	32	34	1.41	1:6	No	$PLLA_{37}$

Nanoparticle formulations were achieved by self-assembling the polymers into spherical micelles depending on their ratio in chapter 2. In this section the crystallization driven self-assembly (CDSA) of these polymers will be explored. As mentioned above the polymers developed, carry a semi-crystallized PLLA core that can be utilized on exploring the different morphologies that can arise by CDSA. The aforementioned process will utilise the crystalline nature of the PLLA to achieve a variation of morphologies. Depending on the corona of the block copolymer driving forces for assemblies with low interfacial curvature will take place leading to the morphological differentiations. Herein the positively charged corona of DMAEMA provided a diamond-shape structures when the core to corona ratio is 1:6. The assembly conditions selected were heating for 2 hours at 90℃ in an alcoholic solvent such as ethanol (scheme 3.2.1). Ethanol was selected as the solvent due to previous research published by the O'Reilly group.[154] After the CDSA process the alcoholic solvent was removed and the platelets were redispersed in water.



Scheme 3.2.1. CDSA of PDMAEMA-b-PLLA in ethanol

To examine further the structures formed, through the CDSA process, the nanoparticles were analysed through dynamic light scattering (DLS), atomic force microscopy (AFM), and transmission electron microscopy (TEM). DLS can provide information depending on the size and size distribution of the nanoparticles structure, even though it should be taken into consideration that the commercial apparatus used for the measurements assumes that the particles analysed are spherical. In this case, the study will proceed considering the geometrical coefficient is negligent as the DLS measurements are regarded, but the data will be also correlated with the sizes provided by the microscopies as well.

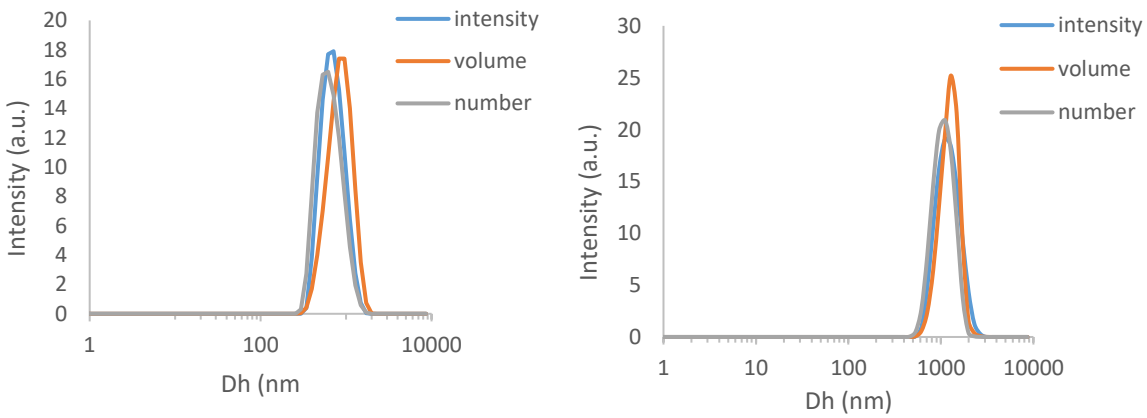


Figure 3.2.1. DLS graph of (a) non-fluorescent $PLLA_{37}$-b-$PDMAEMA_{225}$ in diamond morphology in water with pH 6.5 and (b) of fluorescent $PLLA_{36}$-b- $PDMAEMA_{204}$ with ACM probe in diamond morphology and redispersed in water with pH 6.5

In Figure 3.2.1 above, are the DLS graphs of the $PLLA_{37}$-b-$PDMAEMA_{225}$ and $PLLA_{36}$-b-$PDMAEMA_{204}$ diamond-shaped nanoparticles. It is visible that the sizes between intensity, volume and number correlate and the given $D_h$are 678.5 nm and 1118 nm accordingly. The polydispersity was found to be 0.145 and 0.107 respectively, which exhibits that the size distribution is narrow and the majority of the structures formed have similar size. The samples were taken in water at pH 6.5. Zeta potential measurements verified the positive surface charge for $PLLA_{37}$-b-$PDMAEMA_{225}$ and $PLLA_{36}$-b- $PDMAEMA_{204}$ diamond-shaped nanoparticles with zeta-potentials of +38 mV and +42 mV obtained , respectively.

Above its glass transition temperature (Tg), the PDMAEMA-PLLA polymer does not entirely dissolve in ethanol. The fact that PLLA is neither completely soluble in ethanol at its Tg nor insoluble in it makes ethanol a theta solvent for PLLA. PLLA does not totally dissolve in ethanol, though it may swell to some extent. The hydrophobic PLLA chains aggregate and pack inside the self-assembled particles in the PDMAEMA-PLLA system. The mobility of the PLLA chains rises when the solution is heated and PLLA approaches its Tg, enabling the development of crystalline domains inside the particles. The resulting morphology is influenced by the process by which the PLLA chains are packed within the particles, and in this case, this results in the production of diamond-shaped particles. As the crystal evolves, it retains the nearby molecules, which then arrange themselves to lower the free energy of the system. AFM analysis below provides the clear structure achieved and presents a nucleation centre in the middle of the crystal, which serves as a crystallization nucleus. No differences were observed between the diamond-shaped structures even though one of the polymer carries an intermediate ACM prove. Thus the morphology does not seem to be affected by a small fluorophore between the hydrophilic corona and the hydrophobic core.

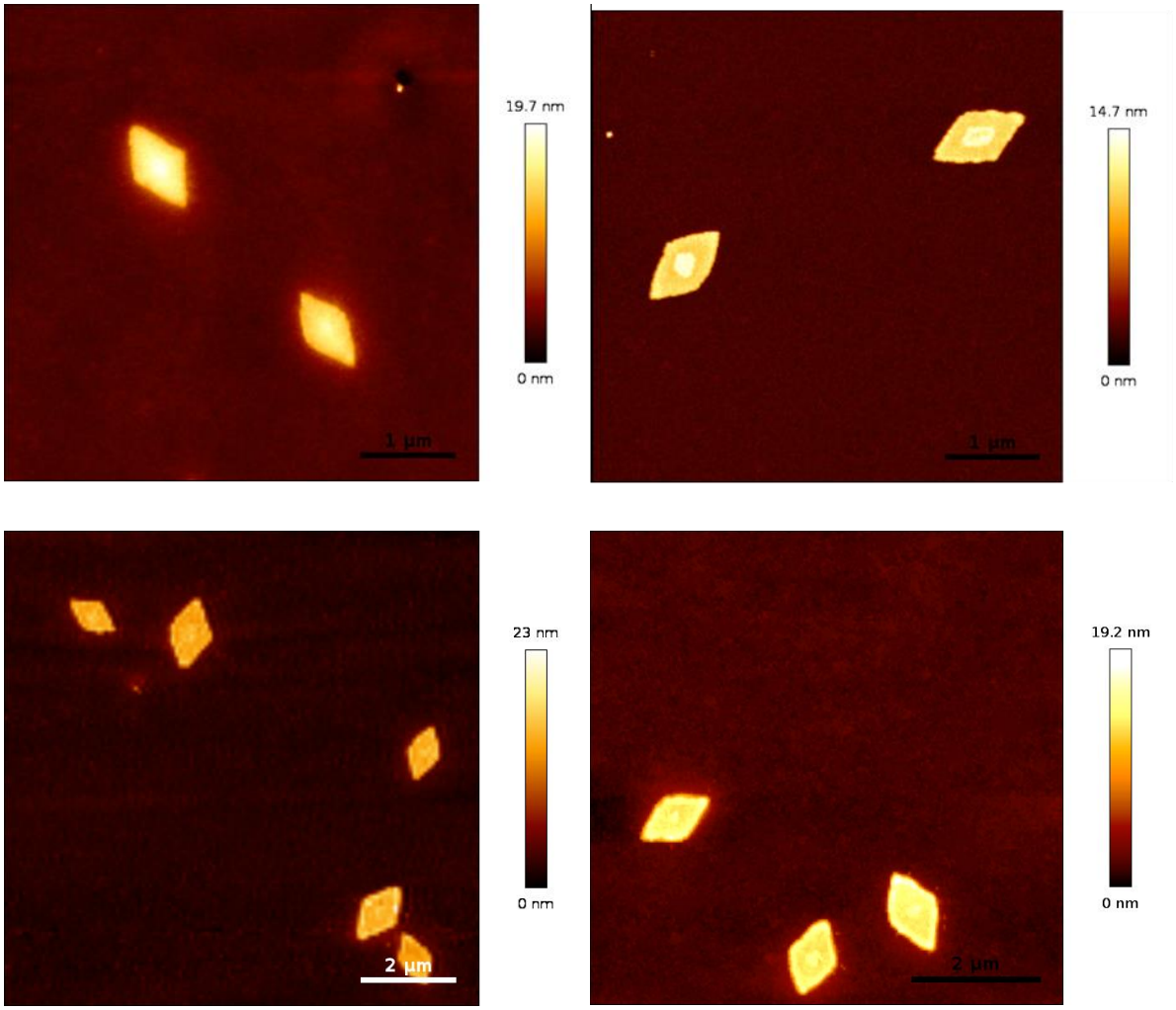


Figure 3.2.2 AFM images of non-fluorescent $PLLA_{37}$-b-$PDMAEMA_{225}$ (left) and of fluorescent $PLLA_{36}$-b-$PDMAEMA_{204}$ with ACM probe (right) with dispersed media water pH 6.5 with concentration 0.25 mg/mL, scale bar 1µm (up) and 2 µm (down)

AFM analysis (figure 3.2.2) indicated a diamond like nanoparticle morphology both polymer self-assemblies. Both polymers exhibit the diamond-shaped morphology due to the semi-crystallinity of the PLLA. After statistical analysis the length of the diamond-shaped structures was found to be 1.1 µm ± 0.3 µm for the non-fluorescence diamonds and 1 µm ± 0.3 µm for the fluorescence ones. The width of the particles was found to be 710 nm ± 90 nm and 697 nm ± 96 nm, accordingly.

The height of the structure gives information about the uneven surface of the diamond-shaped polymer structure. As noticed from the figure 3.2.2 the height distribution is similar

between the fluorescent $PLLA_{36}$-b-$PDMAEMA_{204}$ and non-fluorescent $PLLA_{37}$-b-$PDMAEMA_{225}$. The small difference between 19 nm height of the fluorescent polymer and 23 nm for the non-fluorescent can be caused by the slightly bigger corona of the non-fluorescent polymer.

The size differentiation between AFM and DLS can be explained through the fact that AFM is a dry-state technique in comparison with DLS that the micelles still reside in a solution. The above data are all summarized in the table 3.2.2 below.

Table 3.2.2. DLS analysis of non-fluorescent $PLLA_{37}$-b-$PDMAEMA_{225}$ and of fluorescent $PLLA_{36}$-b- $PDMAEMA_{204}$ with ACM probe in diamond morphology

Polymer	Morphology	Zeta potential (mV)	pH	Length (nm)	Width (nm)	D_h (nm)	PD
Non fluorescent $PLLA_{37}$-b-$PDMAEMA_{225}$	Diamonds	+ 38	6.5	1100 ± 300	710 ± 90	678.5	0.145
Fluorescent $PLLA_{36}$-b-$PDMAEMA_{204}$	Diamonds	+ 42	6.5	1000 ± 300	697 ± 96	1118	0.107

3.2.1.2 Optimisation of size of positively charged microstructures

The primary goal is still to permeate through the BBB but due to the increased size of the particles (~1μm) the possibilities of that happening are minimal. As previously mentioned in ***Chapter 1*** , tight junctions between endothelial cells can be affected and dysfunction in a brain affected by a neurodegenerative disease, allowing larger particles to permeate easier like in a patient with Alzheimer's, Parkinson's disease or those that have suffered an ischemic stroke.[194] For a healthy BBB system though particle self-assembly needs to be optimized in order to obtain smaller nanoparticles. In order to achieve this without disturbing the shape, the crystallization time was reduced. Usually the particles are removed from the hot oil bath and left in the counter for a day to crystallize. Herein , a short period of time was examined in order to reduce the size of the particles. After 3 hours of relaxation the solution vial was immersed into liquid nitrogen which forced the solution to crystallize immediately. DLS measurements in water in pH 6.5 at 0.2 mg/mL concentration showed a hydrodynamic diameter (D_h) 283nm with a polydispersity of 0.080 for the non-fluorescent

$PLLA_{37}$-b-$PDMAEMA_{225}$ and a D_h= 243.6 nm with a polydispersity 0.094 for the fluorescent $PLLA_{36}$-b-$PDMAEMA_{204}$. As depicted in the TEM images below (Figure 3.2.3) the forced crystallization created a variety of crystals. It can be observed that the uniformity of the crystals has drastically decreased . Apart from the smaller diamond-shaped particles a lot of undefined microstructures arise. Additionally, ill-defined diamond shaped crystals were also seen(Figure 3.2.3d), whereas despite the crystallization nucleus formation multiple edges and zigzag formulations can be found.

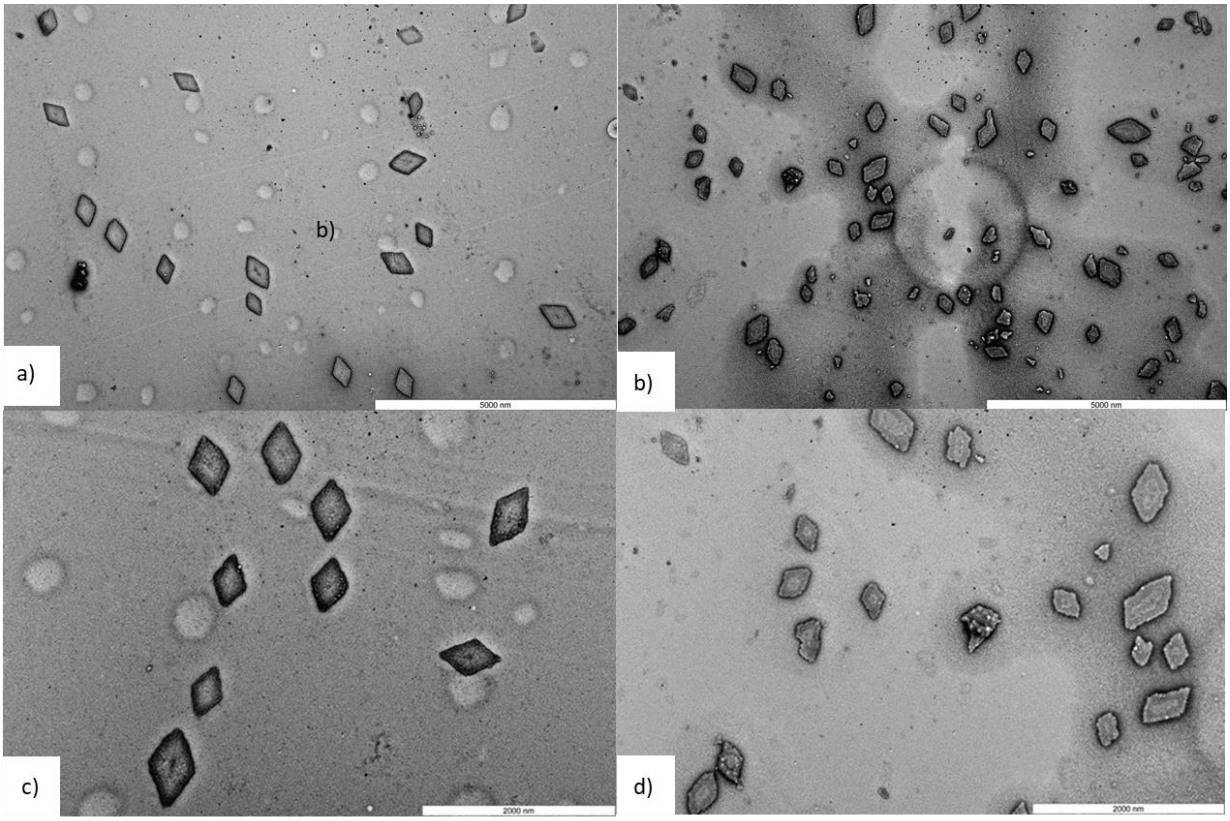


Figure 3.2.3. TEM results of optimisation of non-fluorescent $PLLA_{37}$-b-$PDMAEMA_{225}$ (a,c) and of fluorescent $PLLA_{36}$-b- $PDMAEMA_{204}$ with ACM probe (b,d) diamond shaped nanoparticles with scale bar 5 µm (up) and scale bar 2 µm (down)

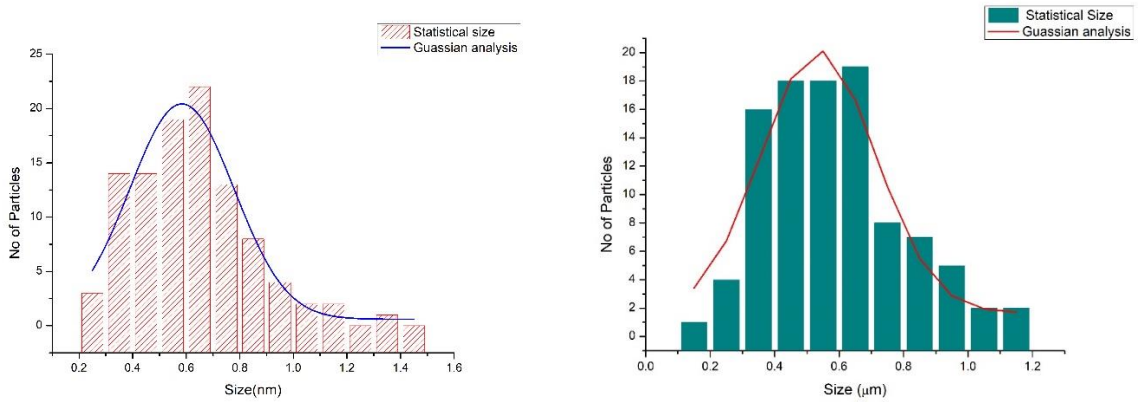


Figure 3.2.4 Statistical analysis from TEM images on the optimisation of non-fluorescent $PLLA_{37}$-b-$PDMAEMA_{225}$ (left) and of fluorescent $PLLA_{36}$-b- $PDMAEMA_{204}$ with ACM probe (right) diamond-shaped structures (sample of 100).

Statistical analysis of nanoparticle length was performed on these TEM images (Figure 3.2.4). highlights the length changes after the optimisation. The statistical analysis above reveals a plethora of sizes with the average distribution being at 617 nm ± 204 nm, but also appear dominate populations between 300-600 nm. Thus, the gaussian analysis is providing a centre at 500nm due to the multiple high distributions to a variation of sizes. Similarly for the fluorescent $PLLA_{36}$-b-$PDMAEMA_{204}$ diamond-shaped particles, the mean size was found to be 582nm ± 210nm. There are a lot of explanations for the polydispersity of the samples above, like the immediate cooling effect. Clearly, immediately cooling the solution has a significantly detrimental impact upon nanoparticle dispersity. This can be explained by reducing the crystallisation time the lamella cannot form coherently so it will create defections in the crystals morphology. The above experiment demonstrated that with prolonged heating in lower temperatures, optimisation of the size cannot happen in a coherent way, to obtain monodisperse smaller diamond-shaped microstructures. Controlling the crystallisation period is essential for obtaining crystals that are well-formed and devoid of defects. Higher crystallinity and better crystal shape are produced by longer crystallisation durations because they enable more thorough organisation and alignment of the polymer chains. To achieve the intended performance of the material, it is crucial to balance the crystallisation time with other parameters, such as processing limitations and desired material attributes.

3.2.1.3 Protein Corona effect

As previously reported, screw dislocation is one of the most frequent defects in crystalline formation. Staggered crystal growth, or a screw dislocation, is seen as many layers of spiral overgrowths, where each layer is a different crystal connected by the defect. As a result, if a polymer chain is long enough, it's able to co-crystallize into two distinct nearby crystals, with the secondary lamella maintaining the same orientation as the first layer. Here after the CDSA process this phenomenon is in effect.

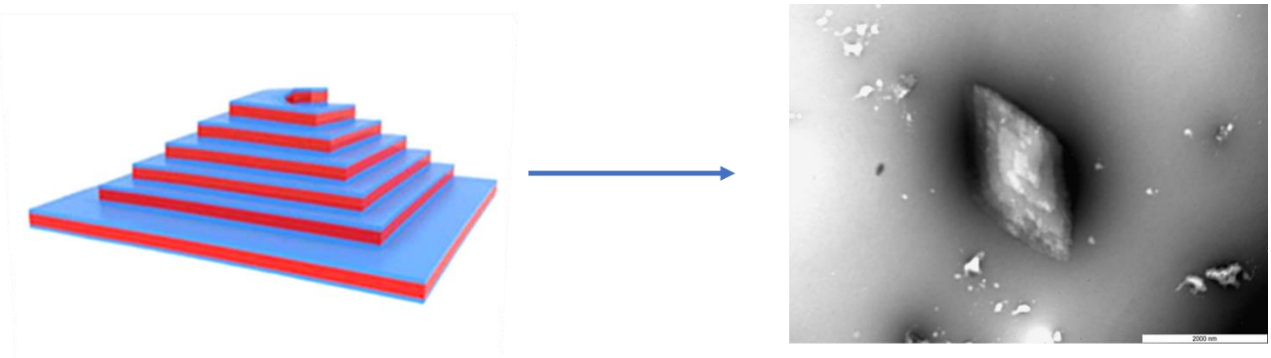


Figure 3.2.5. Screw dislocation of fluorescent $PLLA_{36}$-b- $PDMAEMA_{204}$ with ACM probe dispersed in water with pH 6.5, scale bar 2000 nm.

The diamond shape microstructures produced above with the defect of the screw dislocation in figure 3.2.5 will be used for the protein corona experimentation as follows.

A system that it is designed for drug delivery applications should be examined further. Especially the interactions between proteins and particles should be investigated. In biological fluids there is a plethora of proteins that have specific functions. For example, albumin that is present in the bloodstream, which functions as a carrier of fatty acids and hormones, or fibrinogen that assists in blood clot formation.[195] When a nanoparticle is introduced into a biological fluid system, proteins will start interacting with the nanoparticle leading to a protein coating engulfing the nanoparticle, which may alter their surface charge and characteristics. Following the application of this biological coating, an increase in hydrodynamic size or aggregation may result in performance degradation.[196] Previous attempts, have been made to identify how the protein corona effect influences nanoparticle

behaviour and original shape. Using the methodology described in *Chapter 2*, protein interactions with nanoparticle systems were investigated with a model BSA protein. After the addition of BSA, the nanoparticles appeared to aggregate and macroscopic precipitation could be observed in the reaction vial. This precipitation was due to electrostatic attraction between the BSA and nanoparticles creating large aggregates, which were colloidally unstable. In order to minimise this aggregation, the molar ratio of BSA (molecular weight for BSA 66 kDa): Nanoparticles(molecular weight of $PLLA_{36}$-b- $PDMAEMA_{204}$ 35270 g/mol) was reduced to 1:1.

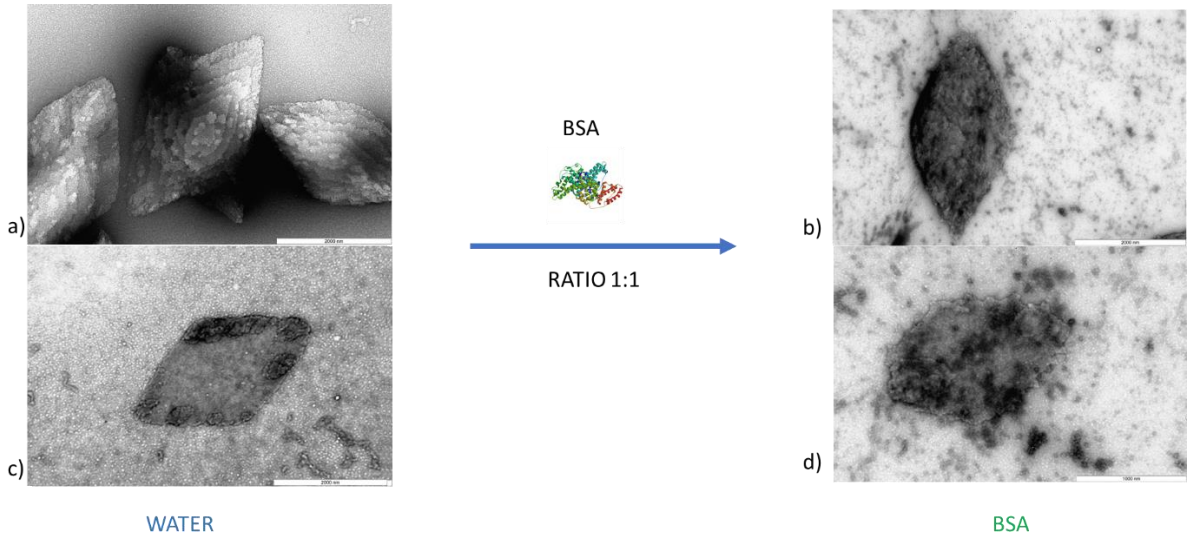


Figure 3.2.6. Protein corona effect with molar ratio 1:1 (a, c) Fluorescent $PLLA_{36}$-b- $PDMAEMA_{204}$ diamond-shaped microstructures in water pH 6.5 , (b, d)BSA, scale bar 1000 nm.

As depicted by figure 3.2.6 the electrostatic interactions are clearly visible. TEM data above provide vital information on the direct influence the protein has in a different morphology. As seen from figure2.3.6 b) multiple layers of coating have been deposited on the surface of the diamond shaped microstructure. Like previously described in *Chapter 2* the positive charged from the PDMAEMA hydrophilic corona will interact with the negatively charged BSA protein and form an electrostatic interaction. In most instances, proteins are adsorbed onto the surfaces of nanoparticles or microstructures to create the protein corona. The exterior chains of the CDSA microstructure, which are frequently exposed at the surface, are more likely to attract the proteins because they prefer interacting with hydrophilic or

charged regions. The behaviour and surface characteristics of the microstructure can alter as a result of the interaction between the hydrophilic exterior chains and the protein corona. Changes in the surface charge, surface roughness, or hydration characteristics may be examples of this. These modifications to the surface properties may have an indirect impact on the microstructure's stability, interactions, or bioactivity inside a biological system. From image 3.2.6 d) though it can be noticed that even morphological changes have occurred to the microstructure. Defections are visible and the diamond shape is not as defined as it was prior to the addition. These defects cannot be attributed to a TEM drying effect since no similar phenomenon was observed with just the diamond NPs. The local surface chemistry, including changes in surface charge or surface roughness, may change as a result of the interaction between the BSA protein and the crystal surface. Zeta potential measurements verify the difference in surface charge from 42 mV to -5 mV for $PLLA_{36}$-b-$PDMAEMA_{204}$ and from 38 mV to -3 mV for the $PLLA_{37}$-b-$PDMAEMA_{225}$. The equilibrium between the crystal and the surrounding solution may be impacted by these changes, which could result in surface remodelling or dissolution-precipitation cycles. It's plausible that the BSA protein adsorption causes changes in the surface energy, which cause partial dissolution and re-precipitation of the crystal surface in the case of the observed defects and enhanced edge presence. New crystal faces, edges, or flaws may emerge as a result of this. The precise interactions between the BSA protein and the surface of the diamond-shaped structure will determine the size and type of these alterations.

In order to determine the type of alterations another molecular ratio of 1:0.25 of $PLLA_{36}$-b-$PDMAEMA_{204}$: BSA was examined. With lowering the amount of protein addition, it can investigated if the electrostatic interactions effect the surface roughness and overall morphology of the diamond shaped microstructure.

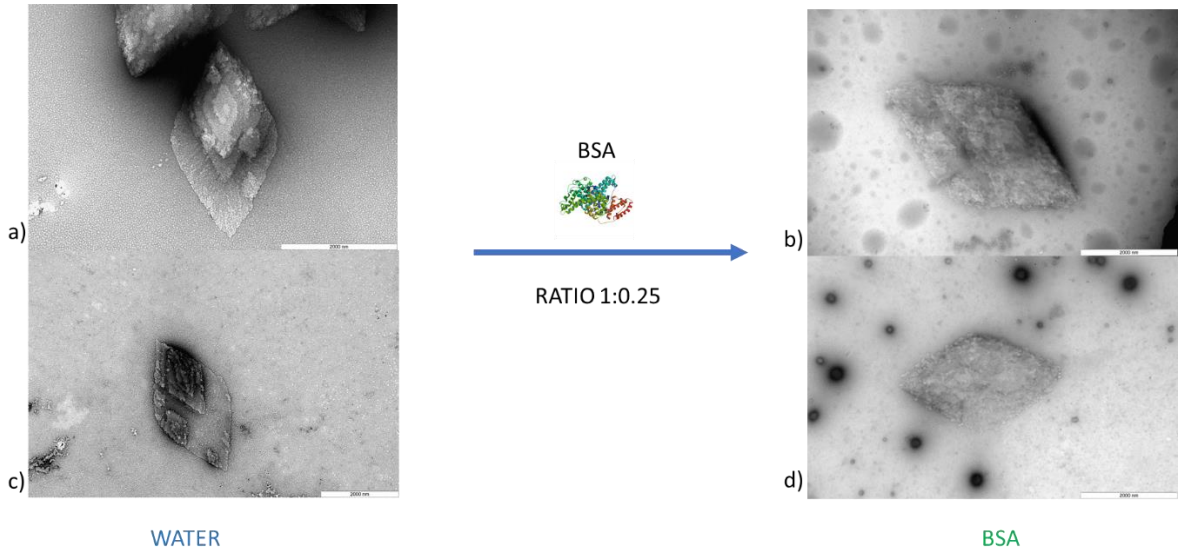


Figure 3.2.7. Protein corona effect with molar ratio 1:0.25 (a, c) Fluorescent $PLLA_{36}$-b- $PDMAEMA_{204}$ diamond-shaped microstructures in water pH 6.5 , (b, d)BSA, scale bar 2000 nm

After addition of 0.25 molecular ratio of protein solution in the diamond shaped microstructure solution, the final solution was mixed thoroughly for 2 hours. The TEM images were taken after a day of aging. The final dilution deposited on the TEM grid was 0.05 mg/mL of the polymer-protein solution. Figure 3.2.7 depicts the protein interactions on the microstructures at a lower molecular ratio. Specifically from image 3.2.7 b) it is clearly represented a formation of a hard protein corona on the positively charged outer layer of the hydrophilic chain. The preservation of the intact structure can indicate the thin layer of protein electrostatic interactions only on the surface of the diamond shaped nanoparticle formulation.

The exposed surfaces or outer layers of the CDSA microstructure, are made of hydrophilic chains, which constitute the main areas where the protein corona interacts. Protein adhesion to these areas may have an impact on the microstructure's surface characteristics, stability, and interactions. The affinity of the proteins on the surface of the microstructure, electrostatic interactions, and general stability of the microstructure will all affect the degree of protein binding and the stability of the protein corona.

Similarly in figure 3.2.7d) it is visible that strong binding interactions between the proteins and the microstructure's surface often result in the formation of a hard protein corona. The

quantity of proteins that may bind to the surface of the microstructure will decrease in the case that the concentration of BSA protein is decreased. As a result, the remaining proteins display greater binding affinities and create a layer of proteins that is more tightly attached while preserving the morphology of the microstructure, resulting in a hard protein corona effect. Protein-microstructure interactions can be modified and the development of a hard protein corona may be encouraged by varying the quantity of protein in the solution.

In order to better understand the interactions between CDSA nanoparticles and proteins, further experimentation is needed. Confocal microscopy can provide essential data, which are necessary for optimisation and design of CDSA microstructures for biomedical applications. Confocal studies provide insight regarding the manner in which the protein corona forms, is composed, and behaves on CDSA structures.

Since our diblock copolymer $PDMAEMA_{204}$-b-$PLLA_{36}$ carries a fluorescent aminochloromalemide (ACM) probe it would respond to wavelength 501nm emission and 377nm excitation (see image in materials and methods), which would correspond to green colour. As presented in ***Chapter 2*** BSA is an amino-bearing biomolecule that can be easily labelled with Cy5-NHS ester dye (see scheme in materials and methods) so it will emit to 662 nm emission and 646 nm excitation wavelength. Thus, both of the above compounds will be visible during confocal microscopy, and can be excited independently. The same molecular ratios as in TEM were used for confocal microscopy(1:1 and 1:0.25), however the samples were too concentrated to be able to visualise, as can be seen from the figure 3.2.8 below.

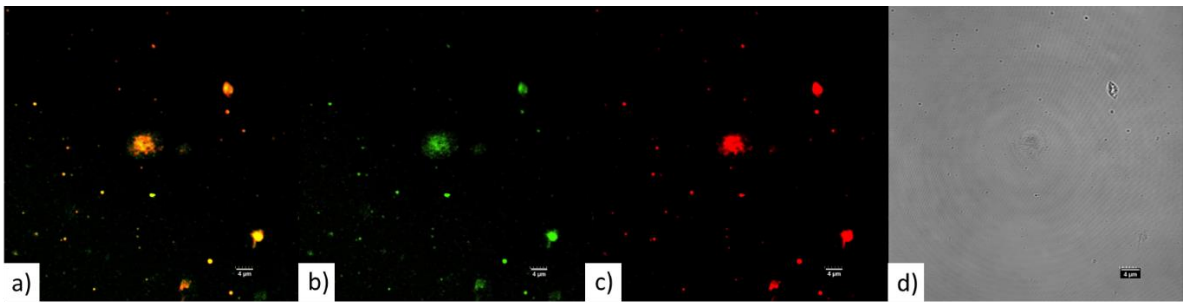


Figure 3.2.8. Confocal image of fluorescent $PDMAEMA_{204}$-b-$PLLA_{36}$ with ACM probe and BSA-Cy5 1:1 molar ratio prior to dialysis 0.05 mg/mL concentration a) composite of green and red channel, b)green channel ACM probe fluorophore emission(533nm), c) red channel Cy5 fluorophore emission (644nm), d) microscope image, scale bar 4µm

From the confocal image above it can be determined that the excessive protein can affect the morphology of the system. Figure 3.2.8 d indicates only one diamond shaped geometry through the microscope image. The composite image depicted in figure 3.2.8 a showed colocalization between the 2 channels red and green. Since the images above exhibit how the soft corona affected the current system, the next step would be to examine the hard corona formation. For this purpose, the samples were dialysed against water 18.2 MΩ for 3 days, which eliminated the soft protein corona phenomenon but that could also show the affinity of the electrostatic interactions in comparison with the weaker interactions of the soft corona.

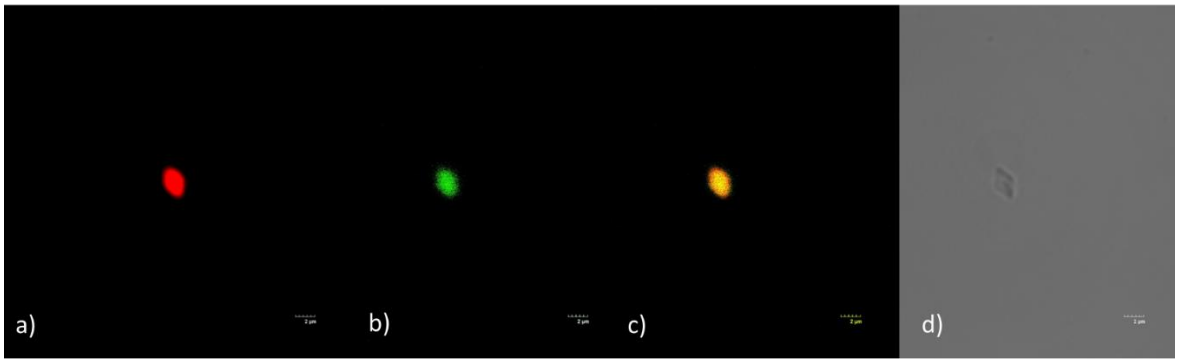


Figure 3.2.9. Confocal image of fluorescent PDMAEMA$_{204}$-b-PLLA$_{36}$ with ACM probe and BSA-Cy5 1:1 molar ratio 0.05 mg/mL concentration a)red channel Cy5 fluorophore emission (644nm), b)green channel ACM probe fluorophore emission(533nm), c)composite of green and red channel, d) microscope image, scale bar 2µm

The confocal image above illustrate the colocalization of the dyes that match the microscopy image. Evidently, the electrostatic interactions of the positively charged diamond shaped microstructures and the negatively charged BSA are apparent since the red dye and the green dye correlate in figure 3.2.9 c) and compose an orange colour. Figure 3.2.9 d) provides evidence that the structure of the diamond has not been affected. BSA appears to form a coating around the diamond shape microstructure, as can be seen in figure 3.2.9 c) since a red halo surrounds the orange colour created by the intertwined dyes. Nonetheless, the halo could also be caused by the overwhelming intensity of the Cy5 dye, even though the system was dialysed. Lastly the appearance of a hard corona is portrayed, but that can be caused due to the fact that the system was dialysed, the molecular ratio in use and the low concentration of the system.

Similarly the same experiment was conducted with molar ration of 1:0.25 diamond :BSA.

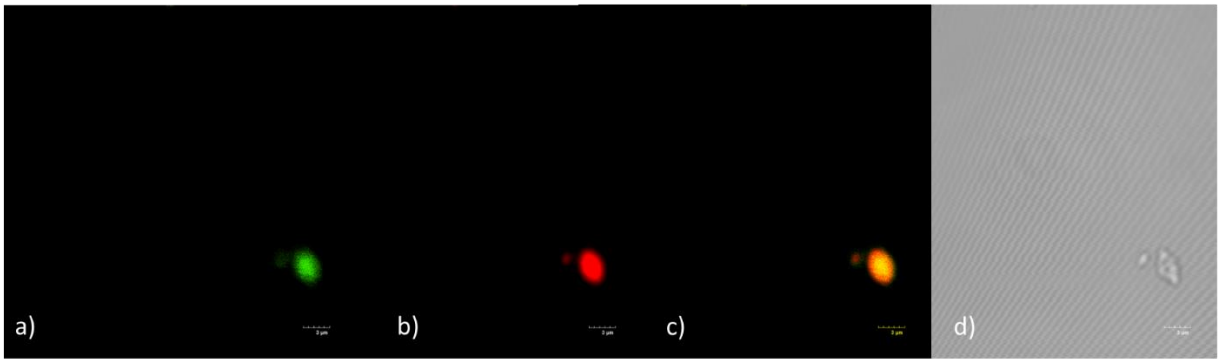


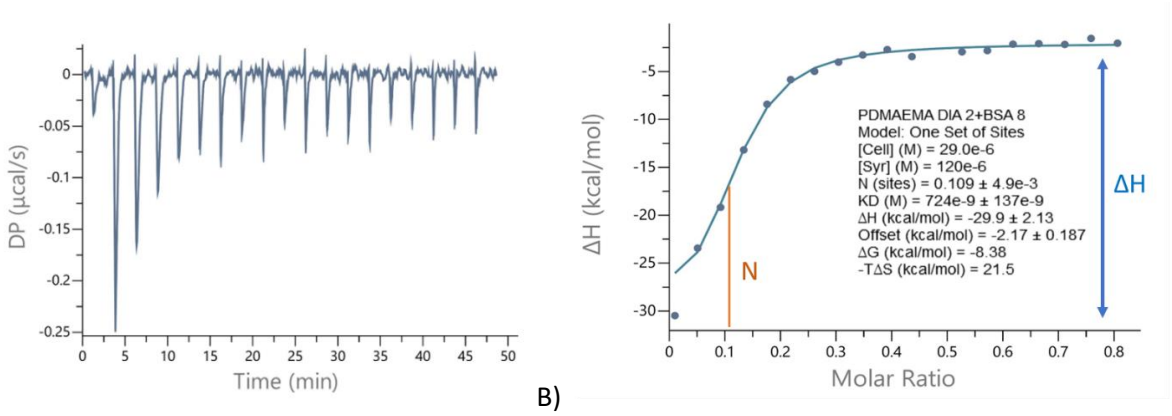
Figure 3.2.10. Confocal image of fluorescent PDMAEMA$_{204}$-b-PLLA$_{36}$ with ACM probe and BSA-Cy5 1:0.25 molar ratio 0.05 mg/mL concentration a)red channel Cy5 fluorophore emission, b)green channel ACM probe fluorophore emission, c)composite of green and red channel, d) microscope image, scale bare 3µm

As per the previous experiment, the confocal data depict the overlap of the dyes that correspond to the microscope image as seen in figure 3.2.10 c) above. Since the red and green dyes in figure 3.2.10 c) are topologically adjacent and produce the colour orange, it is clear that the BSA and the diamond-shaped microstructures are electrostatically interacting. Evidence that the diamond's structural integrity is unaffected is seen in figure 3.2.10 d). As previously, a crimson halo surrounds the orange hue produced by the overlay of the dyes, suggesting that BSA may form a coating surrounding the diamond-shaped microstructure (figure 3.2.10 c).

Confocal microscopy demonstrated the precise position of proteins inside the protein corona and their colocalization with the specific CDSA diamond shaped microstructure. This can assist in determining whether particular proteins have a preference for binding to particular regions or functional groups on the CDSA surfaces. As is apparent in both cases BSA proteins are interacting with the surface of the microstructure, due to the positively charged amino groups on the PDMAEMA chain that is on the surface of the diamond shaped nanoparticle.

It is essential to take into account that depending on the particular system and experimental circµmstances, the precise mechanism and consequences of protein adsorption on the crystal shape can change. To fully comprehend the specific interactions and their effect on the morphology of the diamond-shaped structure after the addition of BSA protein, more experimental research and characterisation methods, such as isothermal titration

calorimetry (ITC), are required. For this purpose an ITC experiment was performed to better understand the BSA binding affinity . ITC monitors the heat generated or consumed during a binding event, giving data on the interaction's thermodynamics (enthalpy and entropy).



A) B)

Figure 3.2.11. ITC experiment of $PLLA_{36}$-b- $PDMAEMA_{204}$ diamond shaped nanoparticles with BSA as ligand in water pH 6.5. A) Heat rate of the titration. B) Normalized heats from each titration step corrected by the heats of dilution (filled spheres) together with a fit corresponding to an independent binding model (straight line). Visual representation of the parameters obtained by ITC experiments within the adsorption isotherm. KD is derived from the curve's slope in its inflection point, ΔH is represented by the difference between the curve's upper and lower plateaus (blue line) and N is the binding sites at the curve's inflection point (orange line).

Here it should be noted that the heat transmission and signal production in an ITC experiment can be affected by the design and shape of the nanoparticles themselves.[197] In planar geometries,[198] the heat transfer from the nanoparticles to the surrounding solution may be hampered, leading to diminished heat signals that are challenging to interpret.

As depicted in figure 3.2.11 B the stoichiometry of the binding interaction is represented by the value of 0.109, which means that on average there are 0.109 binding sites per molecule of the receptor or ligand engaged in the interaction. A higher binding affinity is indicated by a lower KD value. This result points to a partial or substoichiometric binding event, in which not all binding sites are occupied even though that the molar ratio was changed to 2:8 (Diamonds: BSA). The molar ratio used suggests that no free molecules of the positive amino groups of the $PLLA_{36}$-b- $PDMAEMA_{204}$ should have remained but as previously discussed this is a 2D structure so the signals could have incorrect representation. Furthermore, from the

above graph, the heat emitted or absorbed during the binding interaction is demonstrated by the enthalpy change ΔH of -29.9 Kcal/mol. If the contact between the ligand and receptor consists primarily of noncovalent forces like hydrogen bonding, van der Waals interactions, or hydrophobic interactions, a negative H value indicates an exothermic reaction (heat lost). It is crucial to remember that enthalpy interpretation may not always give accurate details about the binding process or particular interactions at play.

The change in free energy during the binding contact is represented by the ΔG value of -8.38 Kcal/mol. A negative ΔG suggests that the interaction is spontaneous since the binding process is thermodynamically advantageous, which confirms the protein corona phenomenon. The strength of the binding is determined by the magnitude of ΔG, with greater negative values suggesting a stronger binding. The -TΔS value of 21.5 Kcal/mol indicates the entropy change related to the binding process. Entropy appears to be decreasing following the binding since -TΔS value has a positive value, suggesting a more ordered or constrained state for the system.

Since, the value of KD that is determined by the slope it cannot be calculated correctly. A variation of reasons can affect the system such as weak interactions, kinetic limitations and solubility or aggregation issues.[199-201] It can be difficult to precisely calculate the dissociation constant (KD) or acquire correct binding parameters in such circumstances. It is possible that the binding process is slow and that the experiment's time constraint prevents equilibrium from being attained. This may be the result of elements like slow attachment or dissociation rates. Issues with solubility or aggregation can interfere with the binding behaviour of the nanoparticles or protein and hinder the achievement of a plateau in the ITC data.

As explored in ***Chapter 2*** the ITC of the spherical micelles for the same molar ratio 2:8 ($PDMAEMA_{204}$-b-$PLLA_{36}$: BSA) indicated the electrostatic interactions between protein and micelles and had similar ΔG value -8.49 kcal/mol with the diamond shaped particles: BSA (2:8) of -8.38 kcal/mol. The 2 plots though have substantial differences since the spherical micelles appear to have an endothermic reaction in opposition to the diamond shape NPs having an exothermic reaction. The surface curvature of the 2D diamond shaped NPs seems

to have different deposition of the protein ligands in comparison to the spherical micelle system.

In the next section PDMAEMA-b-PLLA will be presented as a reconfiguration of the system as a cylindrical one to evaluate if the shape has an immediate effect on the protein corona formation.

3.2.1.4 Morphological variations of positively charged nanoparticles.

Due to the fact that diamond shaped microstructures of PDMAEMA-b-PLLA seem to have a different protein corona effect and there are limitations due to the structure another system was approached. The morphology of diamond-shaped particles may be affected by changing the heating period and lower the temperature of the diblock copolymer, which could additionally promote the growth of cylindrical structures. When temperature and time are changed, the self-assembly behaviour and consequent microstructure morphology can change. This is because crystallization-driven self-assembly (CDSA) processes are frequently temperature and time sensitive. The more effective way to control the morphology of the system would be to change the core:corona ratio, but as mentioned before it is desirable to maintain the same polymer in different morphologies.

The kinetics of the self-assembly process and the crystallisation of the polymer chains can both be controlled by varying the heating time. Longer heating times might enable more thorough crystallisation and chain rearrangement, which might result in the creation of cylindrical structures. Moreover, by lowering the temperature the system will not have sufficient energy for the unimers to form diamond shapes particles. Cylindrical micelles tried to be developed through the CDSA process, by lowering the temperature from 90℃ to 60℃ for an extended period of time. After 2.5 hours of incubation at 60℃ in pure ethanol at 5mg/mL concentration, AFM revealed not a uniform cylindrical system (figure 3.2.12). The sample taken was allowed to cool down for 2 hours prior to the removal of ethanol and redispersion of water. All the samples were examined in water as conditions as close as

possible to the multi-dynamic system of a human organism need to be used when aiming for biomedical applications.

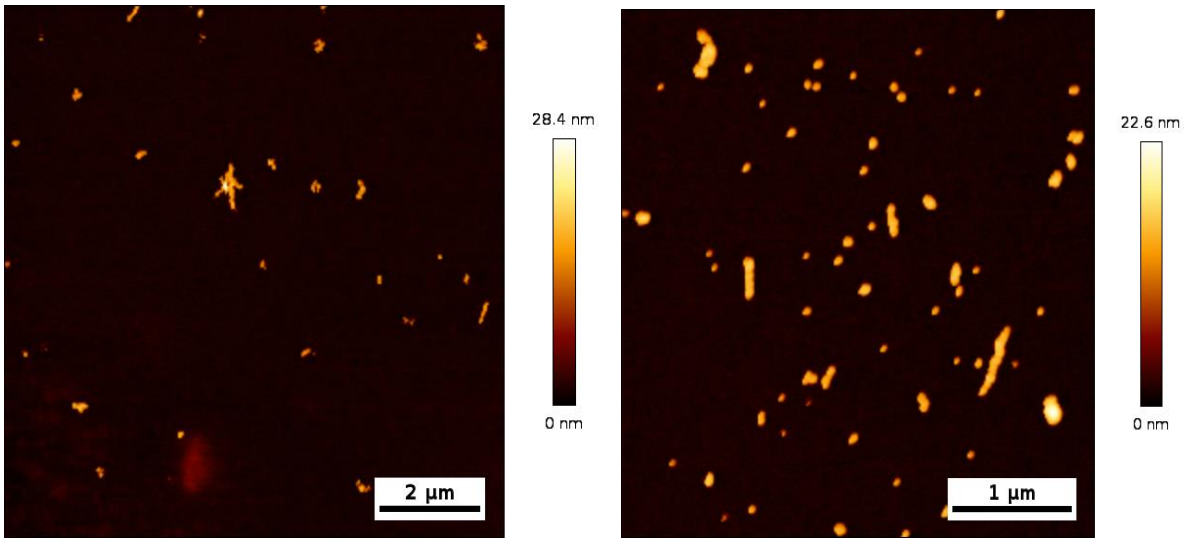


Figure 3.2.12. AFM image of non-fluorescent $PLLA_{37}$-b-$PDMAEMA_{225}$ (right) and of fluorescent $PLLA_{36}$-b-$PDMAEMA_{204}$ with ACM probe (left) at 60°C for 2.5 hours in ethanol.(concentration 0.2 mg/mL in water)

Since, not a pure cylindrical phase could be explored, the incubation time was prolonged and after 16.5 hours a sample was taken. The ethanol was removed and the particles were redispersed in water. The image given didn't not depict a clear view of the solution, a similar state as previously of a mixture of cylinders and agglomerates with not a defined structure. This could be a metastatic phenomenon until the system reached equilibrium. Thus, the incubation time was extended to 36 hours.

Similarly after the 36 hours incubation period (figure 3.2.13), the structures remained a non-uniform mix of cylinders and aggregated clots. In a closer look it can be observed that the seed formations are composing a cylinder like a molecular caterpillar structure. This potentially happens to reduce the Gibbs energy of the system. Longer heating periods at a lower temperature could assist the cylindrical shape maintain its thermodynamic stability. Given the unique characteristics and interactions of the polymers involved, it is plausible that the observed "molecular caterpillar" form indicates a more favourable thermodynamic state than other possible morphologies.

The nucleation and growth mechanisms can be affected by modifying the temperature and heating duration. It appears that lowering the temperature will encourage nucleation events and the development of seed structures, whereas maintaining the heat for a longer period of time permits their continued growth and assembly into the observed morphology. This potentially happens to reduce the Gibbs energy of the system.

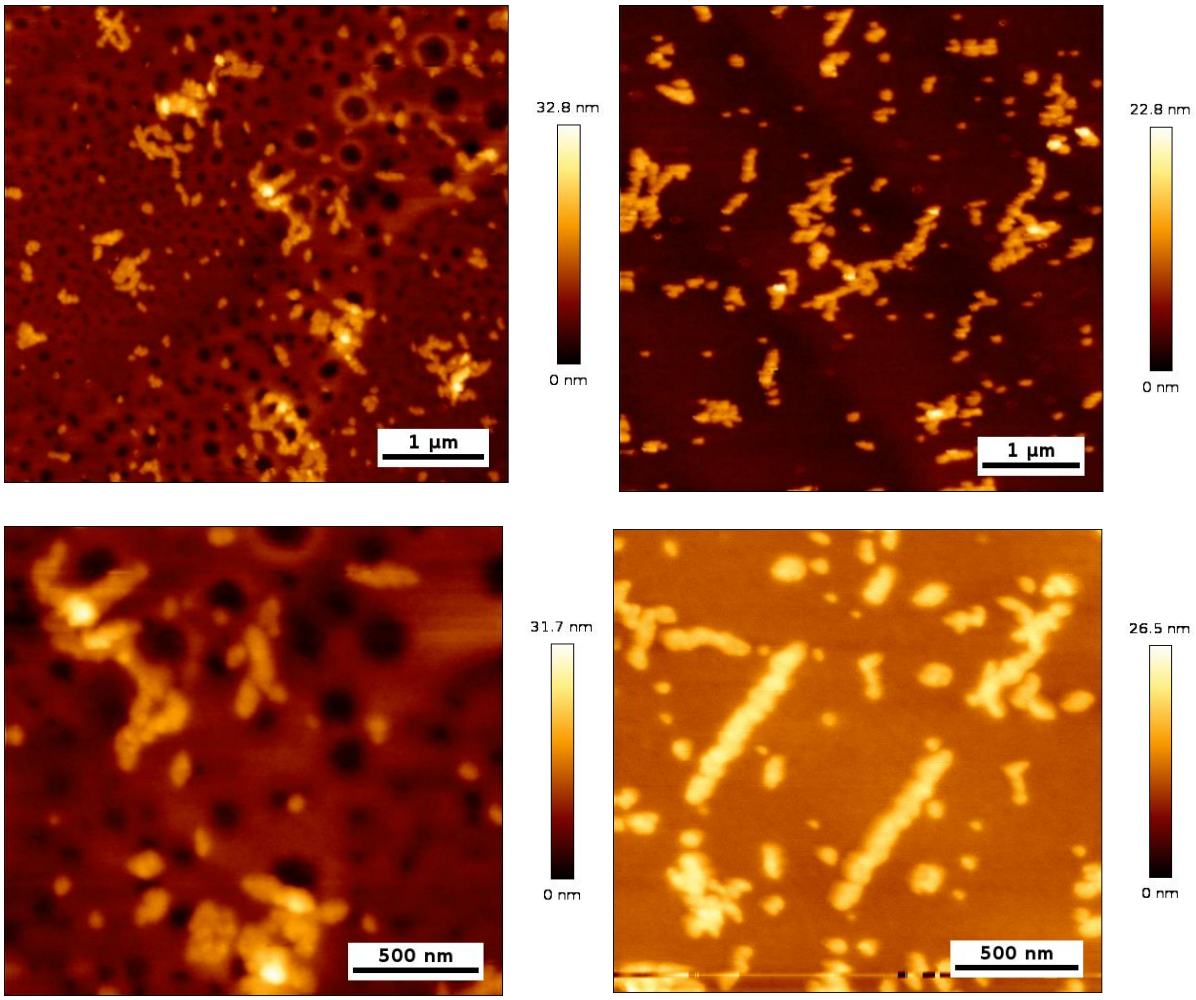


Figure 3.2.13. AFM image of non-fluorescent $PLLA_{37}$-b-$PDMAEMA_{225}$ (right) and of fluorescent $PLLA_{36}$-b-$PDMAEMA_{204}$ with ACM probe (left) at 60 °C for 36 hours in ethanol.(concentration 0.2 mg/mL in water) ,scale bar 1um (up), 500nm (down)

It can be observed from figure 3.2.13 that slower crystal growth kinetics can be achieved by lowering the temperature and lengthening the heating period. It is possible that elongated structures with a "molecular caterpillar" shape will form as a result of this prolonged duration of heating at a lower temperature since it promotes more slow crystal growth.

The polymer chains may not have sufficient energy to reorganise and reconfigure into the desired cylindrical shape because of the lower temperature and longer heating time. If more extensive molecular mobility was made possible by the prolonged heating period, the self-assembly process could advance and produce the necessary structures.

In conclusion, positively charged diamond microstructures were developed and tried to be optimised. Further exploration of the diamond microstructures was conducted, by investigating the protein corona effect on a 2D structure. A comparison with the spherical homologues of the positively charged polymer indicated that protein corona absorbs and behaves differently depending on the morphology of the system. Lastly, the positively charged cylinders were explored as a structure from the same polymer in order to be investigated for the protein corona but no homogeneous cylindrical system was achieved.

3.2.2. Neutrally charged microstructures

In the previous section it was demonstrated that the positively charged nanoparticles can form electrostatic interactions with proteins, which in large quantities, such as those seen in biological systems, it can cause them to aggregate and precipitate. Herein, an examination of neutrally charge structures will be explored. Microstructures that are neutrally charged may interact with biological elements like proteins, cells, or tissues less frequently in a non-specific way.[202] As a result, unintended binding or uptake events may be reduced, improving biocompatibility. Improved stealth characteristics of neutrally charged microstructures can lessen immune system identification and clearance of these objects. Longer circulation periods and better biodistribution may arise from this. A diverse platform for surface functionalization with different chemicals or coatings is offered by neutrally charged microstructures. Due to their adaptability, microstructures can be customised and given special capabilities, such targeting ligands or stealth coatings, to better suit particular applications. Without the interference of electrostatic interactions, they can be easily

changed with a variety of functional groups, such as hydrophilic or hydrophobic moieties or imaging agents. Certain delicate payloads, such proteins or nucleic acids, which are prone to denaturation or disintegration in the presence of strong electrostatic interactions, may be better suited for neutrally charged microstructures.

3.2.2.1 PDMA microstructures through CDSA

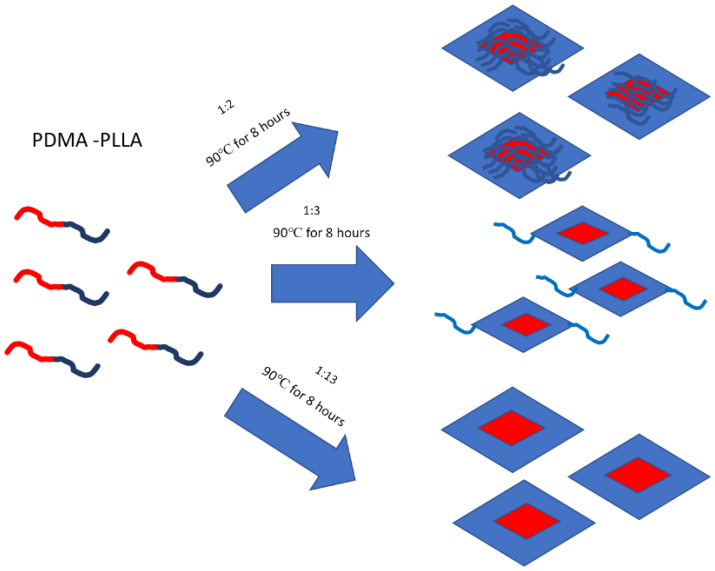
The diblock copolymer PDMA-b-PLLA has been extensively studied by the O'Reilly group and Dove group. [78, 157, 203] Since primary target in this study is a system that can permeate through the BBB, a variety of ratios core: corona will be examined to uncover multiple microstructures of small size.

Table 3.3.3 Library of PDMA-b-PLLA diblock copolymers

Corona	DP	M_n (kDa)	M_w(kDa)	$Đ_M$	Ratio Core: Corona	Fluorescence	Core
DMA	69	5	4	1.24	1:2	Yes	PLLA
DMA	87	15	19	1.10	1:3	No	PLLA
DMA	527	52	71	1.38	1:13	Yes	PLLA

The PDMA-b-PLLA diblock copolymers were synthesized as previously reported (chapter 2) through a ROP and a RAFT polymerization. Full characterization with NMR and GPC can be found in the materials and methods of chapter 2 as well as the synthesis protocol.

With the diblock copolymers above the CDSA process has been conducted as previously reported.[153] The diblock copolymers were introduced in a vial at concentration 5mg/mL with ethanol as solvent and incubated in an oil bath at 90℃ for 8 hours.



Scheme 3.3.1 CDSA of PDMA-b-PLLA in different ratios

In contrast to other findings of platelet nanoparticles,[204, 205] diamond-shaped platelets were produced with same solvent quality (ethanol) for the corona block and high corona to core ratio(13:1), whereas more elongated and poorly defined structures were produced with lower corona to core block ratios(1:1). Shorter corona block copolymers have reduced solubility and thus the tendency to aggregate before crystallisation, limiting the extent to which the crystalline block can adopt a preferred crystal conformation, forming cylindrical assemblies with few crystal defects.[78]

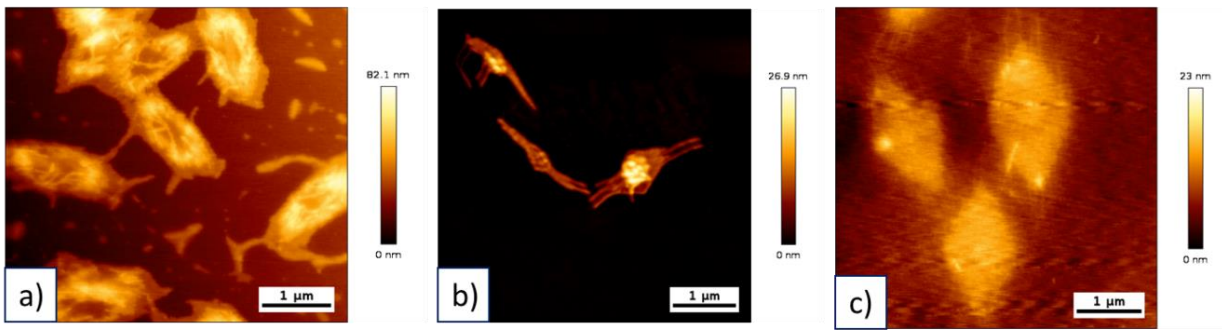


Figure 3.2.14 CDSA microstructures of PDMA-b-PLLA a) $PDMA_{69}$-b-$PLLA_{40}$ 1:2 core : corona ratio, b) $PDMA_{88}$-b-$PLLA_{30}$ 1:3 core : corona ratio, c) $PDMA_{527}$-b-$PLLA_{40}$ 1:13 core : corona ratio.

As depicted from the image above different microstructures were formed when using different core : corona ratio as previously reported.[153] Figure 3.2.14c indicated a diamond-shaped microstructure while having a ratio of 1:13 core : corona, while having a $PLLA_{40}$. Inam *et al* demonstrate a mixed phase of diamonds and cylinders with frequent elongated ends when it comes to the diamond shaped microstructures, while preserving a ratio of 1:12.5 core : corona [153]. The difference in the systems is the length of the PLLA core which will dictate the morphology, since Inam's diblock copolymers carry a $PLLA_{48}$, whereas these polymers had a shorter core of $PLLA_{40}$. The elongated ends system on the diamond shaped microstructure occurs when the system reaches 1 : 3 ratio of core : corona, in contrast with previously reported results indicating a pure cylindrical phase due to crossover composition. [153] Again in the core chemistry remains the same but the length of differs from $PLLA_{48}$ as reported to $PLLA_{30}$ this time, which evidently leading to the conclusion that a smaller core will undergo crystallinity differently. Finally, in figure 3.2.14 a) a peculiar microstructure appears when the system reaches 1: 2 ratio of core : corona, which composed of a cylindrical phase entrapped in the lattice of a diamond shaped crystal. It appears that the crystal's diamond shape serves as a nucleation site or template for the development of the cylindrical phase. A favourable environment or confinement for the assembly of the cylindrical phase may be offered by the diamond-shaped crystal's distinctive lattice structure. The growth of the cylindrical structure might be guided or scaffolded by the diamond-shaped crystal, resulting in their coexistence.[206, 207] Another explanation could be that block copolymers can self-assemble through a number of conflicting methods. The diamond-shaped crystal and cylindrical phase in the PDMA-PLLA system might signify two distinct self-assembly paths that, while both energetically advantageous, take place under various conditions. Both structures may coexist as a result of these processes' competition, where one phase entraps the other.[208]

3.2.2.2 PTEGA microstructures through CDSA

Poly(ethylene glycol)-block-poly(L-lactide) (PEG–PLLA) is a biodegradable copolymer, which is widely applied to medicine and drug systems, and its morphology, organization and mechanical properties have been extensively investigated.[209] While the hydrophilic PEG

blocks remain amorphous in CDSA, the hydrophobic PLLA blocks crystallise into discrete domains.[190] The tendency of PLLA blocks to crystallise and reduce their surface area, which results in the development of distinct microstructures, is the driving force behind self-assembly. The type of microstructures that can be produced depends on a number of variables, including the molecular weight of the building blocks, the block copolymer's composition, and the processing circumstances.[210] Multiple other crystallinities of biocompatible and biodegradable copolymers have been studied like PEO-b-PLLA (poly(ethylene oxide)-block-poly(l-lactide)) [157] and methoxy poly(ethylene glycol)-block-PLLA (MPEG-PLLA).[209, 211] Herein, the study will focus on another member of the ethylene glycol family, poly(Triethylenoglycol)-block-poly(L-lactide) (PTEGA-b-PLLA) It's essential to comprehend PTEGA-b-PLLA's crystalline structures in order to modify the materials' qualities. Many properties, including mechanical strength, thermal stability, and drug release behaviour, are influenced by the arrangement of polymer chains inside the crystalline domains. PTEGA-b-PLLA can perform better in a variety of applications, including as drug delivery systems, scaffolds for tissue engineering, and nanocomposites, by fine-tuning its crystalline structure.

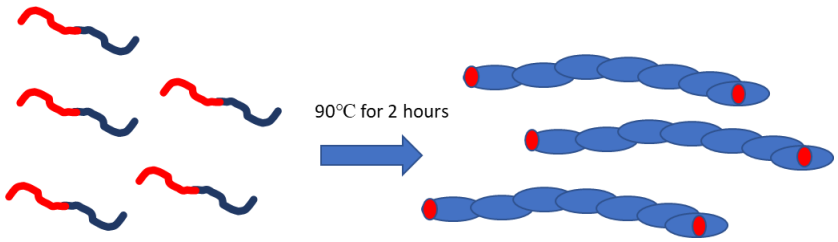
In Chapter 2, the synthesis, characterization and self-assembly of the $PTEGA_{63}$-b-$PLLA_{30}$ took place. The diblock copolymer was synthesized as previously reported (chapter 2) through a ROP and a RAFT polymerization. Full characterization with NMR and GPC can be found in the materials and methods of chapter 2 as well as the synthesis protocol. Here, the same polymer will be utilized to produce CDSA microstructures.

Table 3.3.2. Characterization of $PTEGA_{63}$-b-$PLLA_{30}$ diblock copolymer

Corona	DP	M_n (kDa)	M_w(kDa)	$Đ_M$	Ratio Core: Corona	Fluorescence	Core
TEGA	63	15	20	1.23	1:2	No	PLLA

Similarly with the diblock copolymers above the CDSA process will be conducted as previously reported. The diblock copolymer was introduced in a 7mL vial at concentration 5mg/mL with 2 mL of ethanol as theta solvent and incubated in an oil bath at 90℃ for 2 hours. After the CDSA process the vial left to cool down in room temperature for 1 day.

Ethanol was removed by vacuum and the remaining material was redispersed into water. The zeta potential was calculated to be -17.6 mV but that is because of the interactions of the -OH groups of poly(triethylenoglycol) with the water. The D_h was appear to be 270 nm from the DLS measurement with PD 0.160. This measurement was conducted in room temperature at pH 7.The scheme bellow indicates the procedure and the achieved formulation structure, identified as molecular caterpillar (Scheme 14).



Scheme 14 CDSA of TEGA-b-PLLA

Figure 3.2.15 a) clearly depicts such a formulation of molecular caterpillars. In the figure 3.2.15 b) a linear arrangement of seeds is visible. This line of the repeating units is required for the creation of molecular caterpillar structures. Each seed is approximately 200 nm in length that is connected through interactions with the next one to form the microstructure as presented. The height of the overall microstructure is around 22 nm as it is indicated in the scale bar in figure 3.2.15 a). The length of the molecular caterpillars varies depending on the amount of total seeds connected to the CDSA nanoparticle so it gives as a big length distribution of 1.2 µm- 12µm. The width of the molecular caterpillars also varies between 200nm-400nm, depending on the aggregation format of the seeds.

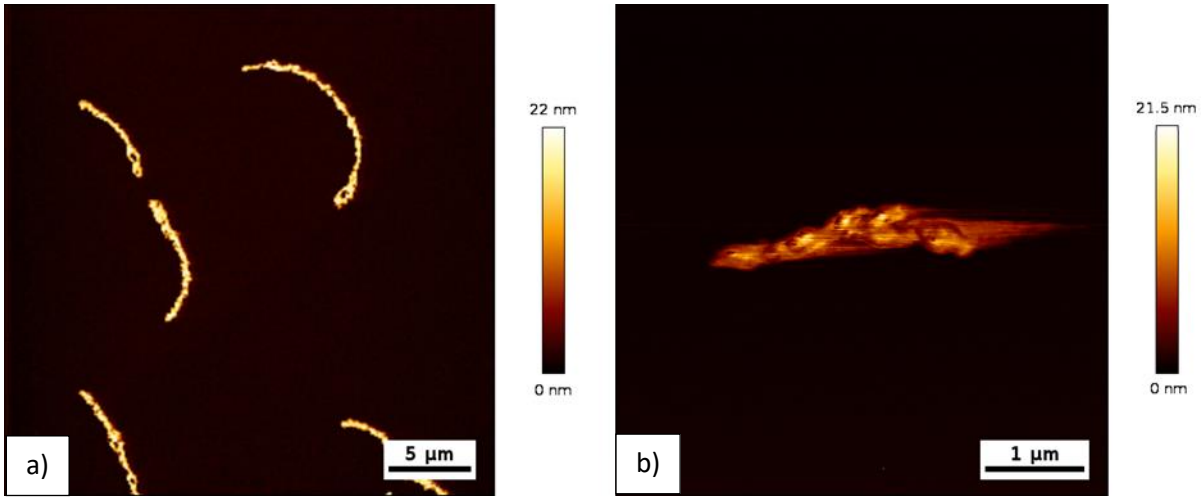


Figure 3.2.15 CDSA microstructure of PTEGA-b-PLLA a) 5µm scale bar b) 1µm scale bar

The small loops that are formed close to the molecular caterpillar tail, could be due to steric interactions. The above microstructure resembles an epitaxial growth of self-nucleation. [207] Depending on the particular system and chemical elements involved, this particular phenomenon can be aided by a variety of interactions such as hydrogen bonding, π-π stacking, or electrostatic interactions.[207] PTEGA carries a lot of -OH groups, which the systems more susceptible of hydrogen bonding. The π-π stacking can not be disqualified as a candidate, but the planar state of the molecular caterpillar should be investigated further.

From the above, we can conclude that the microstructure developed is far from monodisperse so alternative systems should be explored for efficient drug delivery through the BBB. Protein corona studies were not conducted with the neutrally charged structures, since ***Chapter 2*** indicated that there is no protein corona phenomenon forming and no interactions between spherical $PTEGA_{63}$-b-$PLLA_{30}$ and $PDMA_{88}$-b-$PLLA_{30}$. Therefore, to examine the protein corona phenomenon further, negatively charged microstructures should be investigated.

3.2.3 Negatively charged microstructures

3.2.3.1 Negatively charged cylinders

In Chapter 2, the same diblock copolymer $PtBA_{486}$-b-$PLLA_{30}$ was synthesized through a ROP and a RAFT polymerization. Full characterization with NMR and GPC can be found in the materials and methods of chapter 2 as well as the synthesis protocol. As previously reported,[159, 212] the CDSA can happen at the same time with the deprotection of PtBA in one pot and self-assemble, providing the PLLA-b-PAA diblock copolymer microstructure. $PtBA_{486}$-b-$PLLA_{30}$ was added in a THF/H_2O mixture with 20% v/v THF (a good solvent for both blocks) and 6.5 μl of acetic acid, at 65 °C (above the Tg of PLLA) to yield micellar solutions for 30 hours.

Table 3.4.4 Negatively charged cylinders

Corona	DP	M_n (kDa)	M_w(kDa)	$Đ_M$	Ratio Core:corona	Fluorescence	Core
tBA	486	19	22	1.15	1:16	No	PLLA

Unfortunately, as previously the polymer precipitated during the process due to the acidity of the solution. The same CDSA procedure was conducted without the acetic acid but no deprotection occurred.

Since the diblock copolymer of PAA-b-PLLA could not formulate through CDSA, the experiments continued while using a triblock copolymer PAA_{63}-$PLLA_{32}$-PAA_{63} kindly donated by Dr. Wei Yu, which due to its more hydrophilic nature and charge distribution could dissolve and undergo crystallization. The triblock copolymer was synthesized with a ROP, following a RAFT polymerization, to acquire the produced $PtBA_{63}$-b-$PLLA_{32}$-b-$PtBA_{63}$. The tert-butyl ester was deprotected by treatment with trifluoroacetic acid in DCM (TFA/DCM = 1:6 v/v). After the deprotection and purification of the polymer the PAA_{63}-$PLLA_{32}$-PAA_{63} had been synthesized. CDSA was achieved by imputing PAA_{63}-$PLLA_{32}$-PAA_{63} 5mg/mL in methanol

at room temperature for 30 hours. Finally, the methanol was removed and the PAA_{63}-$PLLA_{32}$-PAA_{63} cylinders were redispersed in water. This time the system did not precipitated as the previous one since the polymer was deprotected separately and purified prior to the CDSA process.

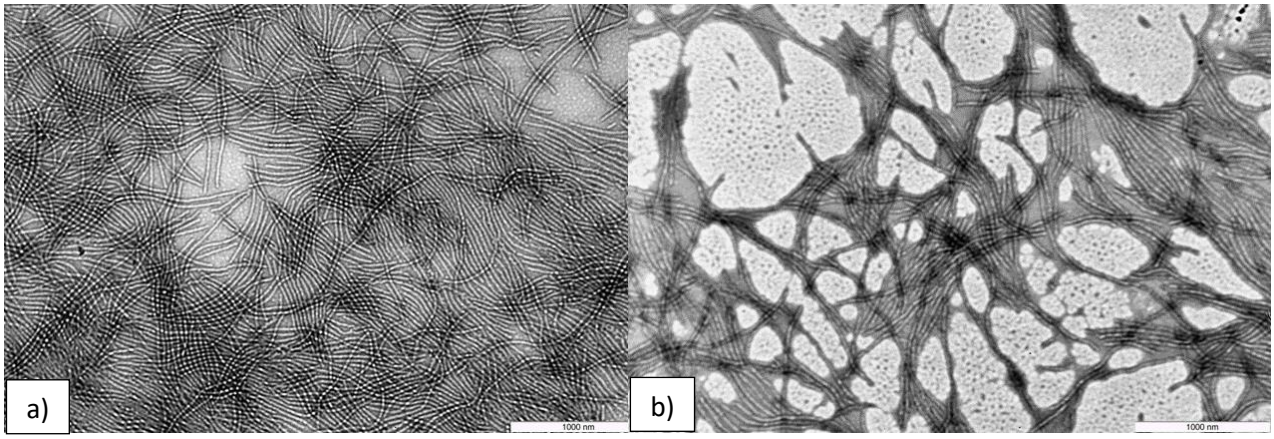


Figure 3.2.16 TEM data of PAA_{63}-b-$PLLA_{32}$-b-PAA_{63} a) 0.2 mg/mL concentration, scale bar 1000nm ,b) 0.05 mg/mL concentration, scale bar 1000nm

From the TEM image above the morphology of the PAA_{63}-$PLLA_{32}$-PAA_{63} appears to be elongated cylinders, more uniform fibres. The width of the microstructures appears to be coherent throughout 12 nm ± 3 nm (calculated by a sample of 100). The length is hard to be calculated since the nanofibers exceed the magnitude used and they are intertwined with each other. Figured 3.2.16 a) seems more dense because of the high concentration in the solution in comparison with b), which is ¼ of the concentration.

3.2.3.2 Protein corona effect of negatively charged cylinders

As previously demonstrated with the positively charged diamonds the electrostatic interactions were examined with a protein in order to examine the protein corona phenomenon. Since in this instance, the cylinders created are negatively charged a positive charged protein was selected for experimentation. Human lysozyme is a globular protein with antimicrobial properties with tendencies to fibrillate and hence is known as a fibril-forming protein.[213] Lysozyme is present in many mucosal secretions (tears, saliva, and

mucus) and tissues of animals and plants, and plays an important role in the innate immunity, providing protection against bacteria, viruses, and fungi.[214] Human lysozyme carries a positive charge of +15 mV when dissolved in distilled water. In order to verify how the positively charged protein influences the negative charged cylinders, a protein corona experiment was conducted. The molecular weight of PAA_{63}-b-$PLLA_{32}$-b-PAA_{63} is 12 g/mol and Human lysozyme is 14300 g/mol. For the cylinders since they are in a solution of 1 mg/mL their molarity was calculated to be 83 nM, and in order to have 1:1 molar ratio of cylinders to protein, lysozyme molarity must be 83 nM, so a solution of lysozyme in water was developed with 1.2 mg/mL that correspond to the molarity needed.

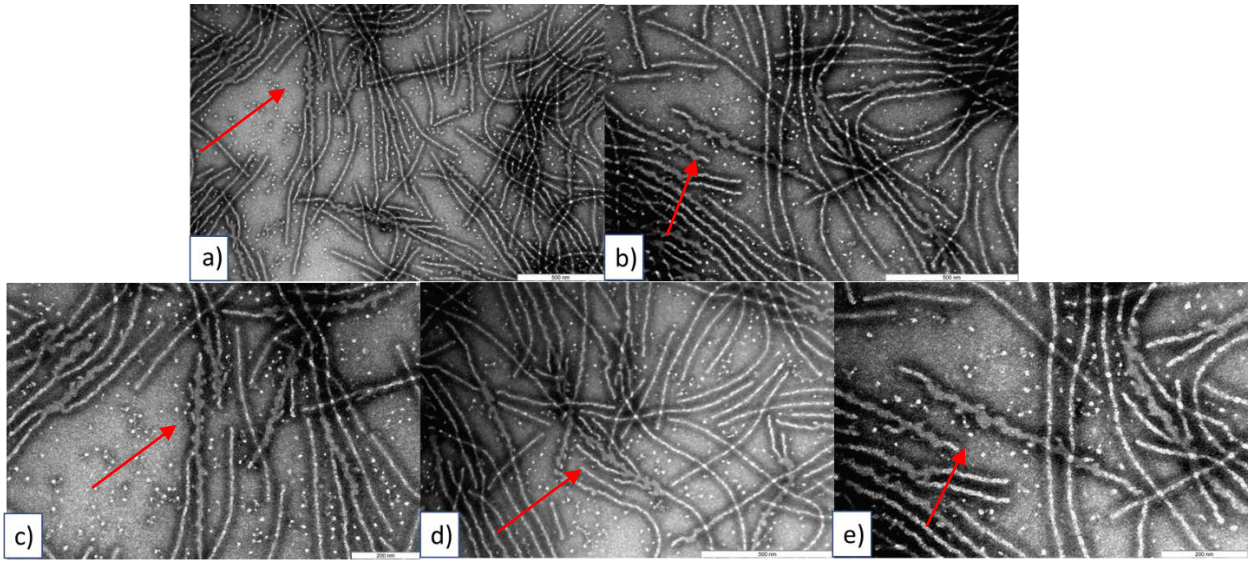


Figure 3.2.17. TEM data of protein corona effect of lysozyme with PAA_{63}-b-$PLLA_{32}$-b-PAA_{63} cylinders 1:1 molar ratio. a,b) scale bar 500 nm, c,d,e) scale bar 200 nm.

From Figure 3.2.17 the interactions between proteins and cylinders are not so obvious. The images appear to have an excess of protein that was to be expected due to the ratio being 4:1. The amount of the free protein though indicates that no soft corona formation is apparent. That could be explained through a variety of reasons such as electrostatic repulsion, kinetic factors, steric hindrance, hydration layer and specificity of protein.[215] The irregularity in some of the cylinders is noticeable, which can be perceived as the protein corona formulation that we were anticipating. In Figure 3.2.17 c) specifically more than 8 cylinders are affected. The lumps created on the cylinders, should be the positively charged

human lysozyme interacting with the negative charged cylinder and due to the electrostatic interactions have caused these excess knots to grow on the cylinder. The width of the modified cylinders is calculated to be 28 ± 7 nm in comparison with the regular cylinders which is 10 ± 2 nm. Also, evidently the zeta potential changed in the solution but that could be just from the addition. The negatively charged particles developed a -20 mV negative charge and after the addition of the lysozyme protein it shifted to -6 mV. Lastly the DLS measurements provide with a D_h = 664 nm for the PAA_{63}-b-$PLLA_{32}$-b-PAA_{63} negative charged cylinders, and with a D_h = 1200 nm after the addition of the protein. Here it has to be noted that the DLS measurements are calculating with the spherical model and the measurements provided were unstable during the runs. From all the above further experimentation is needed in order to verify the exact interactions of the above protein corona examination.

3.3 Conclusions

In this chapter CDSA of diblock copolymers with various charges was examined, in order to create different morphologies for permeation through the BBB. Initially PDMAEMA-b-PLLA diblock copolymers formed diamond shaped microstructures of 1μm, thus it was essential to optimise the system to achieve smaller microstructures. The optimization was found to ruin the crystallinity and homogeneity of the system, even though smaller crystals were developed. An investigation to produced cylindrical micelles using the same positively charge PDMAEMA-b-PLLA by even after 36 hours of incubation, the result was multiple morphologies of seeds and molecular caterpillars.

The studies proceeded, but focusing on the protein corona effect, since chapter 2 had indicated the appearance of one. By characterising the positively charge PDMAEMA-b-PLLA with TEM, AFM, confocal and ITC, the protein corona was verified. A hard protein corona was able to be visualised after dialysing the nanoparticles, and lowering the molar ratio from 4:1 to 1:1 and 0.25:1. Initially the following amount of 4:1 BSA : nanoparticle molar ratio was select due to the overwhelming amount of proteins that exist in the human body, but it caused the positive diamond shaped microstructures to aggregate and precipitate, thus the

molar ratio was shifted to 1:1 and 0.25: 1 BSA: nanoparticle to help with the visualization and examination of the phenomenon. The fact that a screw dislocation effect appeared in our system it made it hard to calculate the height uptake to determine the protein corona adjustment level.

CDSA has proven to be an excellent tool for creating different morphologies. Herein different morphologies of neutrally charged microstructures where developed, but do not agree with the literature due to a difference in the PLLA core. Furthermore, PTEGA neutrally charged microstructure were able to develop molecular caterpillar structures.

Lastly the negatively charged PAA-PLLA-PAA cylinders were investigated for a protein corona effect but it only indicated small deformities in the cylinders width. The reason, why this phenomenon was less intense than with the positive one comes down to charges. The negatively charged particles developed a -20 mV negative charge and after the addition of the lysozyme protein it shifted to -6 mV, which is not a big change, also given to the fact that lysozyme is +15 mV in neutral pH in water solution. In positively charged PDMAEMA-b-PLLA diamond shaped microstructure, the charge given was +42 mV and with the protein corona of BSA changed to -5 mV. With the above statement and data it can be concluded that the electrostatic interactions have different intensity based on the charge of the solution.

In future applications, CDSA can be utilised as a platform for exploring more complicated impacts of nanoparticle shape, a topic that has recently gained a lot of interest. Also the materials' biocompatibility makes them highly suitable for usage in a variety of relevant applications, such as tissue engineering and drug delivery.

APENDIX II

3.4 Experimental

Materials

Chemicals and solvents were purchased from Sigma Aldrich, Acros, Fluka, Fisher Chemical, Alfa Aesar, or VWR.1,4-Dioxane and DMAEMA were purified by passing through basic alumina before use. L-lactide was purified and reduced in dry toluene and dry dichloromethane and after it was sublimed twice before being stored in a glove box. (-)-Sparteine was dried over calcium hydride and distilled before use. Bis[(trifluoromethyl)phenyl]-3-cyclohexylthiourea was prepared as previously reported [42]. 2,2'-azo-bis(isobutyronitrile)AIBN was recrystallized twice from methanol and stored in the dark at 4 °C. Toluene, dichloromethane and tetrahydrofuran were dried using solvent drying towers under a dry N_2 atmosphere.

Instruments

^{1}H NMR & ^{13}C NMR spectroscopy

^{1}H NMR experiments were performed either on a Bruker DPX-400 spectrometer at 400 MHz or a Bruker DPX-300 spectrometer at 300 MHz using deuterated chloroform. Chemical shifts are reported in parts per million (ppm) downfield from trimethylsilane (0 ppm). All spectra were obtained at 25 °C.

Size Exclusion Chromatography (SEC)

SEC measurements were performed in **$CHCl_3$** on an Agilent 1260 Infinity II Multi-Detector GPC/SEC System fitted with RI, ultraviolet (UV, λ = 309 nm), and viscometer detectors. The polymers were eluted through an Agilent guard column (PLGel 5 μM, 50 × 7.5 mm) and two Agilent mixed-C columns (PLGel 5 μM, 300 × 7.5 mm) using $CHCl_3$ (buffered with 0.5% NEt_3) as the mobile phase (flow rate = 1 mL min^{-1}, 40 °C). Number average molecular weights (M_n), weight average molecular weights (M_w) and dispersities ($Đ_M = M_w/M_n$) were determined using Agilent GPC/SEC software (vA.02.01) against a 15-point calibration curve (M_p = 162–3,187,000 g mol^{-1}) based on poly(styrene) standards (Easivial PS-M/H, Agilent) or a 12-point calibration curve (M_p = 550–2,210,000 g mol^{-1}) based on poly(methyl methacrylate) standards (Easivial PM, Agilent).

Size exclusion chromatography (SEC) in **DMF** was performed on an Agilent 1260 Infinity II LC system equipped with a Wyatt DAWN HELEOS II multi-angle laser light scattering (MALLS) detector, a Wyatt Optilab T-rEX differential refractive index detector, an Agilent 1260 Infinity II WR diode array detector, an Agilent guard column (PLGel 5 μM, 50 × 7.5 mm) and two Agilent Mixed-C columns (PLGel 5 μM, 300 × 7.5 mm). The mobile phase was DMF (HPLC grade) containing 5 mM NH_4BF_4 at 50 °C at flow rate of 1.0 mL min^{-1}. Number average molecular weights (M_n), weight average molecular weights (M_w) and dispersities ($Đ_M = M_w/M_n$) were determined using Wyatt ASTRA v7.1.3 software against poly(methyl methacrylate) (PMMA) standards. For molecular weight determination *via* MALLS, dn/dc values were either measured by differential refractometry or calculated from the SEC chromatograms assuming 100% mass elution from the columns.

Size exclusion chromatography (SEC) in **THF** was performed on a system composed of an Agilent 1260 Infinity II LC system equipped with an Agilent guard column (PLGel 5 μM, 50 × 7.5 mm) and two Agilent Mixed-C columns (PLGel 5 μM, 300 × 7.5 mm). The mobile phase used was THF (HPLC grade) containing 2% v/v TEA at 40 °C at flow rate of 1.0 mL min^{-1} (polystyrene (PS) standards used for calibration). Number average molecular weights (M_n), weight average molecular weights (M_w) and dispersity ($Đ_M = M_w/M_n$) were determined using Agilent GPC/SEC software.

Dynamic Light Scattering (DLS)

Hydrodynamic diameters (D_h) of particles were determined by dynamic light scattering (DLS) using a Malvern Zetasizer Nano ZS fitted with a 4 mW He-Ne 633 nm laser module at 25 °C. Measurements were carried out at a detection angle of 173° (back scattering) and the data was analysed using Malvern DTS 7.03 software. All determinations were repeated 5 times. D_h was calculated using the Stokes-Einstein equation where particles are assumed to be spherical. For cylindrical particles, DLS can be used to detect multiple populations and obtain dispersity information.

Zeta potential

Zeta potentials were measured using a Malvern Zetasizer Nano ZS. The zeta potentials of particles in suspension at pH 6.5 were obtained by measuring the electrophoretic mobility of the particles under an applied electric field at 25 °C. All reported zeta potential values were the average of at least three runs with at least 40 measurements recorded for each run. Zeta potential was calculated from the corresponding electrophoretic mobilities (μE) by using the Henry's correction of the Smoluchowski equation ($\mu E = 4\pi \varepsilon 0 \varepsilon r \zeta (1+\kappa r)/6\pi \mu$).

Fluorescence Spectroscopy

Steady-state fluorescence spectra of emission and excitation were recorded using an Edinburgh Instruments FS5 Spectrofluorometer. Quartz cells 3.5 mL cuvettes with screw caps and four polished sides (Starna Cell, Type: 3/Q/10), were used for fluorescence measurements. The analysis was conducted in Fluoracle (Edinburgh Instruments) and Origin 2019 (Origin Labs).

Atomic Force Microscopy (AFM)

Atomic force microscopy (AFM) was performed on a JPK Nanowizard 4 system at room temperature in the supplied acoustic enclosure and vibration isolation using Nanosensor PPP-NCHAuD tips with a force constant of around 42 $N \cdot m^{-1}$. For data acquisition and

handling Nanowizard Control and Data Processing Software V.6.1.117 in QI mode with a setpoint of *25 nN* was used. Samples were prepared on freshly cleaved mica by drop-casting 5ul a solution of *0.2 mg·mL*$^{-1}$ sample in water, settling for 10 mins, removing of excess solution and subsequent drying under compressed air over night.

Confocal Microscopy

Experiments were carried out using an Olympus FV3000 confocal fluorescence microscope. Samples were imaged using a 60 X magnification and exciting using a multi-wavelength nm laser. Z-stacks with an average thickness of 30 µm were collected from different zones of the samples and maximum intensity projections were obtained from each Z-stack. Freshly prepared and purified solutions of FAM-NHS-loaded (green-emitting dye), Cy5-NHS-loaded (red-emitting dye) and diblock copolymer nano-objects at 100-fold dilution were deposited on a glass slide and imaged by confocal laser scanning microscopy (CLSM) after evaporation of the solvent. Images were acquired using an Olympus FV3000 confocal laser Scanning Microscope. Samples were imaged at 60× magnification upon excitation using a 488 nm laser (green channel) and a 640 nm laser (red channel). Images were processed using cellSens (Olympus) and ImageJ image processing software.

Transmission Electron Microscopy (TEM)

Dry-state stained transmission electron microscopy (TEM) imaging was performed on a JEOL JEM-1400 microscope operating at an acceleration voltage of 80 kV. All dry-state samples were diluted with deionized water to appropriate analysis concentration (0.01% w/w solids content) and then deposited onto formvar-coated copper grids. After roughly 1 min, excess sample was blotted from the grid and the grid was stained with an aqueous 1 wt% uranyl acetate (UA) solution for 1 min prior to blotting, drying and microscopic analysis. TEM images were analysed by ImageJ software, where at least 100 particles were counted for each sample to obtain the number-average length.

Isothermal Titration Calorimetry (ITC)

Isothermal titration calorimetry (ITC) was performed in the MicroCal PEAQ-ITC by Malvern. 2 water to water titrations must be done before and after you clean the machine. Blank Method BSA. Adjust molar ratio to appropriate for better sensitivity. One binging side method. Preparation of clear sample, filtrate with 0.45 µm filter before run to avoid dust residues. Fix molar ratio depending on the sample.

Methods

Synthesis of poly(L-lactide) and poly(D,L-lactide)

In a nitrogen-filled glove box, a solution of 1,8-Diazabicyclo(5.4.0)undec-7-ene (DBU)(2.80 mg, 0.0184mmol) and 2- cyano-5-hydroxypentan-2-yl ethyl carbonotrithioate (12.7 mg, 0.0511 mmol) in dry CH_2Cl_2 (1 mL) were added to a solution of *L*-lactide (265.2 mg, 1.84 mmol) or *D,L*-lactide (265.2 mg, 1.84 mmol) in dry CH_2Cl_2 (1 mL). After stirring for 4 minutes at room temperature, the solution was removed from the glove box and precipitated two times into ice-cold n-hexane and one time into diethyl ether. The resultant yellow polymer was filtered and dried under vacuum for two days. Mn, NMR = 5.6 kDa,, DP = 37, Mn SEC =11 kDa, ,ÐM = 1.12. ^{1}H NMR (CDCl3): δ (ppm) 5.30 (q, 74H, $^3J_{H\text{-}H}$ = 7.0 Hz, OCH(CH_3)CO) 4.31 (q, 1H $^3J_{H\text{-}H}$ = 7.0 Hz, CH(CH_3)OH), 4.22 (t, 2H, OCH_2) 3.37 (t, 2H, $^3J_{H\text{-}H}$ = 6.3 Hz, SCH_2) 1.75 (s, 3H, (CN)CCH_3) 1.20- 1.30 (m, 4H, C_2H_4) 1.60 (d, 226H, $^3J_{H\text{-}H}$ = 7.0 Hz, CH_3CHO)), 1.27 (t, 3H, $^3J_{H\text{-}H}$ = 7.40 Hz, CH_3CH_2S).

Synthesis of poly(*L*-lactide) and poly(D,L-lactide) with fluorescent ACM probe

A typical ROP polymerization as previously described was conducted. The only difference is the CTA with the ACM probe adjusted. Mn, NMR = 5.8 kDa,, DP = 36, Mn SEC =11 kDa, ,ÐM = 1.11. ^{1}H NMR (CDCl3): δ (ppm) 5.68 (br t , 1H, *H*NCH_2), 5.30 (q, 72 H, $^3J_{H\text{-}H}$ = 7.06 Hz, OC*H*(CH_3)CO) 4.28 (m, 3H,CH_2CH_2OCO + C*H*(CH_3)OH), 3.81(br m,2H, HNCH_2CH_2), 3.48 (t, 2H, , $^3J_{H\text{-}H}$ = 6.53 Hz, SCH_2) 3.26 (q, 2H, $^3J_{H\text{-}H}$ = 7.57 Hz, CH_2CH_2NCO) 1.77 (s, 3H, (CN)CCH_3) 1.75-

1.60(d, 2H, $^{3}J_{H\text{-}H}$ = 7.09 Hz, $CH_3CH_2CH_2$), 1.50 (d, 250H, $^{3}J_{H\text{-}H}$ = 7.12 Hz, CH_3CHO), 1.43 (m, 2H, $CH_2CH_2CH_2N$), 1.27 (t, 3H, $^{3}J_{H\text{-}H}$ = 7.40 Hz, CH_3CH_2S).

The ROP of L-lactide & DL- lactide was carried out in a nitrogen-filled glove box to avoid any unwanted initiation from water in the atmosphere with 1,8-Diazabicyclo(5.4.0)undec-7-ene (DBU) as a catalyst and the bifunctional initiator with the ACM probe attached.

Synthesis of poly(L-lactide)$_{36}$-b-poly(N,N-dimethylaminoethyl methacrylate)$_{204}$ with fluorescent ACM probe

A typical RAFT polymerization was conducted as previously described with the only difference being the reaction time instead of 6 hours to 4 hours and 30 minutes. The conversion reached was 55.6 %. Mn, NMR = 37.8 kDa, DP = 206. Mn, SEC = 34.8 kDa, ĐM = 1.34. ^{1}H NMR (CDCl3): δ (ppm) 5.18 (q, 36H, $^{3}J_{H\text{-}H}$ = 7.04 Hz, OC*H*(CH3)CO) 4.09 (br s, 206H, OC*H2*CH2N) 2.59 (br t, 211H, C*H2*N(CH3)2) 2.32 (d, 634H, N(C*H3*)2) 2.00-1.84 (br d, 327H, (CH3)CC*H2*, C*H2*S) 1.60 (d, 114 H, 3*J*H-H = 7.02 Hz, C*H3*CHO) 1.59-0.90 (m, 346H, C*H3*C(CN)C3*H6*, C*H3*CH2S, (C*H3*)CCH2).

Synthesis of poly(L-lactide)$_{37}$-b-poly(N,N-dimethylaminoethyl methacrylate)$_{225}$

$PLLA_{37}$, (95.6 mg, 17.6 µmol), N,N-dimethylaminoethyl methacrylate, (1000 mg, 6360 µmol) and AIBN (28.9 µL of a 10 mg mL-1 solution in 1,4-dioxane) were dissolved in 1,4-dioxane (2.14 mL) before transferring to a dried ampoule under nitrogen. After three freeze-pump-thaw cycles, the solution was sealed under nitrogen and heated for 6 hours at 70 °C for 60% conversion. The reaction was quenched in liquid nitrogen and purified by precipitation three times into cold ice-cold n-hexane. The resultant pale yellow solid was dried in vacuo before use. Mn, NMR = 35 kDa, DP = 225. Mn, SEC = 32 kDa, ĐM = 1.41. ^{1}H NMR (CDCl3): δ (ppm) 5.16 (q, 37H, $^{3}J_{H\text{-}H}$ = 6.9 Hz, OC*H*(CH3)CO) 4.05 (br s, 225 H, OC*H2*CH2N) 2.56 (br s, 382H, C*H2*N(CH3)2) 2.28 (s, 716H, N(C*H3*)2) 1.75-2.05 (br d, 196H, (CH3)CC*H2*, C*H2*S) 1.75 (d, 119H $^{3}J_{H\text{-}H}$ = 6.9 Hz, C*H3*CHO) 1.05-0.75 (m, 383H, C*H3*C(CN)C3*H6*, C*H3*CH2S, (C*H3*)CCH2).

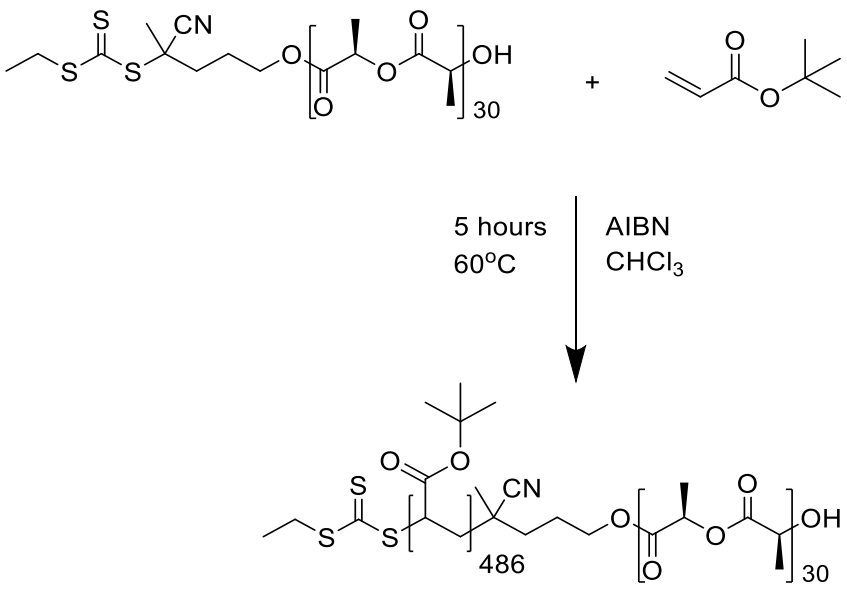
Synthesis of poly(*L*-lactide)$_{36}$-b-poly(N,N-dimethylaminoethyl methacrylate)$_{204}$ with fluorescent ACM probe

A typical RAFT polymerization was conducted as previously described with the only difference being the reaction time instead of 6 hours to 4 hours and 30 minutes. The

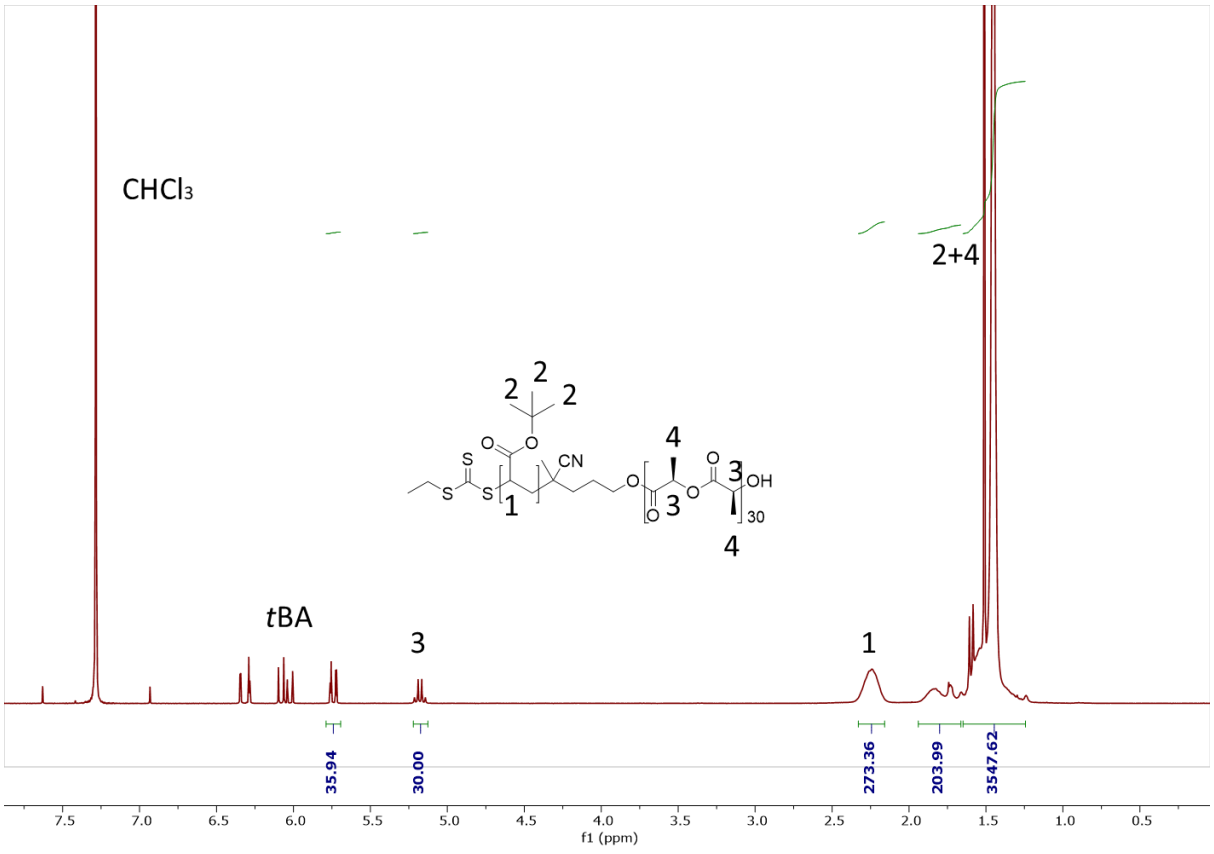
conversion reached was 55.6 %. Mn, NMR = 37.8 kDa, DP = 206. Mn, SEC = 34.8 kDa, ĐM = 1.34. ^{1}H NMR (CDCl3): δ (ppm) 5.18 (q, 36H, $^{3}J_{H\text{-}H}$ = 7.04 Hz, OC*H*(CH3)CO) 4.09 (br s, 206H, OC*H2*CH2N) 2.59 (br t, 211H, C*H2*N(CH3)2) 2.32 (d, 634H, N(C*H3*)2) 2.00-1.84 (br d, 327H, (CH3)CC*H2*, C*H2*S) 1.60 (d, 114 H, 3*J*H-H = 7.02 Hz, C*H3*CHO) 1.59-0.90 (m, 346H, C*H3*C(CN)C3*H6*, C*H3*CH2S, (C*H3*)CCH2).

Synthesis of Poly(L-Lactide)-*b*-Poly(*tert*-Butyl Acrylate)

The RAFT polymerization of *tert*-butyl acrylate was performed. The polymerization was carried out in a 10 mL ampoule containing a magnetic stir bar and fitted with a rubber septum. The monomer, tBA (399 mg, 3118 µmol), was added to the vial containing the PLLA macro CTA (25 mg, 5.4 µmol, tBA/CTA = 571) in chloroform (0.5 mL). The initiator, AIBN (0.9 mg, 0.55 µmol, AIBN/CTA = 0.10), was finally added and 3 cycles freeze pump thaw where executed for 10 minutes per cycle, as the degassing method. After stirring for 5 hours in a 70 °C oil bath, the solution appeared to be viscous and was quenched by freezing the solution. An aliquot was removed and dissolved in CDCl3 to determine the monomer conversion through 1H NMR analysis [monomer conversion = 85% by comparison of the 1H NMR signals of the vinylic monomer (6.29, 6.04, and 5.72 ppm, 3H, integration = 1.00) to the methine polymer backbone signal (2.36–2.10 ppm, 1H, integration = 6.60)]. The viscous solution was dissolved in DCM and precipitated into a cold methanol/water (1:1 v/v) mixture three times and vacuum dried. Yield: 250 mg (62%) 1H NMR (THF-d8): □(ppm, integrated peak areas are based on C6H4 = 4H as the reference) 7.31–7.12 (q, 4H, Ar*H*, integration = 4.00), 5.25–5.07 (q, 1H, PLLA backbone methine, integration = 30), 2.38–2.19 (br, 1H, PtBA backbone methine, integration = 486.20), 1.92–1.78 (br, end group, integration = 29.52), 1.66–1.50 (m, PLLA backbone methyl, integration = 394.18), 1.50–1.38 (s, *tert*-butyl ester, integration = 867.65), 1.38–1.24 (br, end group, integration = 43.54). The degree of polymerization was calculated by comparing the integration of the 1H NMR signals at 5.25–5.07 (PLLA backbone) to that at 2.38–2.19 ppm (PtBA backbone) DPPLLA = 30, and DPPtBA = 486; GPC (THF, RI) *M*n = 79 kDa, *M*w/*M*n = 1.1.

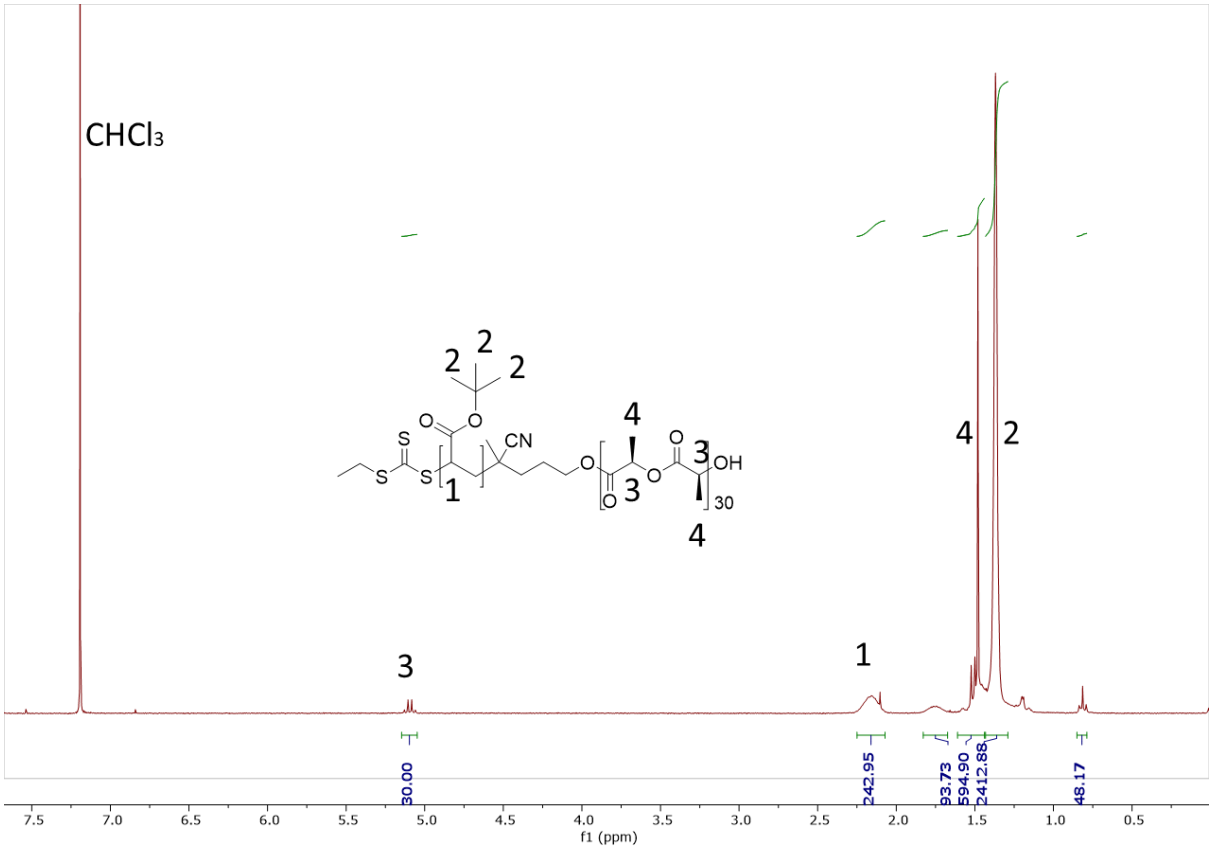


Crude ^{1}H NMR



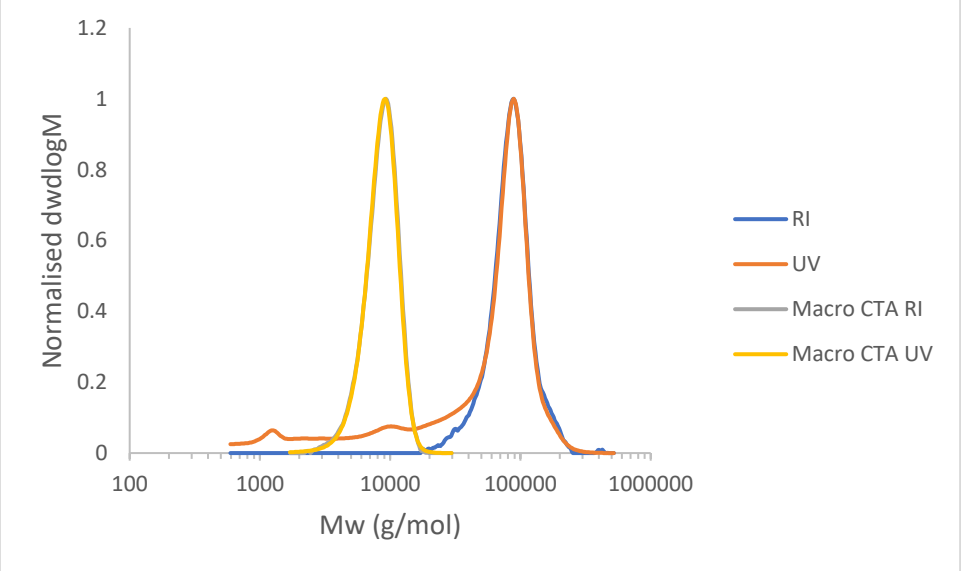
The crude NMR revealed that the conversion reached 85% after 5 hours, instead of the targeted 70%, which we usually get at 5 hours. Next time the kinetics of the reaction will be measured in order to verify our results.

Clean ^{1}H NMR



The proton NMR spectrum presents the degree of polymerization (DP) to be 486 as calculated from peak 1 which corresponds to 1 proton and from peak 3 which corresponds to 2 protons from our Macro CTA PLLA.

$CHCl_3$ GPC



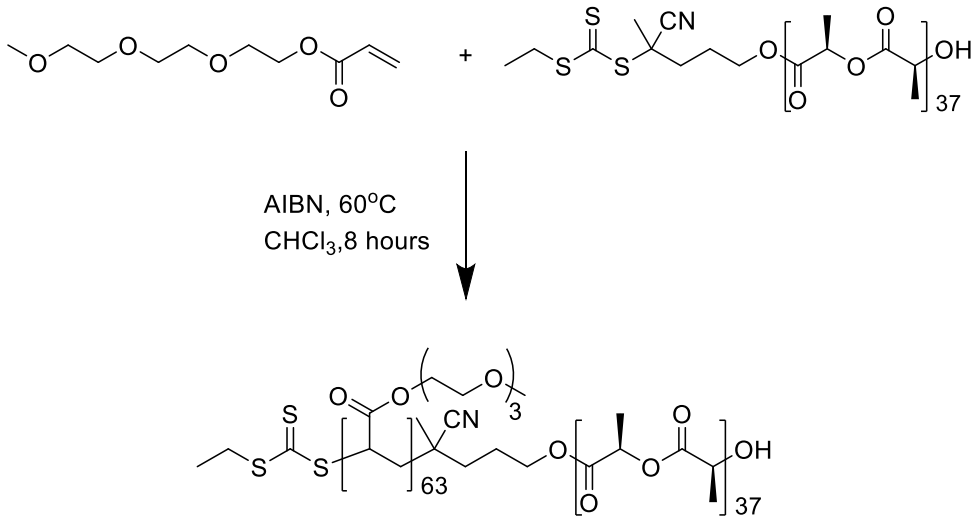
SEC analysis revealed a M_n of 76 KDa and a dispersity $Đ_M$ = 1.17 calculated from the refrective index data. From the UV trace a tail can be observed which can be attributed to any residual solvent, but in order to verify the sample will be dried and repeated. (λ=309 nm)

Similarly the other polymers with various corona chemistries were synthesised.

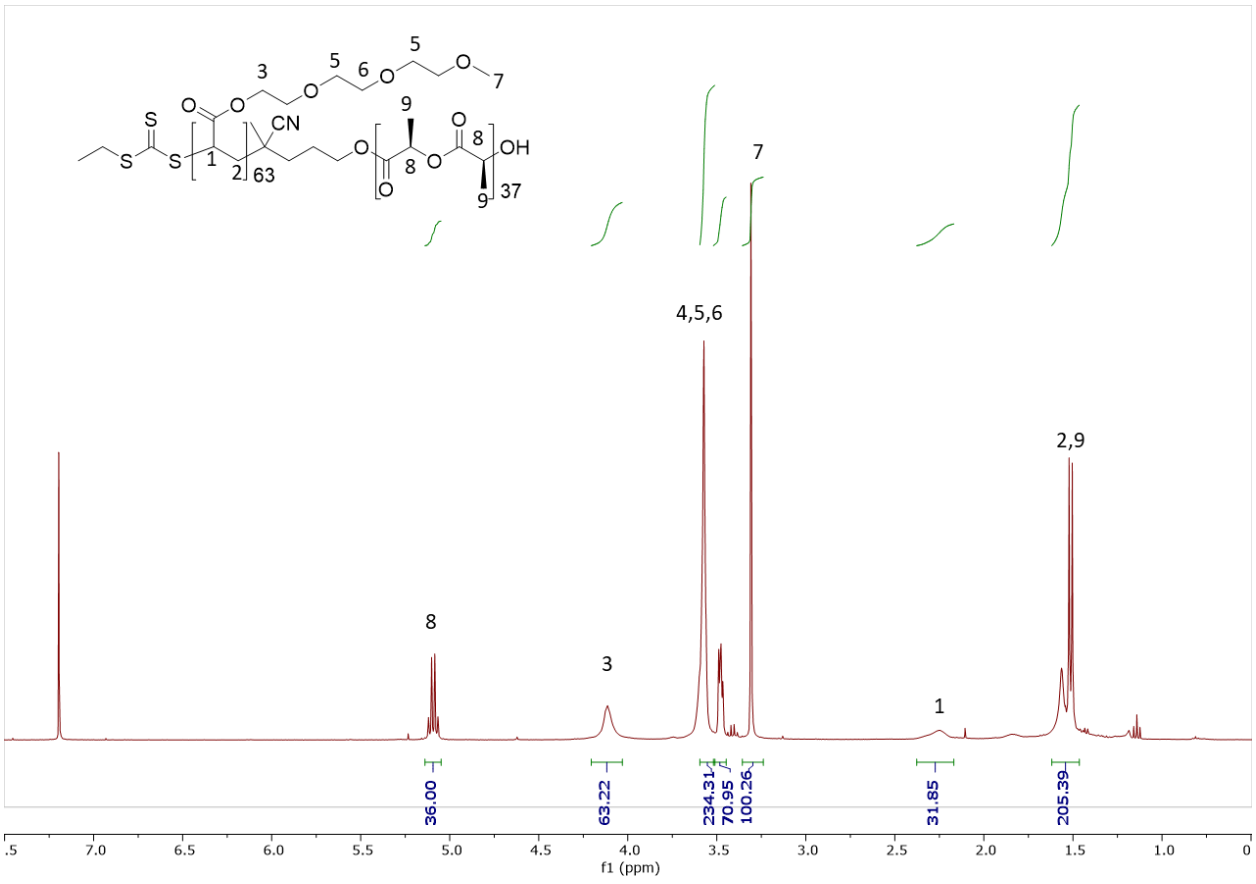
Table 1. Synthesis of diblock copolymers with different corona chemistry with crystalline (PL LA) core and amorphous (PDLLA) core

Corona	**DP**	**M_n (kDa)**	**M_w (kDa)**	**$Đ_M$**	**Ratio Core:corona**	**Fluorescence**	**Core**
DMAEMA	204	35	31	1.31	1:6	Yes	PLLA
DMAEMA	225	32	34	1.41	1:6	No	PLLA
TEGA	82	9	10	1.18	1:2	Yes	PLLA
TEGA	63	15	20	1.23	1:2	No	PLLA
DMA	87	15	19	1.10	1:3	No	PLLA
DMAEMA	200	25	31	1.20	1:6	Yes	PDLLA
DMAEMA	199	26	34	1.27	1:6	No	PDLLA
TEGA	28	9	10	1.18	1:1	Yes	PDLLA
TEGA	65	15	20	1.30	1:2	No	PDLLA
DMA	57	15	19	1.23	1:2	Yes	PDLLA
DMA	114	18	21	1.12	1:3	No	PDLLA
NIPAM	85	8	9	1.19	1:3	Yes	PDLLA

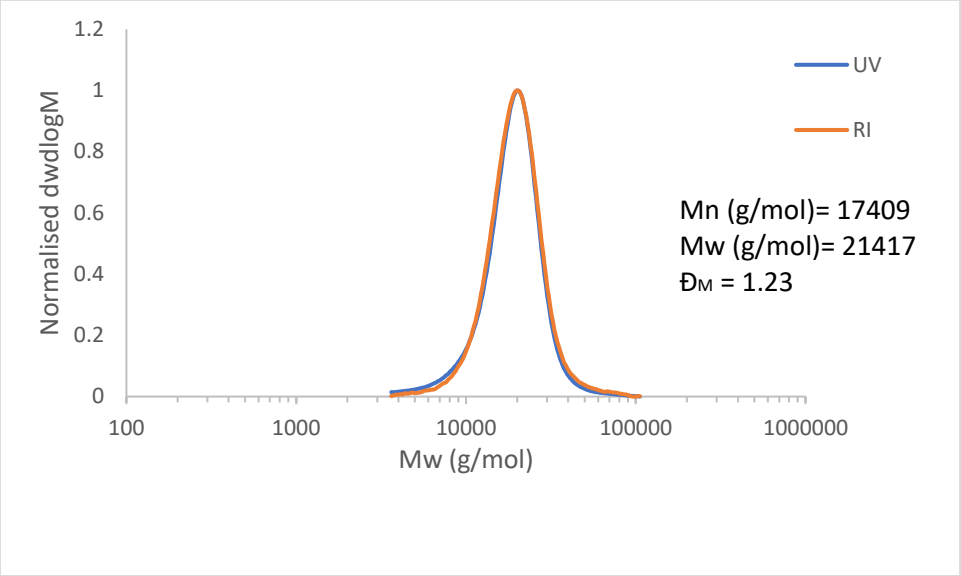
PTEGA$_{63}$-b-PLLA$_{37}$



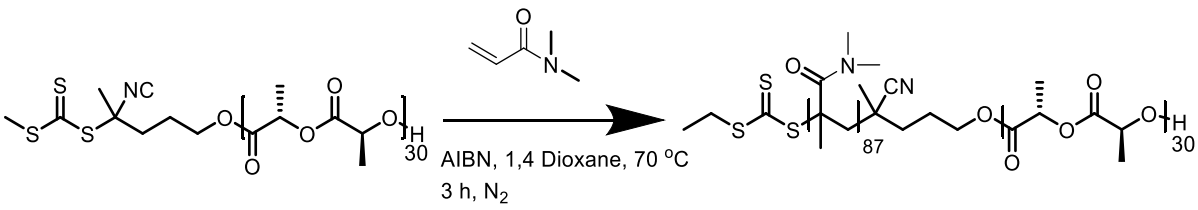
CLEAN ^{1}H NMR



$CHCl_3$ GPC



$PLLA_{30}$-b-$PDMA_{87}$

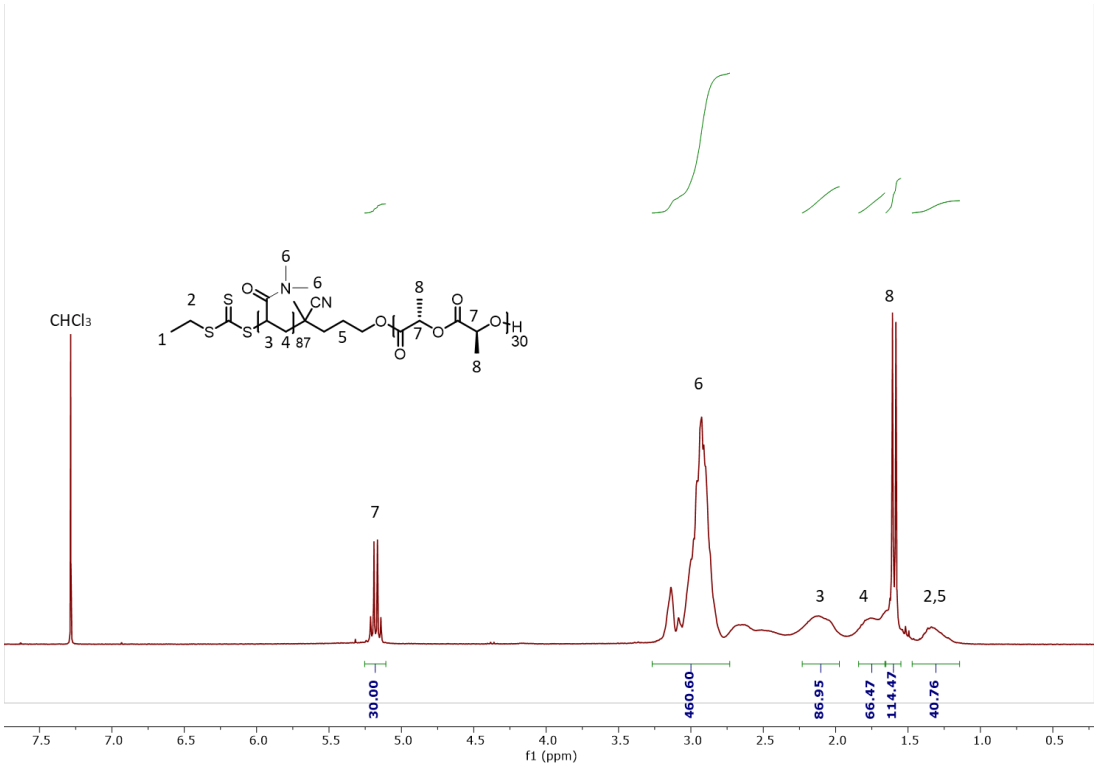


RAFT polymerization of PDMA

The conversion aimed was 60% from crude NMR we get a conversion of 58%.

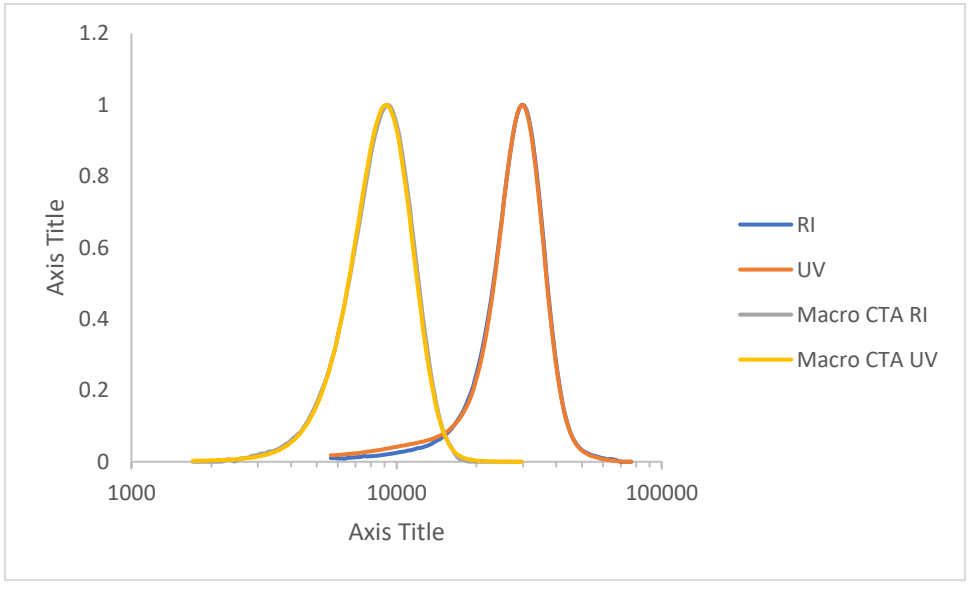
Reaction	Time	DP	Conversion	Mn(kDa)	Mw(kDa)	ĐM
$PLLA_{30}$-b-$PDMA_{87}$ (EE88)	3 hrs	87	58 %	26	28	1.1

CLEAN ^{1}H NMR



^{1}H NMR spectra (300MHz) of clean $PLLA_{30}$-b-$PDMA_{87}$

$CHCl_3$ GPC



Representation of Molecular weight distribution from chloroform GPC (λ=309 nm)of poly(L-lactide)$_{30}$-b-poly(N,N-dimethylacrylamide)$_{87}$ diblock copolymers

Typical crystallisation-driven self-assembly method for poly(L-lactide)$_{30}$-b-poly(N,N-dimethylacrylamide)m block copolymers

PLLA$_{30}$-*b*-PDMAm (10 mg) was added to 2 mL of ethanol (5.0 mg mL-1) in a 7 mL vial. The samples were heated in an oil bath at 90 °C without stirring for an 8 hours period of time before being removed from the oil bath and left to cool to room temperature. Samples were imaged after 1 day of ageing at room temperature.

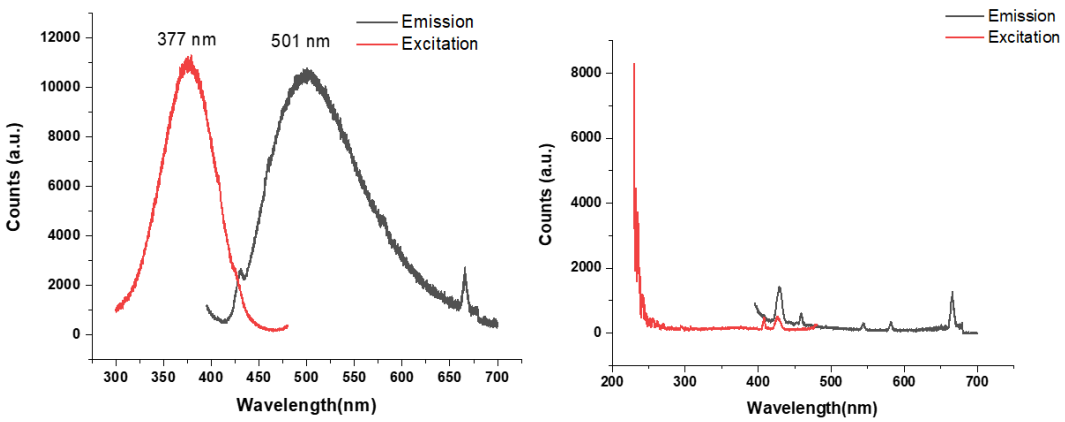
Typical crystallisation-driven self-assembly of poly(L-lactide)$_{30}$-b-poly(N,N dimethylaminoethyl methacrylate)$_{204}$ in alcoholic solvents

PLLA$_{30}$-*b*-PDMAEMA$_{204}$ (10 mg) was added to 2 mL of ethanol (5.0 mg mL-1) in a 7 mL vial. The samples were heated in an oil bath at the specified temperature without stirring for a predetermined period before being removed from the oil bath and left to cool to room temperature. Samples were imaged after 1 day of ageing at room temperature.

Typical preparation of poly(L-lactide)$_{36}$-b-poly(acrylic acid)$_{476}$ cylindrical micelles

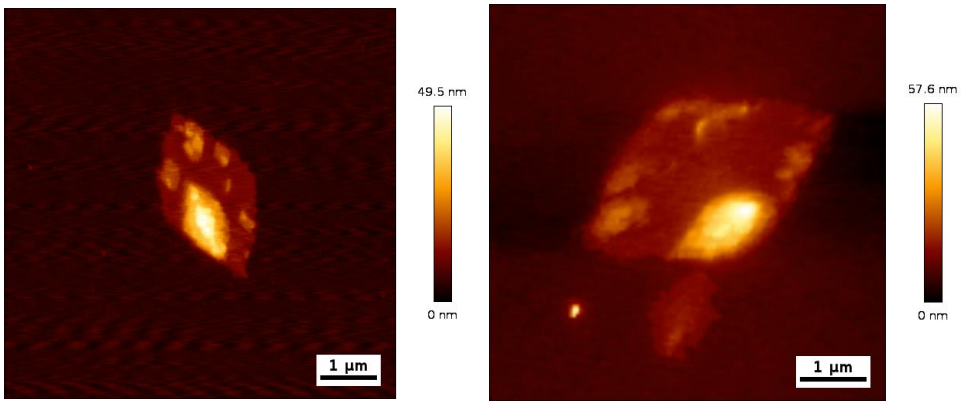
18.2 MΩ·cm water (2 mL) was added to a solution of PLLA$_{30}$-*b*-PTHPA$_{476}$ (50 mg, 0.956 µmol) in THF (0.5 mL) using a peristaltic pump at 0.6 mL hr-1. After addition of acetic acid (16.8 µL, 286 µmol), the reaction was sealed with a needle hole and heated at 65 °C for 30 hours. The reaction was quenched in liquid nitrogen and lyophilised.

Below the graph verifies that the fluorescence is preserved after the CDSA process.



Excitation and emission graphs of PDMAEMA-b-PLLA diamond shapes microstructures with and without ACM probe.

AFM data before and after the protein corona effect $PDMAEMA_{204}$-b-$PLLA_{36}$



AFM data of $PDMAEMA_{204}$-b-$PLLA_{36}$ diamond shapes microstructures with ACM probe without BSA (left) with BSA 1:1 after dialysis (right)

These data were not presented because the screw dislocation can affect the height distribution so we cannot examine the protein corona build up on the diamond structure.

3.5 References

1. N. Poovaiah, Z. Davoudi, H. Peng, B. Schlichtmann, S. Mallapragada, B. Narasimhan and Q. Wang, *Nanoscale*, 2018, **10**, 16962-16983.
2. M. D. Sweeney, Z. Zhao, A. Montagne, A. R. Nelson and B. V. Zlokovic, *Physiol Rev*, 2019, **99**, 21-78.
3. E. Zenaro, G. Piacentino and G. Constantin, *Neurobiol Dis*, 2017, **107**, 41-56.
4. M. D. Sweeney, A. P. Sagare and B. V. Zlokovic, *Nat Rev Neurol*, 2018, **14**, 133-150.
5. J. Baskin, J. E. Jeon and S. J. G. Lewis, *Journal of Neurology*, 2021, **268**, 1981-1994.
6. W. M. Pardridge, *Expert Opinion on Drug Delivery*, 2016, **13**, 963-975.

7. A. Mishra, R. Kumar, J. Mishra, K. Dutta, P. Ahlawat, A. Kumar, S. Dhanasekaran, A. K. Gupta, S. Sinha, D. K. Bishi, P. K. Gupta and S. Nayak, *Journal of Drug Delivery Science and Technology*, 2023, **86**, 104694.
8. D. E. Nayab, F. U. Din, H. Ali, W. A. Kausar, S. Urooj, M. Zafar, I. Khan, K. Shabbir and G. M. Khan, *J Nanobiotechnology*, 2023, **21**, 477-493.
9. A. Janesick, S. C. Wu and B. Blumberg, *Cellular and Molecular Life Sciences*, 2015, **72**, 1559-1576.
10. S. L. B. Oliveira, M. M. Pillat, A. Cheffer, C. Lameu, T. T. Schwindt and H. Ulrich, *Cytometry Part A*, 2013, **83A**, 76-89.
11. B. Srinageshwar, M. Florendo, B. Clark, K. Johnson, N. Munro, S. Peruzzaro, A. Antcliff, M. Andrews, A. Figacz, D. Swanson, G. L. Dunbar, A. Sharma and J. Rossignol, *Pharmaceutics*, 2020, **12**, 619-631.
12. Y. Zhou, Z. Peng, E. S. Seven and R. M. Leblanc, *Journal of Controlled Release*, 2018, **270**, 290-303.
13. H. Luo and E. V. Shusta, *Pharmaceutics*, 2020, **12**, 1085.
14. C. W. Fong, *The Journal of Membrane Biology*, 2015, **248**, 651-669.
15. C. Saraiva, C. Praça, R. Ferreira, T. Santos, L. Ferreira and L. Bernardino, *Journal of Controlled Release*, 2016, **235**, 34-47.
16. R. G. R. Pinheiro, A. J. Coutinho, M. Pinheiro and A. R. Neves, *Int J Mol Sci*, 2021, **22**, 11654-11666.
17. D. Wu, Q. Chen, X. Chen, F. Han, Z. Chen and Y. Wang, *Signal Transduction and Targeted Therapy*, 2023, **8**, 217-230.
18. C. Jiang, Y. Zhou, R. Chen, M. Yang, H. Zhou, Z. Tang, H. Shi and D. Qin, *Pharmaceutics*, 2023, **15**, 2669-2678.
19. P. K. Pandey, A. K. Sharma and U. Gupta, *Tissue Barriers*, 2016, **4**, e1129476.
20. Y. Zhou, Z. Peng, E. S. Seven and R. M. Leblanc, *J Control Release*, 2018, **270**, 290-303.
21. A.-C. Lussint, *Fluids and Barriers of the CNS*, 2012, **23**, 21-32.
22. D. J. Begley, *Pharmacology & Therapeutics*, 2004, **104**, 29-45.
23. C. Saraiva, *Journal of Controlled Release*, 2016, **235**, 34-47.
24. T. Patel, *Adv Drug Deliv Rev*, 2012 May 15, **64**, 701-705.
25. D. M. Teleanu, C. Chircov, A. M. Grumezescu, A. Volceanov and R. I. Teleanu, *Pharmaceutics*, 2018, **10,** 269-285.
26. T. T. Zhang, *Biomaterial Science*, 2016, **4**, 119-129.
27. E. Nance, *J Control Release*, 2014, **189**, 123-132.
28. D. M. Teleanu, C. Chircov, A. M. Grumezescu, A. Volceanov and R. I. Teleanu, 2018, **10**, 269-285.
29. V. Cena, *Nanomedicine*, 2018, **13**, 1513-1516.
30. X. Dong, *Theranostics*, 2018, **8**, 1481-1493.
31. R. L. Roberts, R. E. Fine and A. Sandra, 1993, **104**, 521-532.
32. L. Aloe, P. Bianchi, A. De Bellis, M. Soligo and M. L. Rocco, *Neural Regen Res*, 2014, **9**, 1025-1030.
33. P. Rivera-Gil, *Accounts of chemical research*, 2013, **46**, 743–749.
34. T. C. H Ou , Y. Zhang *Acta Biomater*, 2018, **65**, 339–348
35. Y. W. Yating Zhao, Fu Ran, Yu Cui, Chang Liu, Qinfu Zhao, Yikun Gao, Da Wang & Siling Wang, *Scientific Reports*, 2017, **7**.
36. X. Li, *Journal of Drug Targeting*, 2016, **25**, 17–28.
37. C. M. Plummer, L. Li and Y. Chen, *Macromolecules*, 2023, **56**, 731-750.
38. E. Balla, V. Daniilidis, G. Karlioti, T. Kalamas, M. Stefanidou, N. D. Bikiaris, A. Vlachopoulos, I. Koumentakou and D. N. Bikiaris, *Polymers (Basel)*, 2021, **13**, 1822-1835.

39. A. Peterson, R. Hador, M. Pink, Y. Popowski, M. Kol and W. B. Tolman, *Journal of the American Chemical Society*, 2022, **144**, 20047-20055.
40. J. O. C. de França, D. da Silva Valadares, M. F. Paiva, S. C. L. Dias and J. A. Dias, *Polymers (Basel)*, 2022, **14,** 2317-2329.
41. I. Nifant'ev and P. Ivchenko, *Polymers (Basel)*, 2019, **11**, 2078.
42. A. P. Dove, *ACS Macro Letters*, 2012, **1**, 1409-1412.
43. S. Perrier, *Macromolecules*, 2017, **50**, 7433-7447.
44. A. Postma, T. P. Davis, G. Moad and M. S. O'Shea, *Macromolecules*, 2005, **38**, 5371-5374.
45. N. P. Truong, G. R. Jones, K. G. E. Bradford, D. Konkolewicz and A. Anastasaki, *Nature Reviews Chemistry*, 2021, **5**, 859-869.
46. F. M. Winnik, A. R. Davidson, G. K. Hamer and H. Kitano, *Macromolecules*, 1992, **25**, 1876-1880.
47. E. M. Todd and S. C. Zimmerman, *Journal of the American Chemical Society*, 2007, **129**, 14534-14535.
48. M. H. Stenzel, *Chemical Communications*, 2008, DOI: 10.1039/B805464A, 3486-3503.
49. K. E. B. Doncom, L. D. Blackman, D. B. Wright, M. I. Gibson and R. K. O'Reilly, *Chemical Society Reviews*, 2017, **46**, 4119-4134.
50. Y. Mai and A. Eisenberg, *Chemical Society Reviews*, 2012, **41**, 5969-5985.
51. A. Blanazs, S. P. Armes and A. J. Ryan, 2009, **30**, 267-277.
52. J. K. Oh, *Polylactide (PLA)-based amphiphilic block copolymers: Synthesis, self-assembly, and biomedical applications*, 2011, **7**, 5096-5119.
53. N. Kamaly, B. Yameen, J. Wu and O. C. Farokhzad, *Chem Rev*, 2016, **116**, 2602-2663.
54. Y. Li and D. Ju, in *Neurotoxicity of Nanomaterials and Nanomedicine*, eds. X. Jiang and H. Gao, Academic Press, 2017, **12,** pp. 285-329.
55. P. Bhargava, J. X. Zheng, P. Li, R. P. Quirk, F. W. Harris and S. Z. D. Cheng, *Macromolecules*, 2006, **39**, 4880-4888.
56. L. Zhang and A. Eisenberg, 1995, **268**, 1728-1731.
57. J. X. Zheng, H. Xiong, W. Y. Chen, K. Lee, R. M. Van Horn, R. P. Quirk, B. Lotz, E. L. Thomas, A.-C. Shi and S. Z. D. Cheng, *Macromolecules*, 2006, **39**, 641-650.
58. K. Kuperkar, D. Patel, L. I. Atanase and P. Bahadur, *Polymers (Basel)*, 2022, **14**.
59. Q. Tian, C. Fei, H. Yin and Y. Feng, *Progress in Polymer Science*, 2019, **89**, 108-132.
60. Y. H. A. Hussein and M. Youssry, *Materials (Basel)*, 2018, **11**.
61. A. Vardaxi, M. Kafetzi and S. Pispas, *Polymers (Basel)*, 2022, **14**.
62. N. J. Caggiano, S. K. Nayagam, L. Z. Wang, B. K. Wilson, P. Lewis, S. Jahangir, R. D. Priestley, R. K. Prud'homme and K. D. Ristroph, *Int J Pharm*, 2023, **640**, 122985.
63. X. Yan, J. Bernard and F. Ganachaud, *Advances in Colloid and Interface Science*, 2021, **294**, 102474.
64. J. Tao, S. F. Chow and Y. Zheng, *Acta Pharm Sin B*, 2019, **9**, 4-18.
65. J. He, X. Huang, Y.-C. Li, Y. Liu, T. Babu, M. A. Aronova, S. Wang, Z. Lu, X. Chen and Z. Nie, *Journal of the American Chemical Society*, 2013, **135**, 7974-7984.
66. W. S. Saad and R. K. Prud'homme, *Nano Today*, 2016, **11**, 212-227.
67. S. Damiati, U. B. Kompella, S. A. Damiati and R. Kodzius, *Genes (Basel)*, 2018, **9**,103-113.
68. B. G. Carvalho, B. T. Ceccato, M. Michelon, S. W. Han and L. G. de la Torre, *Pharmaceutics*, 2022, **14**,141-154.
69. B. Küçüktürkmen, W. Inam, F. Howaili, M. Gouda, N. Prabhakar, H. Zhang and J. M. Rosenholm, *Biosensors (Basel)*, 2022, **12,**181-190.
70. V. Uskoković, *Rev J Chem*, 2013, **3**, 271-303.
71. W. Xu, Y. Zheng and P. Pan, *Journal of Polymer Science*, 2022, **60**, 2136-2152.
72. R. M. Michell and A. J. Müller, *Progress in Polymer Science*, 2016, **54-55**, 183-213.
73. J. F. Kang, J. Zaccaro, A. Ulman and A. Myerson, *Langmuir*, 2000, **16**, 3791-3796.

74. P. J. Hurst, A. M. Rakowski and J. P. Patterson, *Nat Commun*, 2020, **11**, 4690.
75. M. Inam, J. C. Foster, J. Gao, Y. Hong, J. Du, A. P. Dove and R. K. O'Reilly, *Journal of Polymer Science Part A: Polymer Chemistry*, 2019, **57**, 255-259.
76. J. C. Foster, S. Varlas, B. Couturaud, Z. Coe and R. K. O'Reilly, *Journal of the American Chemical Society*, 2019, **141**, 2742-2753.
77. S. Ganda and M. H. Stenzel, *Progress in Polymer Science*, 2020, **101**, 101195.
78. W. Yu, M. Inam, J. R. Jones, A. P. Dove and R. K. O'Reilly, *Polymer Chemistry*, 2017, **8**, 5504-5512.
79. L. MacFarlane, C. Zhao, J. Cai, H. Qiu and I. Manners, *Chem Sci*, 2021, **12**, 4661-4682.
80. H. Phan, M. Cossutta, C. Houppe, C. Le Cœur, S. Prevost, I. Cascone, J. Courty, J. Penelle and B. Couturaud, *Journal of Colloid and Interface Science*, 2022, **618**, 173-184.
81. N. J. Warren and S. P. Armes, *Journal of the American Chemical Society*, 2014, **136**, 10174-10185.
82. M. S. Haider, M. M. Lübtow, S. Endres, S. Forster, V. J. Flegler, B. Böttcher, V. Aseyev, A. C. Pöppler and R. Luxenhofer, *ACS Appl Mater Interfaces*, 2020, **12**, 24531-24543.
83. P. P. Fu, Q. Xia, H. M. Hwang, P. C. Ray and H. Yu, *J Food Drug Anal*, 2014, **22**, 64-75.
84. A. Sharma, S. V. Madhunapantula and G. P. Robertson, *Expert Opin Drug Metab Toxicol*, 2012, **8**, 47-69.
85. J. M. Hillegass, A. Shukla, S. A. Lathrop, M. B. MacPherson, N. K. Fukagawa and B. T. Mossman, *Wiley Interdiscip Rev Nanomed Nanobiotechnol*, 2010, **2**, 219-231.
86. M. Niepel, M. Hafner, M. Chung and P. K. Sorger, *Curr Protoc Chem Biol*, 2017, **9**, 55-74.
87. S. J. Cameron, J. Sheng, F. Hosseinian and W. G. Willmore, *Int J Mol Sci*, 2022, **23**.
88. N. Lall, C. J. Henley-Smith, M. N. De Canha, C. B. Oosthuizen and D. Berrington, *Int J Microbiol*, 2013, **2013**, 420601.
89. Q. Mu, G. Jiang, L. Chen, H. Zhou, D. Fourches, A. Tropsha and B. Yan, *Chem Rev*, 2014, **114**, 7740-7781.
90. D. Docter, S. Strieth, D. Westmeier, O. Hayden, M. Gao, S. K. Knauer and R. H. Stauber, *Nanomedicine (Lond)*, 2015, **10**, 503-519.
91. V. H. Nguyen and B. J. Lee, *Int J Nanomedicine*, 2017, **12**, 3137-3151.
92. C. Weber, J. Simon, V. Mailänder, S. Morsbach and K. Landfester, *Acta Biomater*, 2018, **76**, 217-224.
93. W. Ma, L. Yang and L. He, *J Pharm Anal*, 2018, **8**, 147-152.
94. D. Hühn, K. Kantner, C. Geidel, S. Brandholt, I. De Cock, S. J. H. Soenen, P. Rivera_Gil, J.-M. Montenegro, K. Braeckmans, K. Müllen, G. U. Nienhaus, M. Klapper and W. J. Parak, *ACS Nano*, 2013, **7**, 3253-3263.
95. W. Huang, G. Xiao, Y. Zhang and W. Min, *Biomedicine & Pharmacotherapy*, 2021, **139**, 111541.
96. A. I. Khan, Q. Lu, D. Du, Y. Lin and P. Dutta, *Biochim Biophys Acta Gen Subj*, 2018, **1862**, 2779-2787.
97. J. Sargento-Freitas, S. Aday, C. Nunes, M. Cordeiro, A. Gouveia, F. Silva, C. Machado, B. Rodrigues, G. C. Santo, C. Ferreira, A. Amorim, S. Sousa, A. C. Gomes, M. Castelo-Branco, L. Ferreira and L. Cunha, *Neurology*, 2018, **90**, e127-e134.
98. J. Ahlawat, G. Guillama Barroso, S. Masoudi Asil, M. Alvarado, I. Armendariz, J. Bernal, X. Carabaza, S. Chavez, P. Cruz, V. Escalante, S. Estorga, D. Fernandez, C. Lozano, M. Marrufo, N. Ahmad, S. Negrete, K. Olvera, X. Parada, B. Portillo, A. Ramirez, R. Ramos, V. Rodriguez, P. Rojas, J. Romero, D. Suarez, G. Urueta, S. Viel and M. Narayan, *ACS Omega*, 2020, **5**, 12583-12595.
99. M. Heymans, R. Figueiredo, L. Dehouck, D. Francisco, Y. Sano, F. Shimizu, T. Kanda, R. Bruggmann, B. Engelhardt, P. Winter, F. Gosselet and M. Culot, *Fluids Barriers CNS*, 2020, **17**, 48-72.

100. I. Wilhelm and I. A. Krizbai, *Molecular Pharmaceutics*, 2014, **11**, 1949-1963.
101. A. Reichel, *Curr Drug Metab*, 2006, **7**, 183-203.
102. V. Berezowski, C. Landry, S. Lundquist, L. Dehouck, R. Cecchelli, M. P. Dehouck and L. Fenart, *Pharmaceutical Research*, 2004, **21**, 756-760.
103. R. Cecchelli, S. Aday, E. Sevin, C. Almeida, M. Culot, L. Dehouck, C. Coisne, B. Engelhardt, M. P. Dehouck and L. Ferreira, *PLoS One*, 2014, **9**, e99733.
104. S. Nakagawa, M. A. Deli, H. Kawaguchi, T. Shimizudani, T. Shimono, A. Kittel, K. Tanaka and M. Niwa, *Neurochem Int*, 2009, **54**, 253-263.
105. R. Booth and H. Kim, *Lab Chip*, 2012, **12**, 1784-1792.
106. M. Clemens-Hemmelmann, C. Kuffner, V. Metz, L. Kircher, U. Schmitt, C. Hiemke, R. Postina and R. Zentel, *Amphiphilic Copolymers Shuttle Drugs Across the Blood–Brain Barrier* Macromolecular bioscience, 2016.
107. C. Celia, D. Cosco, D. Paolino and M. Fresta, *Med Res Rev*, 2011, **31**, 716-756.
108. W. Zhang, A. Mehta, Z. Tong, L. Esser and N. H. Voelcker, *Adv Sci (Weinh)*, 2021, **8**, 2003937.
109. K. A. Woodrow, Y. Cu, C. J. Booth, J. K. Saucier-Sawyer, M. J. Wood and W. Mark Saltzman, *Nature Materials*, 2009, **8**, 526-533.
110. S. L. Demento, S. C. Eisenbarth, H. G. Foellmer, C. Platt, M. J. Caplan, W. Mark Saltzman, I. Mellman, M. Ledizet, E. Fikrig, R. A. Flavell and T. M. Fahmy, *Vaccine*, 2009, **27**, 3013-3021.
111. T. Patel, J. Zhou, J. M. Piepmeier and W. M. Saltzman, *Advanced Drug Delivery Reviews*, 2012, **64**, 701-705.
112. Y. Bai, F.-Y. Xie and W. Tian, *Chinese Journal of Polymer Science*, 2018, **36**, 406-416.
113. H. Liu, H. Chen, F. Cao, D. Peng, W. Chen and C. Zhang, *Polymers (Basel)*, 2019, **11**, 820.
114. A. Car, P. Baumann, J. T. Duskey, M. Chami, N. Bruns and W. Meier, *Biomacromolecules*, 2014, **15**, 3235-3245.
115. C. A. Figg, R. N. Carmean, K. C. Bentz, S. Mukherjee, D. A. Savin and B. S. Sumerlin, *Macromolecules*, 2017, **50**, 935-943.
116. N. Raval, D. Kalyane, R. Maheshwari and R. K. Tekade, in *Basic Fundamentals of Drug Delivery*, ed. R. K. Tekade, Academic Press, 2019, **5**, pp. 173-201.
117. J. C. Olivier, L. Fenart, R. Chauvet, C. Pariat, R. Cecchelli and W. Couet, *Pharm Res*, 1999, **16**, 1836-1842.
118. L. E. Freed, G. Vunjak-Novakovic, R. J. Biron, D. B. Eagles, D. C. Lesnoy, S. K. Barlow and R. Langer, *Bio/Technology*, 1994, **12**, 689-693.
119. Y. S. Yim, J.-s. Choi, G. T. Kim, C. H. Kim, T.-H. Shin, D. G. Kim and J. Cheon, *Chemical Communications*, 2012, **48**, 61-63.
120. Y. Zhu, C. Liu and Z. Pang, *Biomolecules*, 2019, **9**.
121. D. B. Vieira and L. F. Gamarra, *Int J Nanomedicine*, 2016, **11**, 5381-5414.
122. S. Whitelam and R. L. Jack, *Annu Rev Phys Chem*, 2015, **66**, 143-163.
123. P. J. Lu, E. Zaccarelli, F. Ciulla, A. B. Schofield, F. Sciortino and D. A. Weitz, *Nature*, 2008, **453**, 499-503.
124. R. Gutzler, L. Cardenas and F. Rosei, *Chemical Science*, 2011, **2**, 2290-2300.
125. C.-A. Palma, M. Bonini, T. Breiner and P. Samorì, *Advanced materials* 2009, **21**, 1383-1386.
126. W. Lu, in *Encyclopedia of Nanotechnology*, ed. B. Bhushan, Springer Netherlands, Dordrecht, 2012, DOI: 10.1007/978-90-481-9751-4_274, pp. 2371-2382.
127. M. C. Branco and J. P. Schneider, *Acta Biomater*, 2009, **5**, 817-831.
128. V. P. Torchilin, *Pharm Res*, 2007, **24**, 1-16.
129. D. Bennet and S. Kim, 2014, **8,**pp. 257-310.
130. D. J. Overstreet, H. A. Von Recum and B. L. Vernon, in *Injectable Biomaterials*, ed. B. Vernon, *Woodhead Publishing,* 2011, **6**, pp. 95-141.
131. K. M. Pustulka, A. R. Wohl, H. S. Lee, A. R. Michel, J. Han, T. R. Hoye, A. V. McCormick, J. Panyam and C. W. Macosko, *Molecular pharmaceutics*, 2013, **10**, 4367-4377.

132. X. Wang, P. Gao, Y. Yang, H. Guo and D. Wu, *Nature Communications*, 2018, **9**, 2772.
133. M. C. García, C. Aloisio, R. Onnainty and G. Ullio-Gamboa, in *Nanobiomaterials*, ed. R. Narayan, *Woodhead Publishing*, 2018, **9**, pp. 41-94.
134. Y. Xie, J. T. Husband, M. Torrent-Sucarrat, H. Yang, W. Liu and R. K. O'Reilly, *Chemical Communications*, 2018, **54**, 3339-3342.
135. A. B. Mabire, M. P. Robin, H. Willcock, A. Pitto-Barry, N. Kirby and R. K. O'Reilly, *Chemical Communications*, 2014, **50**, 11492-11495.
136. A. B. Mabire, M. P. Robin, W. D. Quan, H. Willcock, V. G. Stavros and R. K. O'Reilly, *Chem Commun (Camb)*, 2015, **51**, 9733-9736.
137. A. B. Mabire, M. P. Robin, W.-D. Quan, H. Willcock, V. G. Stavros and R. K. O'Reilly, *Chemical Communications*, 2015, **51**, 9733-9736.
138. R. Nicoară, M. Ilieș, A. Uifălean, C. A. Iuga and F. Loghin, *Applied Sciences*, 2019, **9**, 4789.
139. J. Wolfram, Y. Yang, J. Shen, A. Moten, C. Chen, H. Shen, M. Ferrari and Y. Zhao, *Colloids and Surfaces B: Biointerfaces*, 2014, **124**, 17-24.
140. M. P. Monopoli, C. Åberg, A. Salvati and K. A. Dawson, *Nature Nanotechnology*, 2012, **7**, 779-786.
141. S. Milani, F. Baldelli Bombelli, A. S. Pitek, K. A. Dawson and J. Rädler, *ACS Nano*, 2012, **6**, 2532-2541.
142. L. B. Nguyen VH, *Int J Nanomedicine*, 2017, **12**, 3137-3151.
143. T. Cedervall, I. Lynch, S. Lindman, T. Berggård, E. Thulin, H. Nilsson, K. A. Dawson and S. Linse, *Proceedings of the National Academy of Sciences*, 2007, **104**, 2050-2055.
144. F. Alexis, E. Pridgen, L. K. Molnar and O. C. Farokhzad, *Molecular Pharmaceutics*, 2008, **5**, 505-515.
145. Z. J. Deng, M. Liang, I. Toth, M. J. Monteiro and R. F. Minchin, *ACS Nano*, 2012, **6**, 8962-8969.
146. V. Mirshafiee, M. Mahmoudi, K. Lou, J. Cheng and M. L. Kraft, *Chemical Communications*, 2013, **49**, 2557-2559.
147. A. Kurtz-Chalot, C. Villiers, J. Pourchez, D. Boudard, M. Martini, P. N. Marche, M. Cottier and V. Forest, *Materials Science and Engineering: C*, 2017, **75**, 16-24.
148. A. Salvati, A. S. Pitek, M. P. Monopoli, K. Prapainop, F. B. Bombelli, D. R. Hristov, P. M. Kelly, C. Åberg, E. Mahon and K. A. Dawson, *Nature Nanotechnology*, 2013, **8**, 137-143.
149. Q. Dai, C. Walkey and W. C. Chan, *Angew Chem Int Ed Engl*, 2014, **53**, 5093-5096.
150. C.-Y. Sun, S. Shen, C.-F. Xu, H.-J. Li, Y. Liu, Z.-T. Cao, X.-Z. Yang, J.-X. Xia and J. Wang, *Journal of the American Chemical Society*, 2015, **137**, 15217-15224.
151. I. García, A. Sánchez-Iglesias, M. Henriksen-Lacey, M. Grzelczak, S. Penadés and L. M. Liz-Marzán, *Journal of the American Chemical Society*, 2015, **137**, 3686-3692.
152. F. Xu, M. Reiser, X. Yu, S. Gummuluru, L. Wetzler and B. M. Reinhard, *ACS Nano*, 2016, **10**, 1189-1200.
153. M. Inam, G. Cambridge, A. Pitto-Barry, Z. P. L. Laker, N. R. Wilson, R. T. Mathers, A. P. Dove and R. K. O'Reilly, *Chemical Science*, 2017, **8**, 4223-4230.
154. M. Inam, J. R. Jones, M. M. Pérez-Madrigal, M. C. Arno, A. P. Dove and R. K. O'Reilly, *ACS Central Science*, 2018, **4**, 63-70.
155. N. Petzetakis, A. P. Dove and R. K. O'Reilly, *Chemical Science*, 2011, **2**, 955-960.
156. N. Petzetakis, D. Walker, A. P. Dove and R. K. O'Reilly, *Soft Matter*, 2012, **8**, 7408-7414.
157. A. Pitto-Barry, N. Kirby, A. P. Dove and R. K. O'Reilly, *Polymer Chemistry*, 2014, **5**, 1427-1436.
158. L. Sun, A. Pitto-Barry, N. Kirby, T. L. Schiller, A. M. Sanchez, M. A. Dyson, J. Sloan, N. R. Wilson, R. K. O'Reilly and A. P. Dove, *Nature Communications*, 2014, **5**, 5746.
159. L. Sun, N. Petzetakis, A. Pitto-Barry, T. L. Schiller, N. Kirby, D. J. Keddie, B. J. Boyd, R. K. O'Reilly and A. P. Dove, *Macromolecules*, 2013, **46**, 9074-9082.
160. I. Andreana, V. Bincoletto, M. Manzoli, F. Rodà, V. Giarraputo, P. Milla, S. Arpicco and B. Stella, *Materials (Basel)*, 2023, **16,** 1212-1226.

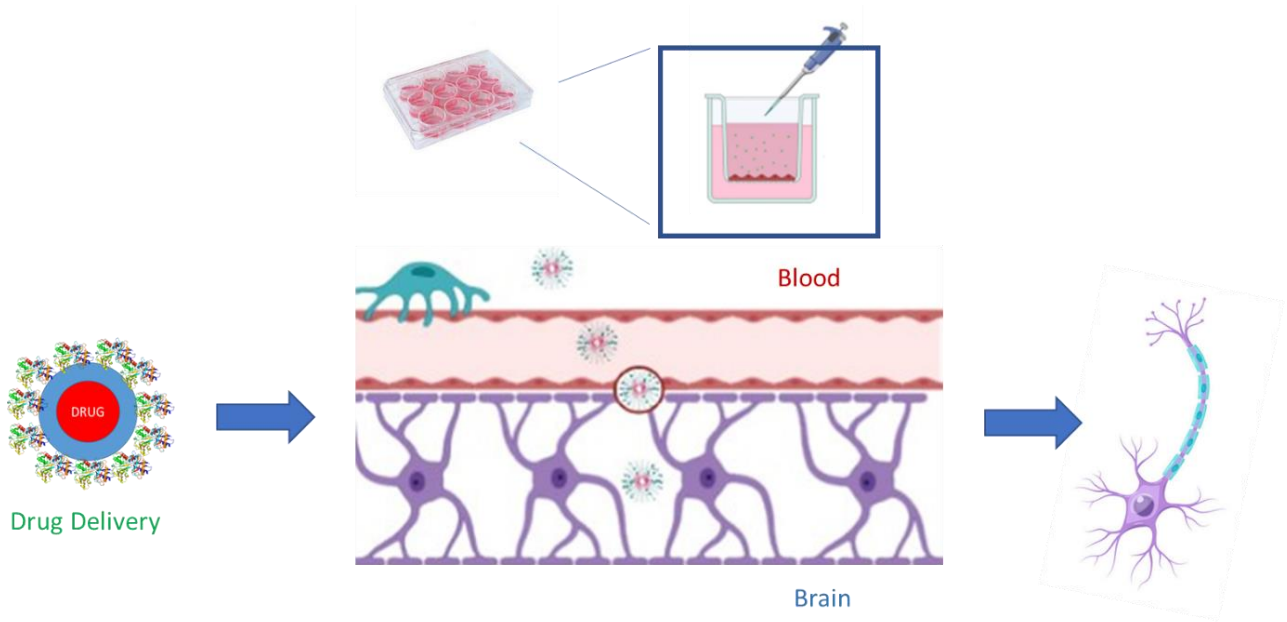
161. E. Trenkenschuh and W. Friess, *European Journal of Pharmaceutics and Biopharmaceutics*, 2021, **165**, 345-360.
162. T. Chen, X. Zhao and Y. Weng, *Front Chem*, 2022, **10**, 1107620.
163. N. Petzetakis, M. P. Robin, J. P. Patterson, E. G. Kelley, P. Cotanda, P. H. Bomans, N. A. Sommerdijk, A. P. Dove, T. H. Epps, 3rd and R. K. O'Reilly, *ACS Nano*, 2013, **7**, 1120-1128.
164. M. Oyo and Y. Masaaki, 1967, **40**, 2380-2382.
165. R. Augustine, A. Hasan, R. Primavera, R. J. Wilson, A. S. Thakor and B. D. Kevadiya, *Materials Today Communications*, 2020, **25**, 101692.
166. L. Johnson, D. M. Gray, E. Niezabitowska and T. O. McDonald, *Nanoscale*, 2021, **13**, 7879-7896.
167. C. Zhu and J. Nicolas, *Biomacromolecules*, 2022, **23**, 3043-3080.
168. L. MacFarlane, C. Zhao, J. Cai, H. Qiu and I. Manners, *Chemical Science*, 2021, **12**, 4661-4682.
169. M. C. Arno, M. Inam, Z. Coe, G. Cambridge, L. J. Macdougall, R. Keogh, A. P. Dove and R. K. O'Reilly, *Journal of the American Chemical Society*, 2017, **139**, 16980-16985.
170. X. He, Y. He, M.-S. Hsiao, R. L. Harniman, S. Pearce, M. A. Winnik and I. Manners, *Journal of the American Chemical Society*, 2017, **139**, 9221-9228.
171. M. Brzeziński and T. Biela, *Polymer International*, 2015, **64**, 1667-1675.
172. G. C. Sosso, J. Chen, S. J. Cox, M. Fitzner, P. Pedevilla, A. Zen and A. Michaelides, *Chem Rev*, 2016, **116**, 7078-7116.
173. U. Tritschler, S. Pearce, J. Gwyther, G. R. Whittell and I. Manners, *Macromolecules*, 2017, **50**, 3439-3463.
174. E. Capuana, F. Lopresti, M. Ceraulo and V. La Carrubba, *Polymers (Basel)*, 2022, **14**, 1153
175. J. R. Finnegan, X. He, S. T. G. Street, J. D. Garcia-Hernandez, D. W. Hayward, R. L. Harniman, R. M. Richardson, G. R. Whittell and I. Manners, *Journal of the American Chemical Society*, 2018, **140**, 17127-17140.
176. H.-x. Lin, Z.-c. Lei, Z.-y. Jiang, C.-p. Hou, D.-y. Liu, M.-m. Xu, Z.-q. Tian and Z.-x. Xie, *Journal of the American Chemical Society*, 2013, **135**, 9311-9314.
177. N. Baig, I. Kammakakam and W. Falath, *Materials Advances*, 2021, **2**, 1821-1871.
178. A. Mattei, R. S. Hong, H. Dietrich, D. Firaha, J. Helfferich, Y. M. Liu, K. Sasikumar, N. S. Abraham, R. Miglani Bhardwaj, M. A. Neumann and A. Y. Sheikh, *Journal of Chemical Theory and Computation*, 2022, **18**, 5725-5738.
179. M. Karimi, P. S. Zangabad, F. Mehdizadeh, H. Malekzad, A. Ghasemi, S. Bahrami, H. Zare, M. Moghoofei, A. Hekmatmanesh and M. R. Hamblin, *Nanoscale*, 2017, **9**, 1356-1392.
180. S. Yadav, A. K. Sharma and P. Kumar, *Front Bioeng Biotechnol*, 2020, **8**, 127.
181. F. C. Meldrum and C. O'Shaughnessy, *Advanced Materials*, 2020, **32**, 2001068.
182. C. E. Ellis, J. D. Garcia-Hernandez and I. Manners, *Journal of the American Chemical Society*, 2022, **144**, 20525-20538.
183. Y. Fu and W. J. Kao, *Expert Opin Drug Deliv*, 2010, **7**, 429-444.
184. Y. Qiao and Y. Men, *Macromolecules*, 2017, **50**, 5490-5497.
185. W. Zhou, S. Z. D. Cheng, S. Putthanarat, R. K. Eby, D. H. Reneker, B. Lotz, S. Magonov, E. T. Hsieh, R. G. Geerts, S. J. Palackal, G. R. Hawley and M. B. Welch, *Macromolecules*, 2000, **33**, 6861-6868.
186. a. B. L. Stephen Z. D. Cheng, *Philosophical Transactions: Mathematical, Physical and Engineering Sciences*, 2003,**156**, 517–537.
187. J. Yang, T. Zhao, Y. Zhou, L. Liu, G. Li, E. Zhou and X. Chen, *Macromolecules*, 2007, **40**, 2791-2797.
188. C. Yang, Z.-X. Li and J.-T. Xu, *Journal of Polymer Science*, 2022, **60**, 2153-2174.
189. C. Park, C. De Rosa, L. J. Fetters and E. L. Thomas, *Macromolecules*, 2000, **33**, 7931-7938.
190. Y. Gong, W. Song, Y. Wu, D. Zhang, Y. Liu, Q. Zhao, M. He and X. Chen, *Polymers and Polymer Composites*, 2019, **28**, 77-88.

191. Y. Zhu, L. Han, H. Fan, M. Wang, R. Qi, Y. Zhao and F. He, *Macromolecules*, 2020, **53**, 3217-3223.
192. M. Awashra and P. Młynarz, *Nanoscale Advances*, 2023, **5**, 2674-2723.
193. M. Inam, J. R. Jones, M. M. Pérez-Madrigal, M. C. Arno, A. P. Dove and R. K. O'Reilly, *ACS Cent Sci*, 2018, **4**, 63-70.
194. E. G. Knox, M. R. Aburto, G. Clarke, J. F. Cryan and C. M. O'Driscoll, *Mol Psychiatry*, 2022, **27**, 2659-2673.
195. M. Brust, O. Aouane, M. Thiébaud, D. Flormann, C. Verdier, L. Kaestner, M. W. Laschke, H. Selmi, A. Benyoussef, T. Podgorski, G. Coupier, C. Misbah and C. Wagner, *Scientific Reports*, 2014, **4**, 4348-4369.
196. A. E. Nel, L. Mädler, D. Velegol, T. Xia, E. M. Hoek, P. Somasundaran, F. Klaessig, V. Castranova and M. Thompson, *Nat Mater*, 2009, **8**, 543-557.
197. M. Jiang, J. D. Olarte-Plata and F. Bresme, *The Journal of Chemical Physics*, 2022, **4,** 044701.
198. Q. Wei, T. Becherer, S. Angioletti-Uberti, J. Dzubiella, C. Wischke, A. T. Neffe, A. Lendlein, M. Ballauff and R. Haag, *Angewandte Chemie International Edition*, 2014, **53**, 8004-8031.
199. J. W. Chang, A. Armaou and R. M. Rioux, *The Journal of Physical Chemistry B*, 2021, **125**, 8075-8087.
200. M. Winiewska, E. Bugajska and J. Poznański, *PLoS One*, 2017, **12**, e0173260.
201. V. K. Srivastava and R. Yadav, in *Data Processing Handbook for Complex Biological Data Sources*, ed. G. Misra, Academic Press, 2019, **4**, pp. 125-137.
202. F. Villanueva-Flores, A. Castro-Lugo, O. T. Ramírez and L. A. Palomares, *Nanotechnology*, 2020, **31**, 132002.
203. M. Inam, G. Cambridge, A. Pitto-Barry, Z. P. L. Laker, N. R. Wilson, R. T. Mathers, A. P. Dove and R. K. O'Reilly, *Chem Sci*, 2017, **8**, 4223-4230.
204. C. Sinturel, M. Vayer, R. Erre and H. Amenitsch, *European Polymer Journal*, 2009, **45**, 2505-2512.
205. T. Vilgis and A. Halperin, *Macromolecules*, 1991, **24**, 2090-2095.
206. L. R. MacFarlane, X. Li, C. F. J. Faul and I. Manners, *Macromolecules*, 2021, **54**, 11269-11280.
207. Y. He, J.-C. Eloi, R. L. Harniman, R. M. Richardson, G. R. Whittell, R. T. Mathers, A. P. Dove, R. K. O'Reilly and I. Manners, *Journal of the American Chemical Society*, 2019, **141**, 19088-19098.
208. Z. Liu, H. Fan, W. Li, G. Bai, X. Li, N. Zhao, J. Xu, F. Zhou, X. Guo, B. Dai, E. Benassi and X. Jia, *Nanoscale*, 2019, **11**, 4751-4758.
209. Y. Chen, L. Wang, W. Chen, C. Zhong, S. Li, J. Shao, G. Li and H. Hou, *CrystEngComm*, 2022, **24**, 3903-3912.
210. J. Sun, Z. Hong, L. Yang, Z. Tang, X. Chen and X. Jing, *Polymer*, 2004, **45**, 5969-5977.
211. R. V. Castillo and A. J. Müller, *Progress in Polymer Science*, 2009, **34**, 516-560.
212. N. Petzetakis, M. P. Robin, J. P. Patterson, E. G. Kelley, P. Cotanda, P. H. H. Bomans, N. A. J. M. Sommerdijk, A. P. Dove, T. H. Epps, III and R. K. O'Reilly, *ACS Nano*, 2013, **7**, 1120-1128.
213. M. Jafari and F. Mehrnejad, *PLoS One*, 2016, **11**, e0165213.
214. P. Ferraboschi, S. Ciceri and P. Grisenti, *Antibiotics (Basel)*, 2021, **10**, 1534-1550
215. G. Bashiri, M. S. Padilla, K. L. Swingle, S. J. Shepherd, M. J. Mitchell and K. Wang, *Lab Chip*, 2023, **23**, 1432-1466.
216. N. J. Warren, O. O. Mykhaylyk, D. Mahmood, A. J. Ryan and S. P. Armes, *Journal of the American Chemical Society*, 2014, **136**, 1023-1033.
217. B. Charleux, G. Delaittre, J. Rieger and F. D'Agosto, *Macromolecules*, 2012, **45**, 6753-6765.
218. H. Phan, V. Taresco, J. Penelle and B. Couturaud, *Biomaterials Science*, 2021, **9**, 38-50.
219. N. J. W. Penfold, J. Yeow, C. Boyer and S. P. Armes, *ACS Macro Letters*, 2019, **8**, 1029-1054.
220. M. J. Derry, L. A. Fielding and S. P. Armes, *Progress in Polymer Science*, 2016, **52**, 1-18.

221. J. Wan, B. Fan and S. H. Thang, *Chem Sci*, 2022, **13**, 4192-4224.
222. P.-E. Millard, L. Barner, M. H. Stenzel, T. P. Davis, C. Barner-Kowollik and A. H. E. Müller, *Macromolecular Rapid Communications*, 2006, **27**, 821-828.
223. M. Y. Khan, M.-S. Cho and Y.-J. Kwark, *Macromolecules*, 2014, **47**, 1929-1934.
224. Y. Ma, P. Gao, Y. Ding, L. Huang, L. Wang, X. Lu and Y. Cai, *Macromolecules*, 2019, **52**, 1033-1041.
225. S. L. Brown, C. M. Rayner, S. Graham, A. Cooper, S. Rannard and S. Perrier, *Chem Commun (Camb)*, 2007, **21**, 2145-2147.
226. J. Yeow and C. Boyer, *Adv Sci (Weinh)*, 2017, **4**, 1700137.
227. L. D. Blackman, K. E. B. Doncom, M. I. Gibson and R. K. O'Reilly, *Polymer Chemistry*, 2017, **8**, 2860-2871.
228. W. M. Pardridge, *J Drug Target*, 2010, **18**, 157-167.
229. J. Kreuter, *J Microencapsul*, 2013, **30**, 49-54.
230. J. Samal, A. L. Rebelo and A. Pandit, *Adv Drug Deliv Rev*, 2019, **148**, 68-145.
231. T. Patel, J. Zhou, J. M. Piepmeier and W. M. Saltzman, *Adv Drug Deliv Rev*, 2012, **64**, 701-705.
232. M. Vert, Y. Doi, K.-H. Hellwich, M. Hess, P. Hodge, P. Kubisa, M. Rinaudo and F. Schué, *Pure and Applied Chemistry*, 2012, **84**, 377-410.
233. T. T. Zhang, W. Li, G. Meng, P. Wang and W. Liao, *Biomater Sci*, 2016, **4**, 219-229.
234. S. Aday, R. Cecchelli, D. Hallier-Vanuxeem, M. P. Dehouck and L. Ferreira, *Trends in Biotechnology*, 2016, **34**, 382-393.
235. C. D. Kuhnline Sloan, P. Nandi, T. H. Linz, J. V. Aldrich, K. L. Audus and S. M. Lunte, *Annu Rev Anal Chem (Palo Alto Calif)*, 2012, **5**, 505-531.
236. S. J. Parkinson, S. Tungsirisurp, C. Joshi, B. L. Richmond, M. L. Gifford, A. Sikder, I. Lynch, R. K. O'Reilly and R. M. Napier, *Nature Communications*, 2022, **13**, 7385-7399.
237. S. Varlas, R. Keogh, Y. Xie, S. L. Horswell, J. C. Foster and R. K. O'Reilly, *Journal of the American Chemical Society*, 2019, **141**, 20234-20248.
238. M. Weiss, J. Fan, M. Claudel, T. Sonntag, P. Didier, C. Ronzani, L. Lebeau and F. Pons, *Journal of Nanobiotechnology*, 2021, **19**, 5.
239. J. K. Patra, G. Das, L. F. Fraceto, E. V. R. Campos, M. d. P. Rodriguez-Torres, L. S. Acosta-Torres, L. A. Diaz-Torres, R. Grillo, M. K. Swamy, S. Sharma, S. Habtemariam and H.-S. Shin, *Journal of Nanobiotechnology*, 2018, **16**, 71.
240. H. Xu, S. Li and Y.-S. Liu, *Signal Transduction and Targeted Therapy*, 2022, **7**, 231.
241. S. Saha, N. Sachivkina, A. Karamyan, E. Novikova and T. Chubenko, *Biomedicines*, 2024, **12**.
242. H. Sun, C. Jiang, L. Wu, X. Bai and S. Zhai, *Front Bioeng Biotechnol*, 2019, **7**, 414.
243. P. Khanna, C. Ong, B. H. Bay and G. H. Baeg, *Nanomaterials (Basel)*, 2015, **5**, 1163-1180.
244. T. Kowada, H. Maeda and K. Kikuchi, *Chemical Society Reviews*, 2015, **44**, 4953-4972.
245. S. J. Byard, M. Williams, B. E. McKenzie, A. Blanazs and S. P. Armes, *Macromolecules*, 2017, **50**, 1482-1493.
246. D. Bartczak and A. G. Kanaras, *Langmuir*, 2011, **27**, 10119-10123.
247. L. D. Field, S. A. Walper, K. Susumu, E. Oh, I. L. Medintz and J. B. Delehanty, *Sensors*, 2015, **15**, 30457-30468.
248. A. S. Pitek, D. O'Connell, E. Mahon, M. P. Monopoli, F. B. Bombelli and K. A. Dawson, *PLOS ONE*, 2012, **7**, e40685.
249. K. Amornwachirabodee, S. Khramchantuk, P. Pienpinijtham, N. Israsena, T. Palaga and S. Wanichwecharungruang, *ACS Omega*, 2018, **3**, 6833-6840.
250. G. D. Byrne, D. Vllasaliu, F. H. Falcone, M. G. Somekh and S. Stolnik, *Molecular Pharmaceutics*, 2015, **12**, 3862-3870.
251. V. Capella, R. E. Rivero, A. C. Liaudat, L. E. Ibarra, D. A. Roma, F. Alustiza, F. Mañas, C. A. Barbero, P. Bosch, C. R. Rivarola and N. Rodriguez, *Heliyon*, 2019, **5**, e01474.

252. H. Yu, Y. Zou, Y. Wang, X. Huang, G. Huang, B. D. Sumer, D. A. Boothman and J. Gao, *ACS Nano*, 2011, **5**, 9246-9255.
253. S. Mazumdar, D. Chitkara and A. Mittal, *Acta Pharmaceutica Sinica B*, 2021, **11**, 903-924.
254. M. S. Khan, N. S. Dosoky and J. D. Williams, *Int J Mol Sci*, 2013, **14**, 21561-21597.
255. W. Au - Zhao, L. Au - Han, Y. Au - Bae and D. S. Au - Manickam, *JoVE*, 2019, DOI: doi:10.3791/58900, e58900.
256. X. Wang, J. Iqbal, D. Rahmat and A. Bernkop-Schnürch, *Int J Pharm*, 2012, **438**, 217-224.
257. F. Leve, D. P. Bonfim, G. Fontes and J. A. Morgado-Díaz, *Nanomedicine*, 2019, **14**, 1565-1578.
258. J. Gavard, *Cell Adh Migr*, 2014, **8**, 158-164.
259. A. Prlj, L. Vannay and C. Corminboeuf, *Helvetica Chimica Acta*, 2017, **100**, e1700093.
260. M. G. Paez-Segala, M. G. Sun, G. Shtengel, S. Viswanathan, M. A. Baird, J. J. Macklin, R. Patel, J. R. Allen, E. S. Howe, G. Piszczek, H. F. Hess, M. W. Davidson, Y. Wang and L. L. Looger, *Nature Methods*, 2015, **12**, 215-218.
261. S. B. Keel, R. Doty, L. Liu, E. Nemeth, S. Cherian, T. Ganz and J. L. Abkowitz, *Exp Hematol*, 2015, **43**, 469-478.e466.
262. B. Srinivasan, A. R. Kolli, M. B. Esch, H. E. Abaci, M. L. Shuler and J. J. Hickman, *J Lab Autom*, 2015, **20**, 107-126.
263. A. M. Butt, H. C. Jones and N. J. Abbott, *J Physiol*, 1990, **429**, 47-62.

Chapter 4-Polymerisation induced self-assembly nanoparticles for blood and brain barrier permeation



4.1 Introduction

4.1.1 Polymerization induced self-assembly (PISA)

Block copolymer nano-objects have traditionally been created using multi-step processes that involve the synthesis, purification after polymerization, and self-assembly of constituent amphiphilic block copolymers in diluted solutions. Apart from the synthetic processes that were described previously, another method was explored in creation of small functional nanoparticles. Polymerization induced self-assembly (PISA) is a polymerization technique that drives a physical polymer self-assembly process, combining block copolymer synthesis and nanoparticle formation efficiently at high polymer concentrations.[81] In the past few years, PISA of block copolymer amphiphiles has emerged as a potent substitute for traditional self-assembly techniques, such as solvent evaporation and emulsification.[216] PISA enables polymerization and in situ development of nano-objects with predictable properties (such as size, morphology, surface chemistry, etc.) in a single synthetic step at high conversions and polymer concentrations, which makes the method appealing for large scale manufacturing. [217] PISA offers various advantages such as scalability, one pot approach, high yielding, cost and time effective that are essential for pharmaceutical industry protocols[218]. This method has swiftly evolved into a potent and adaptable tool for creating a wide range of custom organic diblock copolymer nanoparticles (NPs) with variable size, shape, and surface functionality[81].

PISA has a lot of benefits but disadvantages as well. It can be a relatively difficult approach that necessitates careful optimisation and comprehension of the underlying mechanisms because it involves numerous chemical and physical processes.[219] PISA frequently needs certain reaction conditions, such as a suitable chain growth technique like a controlled radical polymerization process, exact temperature and reaction kinetics control. The PISA's application to certain systems may be constrained by these requirements. Fundamental mechanistic studies conducted in the process of PISA have demonstrated that the chain-extension of a solvophilic steric stabiliser block using either solvent-miscible (dispersion polymerization conditions) or solvent-immiscible (emulsion polymerization conditions) core-

forming monomers drives the formation of block copolymer microstructures.[217, 220] At a critical DP, these core-forming monomers form solvent-insoluble polymers, which in turn aggregate to exclude solvent. [217] To acquire a better understanding of the process of PISA, the self-assembly and synthesis of these PISA NPs will be examined.

4.1.2 PISA assembly, and morphological kinetics

The method of stimulating polymerization and self-assembly with temperature is known as thermo-PISA. This method starts the polymerization reaction and subsequent self-assembly by heating the reaction mixture above a certain temperature. Like any other RAFT polymerization, thermo-PISA is able to polymerize by using initiators and elevated temperature. The temperature required for the polymerization depends on the initiator in use. With strong compatibility with various monomers and solvent systems, the thermal initiation of RAFT-PISA is simply employed in a variety of settings and might be easily realised in the industrial upscaling process.[221]

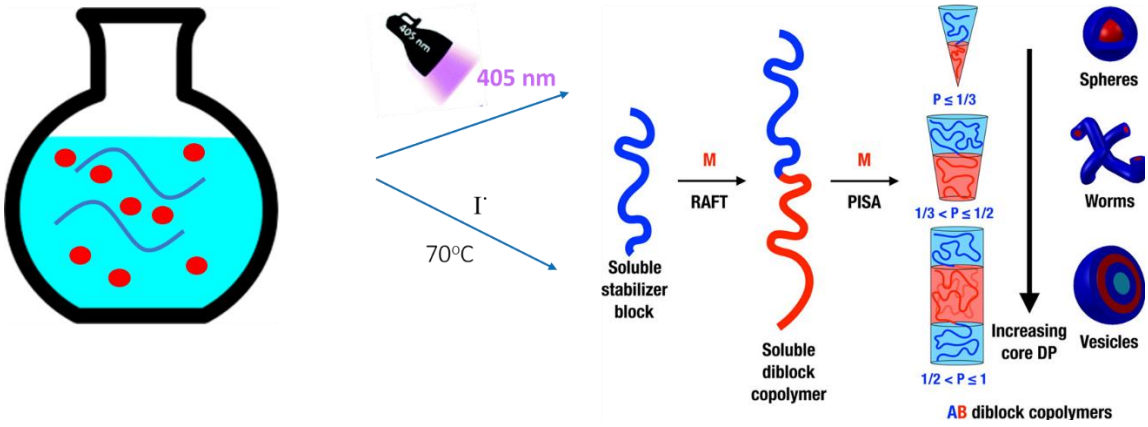


Figure 4.1.1 . Photo and Thermo initiated PISA structures and packing parameter. [217] (Adapted with permission)

In a variety of electromagnetic spectrum, including gamma,[222, 223] ultraviolet (UV),[223] visible,[224] and microwave, RAFT polymerization has been thoroughly investigated.[225] The extension of photo-initiated RAFT polymerizations to the realm of RAFT-mediated PISA then occurred on its own. Due to their low energy nature, induction of fewer side reactions, and

also the potential to control the polymerizations temporally and spatially, visible light and NIR have garnered greater scientific attention.[226] Instead of employing conventional chemical initiators, photo-PISA starts the polymerization reaction using light (often UV or visible light). By including photo-responsive initiators or monomers in the system, this can be accomplished.[226] Self-assembled microstructures are created as a result of the polymerization, which is started when light is irradiated. Thus, PISA can be facilitated by light and heat irradiation as depicted above (figure 4.1.1).[227] The final morphology generated through PISA under thermodynamic and kinetic control is essentially determined by the relative volume fractions of the stabiliser and core-forming blocks, similar to conventional block copolymer self-assembly techniques.[76] As in a regular self-assembly the packing parameter will dictate the morphology of the system implemented and it can vary from spheres, worms and vehicles.[76]

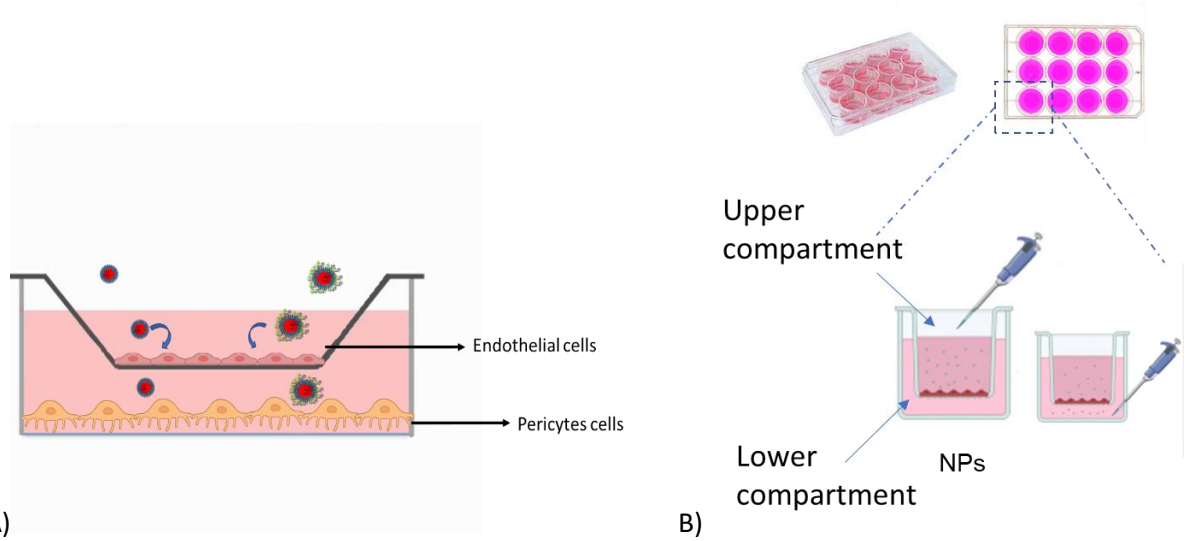
4.1.3 Polymeric nanoparticles for BBB permeation

Nanotechnology has enormous potential of overcoming the challenging requirements for the treatment of neurological disorders, such as the penetration of the BBB and subsequent drug distribution to target cells.[228] Specifically, nanosized drug delivery systems can be designed according to specifications (e.g., composition, size, shape, and surface ligands) to transport pharmaceuticals across the BBB. For instance, nanoparticle designs may prolong the period that blood circulates through brain capillaries and can exploit transcytosis pathways by employing various surface functionalization tactics. Furthermore, due to the presence of certain ligands developed into the particle surface, nanoparticles have the capacity to evade the efflux pumps.[229] To enhance drug distribution, a variety of drug delivery systems have been created. These systems are often classified as either organic or inorganic nanoparticles. Liposomes, polymeric nanoparticles, and lipid nanoparticles are the most prevalent organic nanoparticles.[230] Particularly polymeric nanoparticles are a viable option as a drug delivery platform for CNS targeting because of their configurable architecture, small size (10 to 100 nm), non-toxicity, biocompatibility, and regulated drug release.[231] These polymeric nanoparticles can be easily functionalised with particular ligands

that target the endothelial cells' receptors, increasing the effectiveness of transcytosis. Polymeric nanoparticles are required to have biodegradability and biocompatibility in order for them to be safe to use once administered to humans.[167] Degradable polymers is the preferred word for polymers that break down hydrolytically *in vitro*, *in vivo*, or by the action of enzymes *in vitro*, whereas biodegradable polymers are polymers whose degradation is driven by biological activity (i.e., via cells).[232] Additionally, polymeric nanoparticles depending on their biodegradability can have a longer circulation period.[233] The polymeric matrix may be stimulated to release the medication upon cellular absorption and internalisation, producing a safe, extended, and focused therapeutic impact.[108] Polymeric nanoparticles can transport a variety of medications, for instance, through hydrophilic, hydrophobic, or electrostatic contacts, as well as by responsive covalent bonds.[20] Due to the small, biocompatible and versatile nature PISA nanoparticles would be an ideal candidate for BBB permeation studies. Herein in this study the permeation of the BBB will be examine by utilising PISA nanoparticles.

4.1.4 Biological evaluation of BBB and assessment of permeation

The biological evaluation and assessment can be examined in an *in vitro* or *in vivo* BBB model, where you can evaluate the aspects of your drug delivery system. In *in vitro* co-culture static models, astrocytes (or pericytes) are often seeded on the basolateral (abluminal) side of the membrane, whereas an endothelial cell monolayer is usually seeded on the upper (luminal) side of the membrane. Endothelial cells can co-culture with astrocytes or pericytes (biculture) either in non-contact or in contact. When endothelial cells and pericytes are co-cultured, the upregulation of the efflux pump protein is increased.[99]



A) B)

Scheme 15. A) Representation of *in vitro* BBB with CD34+ brain like endothelial cells (human derived) seeded on matrix gel in the Upper compartment and pericytes in the lower one. B) Visualization of transport efficiency experiment, measuring media every 2 & 24 hours

In this study, $CD34^+$ will be used as brain-like endothelial cells (ECs) human derived for the upper side. Recent studies have shown that CD34+ cells may be an interesting source of ECs that are particularly responsive to instructive induction by the cells. [234] These ECs were co-cultured with pericytes for 6 days for the 0.4 µm transwell filters and for 14 days for the 3 µm filters.[103] In both cases the ECs showed markers of a BBB phenotype, including increased numbers of tight junctions and upregulation of efflux pumps. However, significant differences were observed in transendothelial electrical resistance (TEER) and permeability to small molecules of the neurovascular unit (astrocytes or pericytes). To seed the CD34+ in the filters a matrix gel was used prior to seeding, to ensure the safe culture and growth of the cell lines and to allow them to grow in a monolayer manner.

The susceptibility to permeate or otherwise "leakiness" of the *in vitro* produced BBB is quantified through tests of permeability. Understanding how compounds traverse the BBB is useful for drug research and drug screening investigations. Permeability measurements can also be utilise to access the tight junction formations between the endothelial cells. Numerous fluorescent tracers, including sodium fluorescein (376 Da), and lucifer yellow (LY) (457 Da), are frequently used to measure the permeability.[108] By injecting fluorophores and molecules labelled with fluorophores via the apical side of the BBB and measuring the amount of penetrated molecules in the basolateral side over time, the permeability

coefficient of an analyte may be calculated.[235] In order for a number of nanoparticles to be evaluate for the absorption and transcytosis of nanoparticles across the BBB, they are put to the luminal upper side of the BBB model. After the incubation time allowed (in our case 2 & 24 hours), nanoparticles are gradually transferred from the top (luminal) compartment to the lower (abluminal) compartment. The fluorescence of the media collected from both compartments was measured to evaluate the permeability percentage. Apart from the permeability, the rigidity of the BBB endothelial tight junctions was also accessed by performing TEER and LY measurements. Analytical methodology of the described procedures can be found at the experimental section of this chapter.

In this chapter, innovative spherical PISA NPs were synthesized and characterised. The NPs were tagged with a small fluorophore and transferrin protein, for visualization and specific targeting. Cellular toxicity studies were conducted as well as cellular uptake experiments. The PISA NPs were finally explored for the BBB permeability.

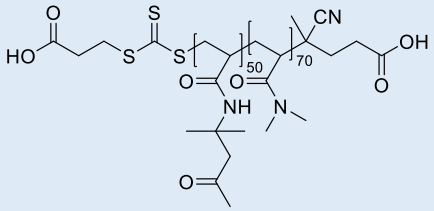
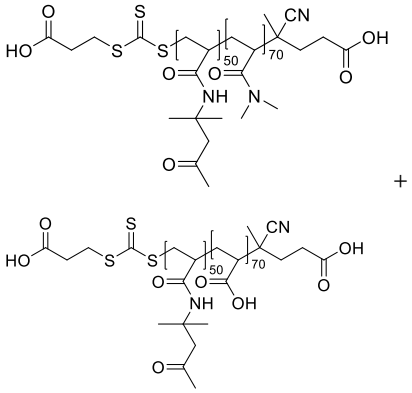
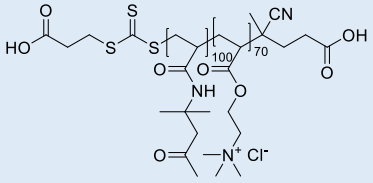
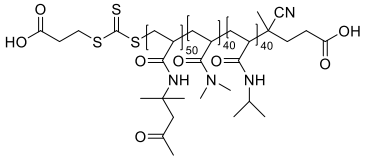
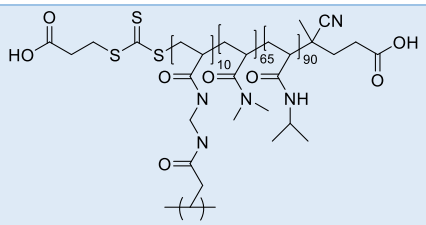
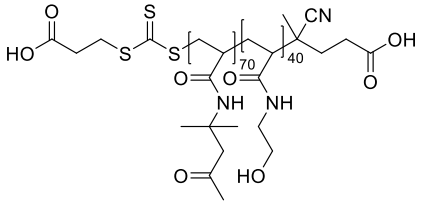
4.2 Results and Discussion

4.2.1 Synthesis and characterization of PISA nanoparticles

A new batch of nanoparticles was synthesized with poly(diacetone acrylamide) (PDAA) as core through polymerisation induced self-assembly (PISA). Diacetone acrylamide (DAA) is a water-soluble monomer that consists of a hydrogen-bonding donator (amide) and an acceptor (ketone). DAA as a monomer is miscible in water but after its polymerization is hydrophobic and will compose the hydrophobic core of the NPs.

A library of polymeric diblock copolymers were synthesized and self-assembled directly through PISA into functional nanoparticles with corona chemistries that allow easy modification (Table 1). Table 1 can provide names structures and abbreviations.

Table 1. Library of PISA NPs

Polymers	Abbreviations	Structure
$PDMA_{70}$-b-$PDAA_{50}$ ***Poly(N,N-dimethylacrylamide)-b-poly(diacetone acrylamide)***	PDMA	
90% $PDMA_{70}$-b-$PDAA_{50}$ + ***10% PAA_{70}-b-$PDAA_{50}$*** ***Poly(N,N-dimethylacrylamide)-b-poly(diacetone acrylamide)*** + ***Poly(Acrylic Acid)-b- poly(diacetone acrylamide)***	PAA	
$PQDMAEMA_{70}$-b-$PDAA_{100}$ ***Poly [2(dimethylamino)ethyl methacrylate]-b-poly (diacetone acrylamide)***	PQDMAE	
$PDMA_{40}$-b-$PNIPAM_{40}$-b-$PDAA_{50}$ (62) ***Poly(N,N-dimethylacrylamide)-b- poly(N-isopropylacrylamide)-b- poly(diacetone acrylamide)***	62	
$PDMA_{65}$-b-P($NIPAM_{90}$-co-MBA_{10}) (67) ***Poly(N,N-dimethylacrylamide)-b-[poly(N-isopropylacrylamide)-co- N,N'-Methylenebisacrylamide]***	67	
$PHEA_{40}$-b-$PDAA_{70}$ (75) ***poly(2-hydroxyethyl acrylate)-b-poly(diacetone acrylamide)***	75	

All PISA NPs were produced as previously reported.[236] In order to create the self-assembled polymeric nanoparticles with different surface charges, five different macromolecular chain transfer agents (mCTAs)—poly(dimethyl acrylamide) (PDMA), poly(acrylic acid) (PAA), poly([2- (methacryloyloxy)ethyl]trimethylammonium chloride)] (PQDMAEMA), poly(N-isopropylacrylamide) (PNIPAM), and poly(2-hydroxyethyl acrylate) (PHEA) were first synthesised via RAFT aqueous polymerisation. The monomers were introduced to a round bottom flask, with BM1433, and ACVA. The water was calculated to be 30% v/v and added with a stirrer bar in the flask. The flask was sealed and was degassed with N_2 for 20 minutes. The solution was then submerged in an oil bath at 70℃ for 2 hours. After the allocated time, the reaction was quenched with oxygen and characterisation occurred with ^{1}H NMR and SEC. The majority of the mCTAs were reaching a 98% conversion or higher, so there is no special need for a purification step. The mCTAs could either be used in a liquid form for the next PISA step or they could be freeze dried and redispersed. Both protocols were conducted and the results were the same. To continue with the polymerizations, by using RAFT aqueous dispersion polymerization, polymeric nanoparticles were created, and each mCTA was chain extended. The procedure is similar to the previous aqueous RAFT. The mCTA (1 eq.) was introduced to a round bottom flask with diacetone acrylamide (DAA) (50 eq.), ACVA (0.1 eq.) and 20% w/w solids. As previously, the flask was sealed and degassed for 20 minutes. The solutions were then heated for 2 hours at 70℃. After the reaction time the PISA was quenched with oxygen and characterised as previously reported.[236] PISA NPs were synthesized and characterized with DLS, Zeta and TEM. To obtain a negative surface charge initially a PAA mCTA was employed. However, the nanoparticles formed during the polymerisation were significantly larger than expected (~200 nm) and did not change with PDAAm DP as is typical with PISA. This was attributed to electrostatic repulsion between the PAA chains. To minimise this interaction PDMA was added to the polymerization reaction of PAA in order to screen the negative charges between the PAA chains during the synthesis of negative nanoparticles. While preserving a general negative charge on the surface of these nanoparticles, the 1:9 ratio of PAA_{70} and $PDMA_{70}$ mCTAs reduced the repulsion of the core acidic groups.[236] Similarly for a positive surface charge PQDMAEMA mCTA was used. No positively charged nanoparticles were achieved with a PDAA core with DP of 50, so it was

concluded that the final polymer was still hydrophilic and that the DP was insufficient to make the polymer chain amphiphilic and, as a result, not cause nanoparticle assembly. Thus the polymerisation with a higher DP 100 PDAA was successful in creating an amphiphilic diblock and the PISA NPs were developed. The polymers of poly(N-isopropylacrylamide)-b-poly(diacetone acrylamide) PNIPAM-b-PDAA were collapsing due to their thermoresponsive nature, so as previously the same strategy was adopted so PDMA was added. Firstly, a new mCTA was designed $PNIPAM_{40}$-b-$PDMA_{40}$, with exactly the same procedure of aqueous RAFT and then it was used to perform RAFT aqueous dispersion polymerization to produce the solution of poly(N-isopropylacrylamide)$_{40}$-b-poly(N,N dimethylacrylamide)$_{40}$ -b-poly(diacetone acrylamide)$_{50}$ $PNIPAM_{40}$-b-$PDMA_{40}$-b-$PDAA_{50}$. The polymer that was developed as a triblock copolymer is the poly(N,N dimethylacrylamide)-b- poly(N-isopropylacrylamide-co- N,N'-methylene bis acrylamide) or $PDMA_{65}$-b-($PNIPAM_{90}$-co-MBA_{10}) and is the only copolymer in our library that does not contain a DAA core. Lastly poly(2-hydroxyethyl acrylate)$_{40}$-b- poly(diacetone acrylamide)$_{50}$ ($PHEA_{40}$-b-$PDAA_{50}$) was synthesized, with a DP 40, because PHEA is very hydrophilic and the -OH groups of the corona could promote the solvability of the polymer in the aqueous system and disallow the formation of nanoparticles based on the core to corona ratio, thus a lower DP has ensured the stability of the system.

As previously discussed the particles were fully characterized though NMR and SEC (Table 2). The molecular weight and dispersity of the polymers PQDMAEMA and 67 were unable to be calculated. PQMAEMA was exceptionally charged and very hard to dissolve in organic solvents so in order to protect the column the SEC measurements was not an option. A cross-linked nanoparticle like 67 with crosslinked polymer networks with a size range of nanometres that present difficulties for SEC characterization. This well packed crosslinked system is hard to be dissolved back into chains, due to swelling effects, therefore any peak presented in SEC would correspond to the nanoparticles and not the diblock copolymer system chains, thus would not provide the information needed from this technique.

Table 2. NMR and GPC data of PISA NPs

Polymer	Abbreviation	Mn (kDa)	Dispersity	Z-average (nm)	Polydispersity (PD)
$PDMA_{70}$-$PDAA_{50}$	PDMA	37750	1.11	23	0.06
$P(DMA_{70}+AA_{70})$-$PDAA_{50}$ 90%+ 10%	PAA	39070	1.12	22	0.14
$PQDMAEMA_{70}$-$PDAA_{100}$	PQDMAE	-	-	28	0.13
$PDMA_{40}$-$PNIPAM_{40}$-$PDAA_{50}$	62	15490	1.22	15	0.07
$PDMA_{65}$-$P(NIPAM_{90}$-co-$MBA_{10})$	67	-	-	25	0.06
$PHEA_{40}$-$PDAA_{50}$	75	18470	1.24	37	0.08

DLS measurements were conducted to measure the nanoparticles size and polydispersity (Figure 4.2.1) (Table 2). The graph depicts the small sizes achieved of the PISA NPs after purification through dialysis for 3 day against 18.2 MΩ to remove any leftover monomer, despite the fact that the polymerizations were conducted to a 100% conversion. Table 2 provides evidence to the low polydispersity (PD) the innovative PISA NPs have.

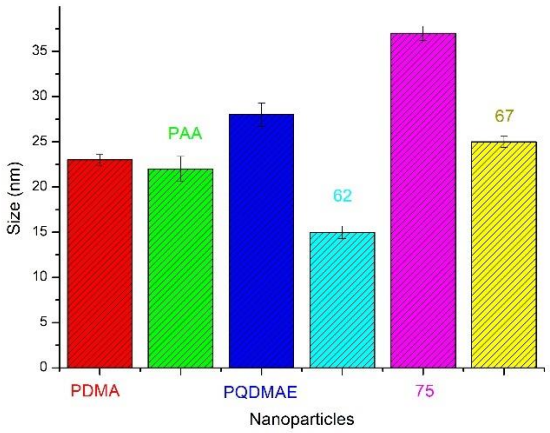


Figure 4. 2.1. PISA NPs DLS size measurements in nm (based on intensity data) at RT in water pH = 7

Interestingly the PISA nanoparticle 62 seems to have the smallest size at 15 nm is the only polymeric triblock copolymer on the above library, but it also has the lowest molecular weight. 75 even though it has one of the lowest molecular weight exhibits the highest hydrodynamic size at 37 nm. That could be due to the interactions of the hydrophilic corona in the aquatic solution so the polymeric chains would be extended.

Zeta potential measurements were also conducted to verify the surface charges functionality (Figure 4.2.2). As expected the PQDMAE is positively charged due to the protonated amino groups and PAA is negatively charged due to the acrylic acid carbonyl groups. The rest of the NPs were deemed as having a neutral charged.

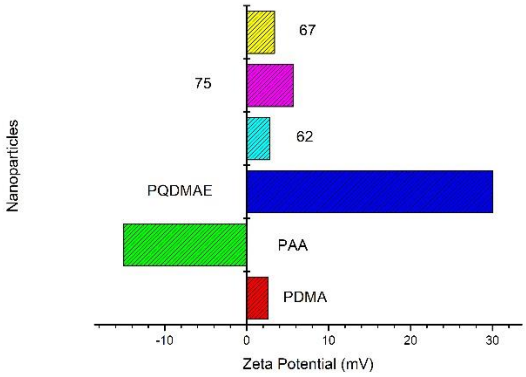


Figure 4.2.2. Zeta Potential measurements of PISA NPs at RT in water pH = 7

Transmission electron Microscopy (TEM) was used in order to verify the morphology, the size and the dispersity of the PISA NPs. Figure 4.2.3 unveils a uniformity in all PISA NPs of spherical nature, small size with good dispersity and comparable sizes, while being in good agreement with the DLS data. In the TEM data of the PDMA are 2 worm-like formations visible and it can due to fusion, since it is one the natures of PISA, but since the tension in the system is low the morphology should stay spherical and controlled.[237] There is a possibility though to be impurities from the TEM grid, since they seem to disassociate with the rest of the particles and a repeatability was noticed in various areas of the grid. For PAA PISA NPs the TEM data present great spherical morphology and very low polydispersity. The PQDMAEMA data present a droplet effect on the TEM grids which could be caused by the positive charge of the NPs. Overall the particles seem to be spherical, with good agreement between TEM and DLS sizes. Some worm formation are visible in the figure 4.2.3 even though the majority is still spherical of the 75 but It can be explained depending on the kinetics, the concentration and the solvent of the system. The OH group of PHEA corona can interact with water so it can form aggregations if the thermodynamic of the system allows it. The DLS though indicates a small monodisperse population forming so it could be caused through the drying effect of the TEM technique.

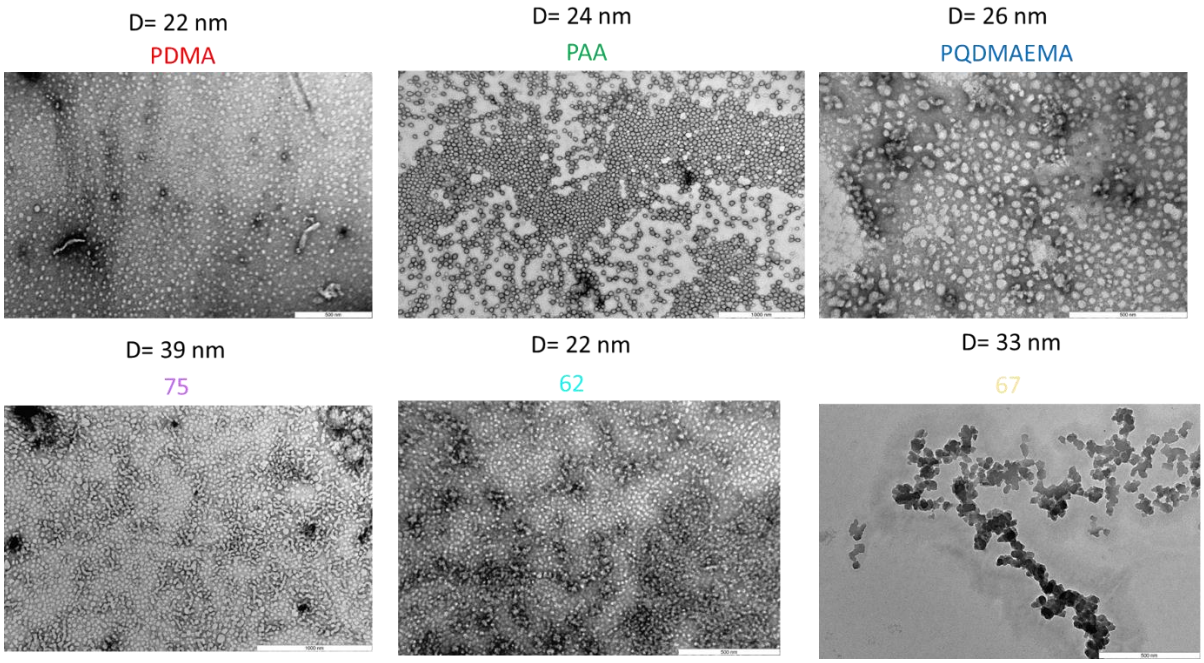


Figure 4.2.3. TEM measurements of PISA NPs in water pH = 7(scale bar 500nm) (D-diameter, size measurements from sample of 100)

62 NPs are overly concentrated, thus some defects are present so the TEM data, but still prove that they are spherical and very small in size. Lastly, 67 NPs are aggregating and are creating clusters due to the dry state effect that the TEM imposes. The aggregates presented in the TEM figure above were not visible with DLS and NTA which are liquid techniques of characterization leading to the conclusion that the evaporation of the solvent created the aggregation of the 67 NPs.

To examine nanoparticles suitability for bioapplications, cytotoxicity studies were performed using a Presto blue bioavailability assay in NIH 3T3 fibroblasts and RAW 264.7 for 48 hours. The nanoparticles were seeded in 80% confluency of mature cell lines in a 96-well plate. The results were repeated 3 times and presented a standard deviation of ± 6%. In Figure 4.2.4 below 100% viability was indicated for all PISA NPs with concentrations up to 1 mg/mL apart from the positively charged nanoparticles PQDMAE where the increased viability starts from 0.1 mg/mL concentrations. This result can be explained due in part to their greater cell uptake and their damaging effect on cell and lysosomal membranes.[238] It is noticeable that in some cases there is overexpression since compared to the control the NPs exhibit viability of over 100%. This could have been caused by a lot of parameters such as cellular stress, upregulation of endogenous pathways or enhanced transcriptional activity etc. In this case,

the presto blue assay used to measure the cell viability, depends on the cellular metabolic activity. Therefore, if the mitochondrial respiration is increasing, a higher viability will occur.

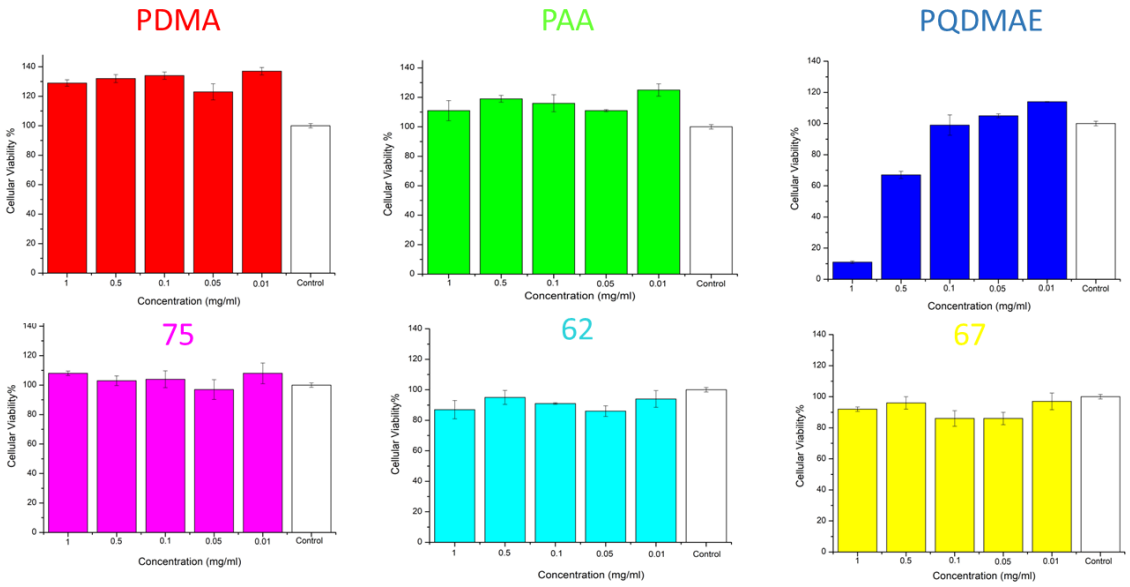
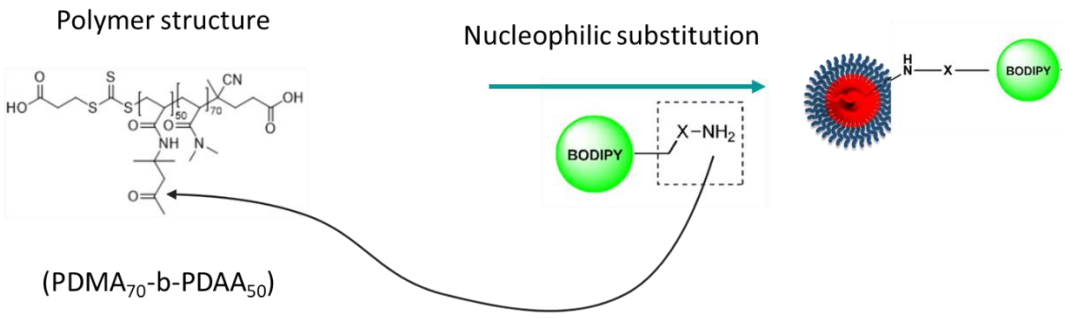


Figure 4.2.4. 3T3 NIH cell viability studies of PISA NPs 48hours concentrations 1-0.01 mg/mL. (Control is define as the untreated cell lines)

Previous studies, have indicated that nanoparticles could also promote cellular growth.[239, 240] Similar results were achieved through the RAW 264.7 macrophages studies, but the phenomenon of overexpression is noticeable as well. Nanoparticles have been found to cause a stress response in various cell lines.[241] Cell lines that proliferate in a stressed environment will have faster metabolic activity, which will increase the cellular functions and number.[87] All formulations appear not to have any cytotoxic effect up to 1 mg/mL apart from PQDMAE, since it is positively charged. Positively charged nanoparticles tend to interact more strongly with negatively charged cell membranes during cellular absorption. They may be more easily absorbed by cells due to this improved contact. Nanoparticle internalisation, however, can impair typical biological functions and cause cytotoxicity.[242] Nanoparticles can enter cells and produce oxidative stress, inflammation, and disruption of biological processes, which can lead to cellular apoptosis. [243]

4.2.2. Fluorescent tagging of PISA nanoparticles

In order to monitor the PISA NPs *in vitro* a 4,4-difluoro-5,7-dimethyl-4-bora-3a,4a-diaza-s-indacene3-propionic acyl hydrazide (BODIPY™ FL hydrazide) was incorporated. The BODIPY FL hydrazide was selected because it had a high fluorescence quantum yield and it will not interfere with the cellular dyes, in creating a FRET phenomenon or cause undesirable non-specific interactions with cellular components.[244] The BODIPY hydrazide group and the carbonyl groups found in the PDAA chains can form a hydrazone bond, which served as the means of attachment. Previous studies have demonstrated that using hydrazone bonds to cross-link PDAA chains boosts particle stability even though they are fundamentally dynamic in nature.[245] Hydrazone linkages can form via the nucleophilic substitution of the pendent ketone groups of PDAA after the reaction with the dye's hydrazide groups.[245] The ratio of polymer: dye was kept at 10:1, since the dye is very effective and it could cause a synergistic effect in fluorescent measurements and lead to hard visualization through confocal. The reaction was left stirring overnight. After the end of the reaction the NPs were purified through spin filtration through a 3 kDa filter 3 times for 20 minutes to remove any the unreacted dye.



Scheme 16. Reaction scheme of EDC coupling of BODIPY™ FL hydrazide reacting with the carbonyl group of PDMA NPs

A UV-SEC trace confirmed that the PISA NPS were in fact tagged. [236] After this easy fluorescent tagging, characterization of the NPs must be repeated to verify that the

physicochemical and morphological characteristics remained intact after the reaction. Multiple characterizations like dynamic light scattering (DLS), zeta potential, nanoparticle tracking analysis (NTA) and transmission electron microscopy (TEM) were conducted to verify that the NPs were not affected in any way. Table 3 below holds the data that prove that the NPs were not affected and they are still spherical and monodispersed with good agreement between DLS, NTA and TEM size analysis. The excitation and emission was measured through a fluorometer to be approximately 360 nm and 512 nm accordingly for each particle (see experimental part).

Table 3. Fluorescent NPs characterisation data. (ECM= endothelial conditioning medium)

Polymers	**Size (nm)**	**Dispersity**	**Zeta (Mv)**	**NTA Size (nm)**	**Stability in ECM 24Hrs (nm)**
PDMA	31	0.03	+3	33	286
PAA	36	0.03	-15	30	13 & 100
PQDMAE	31	0.09	+30	32	35 & 92
62	17	0.20	+3	7/ 11	23 & 125
67	22	0.15	+3	-	17&152
75	45	0.24	-6	47	286

The stability with endothelial conditioning media (ECM) was also examine to evaluate if the PISA NPs will develop a protein corona effect. The PISA NPs were incubated in ECM for 24 hours in a CO_2 incubator at 37 ^oC. As it is obvious from Table 3, PDMA and 75 create aggregations with the biomolecules of the cellular media. The rest of the PISA NPs exhibit 2 populations, the original formulation one and some bigger aggregates that can be attributed to biomolecules in the conditioning media.

Figure 4.2.5 depict that the fluorescent NPs are spherical with a monodispersed population so they can be utilized for the purpose of monitoring through the BBB. It is also shown that the TEM images are in accordance with the TEM data without the use of the fluorophore so PISA NPs are unaffected morphologically by the addition of the fluorophore.

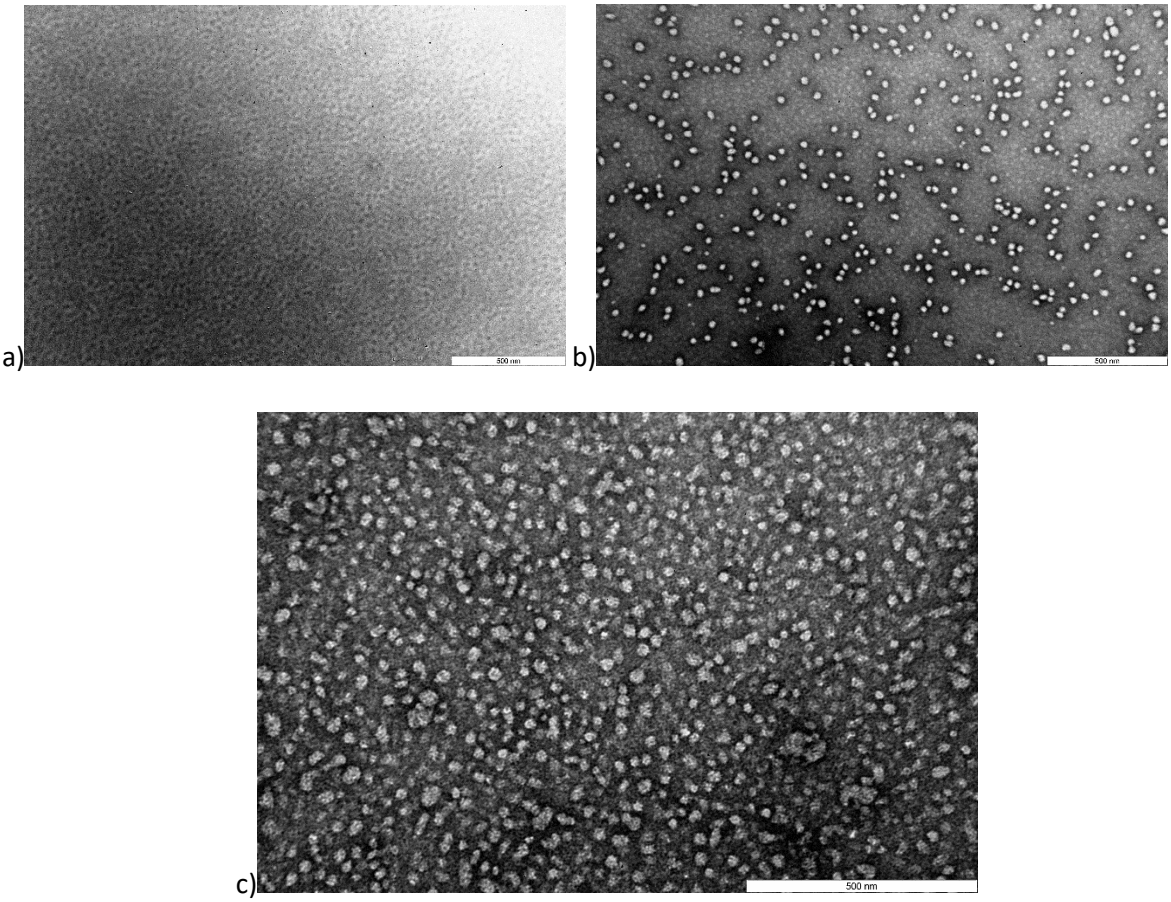


Figure 4.2.5. TEM data of fluorescent NPs a)PDMA b)PAA and c)PQDMAE

Herein, the PISA NPs will have to be examined as per their effects on the cells that will compose the *in vitro* BBB system. A cytotoxicity study on the CD34+ cell line was conducted with concentrations of 1, 0.5, 0.1 mg/mL for all the PISA NPs apart from PQDMAE due to their previous cytotoxic effects on RAW 264.7 and NIH 3T3. The positively charged PQDMAE will be examined in lower concentrations such as 0.1, 0.05 and 0.01 mg/mL. The cell viability was again measured with a presto blue assay. CD34+ as previously where seeded in a 96 well plate with 8000 cells/well. After the CD34+ reached 80% confluency and their level of maturity was satisfactory the PISA NPs were treated in triplicates in the concentrations stated above and were incubated for 24 hours. The cells were checked for morphological

defects in the optical microscope after the 24 hours incubation time. After the 24 hours, PISA NPs were removed via aspiration and were washed with PBS. A dilution assay of presto blue 10% was prepared and was inserted into the wells. The plate was incubated for 1 hour in a CO_2 incubator and afterwards was deposited into the plate shaker for 5 minutes before the UV-vis measurement at 580 nm wavelength. Figure 4.2.6 indicates similar levels of bioavailability as the previous cell lines. PDMA, PAA, 62 and 75 have above 100% viability, at all the concentrations. 67 depicts a 90% viability at 1 mg/mL and 100% for concentrations 0.5 and 0.1 mg/ mL. Like previous experimentation appears to be viable only at 0.01 mg/mL.

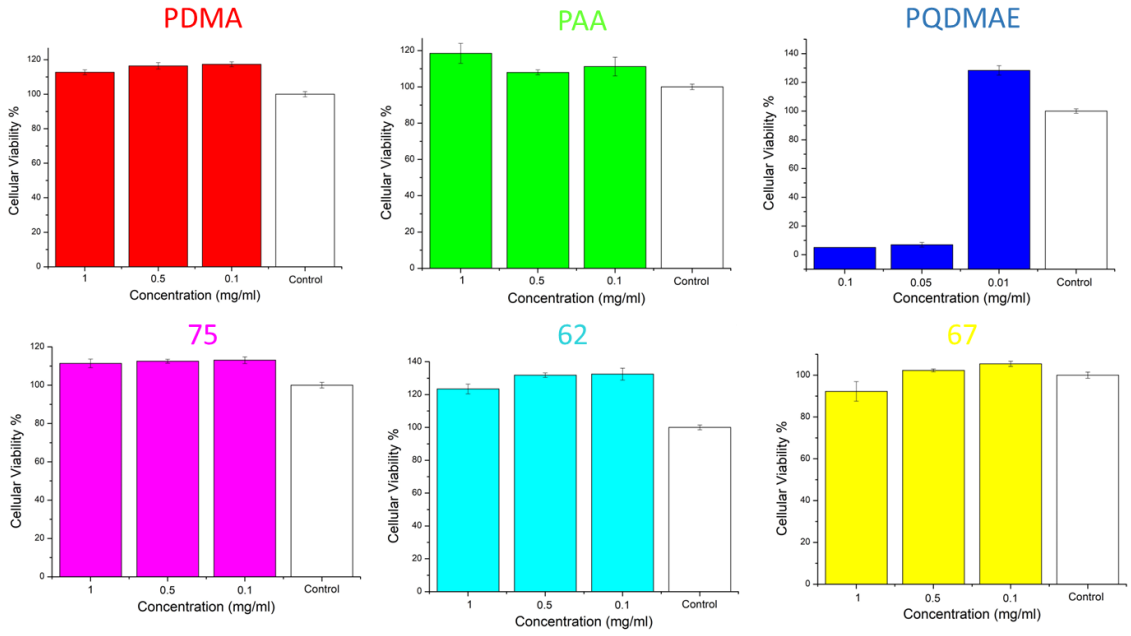


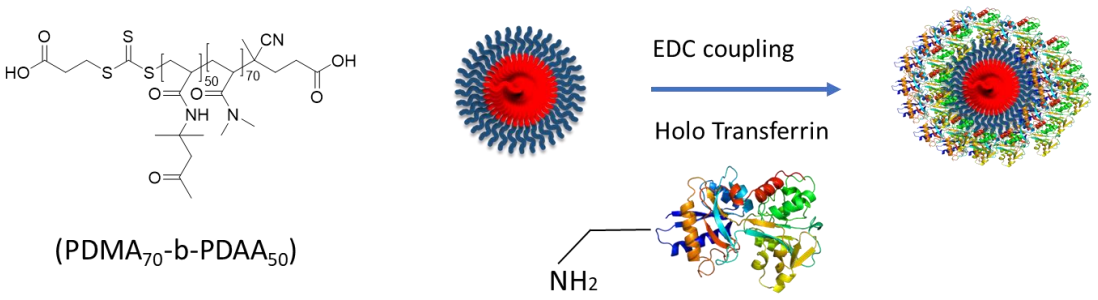
Figure 4.2.6. Endothelial cell line cytotoxicity $CD34^+$ of PISA nanoparticles with BODIPY fluorophore. (Control is define as the untreated cell lines)

Moreover from the interpretation of the results above all the PISA NPs will be studied in the *in vitro* BBB model, except from the 67, since it has lower viability ratios, for 1 mg/mL concentration, it is neutrally charged and the corona of PDMA will be studied in any case.

4.2.3 Protein tagging of PISA nanoparticles

Efficient BBB crossing tends to be challenging for NPs without protein coverings for a variety of reasons. They might not have particular receptors or targeted ligands that can promote receptor-mediated endocytosis. Uncoated NPs' surface characteristics may also make it difficult for them to connect with BBB endothelial cells or encourage transcytosis.

Receptor-mediated transcytosis (RMT), which has been extensively researched, has demonstrated promising outcomes for improving transport through the BBB. To enable effective transcytosis of cargo into the brain, specific receptors have been targeted, including the transferrin receptor (TfR). Studies have shown that NPs are successfully delivered employing RMT-based procedures, with improved permeability ratios when compared to alternative methods. In order to examine if the PISA NPs have better permeability through receptor mediated transcytosis pathway a holo human transferrin will be attached to PISA NPs system. A holo human transferrin was preferred than apotransferrin and other variations of the transferrin protein, due to the fact that exhibits the higher binding affinity with the TfR.



Scheme 17. EDC coupling of Holo Transferrin on PISA NPs (PDMA model)

In Scheme 17 above, the reaction of the EDC coupling of the transferrin with the PISA NPs is depicted. One of the most often used carbodiimides is EDC [1-ethyl-3-(3-dimethylaminopropyl) carbodiimide hydrochloride], which catalyses the creation of amide bonds between carboxy and amine groups.[246] Its appeal stems from its great water solubility and ease of waste removal. By forming active ester functional groups with carboxylates, sulfo-NHS (N-hydroxy sulfosuccinimide) is utilised to boost the stability of active

intermediates in coupling reactions.[247] In this reaction the free amino groups of transferrin will conjugate with the carboxylic groups provided by the PISA NPs initiator but also corona in some instances (PAA) (Scheme 17). An extensive protocol of the reaction can be found in the experimental section.[248] Holo human transferrin was dissolved in MES 50 mM pH 6 at a concentration of 2 mg/mL. The PISA NPs were dissolved in the same buffer at a concentration of 2 mg/mL. While combining the two solutions in equal amounts, the particle solution was pipetted dropwise into the protein solution. After 10 minutes of continuous stirring, 5 mg of EDC dissolved in 20 μl of buffer was added. To stop the reaction, 10 mg of glycine were added to the mixture after two more hours of stirring. The PISA NPs were afterwards purified by spin filtration with a 100 kDa membrane to remove the excess or unattached protein. To verify the attachment of protein on the PISA NPs Maldi-Tof analysis was perform as well as SDS PAGE gel and UV-vis since transferrin will have an absorbance at 280 nm wavelength.

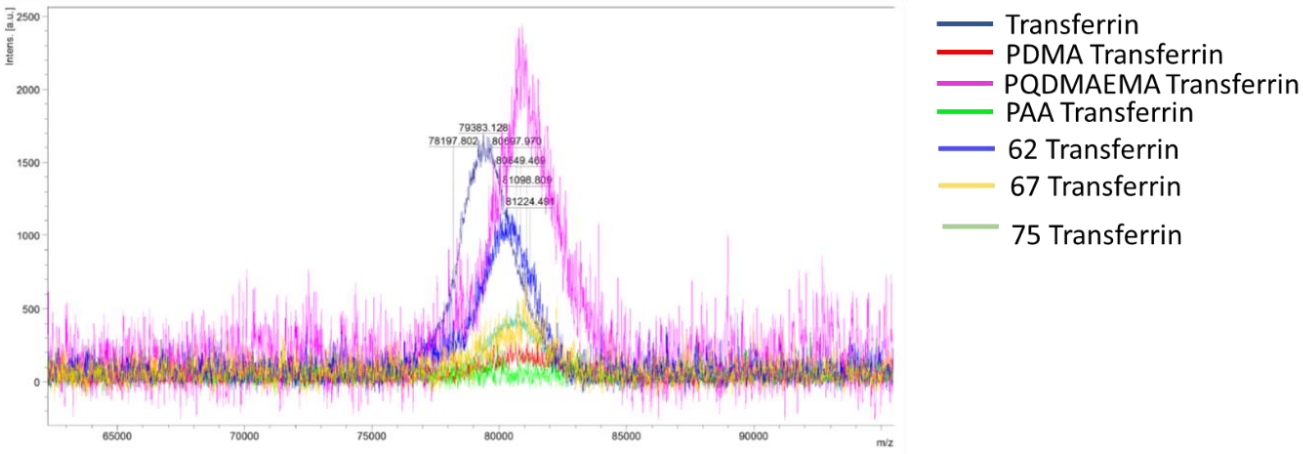


Figure 4.2.7 Maldi-Tof spectra of PISA NPs attached with Transferrin. Matrix used Sinapinic acid 1:1

From Figure 4.2.7 above the placement of all the spectrums to the left minus the transferrin spectrum indicates the higher molecular weight(M_w) of the PISA NPs with the transferrin. The M_w of transferrin is shown to be 78 kDa (even though the actual M_w is 77 kDa), due to the addition of matrix and salts that increase slightly the molecular weight. Transferrin's Mw might have a discrepancy also due to sample preparation, since the samples were not prepared in sterile conditions, hence contaminants or impurities in the sample could contribute to discrepancies in the measured molecular weight. The functionalized PISA NPs presented M_w of 79 kDa and higher. Between the PISA NPs there is a differentiation in

intensity through Maldi-Tof, as the PQDMAE Tf and 62 Tf appear to have higher intensities than the rest. This is due to the ionization of each of the PISA NPs differs and some PISA NPs are harder to ionize and not produce fragments in smaller molecular weights before they reach the detector. The above analysis confirms the attachment of the transferrin protein.

There is always a method of passive absorption of the protein on the PISA NPs depending on the interaction that will form.[249] Electrostatic interactions can develop through PQDMAE that is positively charged with the negatively charged Transferrin protein. To confirm that the NPs' morphological and physicochemical properties held true during the reaction, further analysis of the particles is required.

Table 4. Characterization of PISA NPs after the protein attachment

Polymers	Size (nm)	Zeta (mV)	NTA Size (nm)	Stability in ECM 24Hrs (nm)
PDMA Tf	26	-7	53	13 & 125
PAA Tf	42	-22	32	12 & 82
PQDMAE Tf	43	+15	39 & 57	160
62 Tf	34	-6	33	13 & 180
67 Tf	25	-4	-	315
75 Tf	69	-2	71 & 88	285

All the PISA NPs with the attachment of transferrin protein will be referred at as PDMA Tf so the separation with those that do not carry the protein will be apparent. The sizes examined by DLS and NTA are shown in Table 4 above. An increase in the size of PAA Tf, PQDMAE Tf, 62 Tf and 75 Tf was recorder by the DLS data. PDMA Tf is in good agreement with the previous DLS data but the NTA reports an increase of 20 nm in size. PAA Tf exhibits only a 10 nm increase through the DLS, but the NTA measurements are at 32 nm as previously. NTA utilizes high-speed cameras to capture the Brownian motion of nanoparticles with high temporal resolution. This enables accurate tracking of particle movement and precise measurement of particle size and concentration. DLS, on the other hand, relies on the analysis of temporal fluctuations in scattered light intensity, which may not provide the

same level of resolution, especially for small or fast-moving particles. For the positively charged NPs the sizes are 43 nm from DLS but NTA shows a double population at 39 nm and 57 nm. Since the population of the 39 nm is more dominant in the measurement, it can be assumed that the 57 nm population is due to an aggregation effect. The appearance of several populations by NTA can be due to the higher sensitivity of the machine, that can be attributed to the real time light scattering, that is able to track individual NPs in Brownian motion. While both NTA and DLS are valuable techniques for nanoparticle characterization, NTA is often preferred in situations where high resolution, sensitivity, and the ability to resolve complex nanoparticle populations are required. 62 Tf sizes from DLS and NTA are in coherence and the slight increase from 17 nm to 33 nm could be due to the protein corona formation around the NP. Lastly, 75 Tf indicates an increase from 45 nm to 69 nm and that is big increase to be attributed to the protein corona phenomenon but there should be also aggregation effects which is better depicted with the NTA of 71 nm and 88 nm. Due to its -OH groups 75 Tf and form protein corona effect through hydrogen bonding so it has the potential to adhere more protein molecules. NTA's ability to detect aggregation and distinguish between different populations further supports this observation, as it can capture the complex interactions between nanoparticles and biomolecules.

From stability in ECM the data indicate that PQDMAE Tf, 67 Tf and 75 Tf form aggregations and protein corona effects. The rest of PISA NPs interestingly show 2 populations one at 12-13 nm and one bigger. It is safe to assume that the PISA NPs will not have degraded in such a small time period (24 hours) from the enzymes in the ECM, as it is confirmed by the confocal measurements below. Thus the smaller population could be attributed to a certain biomolecule in the ECM solution. As indicated by the blank DLS of the ECM it appeared to have 3 populations one around 5 nm, at 100 nm and at 1000 nm, which could be due to cellular debris. . The 5 nm could be attributed to proteins in the solution which after aggregation can exhibit a population around 10 nm. The PISA NPs with Tf then present a protein corona interaction in endothelial conditioning medium.

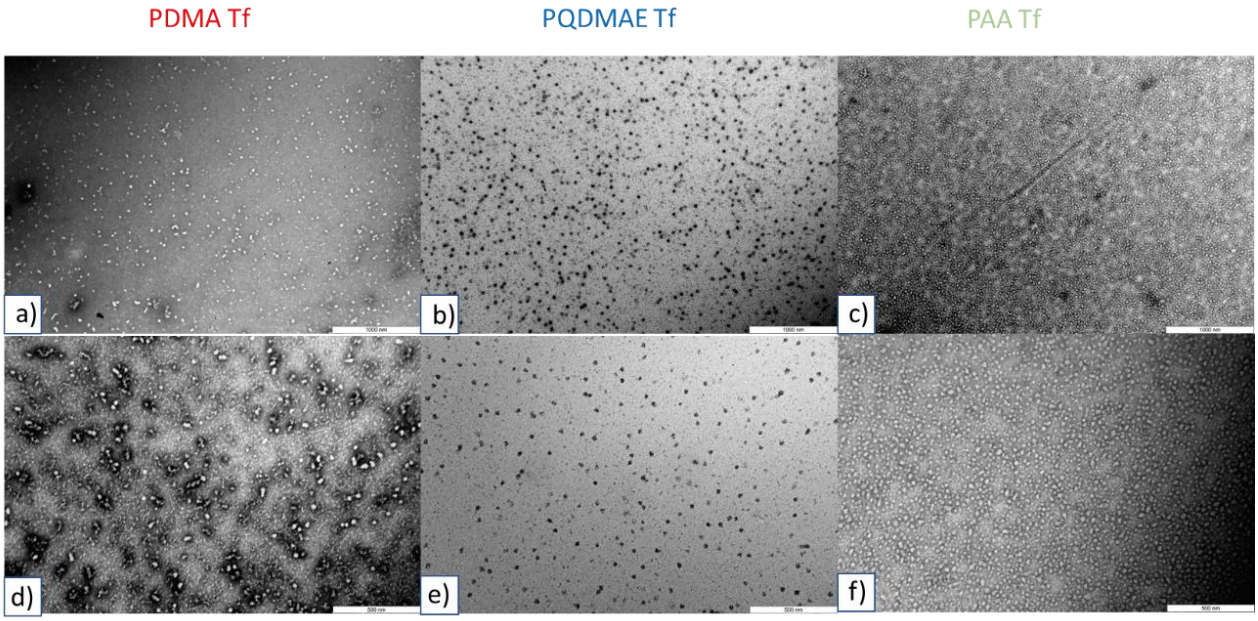


Figure 4.2.8. TEM of PISA NPs a,b,c) PDMA Tf, PQDMAE Tf, PAA Tf scale bar 1000nm, d,e,f) PDMA Tf, PQDMAE Tf, PAA Tf scale bar 500nm

From TEM images provided in Figure 4.2.8 we are able to verify the morphology of PISA NPs after functionalisation with Tf. The morphologies of PQDMAE Tf and PAA Tf appear to be spherical overall and the sizes provided correspond to 27 ± 6 nm and 24 ± 7 nm which appear to be smaller than the DLS and NTA indicated. That can be explained from the fact that TEM is a dry technique and it can have that effect on NPs. For the PDMA Tf some defects in the morphology are visible but still the majority indicates a spherical distribution of NPs. The size provided from a sample of 100 is 25 ± 8 nm, which verifies that the polydispersity of the NPs has changed.

Continuing with the characterisation of the PISA NPs with Tf their cytotoxicity effects were also examined. Since, previously there was a recurring issue with the overexpression of PISA NPs to make sure that there is no synergistic effect from the UV-vis examination of Presto Blue the assay of cytotoxicity evaluation was changed. Herein, the luminescence examination for the cellular viability with a CytoTOX Glo assay from Promega. The protocol can be found in the experimental part. After measuring the luminescence the data below in figure 4.2.9 A) depict the bioactivity of the PISA NPs Tf at 1 mg/mL. All PISA NPs exhibit a 85-95 % viability apart from PQDMAE that is cytotoxic in such high concentration. For figure

4.2.9 B) the non cytotoxic effects of PQDMAE Tf at 0.01 mg/mL concentration (>100% viability) are compared to the PQDMAE NPs with just the fluorophore attachment.

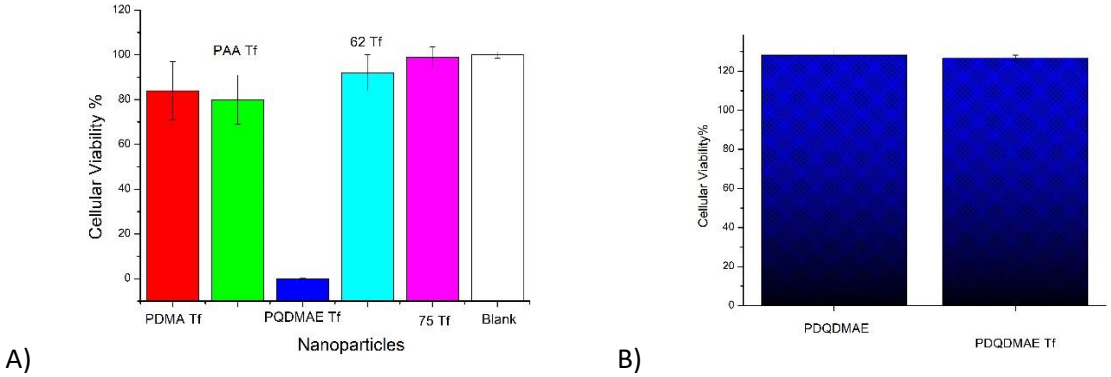


Figure 4.2.9. Endothelial cell line cytotoxicity CD34⁺ of PISA nanoparticles with BODIPY fluorophore and Transferrin coating A) 1mg/mL concentration B) PQDMAE Tf 0.01 mg/mL concentration. Blank is defined as untreated CD34⁺ cells.

From the above we can confirm that it is safe to use the above PISA NPs systems to examine the permeability in an *in vitro* BBB.

4.2.4 Quantification of internalized nanoparticles

Before the introduction of the PISA NPs in the BBB, an evaluation has to be made based on the internalization ability of the NPs in the CD34+ cell line ,which will constitute the luminal compartment in the *in vitro* BBB system. The PISA NPs were examined *in vitro* in CD 34⁺ human endothelial cell line and were analysed for their endocytosis efficiency through live cell imaging Incell fluorescent analysis. Live cell imaging with fluorescence analysis is a useful method to monitor the cellular uptake of fluorescently labelled cargo and evaluate endocytosis effectiveness in real-time.[250]



Scheme 18. Internalization experiment of PISA NPs in CD34+

Scheme 18 explains the experimental plan used to measure the cellular uptake of the PISA NPs. The CD34+ were seeded 20000/well in a 96 well plate and were allowed to grow and form tight junctions mimicking the BBB model. Here we should note that less cells were seeded due to the area difference between the 96 well plate and the BBB filter. After 6 days of growing the cell line into maturity and appropriate density the PISA NPs were introduced to the CD34+ cell line and were incubated for 24 hours, similarly with the protocol that will be used for the *in vitro* BBB. Twenty-four hours later nanoparticles were removed from the cell live via aspiration and were washed with PBS. The cells were incubated with Hoeschst H33342 in 1:2000 dilution for 10 minutes and lysotracker 1:10000 dilution for 30'. Hoeschst dye was used to indicate the nuclei blue and lysozyme tracker is staining the lysosomes red. A lysozyme tracker was used in order to quantify the amount of particles that were in fact internalized by the cells. The 96 well plate was measured via live cell imaging (Figure 4.2.10).

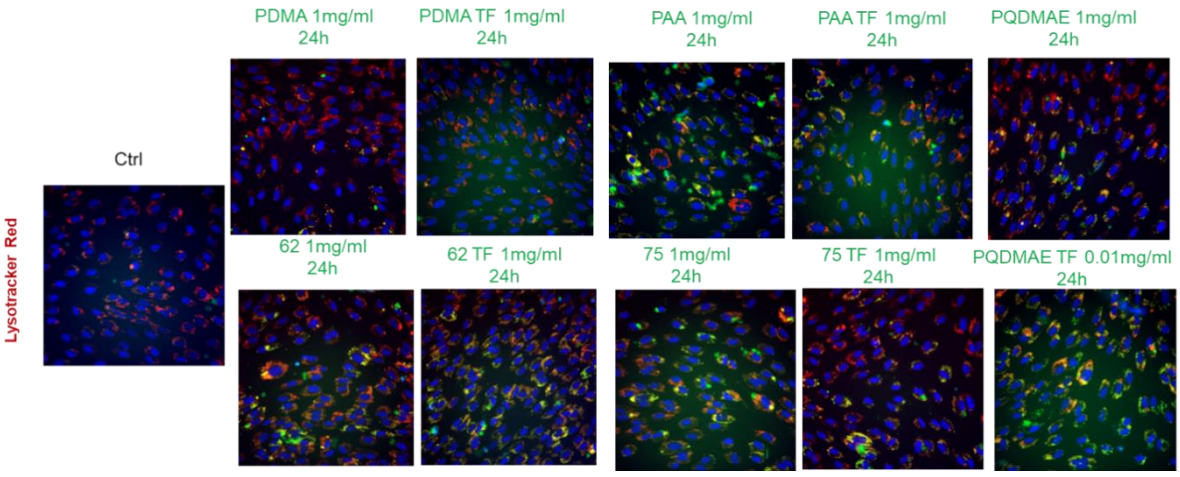


Figure 4.2.10. Live imaging fluorescence data from incell of seeded NPs for 24 hours in CD34+ cell line a)control (no nps) b) PDMA 1mg/mL c) PDMA Tf 1mg/mL d) PAA 1mg/mL e)PAA Tf 1mg/mL f)PQDMAE 0.01 mg/mL g)62 1mgm/mL h)62 Tf 1mg/mL i)75 1mg/mL j) 75 Tf 1mg/mL k)PQDMAE Tf 0.01 mg/mL (green) BODIPY™ FL hydrazide, Nucleus (blue) Hoechst blue, Lysozyme tracker (red) lysosomes

From the images above the synergistic orange colour appears, which is attributed to the green dye from the BODIPY and the red dye from the Lysozyme tracker being colocalized in the same position. It can also be distinguished that the higher amount of internalised particles are for the PAA, PQDMAEMA Tf and 75 NPs as the images dictate the emission intensity. This can be rationalized, since positively charge NPs will interact and have higher

uptake on the negatively charged system the cell line is producing. Thus transferrin functionalization allows receptor mediated pathway to be utilized so permeation in the cells would be easier. The PAA particles seemed to have an impact on the tight junctions of the cells, which results to a higher uptake ratio. The 75 NPs carry a free hydroxyl group (-OH) in their corona chemistry, which can interact and create a protein corona easily through hydrogen bonding, which can lead to better permeation ratio in the $CD34^+$ cell lines. Another thing to be mentioned should be the difference of uptake between PDMA and 62. As is visible from figure 4.2.10 PDMA indicated almost no internalization but the 62 NPs seemed to have one of the highest. At this point it should be reminded to the reader the 62 NPs are very close in chemistry with the PDMA particles the only difference is that 62 carries a $PNIPAM_{40}$ as well. According to previous research,[251] PNIPAM engages with particular cellular receptors and pathways, which could facilitate internalisation. With various cellular receptors, PDMA might not adhere or have the same degree of affinity, which could result in less effective internalisation.[252] Due to their ease of penetration through cellular barriers, smaller polymer chains or nanoparticles typically have higher internalisation. [253] 62 and PDMA's cellular absorption pathways can be impacted by the precise size and shape of the molecules. Since 62 has been proven to be smaller than PDMA exhibits better internalisation.

Moreover, the emission of the fluorescent signal of the colocalization was able to be calibrated, so the images from live imaging could provide quantitative data of internalization. Figure 4.2.11 indicates the aforementioned analysis and internalisation data. 62 Tf appears to have the highest internalisation of the PISA NPs followed by PAA and PQDMAE Tf. It was expected that the particles with the transferrin coating would indicate better internalization but that does not seen to be the case for every PISA NP. PDMA with and without Tf seems to have very low uptake. PAA seems to have better endocytosis than its PAA Tf counterpart that would offer higher levels because of its protein functionalization. PAA can interact with the lipid bilayer of cell membranes, particularly when it is present in higher concentrations or contains larger molecular weights. Because PAA is a polyelectrolyte, it can disrupt the lipid membrane's structure and produce brief pores or openings that help PAA diffuse into cells.[254]

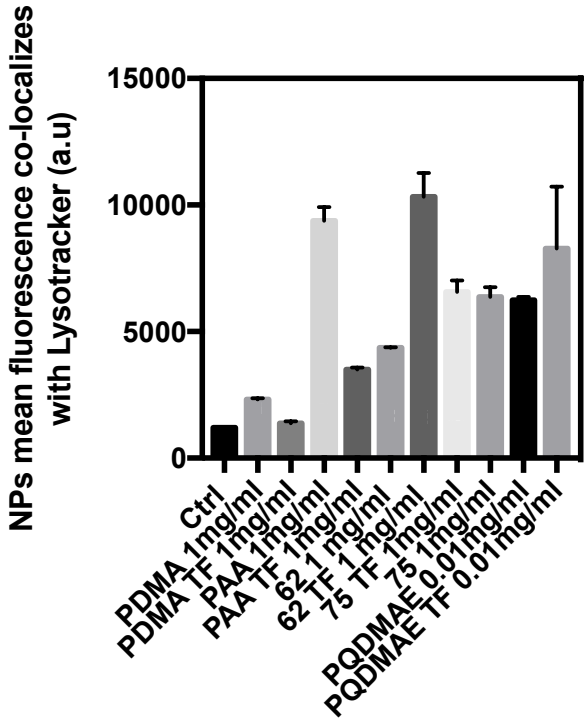
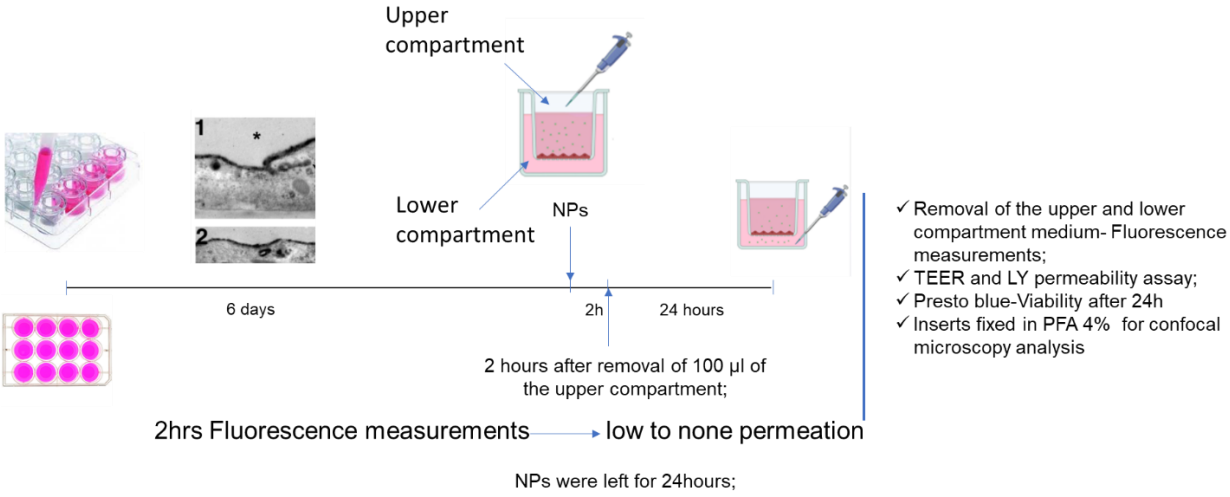


Figure 4.2.11. Colocalization fluorescence of lysotracker with BODIPY analysis of PISA NPs

In addition, 62 Tf appears to have very increased cellular uptake in comparison to 62, even though in the images above it seems the other way around. The percentage that the Tf helps the permeation is apparent in this instance. For the 75 and 75 Tf data are exhibiting similar activity, which supports the hypothesis that 75 forms its own protein corona in the system that facilitates the internalisation. Lastly, PQDMAE Tf also demonstrates better permeation ratios than the PQDMAE alone despite its charge.

Here we should note that this is not a co-culture environment but a simple CD34+ cell line so the transferrin receptors will have different affinity from an *in vitro* BBB system. Thus the evaluation shall be repeated in the *in vitro* BBB system to compare the results.

4.2.5 Permeability evaluation of an *in vitro* BBB



Scheme 19. In vitro BBB permeability and viability control and experimentation explanation

The PISA NPs were examined in a developed *in vitro* blood and brain barrier (BBB) model, which constitutes in a monolayer of CD 34^{+} human endothelial with tight junction formations. The *in vitro* BBB was produced as previously reported. [103] As specified in the introduction part of this chapter, human-derived brain-like endothelial cells (ECs) CD34+ will be used for the luminal side in the filter. For the 0.4µm and 3µm filters, these ECs were co-cultured with pericytes (lower compartment) for 6 days and 12 days accordingly. Although the ECs in both cases displayed signs of a BBB phenotype, such as an increase in tight junctions and the upregulation of efflux pumps, there were notable differences in the permeability to astrocyte or pericyte-derived small molecules and transendothelial electrical resistance (TEER) of the ECs. Prior to seeding, a matrix gel was utilised to assure the cell lines' safe culture and growth and to enable the cells to develop in a monolayer fashion. Here we should state that the composition of the filters and the matric gel applied could influence the outcome of the permeability thus a separate experiment was performed with just the aforementioned 2 components.

Table 5. Permeability of the filters with matrix gel of PISA NPs 1mg/mL concentration (PQDMAE 0.01 mg/mL)

3μm Filters

Polymers	Concentration % at 2 hours	Concentration % at 24 hours
PDMA	13.6%	31.7%
PAA	10.7%	30.0%
PQDMAEMA	0.4%	0.4%
PQDMAEMA Tf	0.4%	0.7%
62	6.8%	24.5%
75	6.8%	17.8%

0.4 μm Filters

Polymers	Concentration % at 2 hours	Concentration % at 24 hours
PDMA	3.8%	14.0%
PAA	1.9%	12.3%
PQDMAEMA	0.3%	0.4%
PQDMAEMA Tf	0.4%	0.4%
62	0.9%	8.6%
75	0.2%	5.7%

As presented in the table 5 above, the permeability of the NPs is not optimal. Here we should explain that the concentrations above were calculated through a Synergy H1 plate reader (Biotek). Since the PISA NPs are caring the fluorophore BODIPY FL hydrazide, the plates were read at 533 nm wavelength. Media with PISA NPs would be in duplicates in a black 96 well plate.

A calibration curve of the different concentrations was designed and afterwards it was utilised to determine the concentrations of the readings of the upper and lower compartments (see experimental) .

After 2 hours of incubation with the filters coated with matrix only a very small amount of PISA NPs seem to have permeated to the lower compartment. Thus the PISA NPs were left incubating for 24 hours. The situation did not improve since the maximum % concentration from the 3 μm filters is PDMA with 31.7 % and for the 0.4 μm filter is again PDMA with 14%. This can be interpreted that from the PISA NPs that will try to permeate the BBB the maximum percentage of permeation can be this one.

After the development of the *in vitro* BBB as mentioned above on day 6 the PISA NPs are introduced to the upper compartment and the incubation period starts. After 2 hours, 100 μl were collected from upper and lower compartment to measure the concentration of permeation that was found to be approximately 0 so the PISA NPs were left to incubate for 24 hours. When the 24 hours passed the same measurements were repeated to evaluate the concentration of the permeability. Table 6 below shows that the permeation maximum concentration that could be reached through 0.4 μm filters is 7.2 % for the PDMA and 62 PISA NPs. The result constitutes a bit of a paradox since previously it was demonstrated that

the internalisation of the PDMA NPs was exceedingly small. The second highest percentage was 4.8% of PDMA Tf ,which also exhibited low cellular uptake in the previous experiment.

Table 6. Permeability concentration % of PISA NPs in 0.05 mg/mL concentration (PQDMAE 0.01 mg/mL) lower compartment data. (N=2)

Polymers	Concentration % at 2 hours	Concentration % at 24 hours
PDMA	0.40%	7.2%
PDMA Tf	0.30%	4.80%
PAA	0.38%	2.80%
PAA Tf	0.45%	0.80%
PQDMAE	0.4%	3.3%
PQDMAE Tf	0%	0.1%
75	0.40%	3.7%
62	0.96%	7.2%
67	0.2%	1.8%

Further measurement were conducted to determine the integrity, permeability and viability of the BBB. Integrity was tested through the TEER measurement as was previously mentioned in the introduction and at this section. For permeability studies we will be using lucifer yellow (LY) (500 Da) a small fluorescent molecule that will give us information about the constitution of the BBB as well. At the end viability studies with presto blue will be conducted to confirm that the cell lines have not been affected by the PISA NPs. In vitro BBB is more dynamic system and needs more analysis to cover all its aspects.

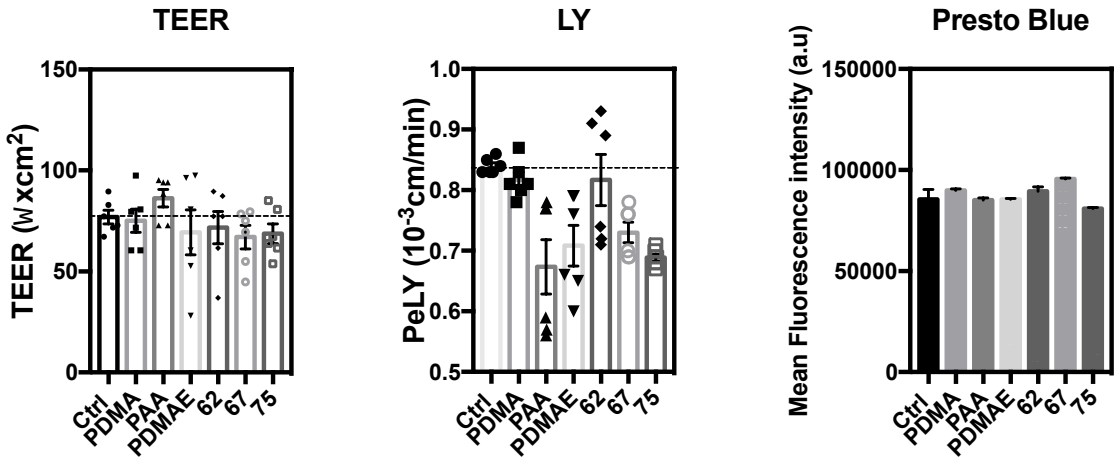


Figure 4.2.12 Integrity of *in vitro* BBB validation via TEER , LY and Presto blue

An epithelial volt-ohm metre or a microelectrode system is a specialised instrument used to measure TEER. The *in vitro* BBB model incorporates electrodes in the apical and basolateral compartments, and a modest electrical current is delivered.[108] The endothelial cell monolayer's resistance to current flow is assessed. Higher resistance values suggest tighter connections and better barrier integrity. Here, from figure 4.2.12 the TEER data indicate an intact *in vitro* BBB for all PISA NPs . Although the resistance portrayed in the graph is not noticeably high (~80 Ωcm^2), all the values approximate the ones of the control system. This observation substantiates the contention that the PISA NPs are not compromising the BBB's structural integrity. PAA appears to be higher than the control but the difference is negligible. PQDMAE seems to have a slightly lower TEER value and that can be due to its positive charge interacting with the BBB if particles have stayed encapsulated in the ECs , but also the value is very close to the control group so it is consider normal.

In order to determine the permeability of the BBB further studies were conducted. In research studies,[108] Lucifer Yellow (LY) is frequently utilised as a tracer molecule to measure the BBB's permeability. Although LY is not frequently used to explicitly evaluate the BBB's integrity, its behaviour can reveal information about the BBB's permeability. In Figure 4.2.12 LY permeability is exhibited. The reverse thing that applies for the TEER applies here, the higher the permeability the worse the integrity appears to be. Increased permeation of LY across the BBB indicates compromised BBB integrity or accelerated paracellular transport.

Numerous things, including inflammation, damage, and disruption of tight junctions, or altered signalling pathways involved in BBB regulation, could trigger dysfunction.[255] All PISA NPs values appear to be lower than the control group (no treatment filter). In some cases like PAA can create the conception that tight junction are actually improved in comparison to the control group, because the value is significantly lower. That could be actually attributed to the nature of the PAA as a polyanionic polymer has the ability to interact with tight junction proteins and change the way they are organised and function. By adhering to the tight junctions, PAA can lead to increase the tightness of the junctional complexes, strengthening the barrier.[256] That comes as contradictory since previously in the internalization experiment PAA was found to have an enhanced ability to permeate but there were references that suggested that PAA is affecting the lipid membranes by disrupting them.[254] Other PISA NPs indicate lower permeability as well like PQDMAE, 67 and 75. Although nanoparticle characteristics, surface changes, and the unique physiological circumstances of the BBB can all have an impact on the tight junctions of the BBB, the consequences of these elements can differ. It is vital to keep in mind that while some nanoparticles may be able to modify tight junction integrity, the precise methods and results are still being researched and may vary depending on the particular nanoparticles employed.[257]

Lastly the presto blue assay demonstrates no cytotoxic effects in any system. The values of the graph clearly indicate a coherent, viable *in vitro* BBB.

So far all data indicate that the *in vitro* BBB was not influenced by the nanoparticles There was low permeation so the rest of the concentration was supposed to be in the upper compartment but there is a notion that part of the PISA NPs is still encapsulated in the ECs. To verify that confocal microscopy was conducted.

The NPs tried to be visualized for their endocytosis efficiency through confocal microscopy. The cells were washed with PBS after 24 hours of NPs seeding and fixed with a 4% paraformaldehyde-PBS solution. The nucleus was dyed with Hoechst blue and through immunocytochemistry a primary antibody for Vascular endothelial Cadherin (VE-CAD) the membrane was stained with immunocytochemistry of Anti-Rabbit antibody Alexa 555.

Vascular endothelial (VE)-cadherin is a strictly endothelial specific adhesion molecule located at junctions between endothelial cells.[258] In that manner it would be easier to evaluate if the NPs were in fact encapsulated or just stuck on the surface of the cells.

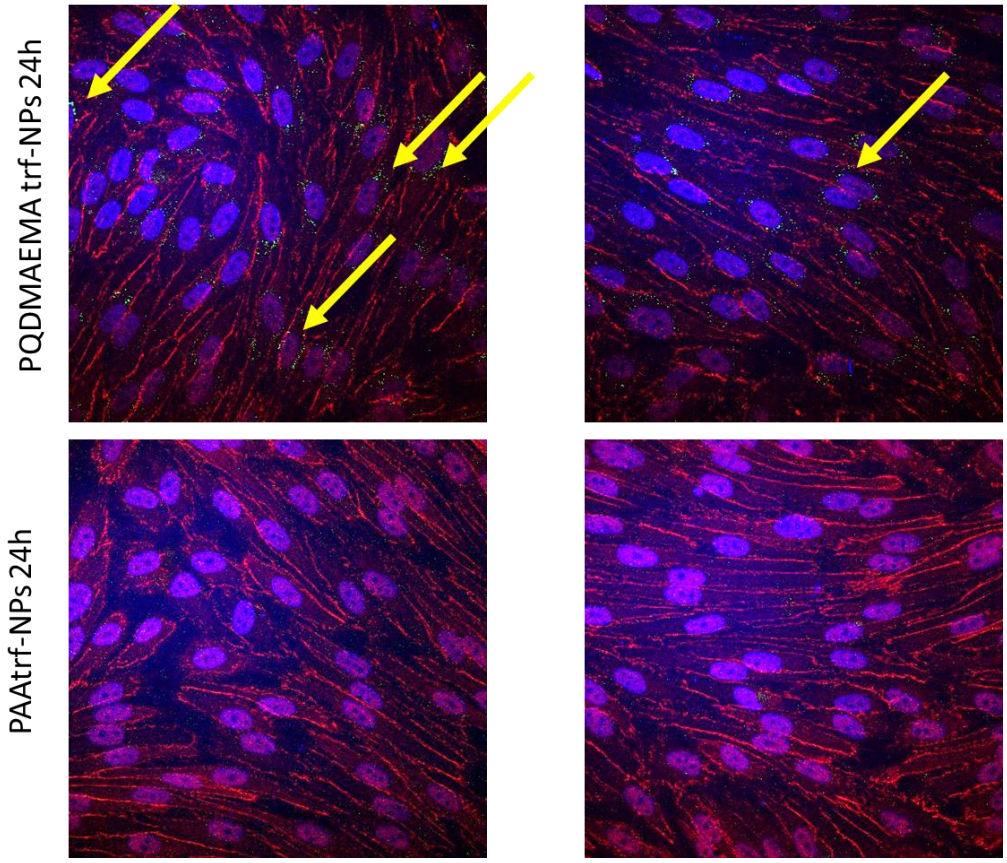
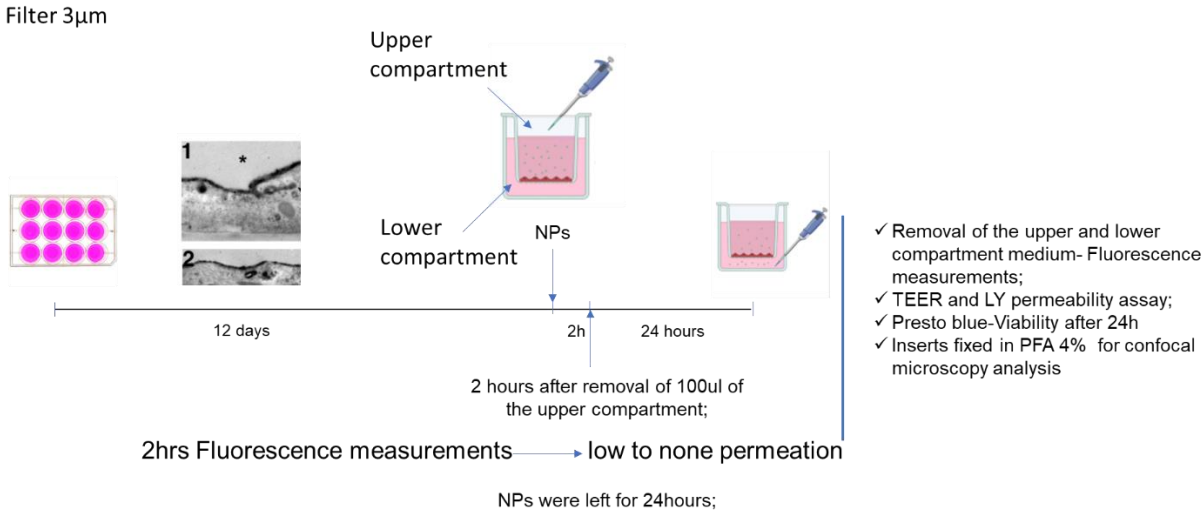


Figure 2.13 Confocal image of ECs of 0.4μm *in vitro* BBB internalisation evaluation.

Unfortunately from Figure 4.2.13 no internalisation can be visible in any of the samples. The low concentration of 0.05 mg/mL could be one factor that the particles are not visible. PQDMAE Tf appears to have a very small quantity of particles internalised by CEs. Only a few nanoparticles can be seen through confocal microscopy which can either mean that the NPs are performing transcytosis, or that the fluorescence is quenching of the attached BODIPY fluorophore. There are various reasons a fluorophore could be quenching but in principal the electron transmittance of the rings is disturb which does not allow the excitation to take place. The importance of intramolecular non-covalent interactions and excited state charge transfer character in 'stabilizing' the intersection and causing nonradiative decay has been established.[259] It has been previously reported that fixation of the cells with

paraformaldehyde can lead to denaturation or quenching of fluorophore as its parental formaldehyde[260].

At this point the progression to another system was proposed with higher concentrations of PISA NPs to evaluate the system more thoroughly.



Scheme 20. In vitro BBB creation 3 µm filters and evaluation of PISA NPs 1 mg/mL concentration and experimentation explanation

An explanation on the production of the BBB has been state above as much as the fact that for the 3 µm filters, these ECs were co-cultured with pericytes (lower compartment) for 12 days. The reason for this is that in order for the cellular density to be similar it requires further time, since at this time the 3 µm filters have bigger porosity. Scheme 20 above indicates the same experimentation plan as previously with higher level of PISA NPs concentration 1 mg/mL apart from PQDMAE that will be added at 0.01 mg/mL as previously due to its cytotoxicity.

Table 7. Permeability concentration % of PISA NPs in 1 mg/mL concentration (PQDMAE 0.01 mg/mL) lower compartment data

Polymers	Concentration % at 2 hours	Concentration % at 24 hours
PDMA	1.39%	6.60%
PDMA Tf	0.30%	4.80%
PAA	1.48%	7.30%
PAA Tf	0.45	0.80%
75	0.40%	3.20%
75 Tf	0.20%	1.22%
62	0.96%	3.70%

From table 7 above it can be seen that the permeability concentration has not improved despite the elevation of the concentration in the system. The highest concentration appears to be attributed to PAA NPs with 7.3% and is followed by PDMA that is presenting a 6.6%. In the previous system PDMA had a high percentage of permeation as well despite that the internalisation studies demonstrated no particular cellular uptake, which can suggest that particles are passing through passively despite their size. This will require further investigation to be proven like confocal, and pathway validation.

Further experimentation about the BBB integrity were examined. As previously, the TEER, LY and presto blue were tested to establish the BBB stability and functionality.

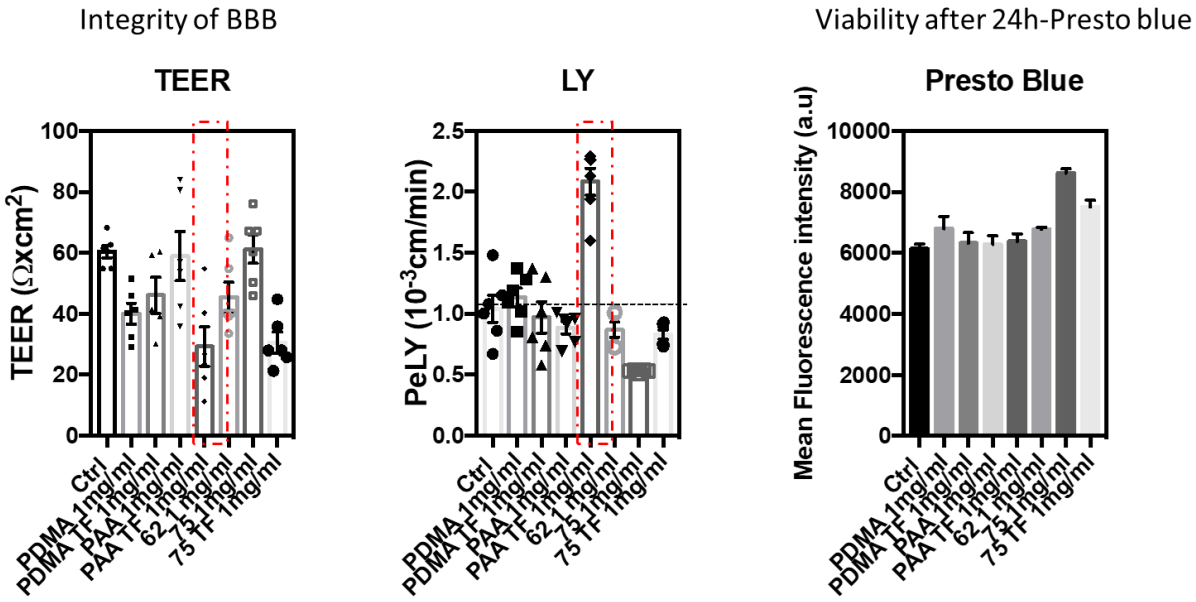


Figure 4.2.14 BBB integrity investigation via TEER, LT and Presto blue PISA NPs 1 mg/mL

Figure 4.2.14 depicts the integrity studies of the BBB and presents a clear indication of interaction between the BBB and PAA Tf. The TEER analysis indicates a value of 30 Ωcm^2 for PAA Tf, which the half of the control value. LY data also validates that the integrity of the BBB has been affected by PAA Tf by having a value twice as much as the control does. Viability of the PAA Tf does not seem to have any cytotoxic effects so it could just be a tight junction interference or disruption. Another theory could be contamination of the system, since PAA does not appear to have the same effect. Interestingly, although PAA Tf seems to have disrupted the BBB it does not appear to have the highest concentration permeability. This difference raises the possibility that the nanoparticles' size, charge, or surface characteristics may have an impact on how permeable they are to the BBB. It draws attention to the intricate nature of interactions between nanoparticles and the BBB and the demand for more research to comprehend the underlying mechanisms. Since PAA does not indicate to have any interference of the BBB unlike PAA Tf, a potential explanation could be that the Tf receptor interactions with Tf-conjugated nanoparticles can promote the internalisation of these particles and perhaps cause tight junction breakdown. Further

experimentation is necessary to uncover the mechanisms of the interaction between PAA Tf and the tight junctions. Lastly more PISA NPs like 75 and PDMA seem to have low TEER values but there is no leakage through the LY, and there is no cell death indication from presto blue analysis, the tight junctions should not be affected.

To verify the internalisation of the PISA NPs and acquire further evidence, confocal microscopy was conducted with the CD34+ filter inlets.

In the figure 4.2.13 below is actually visible from the qualitative data that confocal images present that there is a higher amount of uptake NPs of PDMA (Figure 4.2.13 a) than in 62(Figure 4.2.13 d), which is a paradox if its considered that in the previous internalisation experiment it was other way around. Also the fact that they have the same corona chemistry thus, the interactions should be of similar nature but other conditions can affect the internalisation mechanism. Interestingly the PAA Tf (Figure 4.2.13 c), which is indicated disruption of the BBB does not appear to have higher internalisation than PDMA, but it shows the particles are closer to the (VE)-cadherin than the nuclei of the cell so it could potential interact with protein. PAA (Figure 4.2.13 b) exhibits similar higher cellular uptake with PAA Tf . Lastly ,75 Tf (Figure 4.2.13 f), indicates less internalisation that 75 (Figure 4.2.13 e),but that can be explained since due to the OH groups 75 can form protein coronas and effectively permeate through the BBB.

Overall, the fluorescence uptake recorded were exceedingly higher than the findings through confocal microscopy, which promotes the hypothesis that the fluorescence might be quenching due to the paraformaldehyde or due to another agent. There is also a hypothesis that the PISA NPs could be diffusing from the cells due to the addition of Triton-X100, that is necessary for the immunocytochemistry. That could be further investigated through fluorescence spectroscopy of the PISA NPs with addition of each agent. To avoid the diffusion we could add a control that we would not have to stain, thus examine if the dye of the NPs is more apparent.

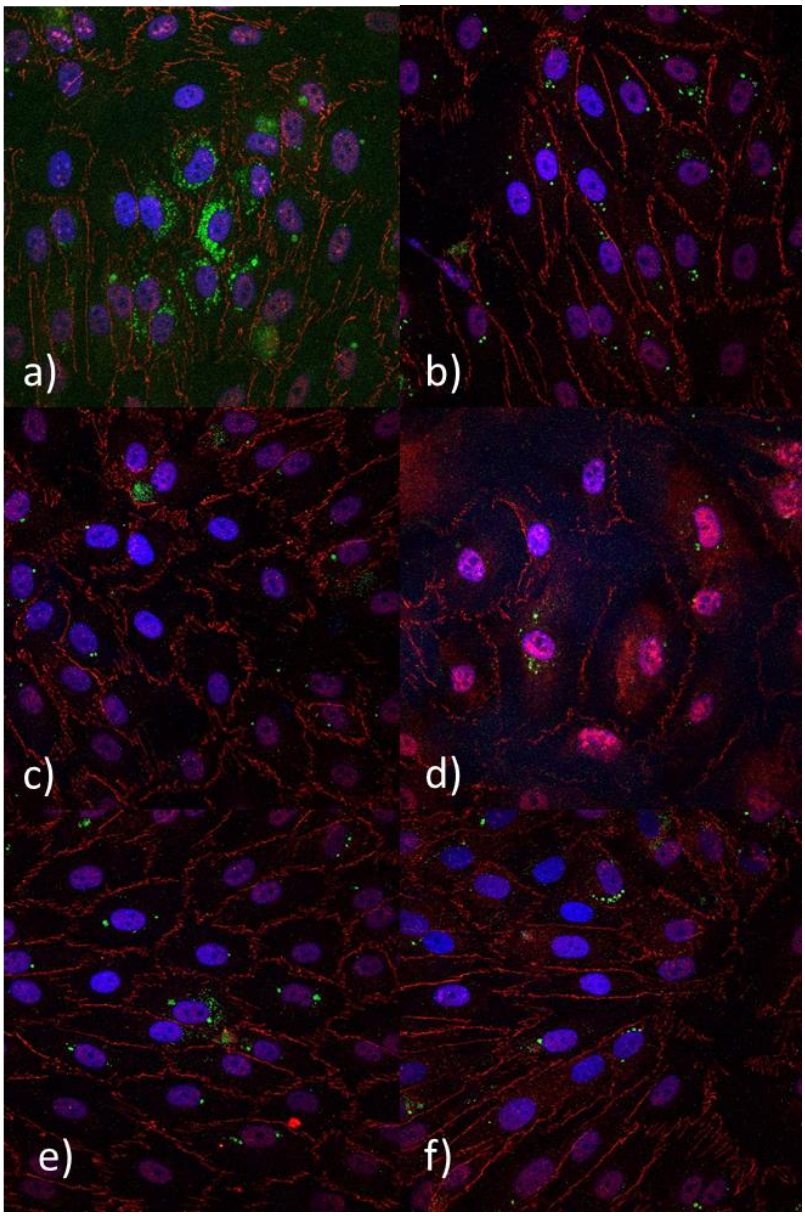


Figure 4.2.15. Confocal microscopy data of 24hours seeded BBB model ($CD34^+$monolayer with tight junctions developed) a)PDMA 1 mg/mL b) PAA 1mg/mL, c) PAA Tf 1 mg/mL, d) 62 1mg/mL and e) 75 1mg/mL, f) 75 Tf 1mg/mL NPs (green) BODIPY™ FL EDA, Nucleus (blue) DAPI , Membrane (red) Anti-Rabbit antibody Alexa 555

From the above data PDMA seem to have the greatest internalisation and the second highest permeability concentration, which makes it the best system so far for drug delivery applications through the BBB. Obviously, further experimentation is required to address the issues of the lack of fluorescence and internalisation and permeation correspondence.

4.2.6 Transferrin receptor efficiency for nanoparticles permeation

To verify if the PISA NPs with Tf are using in fact the transferrin receptor mediated pathway for the transcytosis, the transferrin receptor will have to be evaluated and explored. Herein the transferrin receptor was evaluated in a simple cellular system of CD34+ cell line, in CD34+ cell line with pericyte derived conditioning medium and *in vitro* BBB co-culture system.

The cells were extracted from the flask and kept in suitable medium. A Transferrin Receptor (CD71) monoclonal antibody was used to detect the Transferrin receptor. After the incubation the cells were washed to remove any unattached antibody. The flow cytometry was run with forward scattering and provided the data appearing in figure 2.4.15

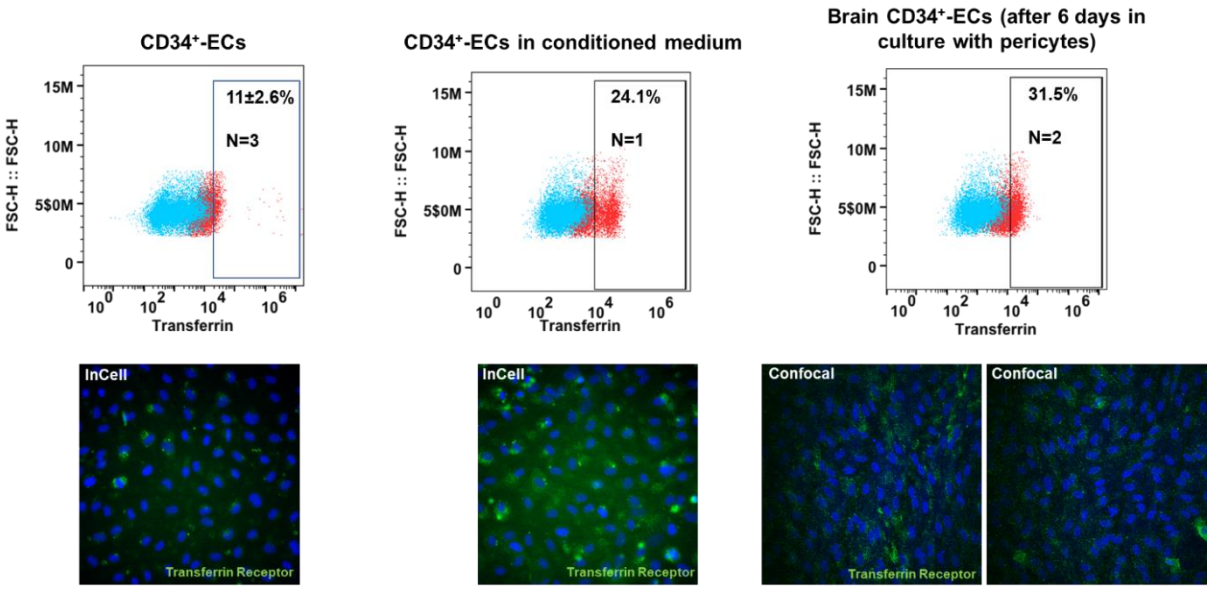


Figure 4.2.16. Transferrin receptor in CD34+, in CD34+ in conditioned pericyte media and in an *in vitro* BBB environment. Data analysed with flow cytometry, incell and confocal

From figure 4.2.16, the amount of the transferrin receptor per cell line system was quantified. In the cell culture CD34+ only an 11% had an active transferrin receptor expression. This suggests that only a small number of the CD34+ cell line could indicate the

presence of the transferrin receptor. For the CD34+ cell line with conditioning pericyte media the expression of the transferrin receptor was higher at 24.1 % but as indicated in figure 4.2.16 the measurement was conducted only N= 1 time so the measurements should be repeated for validation. Lastly , from the CD34+ cell line that was harvest after the creation of the *in vitro* BBB system, the transferring receptor expression is 31.5%, which was higher than the rest and similar in comparison with other cell lines like erythroid precursor cells.[261] Since the confocal microscopy leads to loss of fluorescence, the CD34+ transferrin receptors acquired from the *in vitro* BBB cannot be utilised. In order for the examination of the transferrin receptor efficiency to be conducted in the incell it cannot be in a co-culture environment . Figure 4.2.16 shows effectively that the transferrin receptor appears more dominant in the incell image of the CD34+ cell line with conditioning media. The intensity of fluorescence of the Transferrin receptor between the CD34+ cell line with conditioning media and with just the CD34+ cell line is apparent. The confocal imaging for the *in vitro* BBB transferrin receptor exhibits a quenching effect after immunocytochemistry so the receptor cannot be visualized clearly.

Thus, from the above information the experiments of the evaluation permeation through the transferrin receptor of the PISA NPs cannot be facilitated, since there is a need for a stable system with high expression of the transferrin receptor that can be executed in Incell.

4.3 Conclusions

In conclusion, different diblock copolymers were synthesized through PISA polymerization and characterized. After the assembly into nanoparticles they were examined with multiple techniques to verify if potentially can serve as drug delivery systems for the permeation of BBB. The sizes were measured to be 15-47 nm so they would eligible to permeate through the BBB.

The small, monodisperse and reproducible spherical PISA NPs , post polymerization were tagged with a BODIPY fluorophore. The nanoparticles were characterized fully with the DLS,

NTA and TEM measurements being on good agreement and proving the monodispersed nature of the particles. The fluorescence of the nanoparticles was assessed with Uv-SEC trail and fluorescent measurements.

The PISA NPs were also successfully tagged by Holo human Transferrin and the attachment was evaluated with Maldi-Tof, SDS PAGE gel and Uv-vis measurements. The PISA NPs were characterized fully with the same instrumentation as before where it exhibited a small size increase and some morphological defections, but the majority of the populations were spherical.

After the complete synthesis and characterization of the NPs they were accessed for their cytotoxicity and their stability in endothelium conditioning media. All the PISA NPs present cellular viability even in concentrations 1mg/mL, apart from the positively charged PQDMAE, whereas the 0.01 mg/mL exhibit viability for this nanoparticle system.

The live cell internalization studies through incell portraited better the endocytosis of the nanoparticles after 24 hours incubation and provided us with a quantifiable measurement on the permeation of the PISA NPs. The internalisation of the PISA NPs was in order to be examine in CD34+ cell lines where the maximum internalization of the 62 Tf particle was recorded.

The evaluation of the permeability through the *in vitro* BBB model was presented ,where the PAA Tf would appear to have the functionality to disrupt the integrity of the BBB. After the permeation the quantification of the concentration percentage was calculated through fluorescence and the PDMA particle had the highest concentration percentage without altering any of the characteristics of the BBB. The confocal measurements showed only a very small amount of nanoparticle uptake by the cells, which come in contrast with fluorescent plate reader measurements, so there is a possibility that the fluorescence of the nanoparticles is quenching.

Lastly to address if the PISA NPs with Tf are utilising the receptor mediated transcytosis of transferrin or using another receptor some studies were conducted to determine the efficiency of the transferrin receptor in CD34+ cell lines in different conditions. The highest percentage of transferrin receptor efficiency was in the *in vitro* BBB system, but since the

fluorescent particles are quenching through the immunocytochemistry steps, they can not be visualize in confocal microscopy.

In conclusion, PISA NPs appears to be a potent drug delivery system for permeation through the BBB. Their small size and their electrophoretic mobility recommend that they are molecules easily to functionalize a ligand and to upload a drug substance. PISA NPs have exhibited a biocompatible nature throughout the experimentations and high levels of endocytosis. Further experimentation and optimization of the systems is required before it progresses to *in vivo* studies.

APENDIX III

4.4 Experimental

Materials

Materials Dimethyl acrylamide (DMAm, 99 %; Sigma Aldrich 274135), Acrylic Acid (AA, 99 %; Sigma Aldrich 147230), (Methacryloyloxy)ethyl] trimethylammonium chloride (QDMAEMA, 75 % in H2O; Sigma Aldrich 408107), (Methacryloyloxy)ethyl]dimethyl-(3-sulfopropyl)ammonium hydroxide (DMAPS, 95 %; Sigma Aldrich 537284), 4,4'-azobis(4-cyanovaleric acid) (ACVA, 99%; Sigma Aldrich 11590), 1-ethyl-3-(3-dimethylaminopropyl)carbodiimide (EDC, 98%; Sigma Aldrich 341006), deuterated methanol (CD3OD, 99.8%; Sigma Aldrich 151947-10G-GL) and deuterium oxide (D2O, 99.9%; Sigma Aldrich 151882) were purchased from Sigma Aldrich (UK). DAAm (99%) was purchased from Alfa Aesar (UK; A15940.30). 4,4-Difluoro-5,7-dimethyl-4-bora-3a,4a-diaza-s-indacene3-propionic acyl hydrazide (BODIPY FL, 99 %) was purchased from ThermoFisher Scientific (UK; D2371). 4-((((2-Carboxyethyl)thio)carbonothioyl)thio)−4-cyanopentanoic acid (BM1433, 95%) was purchased from Boron Molecular (USA; BM1433), Holo-Transferrin Human (cat. no. T4132), HSA (cat. No. A9511), MES (cat. no. M3671), EDAC (cat. no. E6383) and glycine

(cat. no. G7126) were all purchased from Sigma-Aldrich, Vascular endothelial Cadherin (VE-CAD)- Ref: SC-9989 Santa Cruz, anti-mouse Alexa fluor-555 (Life Technologies).

Instruments

Dynamic Light Scattering (DLS)

Hydrodynamic diameters (D_h) of particles were determined by dynamic light scattering (DLS) using a Malvern Zetasizer Nano ZS fitted with a 4 mW He-Ne 633 nm laser module at 25 °C. Measurements were carried out at a detection angle of 173° (back scattering) and the data was analysed using Malvern DTS 7.03 software. All determinations were repeated 5 times. D_h was calculated using the Stokes-Einstein equation where particles are assumed to be spherical. For cylindrical particles, DLS can be used to detect multiple populations and obtain dispersity information.

Zeta potential

Zeta potentials were measured using a Malvern Zetasizer Nano. The zeta potentials of particles in suspension at pH 6.5 were obtained by measuring the electrophoretic movement of the particles under an applied electric field at 25 °C. All determinations were repeated 3 times.

MALDI-TOF

Matrix-assisted laser desorption/ionization (MALDI) was conducted with a Bruker Ultraflextreme MALDI to show molecular weight distribution change after the addition of Transferrin 80 kDa.The matrix used for all measurements is cinammic acid.

InCell-analyzer (highthrouput microscope)

After 24 h of incubation with the PISA NPs, CD34+ cells were washed to remove any remaining particles in the media and cells were stained with Hoeschst H33342 and LysoTracker Red DND-99 , both at 1 μg mL^{-1} (Sigma) in DMEM, and analyzed in a high-content microscope (InCell Analyzer 2200, GE Healthcare) with excitation wavelength

577/590nm for lysotracker and 350nm for Hoeschst. Cellular internalizations were verified and assessed nased on fluorescence intensity. For incell imaging an excitation filter of 475 nm (28 nm aperture) and an emission filter of 511 nm (23 nm aperture) were used.

UV/Vis spectrophotometry plate reader

Uv-vis permeation studies were conducted using a Synergy H1 plate reader (Biotek). Media would be in duplicates in a black 96well plate. Since the PISA NPs are caring BODIPY FL hydrazide, the plates are read at 533 nm wavelength.

DLS and zeta potential

The measurements contacted in Coimbra were executed by a different machine. Size and ζ-potential were measured by dynamic light scattering (DLS) using a ZetaPALS Analyzer (Brookhaven Instruments Corporation). All size measurements were performed using the same incident laser power and recorded with a scattering angle of 90°, following an equilibration time of 5 min. Each measurement corresponded to the average result of 5 runs of 1 min each.

Confocal Microscopy and Immunofluorescence

Fixed ECs monolayer on glass coverslips were permeabilized using 0.2% (vol/vol) Triton X-100 in PBS, rinsed with PBS, fixed with 4% paraformaldehyde (PFA), and blocked with 2.5% bovine serum albumin (BSA). Primary antibodies were incubated for an entire night at 4° C. Following a PBS wash, the samples were incubated with the secondary antibody for a further hour at room temperature. DAPI was used to stain the nuclei. The samples were cleaned in PBS before being mounted using MOWIOL 4-88 Reagent from Calbiochem. Using a Zeiss LSM 710 (Carl Zeiss) microscope, the images were captured. Sources of antibodies were goat anti-VE-cadherin (SC-28644, Santa Cruz Biotechnology), rabbit anti-ki67 (AB16667, abcam), rabbit anti-ZO1 (G17300, Thermo Scientific), and rabbit anti-von Willebrand factor (A0082, Dako).

Nanoparticle Traking Analysis (NTA)

Analysis of PISA NPs size distribution and concentration was performed through NTA by NanoSight NS300 (Malvern Instruments, Malvern, UK). The system used an O-Ring Top Plate, and the sample was injected manually at an approximate flow of 1 mL every 20 s. PISA NPs were diluted in PBS until they reached a concentration between 15 and 45 particles/frame. Five 30 s measurements were done for each sample with the camera level set at 16. All the videos were processed with NTA 3.2 analytical software, using the software threshold between 2 and 4 depending on the quality of the videos.

Size exclusion chromatography

SEC measurements were executed by a Varian 390-LC-Multi detector suite system equipped with Refractive Index (RI) and ultraviolet (UV) detectors (= 309, 490 nm), and two PLGel 5 m (300 7.5 mm) mixed-D columns. The eluent used was DMF with 5 mM NH4BF4 at 50 °C, and the flow rate was 1.0 mL/min. Software called Cirrus v3.3 was used to evaluate the SEC data after calibrating it against polystyrene standards.

Methods

Synthesis of hydrophilic macro-chain transfer agents (macro-CTAs)

The synthesis was conducted as reported.[236]

Dimethyl acrylamide (10 g, 100 mmol, 70 eq.), BM1433 (0.44 g, 1.4 mmol, 1 eq.), and ACVA (0.04 g, 140 mol, 0.1 eq.) were added to a flask with a flat bottom and diluted in water (24 mL) to generate a 30% weight-to-weight reaction solution. The flask was sealed after adding a stirrer bar, and nitrogen was then sparged for 20 minutes. After 120 minutes, the sealed flask was withdrawn from the oil bath and quenched by exposure to oxygen. The oil bath had been heated to 70 °C. The mCTAs were characterised with ^{1}H NMR and SEC.

The macro CTAs were kindly synthesized and contributed by Dr. Sam Parkinson

PISA NPs synthesis

The synthesis was conducted as reported.[236]

The following compounds were used in a typical synthesis of a $PDMA_{70}$-$PDAA_{50}$: diacetone acrylamide (1 g, 6 mmol, 50 eq.), $PDMA_{70}$ mCTA (0.85 g, 120 mol 1 eq.), and ACVA (3 mg, 12 mol 0.1 eq.) giving a 20% w/w reaction solution, was added to a round bottom flask and dissolved in water (7.4 mL). The flask was sealed after adding a stirrer bar, and nitrogen was bubbled through the solution for 20 minutes. The sealed flask was then submerged for 120 minutes in an oil bath at 70 °C, withdrawn from the oil bath, and quenched by exposure to oxygen. ^{1}HNR analysis was conducted in D_2O and the samples were run on an aquatic SEC.

The same procedure was conducted for all the diblock copolymer PISA NPs.

BODIPY fluorophore attachment to PISA NPs

The attachment was conducted as reported.[236]

The following was a typical BODIPY FL attachment to $PDMA_{70}$-$PDAA_{50}$ nanoparticles: After adding EDC (240 µg, 0.6 µmol, 1 eq.) to $PDMA_{70}$-$PDAA_{50}$ (100 mg, 0.6 µmol, 1 eq.) in water (10 mL), the mixture was left stirring for five minutes. The mixture was then supplemented with BODIPY FL (19 µg, 0.06 µmol, 0.1 eq.) diluted in DMSO (15 µl), and stirred overnight. After that, the solution was purified using spin centrifugation in opposition to a 3k MWCO membrane. A sample was collected so that SEC could verify BODIPY's adhesion to the polymer chains. All other PISA NPs followed the same process.

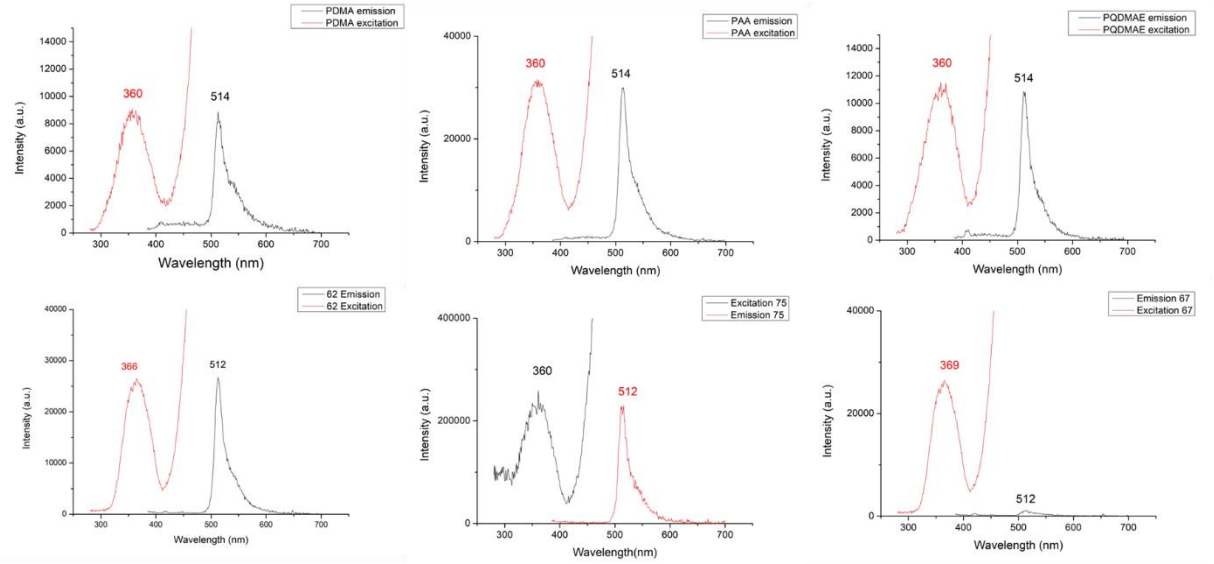


Figure 4.4.1. Emission- excitation graphs after addition of BODIPY in PISA NPs

Transferrin attachment to PISA NPs

Similar protocol was followed as reported.[248] 5 mg of Holo human Transferin were dissolved at a concentration of 2 mg/mL in MES 50 mM pH = 6. The same buffer was used to disperse the PISA NPs at a concentration of 2 mg/mL. The particle solution was pipetted dropwise into the protein solution while stirring the mixture at 500rpm, equal proportions of both were combined. The solution was left stirring for 10 minutes and afterwards, 5 mg of EDAC dissolved in 20 µl of buffer was added. After another two hours of stirring 10 mg of glycine was introduced to the solution to quench the reaction. The mixture was purified using spin centrifugation in opposition to a 100 kDa MWCO membrane for 3 runs at 500xg for 30' each run. The attachment was afterwards, verified via Maldi-Tof, SDS page gel and UV-vis.

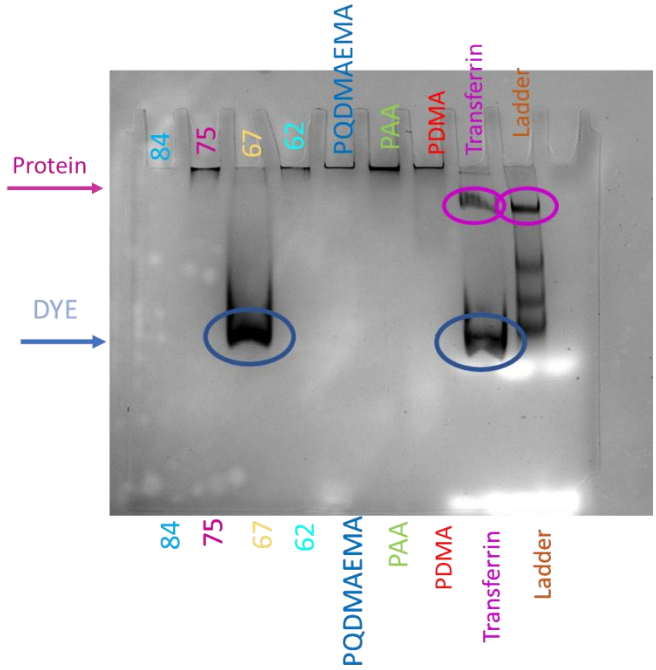


Figure 4.4.2. SDS PAGE Polyacrylamide Gel for verification of Transferrin attachment

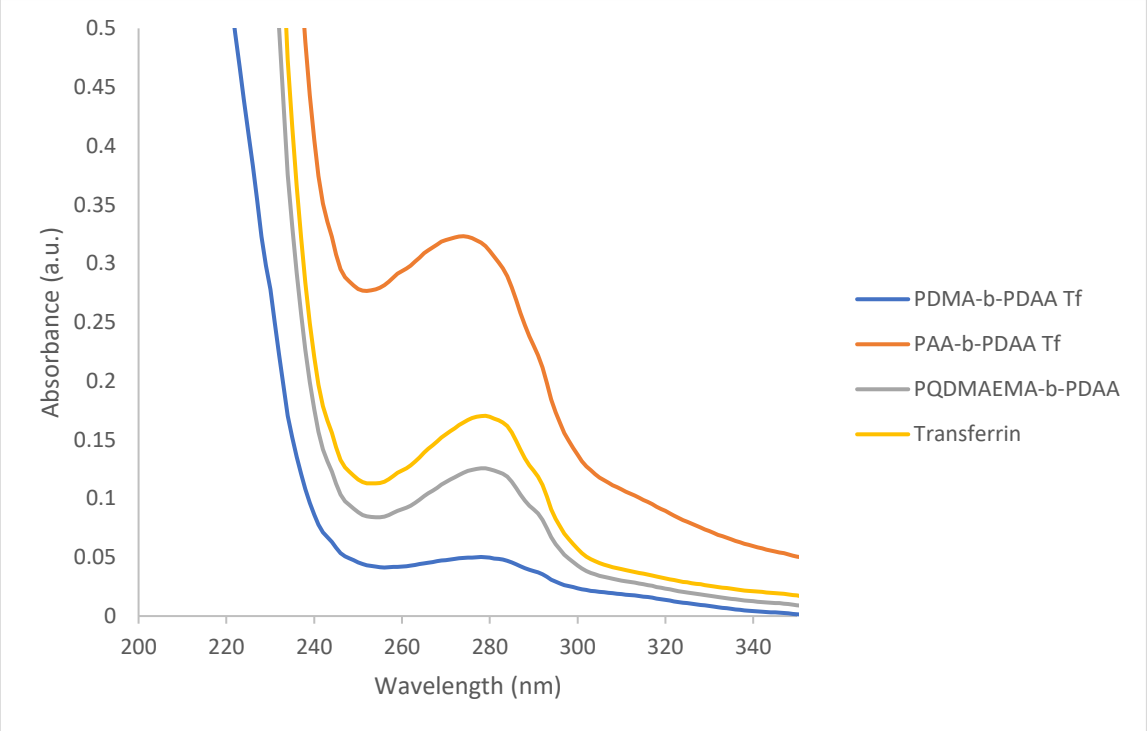
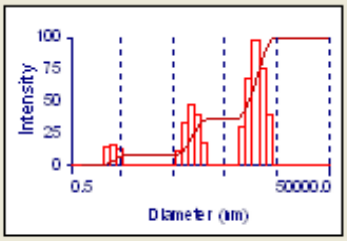


Figure 4.4.3 UV-VIS graph after the attachment of Transferrin in MES buffer in pH=7.4, concentration 1 mg/mL

Sample ID	EGM after cell culture (Combined)
Operator ID	EE
Elapsed Time	00:03:00
Mean Diam.	1234.1 nm
Rel. Var.	0.686
Skew	0.226



d(nm)	G(d)	C(d)	d(nm)	G(d)	C(d)	d(nm)	G(d)	C(d)
1.0	0	0	23.7	0	8	562.3	0	38
1.3	0	0	31.6	0	8	749.9	0	38
1.8	0	0	42.2	0	8	1000.0	30	44
2.4	14	3	56.2	10	10	1333.5	68	57
3.2	15	6	75.0	33	17	1778.3	100	77
4.2	13	8	100.0	47	26	2371.4	77	92
5.6	0	8	133.4	40	34	3162.3	39	100
7.5	0	8	177.8	17	38	4217.0	0	100
10.0	0	8	237.1	0	38	5623.4	0	100
13.3	0	8	316.2	0	38	7498.9	0	100
17.8	0	8	421.7	0	38	10000.0	0	100

Intensity

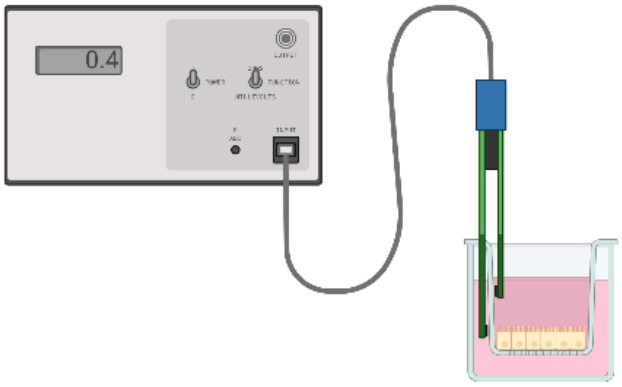
Figure 4.4.4 DLS data of conditioning media ECM after incubation 24hrs with CD34^{+} cells (Blank = with no PISA NPs)

TEER permeability assessment

For 24 hours, nanoparticles are gradually transferred from the top (luminal) compartment to the lower (abluminal) compartment. At various intervals (2, 24 hours), the medium (containing nanoparticles) from the upper and lower compartments is collected separately and its fluorescence intensity is determined. The fluorescence intensity of pure DMEM media (devoid of any nanoparticles) is also measured at the same time. To quantify the time-dependent nanoparticle transport mechanism across the BBB endothelial cells, fluorescence intensity data are used. The formula for calculating the BBB transport efficiency (TE) of nanoparticles is:

$$TE = \frac{F_{lo} - F_b}{F_{up0} - F_b} \times 100$$

The most commonly used technique to evaluate the integrity of the developed BBB *in vitro* is by using electrodes the trans-endothelial electrical resistance (TEER).[262] Over the endothelial cell monolayer, a square waveform alternating current voltage signal is delivered.



Scheme 21. Schematic representation of TEER

TEER, quantifies the resistance produced by the endothelium monolayer R_{Tissue} (Ω), which is inversely proportional to the effective area of the monolayer and it can be calculated by the following equation:

$$R_{Tissue} = R_{Total} - R_{Blank}$$

where R_{total} (Ω) is the overall resistance measured in the presence of endothelial cells and R_{Blank} (Ω) is the system resistance measured in the absence of cells. In the equation below is used to calculate the final TEER (Ω cm^2):

$$TEER = R_{Tissue} \times Area$$

Area refers to the total area of the endothelium cell layer.

Endothelial cells cultivated in static *in vitro* BBB models are thought to have a TEER value of at least 150 cm^2, whereas the *in vivo* TEER value is typically 1500–2000 cm.[2,263] High TEER values point to tight connections between endothelial cells being more upregulated, which suggests that passive diffusion across the BBB is constrained.

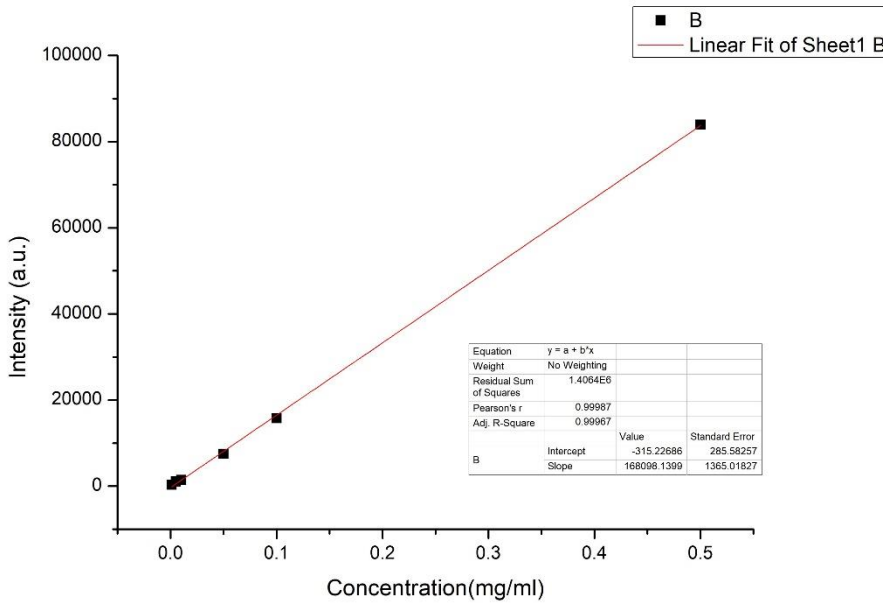


Figure 4.4.5. Calibration curve of PISA NPs concentration determination through BBB

4.5 References

1. N. Poovaiah, Z. Davoudi, H. Peng, B. Schlichtmann, S. Mallapragada, B. Narasimhan and Q. Wang, *Nanoscale*, 2018, **10**, 16962-16983.
2. M. D. Sweeney, Z. Zhao, A. Montagne, A. R. Nelson and B. V. Zlokovic, *Physiol Rev*, 2019, **99**, 21-78.
3. E. Zenaro, G. Piacentino and G. Constantin, *Neurobiol Dis*, 2017, **107**, 41-56.
4. M. D. Sweeney, A. P. Sagare and B. V. Zlokovic, *Nat Rev Neurol*, 2018, **14**, 133-150.
5. J. Baskin, J. E. Jeon and S. J. G. Lewis, *Journal of Neurology*, 2021, **268**, 1981-1994.
6. W. M. Pardridge, *Expert Opinion on Drug Delivery*, 2016, **13**, 963-975.
7. A. Mishra, R. Kumar, J. Mishra, K. Dutta, P. Ahlawat, A. Kumar, S. Dhanasekaran, A. K. Gupta, S. Sinha, D. K. Bishi, P. K. Gupta and S. Nayak, *Journal of Drug Delivery Science and Technology*, 2023, **86**, 104694.
8. D. E. Nayab, F. U. Din, H. Ali, W. A. Kausar, S. Urooj, M. Zafar, I. Khan, K. Shabbir and G. M. Khan, *J Nanobiotechnology*, 2023, **21**, 477-493.
9. A. Janesick, S. C. Wu and B. Blumberg, *Cellular and Molecular Life Sciences*, 2015, **72**, 1559-1576.
10. S. L. B. Oliveira, M. M. Pillat, A. Cheffer, C. Lameu, T. T. Schwindt and H. Ulrich, *Cytometry Part A*, 2013, **83A**, 76-89.
11. B. Srinageshwar, M. Florendo, B. Clark, K. Johnson, N. Munro, S. Peruzzaro, A. Antcliff, M. Andrews, A. Figacz, D. Swanson, G. L. Dunbar, A. Sharma and J. Rossignol, *Pharmaceutics*, 2020, **12**, 619-631.
12. Y. Zhou, Z. Peng, E. S. Seven and R. M. Leblanc, *Journal of Controlled Release*, 2018, **270**, 290-303.
13. H. Luo and E. V. Shusta, *Pharmaceutics*, 2020, **12**, 1085.

14. C. W. Fong, *The Journal of Membrane Biology*, 2015, **248**, 651-669.
15. C. Saraiva, C. Praça, R. Ferreira, T. Santos, L. Ferreira and L. Bernardino, *Journal of Controlled Release*, 2016, **235**, 34-47.
16. R. G. R. Pinheiro, A. J. Coutinho, M. Pinheiro and A. R. Neves, *Int J Mol Sci*, 2021, **22**, 11654-11666.
17. D. Wu, Q. Chen, X. Chen, F. Han, Z. Chen and Y. Wang, *Signal Transduction and Targeted Therapy*, 2023, **8**, 217-230.
18. C. Jiang, Y. Zhou, R. Chen, M. Yang, H. Zhou, Z. Tang, H. Shi and D. Qin, *Pharmaceutics*, 2023, **15**, 2669-2678.
19. P. K. Pandey, A. K. Sharma and U. Gupta, *Tissue Barriers*, 2016, **4**, e1129476.
20. Y. Zhou, Z. Peng, E. S. Seven and R. M. Leblanc, *J Control Release*, 2018, **270**, 290-303.
21. A.-C. Lussint, *Fluids and Barriers of the CNS*, 2012, **23**, 21-32.
22. D. J. Begley, *Pharmacology & Therapeutics*, 2004, **104**, 29-45.
23. C. Saraiva, *Journal of Controlled Release*, 2016, **235**, 34-47.
24. T. Patel, *Adv Drug Deliv Rev*, 2012 May 15, **64**, 701-705.
25. D. M. Teleanu, C. Chircov, A. M. Grumezescu, A. Volceanov and R. I. Teleanu, *Pharmaceutics*, 2018, **10,** 269-285.
26. T. T. Zhang, *Biomaterial Science*, 2016, **4**, 119-129.
27. E. Nance, *J Control Release*, 2014, **189**, 123-132.
28. D. M. Teleanu, C. Chircov, A. M. Grumezescu, A. Volceanov and R. I. Teleanu, 2018, **10**, 269-285.
29. V. Cena, *Nanomedicine*, 2018, **13**, 1513-1516.
30. X. Dong, *Theranostics*, 2018, **8**, 1481-1493.
31. R. L. Roberts, R. E. Fine and A. Sandra, 1993, **104**, 521-532.
32. L. Aloe, P. Bianchi, A. De Bellis, M. Soligo and M. L. Rocco, *Neural Regen Res*, 2014, **9**, 1025-1030.
33. P. Rivera-Gil, *Accounts of chemical research*, 2013, **46**, 743–749.
34. T. C. H Ou , Y. Zhang *Acta Biomater*, 2018, **65**, 339–348
35. Y. W. Yating Zhao, Fu Ran, Yu Cui, Chang Liu, Qinfu Zhao, Yikun Gao, Da Wang & Siling Wang, *Scientific Reports*, 2017, **7**.
36. X. Li, *Journal of Drug Targeting*, 2016, **25**, 17–28.
37. C. M. Plummer, L. Li and Y. Chen, *Macromolecules*, 2023, **56**, 731-750.
38. E. Balla, V. Daniilidis, G. Karlioti, T. Kalamas, M. Stefanidou, N. D. Bikiaris, A. Vlachopoulos, I. Koumentakou and D. N. Bikiaris, *Polymers (Basel)*, 2021, **13**, 1822-1835.
39. A. Peterson, R. Hador, M. Pink, Y. Popowski, M. Kol and W. B. Tolman, *Journal of the American Chemical Society*, 2022, **144**, 20047-20055.
40. J. O. C. de França, D. da Silva Valadares, M. F. Paiva, S. C. L. Dias and J. A. Dias, *Polymers (Basel)*, 2022, **14,** 2317-2329.
41. I. Nifant'ev and P. Ivchenko, *Polymers (Basel)*, 2019, **11**, 2078.
42. A. P. Dove, *ACS Macro Letters*, 2012, **1**, 1409-1412.
43. S. Perrier, *Macromolecules*, 2017, **50**, 7433-7447.
44. A. Postma, T. P. Davis, G. Moad and M. S. O'Shea, *Macromolecules*, 2005, **38**, 5371-5374.
45. N. P. Truong, G. R. Jones, K. G. E. Bradford, D. Konkolewicz and A. Anastasaki, *Nature Reviews Chemistry*, 2021, **5**, 859-869.
46. F. M. Winnik, A. R. Davidson, G. K. Hamer and H. Kitano, *Macromolecules*, 1992, **25**, 1876-1880.
47. E. M. Todd and S. C. Zimmerman, *Journal of the American Chemical Society*, 2007, **129**, 14534-14535.
48. M. H. Stenzel, *Chemical Communications*, 2008, DOI: 10.1039/B805464A, 3486-3503.

49. K. E. B. Doncom, L. D. Blackman, D. B. Wright, M. I. Gibson and R. K. O'Reilly, *Chemical Society Reviews*, 2017, **46**, 4119-4134.
50. Y. Mai and A. Eisenberg, *Chemical Society Reviews*, 2012, **41**, 5969-5985.
51. A. Blanazs, S. P. Armes and A. J. Ryan, 2009, **30**, 267-277.
52. J. K. Oh, *Polylactide (PLA)-based amphiphilic block copolymers: Synthesis, self-assembly, and biomedical applications*, 2011, **7**, 5096-5119.
53. N. Kamaly, B. Yameen, J. Wu and O. C. Farokhzad, *Chem Rev*, 2016, **116**, 2602-2663.
54. Y. Li and D. Ju, in *Neurotoxicity of Nanomaterials and Nanomedicine*, eds. X. Jiang and H. Gao, Academic Press, 2017, **12,** pp. 285-329.
55. P. Bhargava, J. X. Zheng, P. Li, R. P. Quirk, F. W. Harris and S. Z. D. Cheng, *Macromolecules*, 2006, **39**, 4880-4888.
56. L. Zhang and A. Eisenberg, 1995, **268**, 1728-1731.
57. J. X. Zheng, H. Xiong, W. Y. Chen, K. Lee, R. M. Van Horn, R. P. Quirk, B. Lotz, E. L. Thomas, A.-C. Shi and S. Z. D. Cheng, *Macromolecules*, 2006, **39**, 641-650.
58. K. Kuperkar, D. Patel, L. I. Atanase and P. Bahadur, *Polymers (Basel)*, 2022, **14**.
59. Q. Tian, C. Fei, H. Yin and Y. Feng, *Progress in Polymer Science*, 2019, **89**, 108-132.
60. Y. H. A. Hussein and M. Youssry, *Materials (Basel)*, 2018, **11**.
61. A. Vardaxi, M. Kafetzi and S. Pispas, *Polymers (Basel)*, 2022, **14**.
62. N. J. Caggiano, S. K. Nayagam, L. Z. Wang, B. K. Wilson, P. Lewis, S. Jahangir, R. D. Priestley, R. K. Prud'homme and K. D. Ristroph, *Int J Pharm*, 2023, **640**, 122985.
63. X. Yan, J. Bernard and F. Ganachaud, *Advances in Colloid and Interface Science*, 2021, **294**, 102474.
64. J. Tao, S. F. Chow and Y. Zheng, *Acta Pharm Sin B*, 2019, **9**, 4-18.
65. J. He, X. Huang, Y.-C. Li, Y. Liu, T. Babu, M. A. Aronova, S. Wang, Z. Lu, X. Chen and Z. Nie, *Journal of the American Chemical Society*, 2013, **135**, 7974-7984.
66. W. S. Saad and R. K. Prud'homme, *Nano Today*, 2016, **11**, 212-227.
67. S. Damiati, U. B. Kompella, S. A. Damiati and R. Kodzius, *Genes (Basel)*, 2018, **9**,103-113.
68. B. G. Carvalho, B. T. Ceccato, M. Michelon, S. W. Han and L. G. de la Torre, *Pharmaceutics*, 2022, **14**,141-154.
69. B. Küçüktürkmen, W. Inam, F. Howaili, M. Gouda, N. Prabhakar, H. Zhang and J. M. Rosenholm, *Biosensors (Basel)*, 2022, **12,**181-190.
70. V. Uskoković, *Rev J Chem*, 2013, **3**, 271-303.
71. W. Xu, Y. Zheng and P. Pan, *Journal of Polymer Science*, 2022, **60**, 2136-2152.
72. R. M. Michell and A. J. Müller, *Progress in Polymer Science*, 2016, **54-55**, 183-213.
73. J. F. Kang, J. Zaccaro, A. Ulman and A. Myerson, *Langmuir*, 2000, **16**, 3791-3796.
74. P. J. Hurst, A. M. Rakowski and J. P. Patterson, *Nat Commun*, 2020, **11**, 4690.
75. M. Inam, J. C. Foster, J. Gao, Y. Hong, J. Du, A. P. Dove and R. K. O'Reilly, *Journal of Polymer Science Part A: Polymer Chemistry*, 2019, **57**, 255-259.
76. J. C. Foster, S. Varlas, B. Couturaud, Z. Coe and R. K. O'Reilly, *Journal of the American Chemical Society*, 2019, **141**, 2742-2753.
77. S. Ganda and M. H. Stenzel, *Progress in Polymer Science*, 2020, **101**, 101195.
78. W. Yu, M. Inam, J. R. Jones, A. P. Dove and R. K. O'Reilly, *Polymer Chemistry*, 2017, **8**, 5504-5512.
79. L. MacFarlane, C. Zhao, J. Cai, H. Qiu and I. Manners, *Chem Sci*, 2021, **12**, 4661-4682.
80. H. Phan, M. Cossutta, C. Houppe, C. Le Cœur, S. Prevost, I. Cascone, J. Courty, J. Penelle and B. Couturaud, *Journal of Colloid and Interface Science*, 2022, **618**, 173-184.
81. N. J. Warren and S. P. Armes, *Journal of the American Chemical Society*, 2014, **136**, 10174-10185.
82. M. S. Haider, M. M. Lübtow, S. Endres, S. Forster, V. J. Flegler, B. Böttcher, V. Aseyev, A. C. Pöppler and R. Luxenhofer, *ACS Appl Mater Interfaces*, 2020, **12**, 24531-24543.

83. P. P. Fu, Q. Xia, H. M. Hwang, P. C. Ray and H. Yu, *J Food Drug Anal*, 2014, **22**, 64-75.
84. A. Sharma, S. V. Madhunapantula and G. P. Robertson, *Expert Opin Drug Metab Toxicol*, 2012, **8**, 47-69.
85. J. M. Hillegass, A. Shukla, S. A. Lathrop, M. B. MacPherson, N. K. Fukagawa and B. T. Mossman, *Wiley Interdiscip Rev Nanomed Nanobiotechnol*, 2010, **2**, 219-231.
86. M. Niepel, M. Hafner, M. Chung and P. K. Sorger, *Curr Protoc Chem Biol*, 2017, **9**, 55-74.
87. S. J. Cameron, J. Sheng, F. Hosseinian and W. G. Willmore, *Int J Mol Sci*, 2022, **23**.
88. N. Lall, C. J. Henley-Smith, M. N. De Canha, C. B. Oosthuizen and D. Berrington, *Int J Microbiol*, 2013, **2013**, 420601.
89. Q. Mu, G. Jiang, L. Chen, H. Zhou, D. Fourches, A. Tropsha and B. Yan, *Chem Rev*, 2014, **114**, 7740-7781.
90. D. Docter, S. Strieth, D. Westmeier, O. Hayden, M. Gao, S. K. Knauer and R. H. Stauber, *Nanomedicine (Lond)*, 2015, **10**, 503-519.
91. V. H. Nguyen and B. J. Lee, *Int J Nanomedicine*, 2017, **12**, 3137-3151.
92. C. Weber, J. Simon, V. Mailänder, S. Morsbach and K. Landfester, *Acta Biomater*, 2018, **76**, 217-224.
93. W. Ma, L. Yang and L. He, *J Pharm Anal*, 2018, **8**, 147-152.
94. D. Hühn, K. Kantner, C. Geidel, S. Brandholt, I. De Cock, S. J. H. Soenen, P. Rivera_Gil, J.-M. Montenegro, K. Braeckmans, K. Müllen, G. U. Nienhaus, M. Klapper and W. J. Parak, *ACS Nano*, 2013, **7**, 3253-3263.
95. W. Huang, G. Xiao, Y. Zhang and W. Min, *Biomedicine & Pharmacotherapy*, 2021, **139**, 111541.
96. A. I. Khan, Q. Lu, D. Du, Y. Lin and P. Dutta, *Biochim Biophys Acta Gen Subj*, 2018, **1862**, 2779-2787.
97. J. Sargento-Freitas, S. Aday, C. Nunes, M. Cordeiro, A. Gouveia, F. Silva, C. Machado, B. Rodrigues, G. C. Santo, C. Ferreira, A. Amorim, S. Sousa, A. C. Gomes, M. Castelo-Branco, L. Ferreira and L. Cunha, *Neurology*, 2018, **90**, e127-e134.
98. J. Ahlawat, G. Guillama Barroso, S. Masoudi Asil, M. Alvarado, I. Armendariz, J. Bernal, X. Carabaza, S. Chavez, P. Cruz, V. Escalante, S. Estorga, D. Fernandez, C. Lozano, M. Marrufo, N. Ahmad, S. Negrete, K. Olvera, X. Parada, B. Portillo, A. Ramirez, R. Ramos, V. Rodriguez, P. Rojas, J. Romero, D. Suarez, G. Urueta, S. Viel and M. Narayan, *ACS Omega*, 2020, **5**, 12583-12595.
99. M. Heymans, R. Figueiredo, L. Dehouck, D. Francisco, Y. Sano, F. Shimizu, T. Kanda, R. Bruggmann, B. Engelhardt, P. Winter, F. Gosselet and M. Culot, *Fluids Barriers CNS*, 2020, **17**, 48-72.
100. I. Wilhelm and I. A. Krizbai, *Molecular Pharmaceutics*, 2014, **11**, 1949-1963.
101. A. Reichel, *Curr Drug Metab*, 2006, **7**, 183-203.
102. V. Berezowski, C. Landry, S. Lundquist, L. Dehouck, R. Cecchelli, M. P. Dehouck and L. Fenart, *Pharmaceutical Research*, 2004, **21**, 756-760.
103. R. Cecchelli, S. Aday, E. Sevin, C. Almeida, M. Culot, L. Dehouck, C. Coisne, B. Engelhardt, M. P. Dehouck and L. Ferreira, *PLoS One*, 2014, **9**, e99733.
104. S. Nakagawa, M. A. Deli, H. Kawaguchi, T. Shimizudani, T. Shimono, A. Kittel, K. Tanaka and M. Niwa, *Neurochem Int*, 2009, **54**, 253-263.
105. R. Booth and H. Kim, *Lab Chip*, 2012, **12**, 1784-1792.
106. M. Clemens-Hemmelmann, C. Kuffner, V. Metz, L. Kircher, U. Schmitt, C. Hiemke, R. Postina and R. Zentel, *Amphiphilic Copolymers Shuttle Drugs Across the Blood–Brain Barrier* Macromolecular bioscience, 2016.
107. C. Celia, D. Cosco, D. Paolino and M. Fresta, *Med Res Rev*, 2011, **31**, 716-756.
108. W. Zhang, A. Mehta, Z. Tong, L. Esser and N. H. Voelcker, *Adv Sci (Weinh)*, 2021, **8**, 2003937.

109. K. A. Woodrow, Y. Cu, C. J. Booth, J. K. Saucier-Sawyer, M. J. Wood and W. Mark Saltzman, *Nature Materials*, 2009, **8**, 526-533.
110. S. L. Demento, S. C. Eisenbarth, H. G. Foellmer, C. Platt, M. J. Caplan, W. Mark Saltzman, I. Mellman, M. Ledizet, E. Fikrig, R. A. Flavell and T. M. Fahmy, *Vaccine*, 2009, **27**, 3013-3021.
111. T. Patel, J. Zhou, J. M. Piepmeier and W. M. Saltzman, *Advanced Drug Delivery Reviews*, 2012, **64**, 701-705.
112. Y. Bai, F.-Y. Xie and W. Tian, *Chinese Journal of Polymer Science*, 2018, **36**, 406-416.
113. H. Liu, H. Chen, F. Cao, D. Peng, W. Chen and C. Zhang, *Polymers (Basel)*, 2019, **11**, 820.
114. A. Car, P. Baumann, J. T. Duskey, M. Chami, N. Bruns and W. Meier, *Biomacromolecules*, 2014, **15**, 3235-3245.
115. C. A. Figg, R. N. Carmean, K. C. Bentz, S. Mukherjee, D. A. Savin and B. S. Sumerlin, *Macromolecules*, 2017, **50**, 935-943.
116. N. Raval, D. Kalyane, R. Maheshwari and R. K. Tekade, in *Basic Fundamentals of Drug Delivery*, ed. R. K. Tekade, Academic Press, 2019, **5**, pp. 173-201.
117. J. C. Olivier, L. Fenart, R. Chauvet, C. Pariat, R. Cecchelli and W. Couet, *Pharm Res*, 1999, **16**, 1836-1842.
118. L. E. Freed, G. Vunjak-Novakovic, R. J. Biron, D. B. Eagles, D. C. Lesnoy, S. K. Barlow and R. Langer, *Bio/Technology*, 1994, **12**, 689-693.
119. Y. S. Yim, J.-s. Choi, G. T. Kim, C. H. Kim, T.-H. Shin, D. G. Kim and J. Cheon, *Chemical Communications*, 2012, **48**, 61-63.
120. Y. Zhu, C. Liu and Z. Pang, *Biomolecules*, 2019, **9**.
121. D. B. Vieira and L. F. Gamarra, *Int J Nanomedicine*, 2016, **11**, 5381-5414.
122. S. Whitelam and R. L. Jack, *Annu Rev Phys Chem*, 2015, **66**, 143-163.
123. P. J. Lu, E. Zaccarelli, F. Ciulla, A. B. Schofield, F. Sciortino and D. A. Weitz, *Nature*, 2008, **453**, 499-503.
124. R. Gutzler, L. Cardenas and F. Rosei, *Chemical Science*, 2011, **2**, 2290-2300.
125. C.-A. Palma, M. Bonini, T. Breiner and P. Samorì, *Advanced materials* 2009, **21**, 1383-1386.
126. W. Lu, in *Encyclopedia of Nanotechnology*, ed. B. Bhushan, Springer Netherlands, Dordrecht, 2012, DOI: 10.1007/978-90-481-9751-4_274, pp. 2371-2382.
127. M. C. Branco and J. P. Schneider, *Acta Biomater*, 2009, **5**, 817-831.
128. V. P. Torchilin, *Pharm Res*, 2007, **24**, 1-16.
129. D. Bennet and S. Kim, 2014, **8,**pp. 257-310.
130. D. J. Overstreet, H. A. Von Recum and B. L. Vernon, in *Injectable Biomaterials*, ed. B. Vernon, *Woodhead Publishing,* 2011, **6**, pp. 95-141.
131. K. M. Pustulka, A. R. Wohl, H. S. Lee, A. R. Michel, J. Han, T. R. Hoye, A. V. McCormick, J. Panyam and C. W. Macosko, *Molecular pharmaceutics*, 2013, **10**, 4367-4377.
132. X. Wang, P. Gao, Y. Yang, H. Guo and D. Wu, *Nature Communications*, 2018, **9**, 2772.
133. M. C. García, C. Aloisio, R. Onnainty and G. Ullio-Gamboa, in *Nanobiomaterials*, ed. R. Narayan, *Woodhead Publishing*, 2018, **9**, pp. 41-94.
134. Y. Xie, J. T. Husband, M. Torrent-Sucarrat, H. Yang, W. Liu and R. K. O'Reilly, *Chemical Communications*, 2018, **54**, 3339-3342.
135. A. B. Mabire, M. P. Robin, H. Willcock, A. Pitto-Barry, N. Kirby and R. K. O'Reilly, *Chemical Communications*, 2014, **50**, 11492-11495.
136. A. B. Mabire, M. P. Robin, W. D. Quan, H. Willcock, V. G. Stavros and R. K. O'Reilly, *Chem Commun (Camb)*, 2015, **51**, 9733-9736.
137. A. B. Mabire, M. P. Robin, W.-D. Quan, H. Willcock, V. G. Stavros and R. K. O'Reilly, *Chemical Communications*, 2015, **51**, 9733-9736.
138. R. Nicoară, M. Ilieș, A. Uifălean, C. A. Iuga and F. Loghin, *Applied Sciences*, 2019, **9**, 4789.
139. J. Wolfram, Y. Yang, J. Shen, A. Moten, C. Chen, H. Shen, M. Ferrari and Y. Zhao, *Colloids and Surfaces B: Biointerfaces*, 2014, **124**, 17-24.

140. M. P. Monopoli, C. Åberg, A. Salvati and K. A. Dawson, *Nature Nanotechnology*, 2012, **7**, 779-786.
141. S. Milani, F. Baldelli Bombelli, A. S. Pitek, K. A. Dawson and J. Rädler, *ACS Nano*, 2012, **6**, 2532-2541.
142. L. B. Nguyen VH, *Int J Nanomedicine*, 2017, **12**, 3137-3151.
143. T. Cedervall, I. Lynch, S. Lindman, T. Berggård, E. Thulin, H. Nilsson, K. A. Dawson and S. Linse, *Proceedings of the National Academy of Sciences*, 2007, **104**, 2050-2055.
144. F. Alexis, E. Pridgen, L. K. Molnar and O. C. Farokhzad, *Molecular Pharmaceutics*, 2008, **5**, 505-515.
145. Z. J. Deng, M. Liang, I. Toth, M. J. Monteiro and R. F. Minchin, *ACS Nano*, 2012, **6**, 8962-8969.
146. V. Mirshafiee, M. Mahmoudi, K. Lou, J. Cheng and M. L. Kraft, *Chemical Communications*, 2013, **49**, 2557-2559.
147. A. Kurtz-Chalot, C. Villiers, J. Pourchez, D. Boudard, M. Martini, P. N. Marche, M. Cottier and V. Forest, *Materials Science and Engineering: C*, 2017, **75**, 16-24.
148. A. Salvati, A. S. Pitek, M. P. Monopoli, K. Prapainop, F. B. Bombelli, D. R. Hristov, P. M. Kelly, C. Åberg, E. Mahon and K. A. Dawson, *Nature Nanotechnology*, 2013, **8**, 137-143.
149. Q. Dai, C. Walkey and W. C. Chan, *Angew Chem Int Ed Engl*, 2014, **53**, 5093-5096.
150. C.-Y. Sun, S. Shen, C.-F. Xu, H.-J. Li, Y. Liu, Z.-T. Cao, X.-Z. Yang, J.-X. Xia and J. Wang, *Journal of the American Chemical Society*, 2015, **137**, 15217-15224.
151. I. García, A. Sánchez-Iglesias, M. Henriksen-Lacey, M. Grzelczak, S. Penadés and L. M. Liz-Marzán, *Journal of the American Chemical Society*, 2015, **137**, 3686-3692.
152. F. Xu, M. Reiser, X. Yu, S. Gummuluru, L. Wetzler and B. M. Reinhard, *ACS Nano*, 2016, **10**, 1189-1200.
153. M. Inam, G. Cambridge, A. Pitto-Barry, Z. P. L. Laker, N. R. Wilson, R. T. Mathers, A. P. Dove and R. K. O'Reilly, *Chemical Science*, 2017, **8**, 4223-4230.
154. M. Inam, J. R. Jones, M. M. Pérez-Madrigal, M. C. Arno, A. P. Dove and R. K. O'Reilly, *ACS Central Science*, 2018, **4**, 63-70.
155. N. Petzetakis, A. P. Dove and R. K. O'Reilly, *Chemical Science*, 2011, **2**, 955-960.
156. N. Petzetakis, D. Walker, A. P. Dove and R. K. O'Reilly, *Soft Matter*, 2012, **8**, 7408-7414.
157. A. Pitto-Barry, N. Kirby, A. P. Dove and R. K. O'Reilly, *Polymer Chemistry*, 2014, **5**, 1427-1436.
158. L. Sun, A. Pitto-Barry, N. Kirby, T. L. Schiller, A. M. Sanchez, M. A. Dyson, J. Sloan, N. R. Wilson, R. K. O'Reilly and A. P. Dove, *Nature Communications*, 2014, **5**, 5746.
159. L. Sun, N. Petzetakis, A. Pitto-Barry, T. L. Schiller, N. Kirby, D. J. Keddie, B. J. Boyd, R. K. O'Reilly and A. P. Dove, *Macromolecules*, 2013, **46**, 9074-9082.
160. I. Andreana, V. Bincoletto, M. Manzoli, F. Rodà, V. Giarraputo, P. Milla, S. Arpicco and B. Stella, *Materials (Basel)*, 2023, **16,** 1212-1226.
161. E. Trenkenschuh and W. Friess, *European Journal of Pharmaceutics and Biopharmaceutics*, 2021, **165**, 345-360.
162. T. Chen, X. Zhao and Y. Weng, *Front Chem*, 2022, **10**, 1107620.
163. N. Petzetakis, M. P. Robin, J. P. Patterson, E. G. Kelley, P. Cotanda, P. H. Bomans, N. A. Sommerdijk, A. P. Dove, T. H. Epps, 3rd and R. K. O'Reilly, *ACS Nano*, 2013, **7**, 1120-1128.
164. M. Oyo and Y. Masaaki, 1967, **40**, 2380-2382.
165. R. Augustine, A. Hasan, R. Primavera, R. J. Wilson, A. S. Thakor and B. D. Kevadiya, *Materials Today Communications*, 2020, **25**, 101692.
166. L. Johnson, D. M. Gray, E. Niezabitowska and T. O. McDonald, *Nanoscale*, 2021, **13**, 7879-7896.
167. C. Zhu and J. Nicolas, *Biomacromolecules*, 2022, **23**, 3043-3080.
168. L. MacFarlane, C. Zhao, J. Cai, H. Qiu and I. Manners, *Chemical Science*, 2021, **12**, 4661-4682.
169. M. C. Arno, M. Inam, Z. Coe, G. Cambridge, L. J. Macdougall, R. Keogh, A. P. Dove and R. K. O'Reilly, *Journal of the American Chemical Society*, 2017, **139**, 16980-16985.

170. X. He, Y. He, M.-S. Hsiao, R. L. Harniman, S. Pearce, M. A. Winnik and I. Manners, *Journal of the American Chemical Society*, 2017, **139**, 9221-9228.
171. M. Brzeziński and T. Biela, *Polymer International*, 2015, **64**, 1667-1675.
172. G. C. Sosso, J. Chen, S. J. Cox, M. Fitzner, P. Pedevilla, A. Zen and A. Michaelides, *Chem Rev*, 2016, **116**, 7078-7116.
173. U. Tritschler, S. Pearce, J. Gwyther, G. R. Whittell and I. Manners, *Macromolecules*, 2017, **50**, 3439-3463.
174. E. Capuana, F. Lopresti, M. Ceraulo and V. La Carrubba, *Polymers (Basel)*, 2022, **14**, 1153
175. J. R. Finnegan, X. He, S. T. G. Street, J. D. Garcia-Hernandez, D. W. Hayward, R. L. Harniman, R. M. Richardson, G. R. Whittell and I. Manners, *Journal of the American Chemical Society*, 2018, **140**, 17127-17140.
176. H.-x. Lin, Z.-c. Lei, Z.-y. Jiang, C.-p. Hou, D.-y. Liu, M.-m. Xu, Z.-q. Tian and Z.-x. Xie, *Journal of the American Chemical Society*, 2013, **135**, 9311-9314.
177. N. Baig, I. Kammakakam and W. Falath, *Materials Advances*, 2021, **2**, 1821-1871.
178. A. Mattei, R. S. Hong, H. Dietrich, D. Firaha, J. Helfferich, Y. M. Liu, K. Sasikumar, N. S. Abraham, R. Miglani Bhardwaj, M. A. Neumann and A. Y. Sheikh, *Journal of Chemical Theory and Computation*, 2022, **18**, 5725-5738.
179. M. Karimi, P. S. Zangabad, F. Mehdizadeh, H. Malekzad, A. Ghasemi, S. Bahrami, H. Zare, M. Moghoofei, A. Hekmatmanesh and M. R. Hamblin, *Nanoscale*, 2017, **9**, 1356-1392.
180. S. Yadav, A. K. Sharma and P. Kumar, *Front Bioeng Biotechnol*, 2020, **8**, 127.
181. F. C. Meldrum and C. O'Shaughnessy, *Advanced Materials*, 2020, **32**, 2001068.
182. C. E. Ellis, J. D. Garcia-Hernandez and I. Manners, *Journal of the American Chemical Society*, 2022, **144**, 20525-20538.
183. Y. Fu and W. J. Kao, *Expert Opin Drug Deliv*, 2010, **7**, 429-444.
184. Y. Qiao and Y. Men, *Macromolecules*, 2017, **50**, 5490-5497.
185. W. Zhou, S. Z. D. Cheng, S. Putthanarat, R. K. Eby, D. H. Reneker, B. Lotz, S. Magonov, E. T. Hsieh, R. G. Geerts, S. J. Palackal, G. R. Hawley and M. B. Welch, *Macromolecules*, 2000, **33**, 6861-6868.
186. a. B. L. Stephen Z. D. Cheng, *Philosophical Transactions: Mathematical, Physical and Engineering Sciences*, 2003,**156**, 517–537.
187. J. Yang, T. Zhao, Y. Zhou, L. Liu, G. Li, E. Zhou and X. Chen, *Macromolecules*, 2007, **40**, 2791-2797.
188. C. Yang, Z.-X. Li and J.-T. Xu, *Journal of Polymer Science*, 2022, **60**, 2153-2174.
189. C. Park, C. De Rosa, L. J. Fetters and E. L. Thomas, *Macromolecules*, 2000, **33**, 7931-7938.
190. Y. Gong, W. Song, Y. Wu, D. Zhang, Y. Liu, Q. Zhao, M. He and X. Chen, *Polymers and Polymer Composites*, 2019, **28**, 77-88.
191. Y. Zhu, L. Han, H. Fan, M. Wang, R. Qi, Y. Zhao and F. He, *Macromolecules*, 2020, **53**, 3217-3223.
192. M. Awashra and P. Młynarz, *Nanoscale Advances*, 2023, **5**, 2674-2723.
193. M. Inam, J. R. Jones, M. M. Pérez-Madrigal, M. C. Arno, A. P. Dove and R. K. O'Reilly, *ACS Cent Sci*, 2018, **4**, 63-70.
194. E. G. Knox, M. R. Aburto, G. Clarke, J. F. Cryan and C. M. O'Driscoll, *Mol Psychiatry*, 2022, **27**, 2659-2673.
195. M. Brust, O. Aouane, M. Thiébaud, D. Flormann, C. Verdier, L. Kaestner, M. W. Laschke, H. Selmi, A. Benyoussef, T. Podgorski, G. Coupier, C. Misbah and C. Wagner, *Scientific Reports*, 2014, **4**, 4348-4369.
196. A. E. Nel, L. Mädler, D. Velegol, T. Xia, E. M. Hoek, P. Somasundaran, F. Klaessig, V. Castranova and M. Thompson, *Nat Mater*, 2009, **8**, 543-557.
197. M. Jiang, J. D. Olarte-Plata and F. Bresme, *The Journal of Chemical Physics*, 2022, **4,** 044701.

198. Q. Wei, T. Becherer, S. Angioletti-Uberti, J. Dzubiella, C. Wischke, A. T. Neffe, A. Lendlein, M. Ballauff and R. Haag, *Angewandte Chemie International Edition*, 2014, **53**, 8004-8031.
199. J. W. Chang, A. Armaou and R. M. Rioux, *The Journal of Physical Chemistry B*, 2021, **125**, 8075-8087.
200. M. Winiewska, E. Bugajska and J. Poznański, *PLoS One*, 2017, **12**, e0173260.
201. V. K. Srivastava and R. Yadav, in *Data Processing Handbook for Complex Biological Data Sources*, ed. G. Misra, Academic Press, 2019, **4**, pp. 125-137.
202. F. Villanueva-Flores, A. Castro-Lugo, O. T. Ramírez and L. A. Palomares, *Nanotechnology*, 2020, **31**, 132002.
203. M. Inam, G. Cambridge, A. Pitto-Barry, Z. P. L. Laker, N. R. Wilson, R. T. Mathers, A. P. Dove and R. K. O'Reilly, *Chem Sci*, 2017, **8**, 4223-4230.
204. C. Sinturel, M. Vayer, R. Erre and H. Amenitsch, *European Polymer Journal*, 2009, **45**, 2505-2512.
205. T. Vilgis and A. Halperin, *Macromolecules*, 1991, **24**, 2090-2095.
206. L. R. MacFarlane, X. Li, C. F. J. Faul and I. Manners, *Macromolecules*, 2021, **54**, 11269-11280.
207. Y. He, J.-C. Eloi, R. L. Harniman, R. M. Richardson, G. R. Whittell, R. T. Mathers, A. P. Dove, R. K. O'Reilly and I. Manners, *Journal of the American Chemical Society*, 2019, **141**, 19088-19098.
208. Z. Liu, H. Fan, W. Li, G. Bai, X. Li, N. Zhao, J. Xu, F. Zhou, X. Guo, B. Dai, E. Benassi and X. Jia, *Nanoscale*, 2019, **11**, 4751-4758.
209. Y. Chen, L. Wang, W. Chen, C. Zhong, S. Li, J. Shao, G. Li and H. Hou, *CrystEngComm*, 2022, **24**, 3903-3912.
210. J. Sun, Z. Hong, L. Yang, Z. Tang, X. Chen and X. Jing, *Polymer*, 2004, **45**, 5969-5977.
211. R. V. Castillo and A. J. Müller, *Progress in Polymer Science*, 2009, **34**, 516-560.
212. N. Petzetakis, M. P. Robin, J. P. Patterson, E. G. Kelley, P. Cotanda, P. H. H. Bomans, N. A. J. M. Sommerdijk, A. P. Dove, T. H. Epps, III and R. K. O'Reilly, *ACS Nano*, 2013, **7**, 1120-1128.
213. M. Jafari and F. Mehrnejad, *PLoS One*, 2016, **11**, e0165213.
214. P. Ferraboschi, S. Ciceri and P. Grisenti, *Antibiotics (Basel)*, 2021, **10**, 1534-1550
215. G. Bashiri, M. S. Padilla, K. L. Swingle, S. J. Shepherd, M. J. Mitchell and K. Wang, *Lab Chip*, 2023, **23**, 1432-1466.
216. N. J. Warren, O. O. Mykhaylyk, D. Mahmood, A. J. Ryan and S. P. Armes, *Journal of the American Chemical Society*, 2014, **136**, 1023-1033.
217. B. Charleux, G. Delaittre, J. Rieger and F. D'Agosto, *Macromolecules*, 2012, **45**, 6753-6765.
218. H. Phan, V. Taresco, J. Penelle and B. Couturaud, *Biomaterials Science*, 2021, **9**, 38-50.
219. N. J. W. Penfold, J. Yeow, C. Boyer and S. P. Armes, *ACS Macro Letters*, 2019, **8**, 1029-1054.
220. M. J. Derry, L. A. Fielding and S. P. Armes, *Progress in Polymer Science*, 2016, **52**, 1-18.
221. J. Wan, B. Fan and S. H. Thang, *Chem Sci*, 2022, **13**, 4192-4224.
222. P.-E. Millard, L. Barner, M. H. Stenzel, T. P. Davis, C. Barner-Kowollik and A. H. E. Müller, *Macromolecular Rapid Communications*, 2006, **27**, 821-828.
223. M. Y. Khan, M.-S. Cho and Y.-J. Kwark, *Macromolecules*, 2014, **47**, 1929-1934.
224. Y. Ma, P. Gao, Y. Ding, L. Huang, L. Wang, X. Lu and Y. Cai, *Macromolecules*, 2019, **52**, 1033-1041.
225. S. L. Brown, C. M. Rayner, S. Graham, A. Cooper, S. Rannard and S. Perrier, *Chem Commun (Camb)*, 2007, **21**, 2145-2147.
226. J. Yeow and C. Boyer, *Adv Sci (Weinh)*, 2017, **4**, 1700137.
227. L. D. Blackman, K. E. B. Doncom, M. I. Gibson and R. K. O'Reilly, *Polymer Chemistry*, 2017, **8**, 2860-2871.
228. W. M. Pardridge, *J Drug Target*, 2010, **18**, 157-167.
229. J. Kreuter, *J Microencapsul*, 2013, **30**, 49-54.

230. J. Samal, A. L. Rebelo and A. Pandit, *Adv Drug Deliv Rev*, 2019, **148**, 68-145.
231. T. Patel, J. Zhou, J. M. Piepmeier and W. M. Saltzman, *Adv Drug Deliv Rev*, 2012, **64**, 701-705.
232. M. Vert, Y. Doi, K.-H. Hellwich, M. Hess, P. Hodge, P. Kubisa, M. Rinaudo and F. Schué, *Pure and Applied Chemistry*, 2012, **84**, 377-410.
233. T. T. Zhang, W. Li, G. Meng, P. Wang and W. Liao, *Biomater Sci*, 2016, **4**, 219-229.
234. S. Aday, R. Cecchelli, D. Hallier-Vanuxeem, M. P. Dehouck and L. Ferreira, *Trends in Biotechnology*, 2016, **34**, 382-393.
235. C. D. Kuhnline Sloan, P. Nandi, T. H. Linz, J. V. Aldrich, K. L. Audus and S. M. Lunte, *Annu Rev Anal Chem (Palo Alto Calif)*, 2012, **5**, 505-531.
236. S. J. Parkinson, S. Tungsirisurp, C. Joshi, B. L. Richmond, M. L. Gifford, A. Sikder, I. Lynch, R. K. O'Reilly and R. M. Napier, *Nature Communications*, 2022, **13**, 7385-7399.
237. S. Varlas, R. Keogh, Y. Xie, S. L. Horswell, J. C. Foster and R. K. O'Reilly, *Journal of the American Chemical Society*, 2019, **141**, 20234-20248.
238. M. Weiss, J. Fan, M. Claudel, T. Sonntag, P. Didier, C. Ronzani, L. Lebeau and F. Pons, *Journal of Nanobiotechnology*, 2021, **19**, 5.
239. J. K. Patra, G. Das, L. F. Fraceto, E. V. R. Campos, M. d. P. Rodriguez-Torres, L. S. Acosta-Torres, L. A. Diaz-Torres, R. Grillo, M. K. Swamy, S. Sharma, S. Habtemariam and H.-S. Shin, *Journal of Nanobiotechnology*, 2018, **16**, 71.
240. H. Xu, S. Li and Y.-S. Liu, *Signal Transduction and Targeted Therapy*, 2022, **7**, 231.
241. S. Saha, N. Sachivkina, A. Karamyan, E. Novikova and T. Chubenko, *Biomedicines*, 2024, **12**.
242. H. Sun, C. Jiang, L. Wu, X. Bai and S. Zhai, *Front Bioeng Biotechnol*, 2019, **7**, 414.
243. P. Khanna, C. Ong, B. H. Bay and G. H. Baeg, *Nanomaterials (Basel)*, 2015, **5**, 1163-1180.
244. T. Kowada, H. Maeda and K. Kikuchi, *Chemical Society Reviews*, 2015, **44**, 4953-4972.
245. S. J. Byard, M. Williams, B. E. McKenzie, A. Blanazs and S. P. Armes, *Macromolecules*, 2017, **50**, 1482-1493.
246. D. Bartczak and A. G. Kanaras, *Langmuir*, 2011, **27**, 10119-10123.
247. L. D. Field, S. A. Walper, K. Susumu, E. Oh, I. L. Medintz and J. B. Delehanty, *Sensors*, 2015, **15**, 30457-30468.
248. A. S. Pitek, D. O'Connell, E. Mahon, M. P. Monopoli, F. B. Bombelli and K. A. Dawson, *PLOS ONE*, 2012, **7**, e40685.
249. K. Amornwachirabodee, S. Khramchantuk, P. Pienpinijtham, N. Israsena, T. Palaga and S. Wanichwecharungruang, *ACS Omega*, 2018, **3**, 6833-6840.
250. G. D. Byrne, D. Vllasaliu, F. H. Falcone, M. G. Somekh and S. Stolnik, *Molecular Pharmaceutics*, 2015, **12**, 3862-3870.
251. V. Capella, R. E. Rivero, A. C. Liaudat, L. E. Ibarra, D. A. Roma, F. Alustiza, F. Mañas, C. A. Barbero, P. Bosch, C. R. Rivarola and N. Rodriguez, *Heliyon*, 2019, **5**, e01474.
252. H. Yu, Y. Zou, Y. Wang, X. Huang, G. Huang, B. D. Sumer, D. A. Boothman and J. Gao, *ACS Nano*, 2011, **5**, 9246-9255.
253. S. Mazumdar, D. Chitkara and A. Mittal, *Acta Pharmaceutica Sinica B*, 2021, **11**, 903-924.
254. M. S. Khan, N. S. Dosoky and J. D. Williams, *Int J Mol Sci*, 2013, **14**, 21561-21597.
255. W. Au - Zhao, L. Au - Han, Y. Au - Bae and D. S. Au - Manickam, *JoVE*, 2019, DOI: doi:10.3791/58900, e58900.
256. X. Wang, J. Iqbal, D. Rahmat and A. Bernkop-Schnürch, *Int J Pharm*, 2012, **438**, 217-224.
257. F. Leve, D. P. Bonfim, G. Fontes and J. A. Morgado-Díaz, *Nanomedicine*, 2019, **14**, 1565-1578.
258. J. Gavard, *Cell Adh Migr*, 2014, **8**, 158-164.
259. A. Prlj, L. Vannay and C. Corminboeuf, *Helvetica Chimica Acta*, 2017, **100**, e1700093.
260. M. G. Paez-Segala, M. G. Sun, G. Shtengel, S. Viswanathan, M. A. Baird, J. J. Macklin, R. Patel, J. R. Allen, E. S. Howe, G. Piszczek, H. F. Hess, M. W. Davidson, Y. Wang and L. L. Looger, *Nature Methods*, 2015, **12**, 215-218.

261. S. B. Keel, R. Doty, L. Liu, E. Nemeth, S. Cherian, T. Ganz and J. L. Abkowitz, *Exp Hematol*, 2015, **43**, 469-478.e466.
262. B. Srinivasan, A. R. Kolli, M. B. Esch, H. E. Abaci, M. L. Shuler and J. J. Hickman, *J Lab Autom*, 2015, **20**, 107-126.
263. A. M. Butt, H. C. Jones and N. J. Abbott, *J Physiol*, 1990, **429**, 47-62.

CHAPTER 5- Conclusions and future work

5.1 Overview

The main focus of this thesis has been investigation and development of polymeric nanoparticles (NPs) as drug delivery systems for blood and brain barrier (BBB) permeation. Three critical parameters governing NPs interaction with the BBB were identified and meticulously studied: charge, size, and shape. The polymeric NPs were self-assembled with three different methodologies flash nanoprecipitation (FNP), microfluidics reactor and slow addition from amphiphilic diblock copolymers Furthermore, employing the same polymers, diverse morphologies were achieved through crystallization-driven self-assembly (CDSA) methodology. Within both systems, thorough investigations into the protein corona phenomenon were conducted to ascertain NPs-protein interactions. Lastly, polymerisation induced self-assembly (PISA) NPs were synthesised and characterised. These PISA NPs underwent rigorous evaluation of their protein corona effect, viability, and capability to permeate an *in vitro* BBB model. The assessment of all systems encompassed considerations of manufacturing feasibility, versatility, and their potential biomedical applications within the field of drug delivery.

5.2 Conclusions

5.2.1 Diblock copolymers & protein corona limitations

In this study different diblock copolymers were synthesized through controlled polymerization and characterized. After the assembly into nanoparticles they were examined with multiple techniques like DLS, zeta, TEM and AFM to examine the characteristics of the nanoparticle. Herein three different self-assembly techniques and their effect on the NPs formulation have been demonstrated. FNP and microfluidic reactor are fast and scalable, but they tend to make two different size populations because of the kinetic entrapment in the solutions. Positive, neutral and negative charged particles were

synthesized, characterized and optimised. An evaluation of the protein corona formation was conducted with a 4:1 BSA : polymer molar ratio. While the neutral particles remain unaffected with addition of the negatively charged BSA, the positively charged nanoparticles exhibited an increase in the hydrodynamic radius from 60 nm to 223 nm. AFM measurements revealed protein-nanoparticles agglomeration due to their electrostatic interactions. Confocal studies verified the colocalization that positively charged NPs interact with negatively charged protein, and ITC confirmed that this is a strong interaction. Finally, zebrafish experiments were conducted and confirmed that positively charged NPs are cytotoxic but the neutrally charged particles are viable.

5.2.2 CDSA microstructures & protein corona limitations

The investigation into crystallization-driven self-assembly (CDSA) of diblock copolymers yielded valuable insights into diverse morphologies conducive to blood-brain barrier (BBB) permeation. Various structures, including positively charged diamond-shaped microstructures, negatively charged cylindrical micelles, and neutrally charged molecular caterpillars, were synthesized and characterized. Moreover, elucidation of the protein corona phenomenon on positively charged nanoparticles provided crucial understanding of nanoparticle-protein interactions, emphasizing the significance of surface properties in nanoparticle design.

Despite challenges in optimizing CDSA parameters for desired morphology, such as the observed screw dislocation effect, the technique proved versatile in generating various morphologies. Furthermore, the investigation into protein corona formation highlighted the influence of electrostatic charges on corona composition, underscoring the complexity of nanoparticle interactions in biological environments.

Looking ahead, CDSA holds promise as a platform for exploring intricate nanoparticle shapes, with potential applications in tissue engineering and drug delivery. Continued research and optimization efforts are essential for harnessing the full potential of CDSA in biomedical applications, paving the way for innovative therapeutic strategies targeting neurodegenerative diseases and beyond.

However, optimization will be necessary as certain microstructures, particularly the larger ones, may not be suitable for BBB applications due to their size. Therefore, further refinement and optimization of CDSA parameters are imperative to tailor nanoparticle morphology for enhanced BBB permeation

5.2.3 PISA NPs and BBB permeation

Polymerization-Induced Self-Assembly (PISA) yielded small, monodisperse, and readily reproducible spherical nanoparticles (NPs), which proved facile to manufacture, label with fluorescence, and functionalize with Transferrin. Following comprehensive synthesis and characterization, the NPs underwent evaluation for cytotoxicity and stability in endothelium conditioning media. Remarkably, all PISA NPs demonstrated cellular viability, even at concentrations of 1 mg/mL, with the exception of the positively charged PQDMAE, which exhibited viability only at 0.01 mg/mL.

Live cell internalization studies showcased enhanced endocytosis of the nanoparticles following 24 hours of incubation, providing quantifiable insights into PISA NP permeation. Internalization assays in CD34+ cell lines revealed maximal uptake of the 62 Tf particle with a substantial difference from its counterparts NPs. Evaluation of permeability through an in vitro blood-brain barrier (BBB) model indicated that PAA Tf had the potential to disrupt BBB integrity. Fluorescence-based quantification post-permeation revealed PDMA particles with the highest concentration, permeability percentage, while maintaining BBB characteristics unchanged. However, confocal microscopy revealed minimal nanoparticle uptake by cells, suggesting either possible fluorescence quenching or diffusion of the PISA NPs, due to immunocytochemistry treatments. This is an issue that needs further investigation.

Furthermore, investigations into the mechanism of PISA NPs with Tf revealed potential utilization of transferrin receptor-mediated transcytosis. Despite this, only 30% expression of the transferrin receptor was observed in the *in vitro* BBB model. Therefore, improvements in transferrin receptor abundance are warranted to ascertain the functionalization benefits. Alternative pathways such as insulin or albumin may offer viable alternatives for exploration.

In conclusion, PISA NPs demonstrate promise as potent drug delivery systems for BBB permeation. Their small size and electrophoretic mobility, easy functionalisation with ligands and suitable for drug loading constitutes them as an exceptional drug delivery system. Notably, PISA NPs exhibit biocompatibility and high levels of endocytosis. However, further experimentation and optimization are imperative before progression to in vivo studies.

5.3 Future work

Given its prominent role in this study, Polymerization-Induced Self-Assembly (PISA) nanoparticles (NPs) warrant thorough investigation. PISA presents notable advantages such as scalability, one-step synthesis, and the ability to achieve small nanoparticle sizes through self-assembly. Diblock copolymers, comprising the core of PISA, demand scrutiny across multiple self-assembly methodologies to optimize the resulting nanoparticles. While Crystallization-Driven Self-Assembly (CDSA) offers alternative shapes, achieving size and crystallinity optimization may prolong the process. Therefore, future studies will emphasize the exploration and refinement of PISA NPs.

Priority in future experimentation and investigation should focus on the examination of the fluorophore used in the PISA NPs. Without coherent confocal data to substantiate our findings, further experimentation cannot proceed effectively. A straightforward approach involves conducting fluorescence measurements with the fluorophore and selected agents to determine whether the observed issues are due to fluorophore quenching or diffusion issues related to immunocytochemistry protocols. If the fluorophore presents challenges, an alternative option such as Rhodamine, known for its resilience under confocal microscopy, could be considered.

Assessing enzymatic catalysis and degradation ratio, along with drug encapsulation and release characteristics, is vital for evaluating the effectiveness and feasibility of PISA NPs as drug delivery systems. Enzymatic degradation studies provide insights into nanoparticle stability in biological environments, while encapsulation efficiency and release kinetics determine drug loading capacity and delivery profiles. Optimization of nanoparticle design parameters is essential to achieve controlled drug release and enhance therapeutic efficacy.

Thorough characterization of enzymatic catalysis, degradation ratio, and drug release properties informs the design and optimization of PISA NPs for targeted drug delivery. Understanding these parameters enables the development of nanoparticle formulations with enhanced biocompatibility, stability, and therapeutic potential, paving the way for advanced drug delivery applications in various biomedical contexts.

Furthermore, the adoption of a three-dimensional (3D) blood-brain barrier (BBB) model offers several advantages over traditional two-dimensional (2D) models, rendering it a more representative and dynamic platform for studying nanoparticle permeability and interactions. Unlike 2D models, which often lack physiological relevance and fail to capture the intricate spatial organization of cellular components, a 3D BBB model better mimics the complex microenvironment of the brain vasculature. The dynamic nature of 3D BBB models, which allows for the flow of culture media and exchange of signalling molecules between cells, can facilitate the development and maintenance of higher levels of transferrin receptors on endothelial cells. The proximity of different cell types within the 3D model, coupled with the presence of physiological shear stress, may stimulate endothelial cells to upregulate transferrin receptor expression, thereby enhancing the efficiency of receptor-mediated transcytosis.

Lastly, extensive animal studies would be essential to ascertain the translational relevance of the obtained permeability data for biomedical applications. While *in vitro* models provide valuable insights into nanoparticle behaviour and interaction with biological systems, they may not fully recapitulate the complexities of in vivo environments. Animal studies, particularly in relevant disease models, allow for a comprehensive evaluation of the nanoparticles' efficacy, safety, and pharmacokinetics in a physiological context.